Astrophysical phenomena related to supermassive black holes

Searching for local particularities in the center of the Milky Way and extragalactic nuclei at high angular resolution

vorgelegt von
Jörg-Uwe Pott
aus Düsseldorf

Köln 2006

Dedicated to the European taxpayer.

Contents

Zusammenfassung (German abstract)

Die Arbeit enthält die Ergebnisse meiner Forschungsprojekte der vergangenen drei Jahre. Alle Projekte sind im Forschungsgebiet der Wechselwirkung zwischen einer Galaxie und einem super-massiven schwarzen Loch (SMSL) im Zentrum der Galaxie angesiedelt. Heutzutage geht man davon aus, dass zumindest in den meisten grossen Galaxien, die eine zentrale Verdickung in der Sternverteilung aufweisen, den sog. bulge, sich im Zentrum ein SMSL befindet. Diese SMSL können von einigen Millionen Sonnenmassen zu vielen Milliarden Sonnenmassen schwer sein. Die Existenz einer solchen enormen Massenkonzentration in Form eines schwarzen Lochs hat weitreichendere Auswirkungen, als die blosse Attraktion der umgebenden Materie. Die meist rotierende akkretierte Materie bildet eine sogenannte Akkretionsscheibe aus, die potentielle Energie z.B. über die magnetische Wechselwirkung in Strahlungsenergie umwandeln kann. Dieser Prozess kann bis zu hundert Mal stärker sein, als die Kernfusion, die das stellare Leuchten des allnächtlichen Sternenhimmels hervorruft. Galaxien, in deren Zentren eine solche leuchtende Akkretionsmaschine sitzt, werden aktive Galaxien genannt. Es ist anzunehmen, dass in den leuchtkräftigsten aktiven Galaxien auch die Wechselwirkung zwischen aktivem Kern und der umgebenden Galaxie am grössten ist. Tatsächlich sind z.B. Radiojets von sehr leuchtkräftigen aktiven Galaxien beobachtet worden, die aus dem allerinnersten mit sehr hoher Geschwindigkeit einen Elektronenstrahl ausstossen, der bis weit in die umgebende Galaxie hinreichen und dort mit der Umgebung wechselwirken kann. Auch Sternentstehung in der Galaxie kann durch eine Wech-selwirkung mit dem Zentralkörper angeregt oder verhindert werden und Untersuchungen haben gezeigt, dass die Leuchtkraft der stellaren Verdickung mit der Masse des zentralen SMSL korre-liert, obwohl der bulge nicht unter dem direkten gravitativen Einfluss des schwarzen Lochs steht.

Die Erforschung solcher Wechselwirkungen innerhalb eine SMSL/Galaxie-Systems ist oft durch die Entwicklung neuer Beobachtungstechniken vorangetrieben worden. Neuere, empfindlichere Instrumente können sowohl näher an die Zentralmasse heran, als auch besser weiter entfernte SMSL/Galaxie-Systeme beobachten, die typischerweise einen höheren Anteil von sehr aktiven Galaxien haben. Die Entwicklung neuer Beobachtungstechnologien ist für die astrophysikalische Forschung von zentraler Bedeutung. Ich stelle in der vorliegenden Arbeit sowohl Projekte vor, in denen neue Technologien getestet und eingesetzt werden, als auch Projekte in denen mit an-erkannten Methoden neue Erkenntnisse über SMSL/Galaxien Systeme gesammelt werden. Meine Forschungobjekte weisen alle unterschiedlichen Skalen auf, die in einem SMSL/Galaxie-System vorkommen können. Während ein Teil der gemachten Beobachtungen die Sterne in nächster Nähe unseres eigenen SMSL im Zentrum der Milchstrasse untersuchen, zielen andere auf globale Eigen-schaften der Galaxien ab, die Quasare enthalten. Quasare wiederum haben im Gegensatz zum zentralen SMSL der Milchstrasse ein sehr hohe Strahlungseffizienz.

Nach einer zusammenfassenden Darstellung der kompletten Arbeit ("summary") und deren Ein-bettung in den aktuellen astrophysikalischen Forschungszusammenhang folgen Einführungen in die astronomischen (Kapitel 1) und technischen Grundlagen (Kapitel 2), die für das Verständnis der Arbeit unerlässlich sind. In Kapitel 3 berichte ich von den ersten Messungen mit dem opti-schen Interferometer der Europäischen Südsternwarte (ESO), dem sog. VLTI in Chile. Ich habe anhand von Messungen einiger staubumhüllter Sterne in der zentralen Bogensekunde der Milch-strasse gezeigt, dass das VLTI bereits in seiner jetzigen begrenzten Ausbaustufe wissenschaftlich interessante Beiträge zur Erforschung der Stern- und Staubentstehung im Einflussbereich des SMSL liefern kann. In diesem Kapitel werden sowohl die verschiedenen neuen Beobach-tungsmöglichkeiten als auch direkte Anwendungen dargestellt.

Die folgenden Kapitel beschäftigen sich mit verschiedenen extragalaktischen Forschungsthemen,

in denen aber immer die Wechselwirkung zwischen einem aktiven Galaxienkern, hinter dem ein SMSL vermutet wird, und der umgebenden Galaxie im Vordergrund steht. In Kapitel 4 zeige ich, dass das neue sub-mm Teleskop der ESO bereits in der Lage ist, breite extragalaktische molekulare Emissionslinien zu messen, die Hinweise auf den Anregungszustand und -mechnismus des molekularen Gases liefern. Es wird vermutet, dass zumindest ein Teil des molekularen Gases als Futter für den zentralen Akkretionsprozess ein wichtige Rolle spielt. In Kapitel 5 stelle ich die Suche nach Hinweisen auf dieses dichte molekulare Gas in SMSL/Galaxie Systemen dar, die von sehr leuchtkräftigen aktiven Kernen dominiert sind. Ziel ist es, über die bekannten Anregungsmechanismen durch Sternentstehung hinaus Hinweise auf direkte Interaktion der Schwarzlochstrahlung mit dem molekularen Gas zu finden, die in einigen wenigen leuchtschwachen aktiven Kernen naher SMSL/Galaxie-Systemen bereits beobachtet wurde. Im Kapitel 6 der Arbeit wird mit der hochauflösenden Methode der Radiointerferometrie mit sehr langen Basislinien der Radiojet eines radio-lauten Quasars von der Nähe seiner inneren Entstehungsregion bis weit in die umgebende Galaxie hinein verfolgt. Ich kann sehr hohe Geschwindigkeiten in ungewöhnlich weiter Entfernung von dem Ursprung des Jets nachweisen.

Die Unterschiedlichkeit der gemachten Beobachtungen und Resultate zeigt, wie vielfältig der Forschungsgegenstand SMSL/Galaxien-Wechselwirkung sein kann. Die Dimension des Zentralkörpers spielt dabei eine wichtige Rolle. In unserer eigenen Galaxie befindet sich ein SMSL von relativ geringer Masse und sehr geringer Leuchtkraft, weswegen geringere Auswirkungen auf die umgebende Galaxie vermutet werden können. Allerdings sind durch die einzigartige Nähe zu, Zentrum unserer Galaxie trotzdem viele Effekte eines SMSL/Galaxie-Systems nur dort technisch auflösbar. Man kann annehmen, dass im Zentrum der Milchstrasse beobachtete Phänomene mit grösserer Intensität in anderen Galaxienkernen stattfinden, die eine relativ grössere Zentralmasse beherbergen. Das unterstreicht den Modellcharakter der Forschung am Galaktischen Zentrum. Die Beobachtungen der leuchtkräftigeren Quasare hingegen werden immer häufiger in Zusammenhang mit der kompletten Entstehung und Entwicklung ganzer Galaxien gebracht und tragen zum Verständnis unserer Kosmologie bei.

Summary

The thesis contains the results of my recent projects in astrophysical research. All projects aim at pushing the limits of our knowledge about the interaction between a galaxy, the fundamental building block of today's universe, and a supermassive black hole (SMBH) at its center. Over the past years a lot of observational evidence has been gathered for the current understanding, that at least a major part of the galaxies with a stellar bulge contain central SMBHs. The typical extragalactic approach consists of searching for the spectroscopic pattern of Keplerian rotation, produced by stars and gas, when orbiting a central dark mass (Kormendy & Richstone 1995). It suggests that a significant fraction of large galaxies host in their very nucleus a SMBH of millions to billions of solar masses (Kormendy & Gebhardt 2001). In the closest case, the center of our Milky Way, the most central stars, which can be imaged, were shown to move on orbits with circulation times of a few decades only, evidencing a mass and compactness of the dark counter part of the Keplerian motion, which can only be explained by a SMBH (Eckart & Genzel 1996; Ghez et al. 2000; Schödel et al. 2002).

Having acknowledged the widespread existence of SMBHs the obvious next step is investigating the interaction with their environment. Although the basic property of a SMBH, which is concentrating a huge amount of mass in a ludicrously small volume defined by the Schwarzschild radius, only creates a deep gravitational trough, its existence evokes much more phenomena than simply attracting the surrounding matter. It can trigger or exacerbate star formation via tidal forces (Morris 1993). It shapes the distribution of its surrounding matter to accretion discs, which themselves release gravitational potential energy as radiation, possibly due to magnetic friction (Blandford 1995). The radiation efficiency of such active galactic nuclei (AGN) can become roughly 100 times more efficient than atomic nuclear reactions in stars. In the most active galaxies known, the radiating accretion disc of the central SMBH engine easily outshines the stellar light of the entire galaxy (Blandford 1995). In addition to the light, plasma streams can emerge from the innermost regions at relativistic velocities, returning energy to the host galaxy (host) and creating jets and lobes with strong observational signatures, especially at radio and X-ray wavelengths (Wilson 2003).

New insights in the wide field of SMBH/host interaction are often related to the development of new, more sensitive instruments and telescopes. For example the idea, that a high luminosity AGN may result from a merger event between two galaxies, could only develop with the upcoming high resolution and sensitive imaging capabilities needed to detect the highly distorted host galaxy morphologies of (post-)merger galaxies (Heckman et al. 1986). Furthermore multi-wavelength approaches, which combine the results of measurements at different wavelengths, often lead to new conclusions or confirm unsecured hypotheses. Thus developing a new instrument can be as valuable as combining different datasets. I follow both approaches and developed projects which (i) deal with new instrumentation and telescope technology, (ii) combine datasets from different wavelengths and resolutions, and (iii) incorporate recent theoretical models and predictions, which can be verified empirically. While some projects are more focused on investigating the power of new observational techniques, others incorporate acknowledged instruments to probe predictions based on previous observations and models and trace special phenomena of SMBH/host interaction. But in most cases aspects of all three items appear.

The SMBH/host interaction results in phenomena at all linear size scales of the system, from the direct accretion of matter onto the central black hole up to radio jets crossing the entire galaxy. Thus interaction effects do not simply concentrate on the innermost region of a galaxy. Furthermore an increasing number of apparently totally distinct phenomena and properties of the SMBH/host sys-

tem appear to be related to each other, provoking unifying ideas and models to explain the galaxy formation and evolution. For example several different types of AGN are understood as projection or orientation effects, claiming that the same AGN looks totally different as viewed from different sides (e.g. Antonucci & Miller 1985).

The thesis is structured to reflect this general perception. All scales of size, AGN luminosity, and nuclear activity appear. The thesis consists of six chapters. The first two compile astrophysical and technical background of the individual projects, which themselves are presented in the following four chapters. While the first project (Chapter 3) deals with observations of the innermost parsec of our Galaxy, Chapter 4 presents data of the inner kpc of an active galaxy. The subjects of Chapters 5 and 6 are very luminous AGN/host systems, so-called QSOs. Whereas Chapter 5 presents global, spatially unresolved properties of SMBH/host systems, the radio jet, analyzed in the final Chapter 6, combines all size scales. It is investigated from close to its origin out to several kpc. The accretion onto the black hole of the Milky Way (Chapter 3) is extremely inefficient (Genzel et al. 2003a) and the SMBH possibly interacts dominantly via tidal forces only. The next discussed system (Chapter 4) is the prototype of moderately luminous Seyfert 2 AGN, NGC 1068. Here a strong local influence of the nuclear X-ray radiation is observed (Usero et al. 2004). Chapter 5 deals with the possible global importance of radiative interaction between highly luminous QSO AGN and the host. The radio jet in Chapter 6 definitely shows signs of interaction with the matter of its host several kpc away from the nucleus. Chapters 3-6 include a dedicated introductory and a conclusive section, which put the results obtained in the larger astrophysical context of the observation.

The observational techniques chosen vary in dependence of the observed phenomenon. One major goal of especially Chapters 3 and 4 is to prove by successful explorative observations the scientific perspectives of the new instruments. Chapter 3 deals with the pioneering interferometric infrared study of stellar sources and their surroundings in the immediate vicinity of the SMBH at the center of the Milky Way. I was able to use the resolving power of an optical large baseline interferometer (OLBI) to investigate for the first time the different structures and excitation conditions of interstellar and circumstellar dust in 200 mpc distance to the SMBH. It is unknown whether the standard models for star and dust formation, which themselves dominate the infrared appearance of an inactive galaxy as the Milky Way, still apply under the strong tidal forces of gravity, exerted by the central SMBH.

During the course of my doctoral research, I worked 2.5 years within the VLT Interferometry (VLTI) group of the European Southern Observatory (ESO) in München and Chile. I obtained the very first infrared fringes on GC sources and investigated the different instrument capabilities at the current sensitivity limit of the VLTI. The VLTI is the world leading stellar interferometric facility providing the infrastructure to combine the light of up to four 8m-class Adaptive Optics corrected telescopes, which themselves represent the state-of-the-art of optical-infrared telescope technology. The accomplished work includes the investigation of different data reduction techniques with respect to maximum accuracy and signal-to-noise ratios. The VLTI is right in the process of construction. While first modes are already open to the astronomical community, several advanced modes and instruments are still at different preliminary stages, ranging from early design studies to advanced instrument commissioning. The experiences of my VLTI observations, fully exploiting the currently available observing modes, and the data reduction were fed back via close collaboration to the Paranal Observatory and to the European science institutes of the instrument developing consortia[1]. I contributed to improve the observing process (in particular to

---

[1]Max-Planck Institut für Astronomie in Heidelberg (MPIA, `http://www.mpia.de`); Leiden Observatory (`http://www.strw.leidenuniv.nl`); Observatoire de la Cote d'Azur (`http://www.obs-nice.fr`)

the infrared-based target acquisition of the instrument, and to the clarification of the chopping parameters) and the standard data reduction package (wavelength calibration, software debugging). The most recent NIR three-baseline observations of the GCIRS 7 helped to uncover imperfections in the numerical delay line model, which is needed to track the fringes during the observations. The smaller coherence lengths of these wide band observations were an ideal case to optimize the detector integration times for reaching highest signal-to-noise-ratios (SNR).

The VLTI observations, described in Chapter 3, are the first observations of stellar interferometry in the infrared, which target objects through the 25 magnitudes of optical extinction along the line of sight toward the GC. One motivation for these observations, in addition to the direct scientific intention, was to create a showcase for advanced optical interferometry applications at the GC. An important part of the thesis is the detailed analysis of the achievable accuracy of the interferometric measurements. Such a precision study under the challenging conditions of off-axis optical AO guiding and faint target brightnesses close to the system limits has not been published before.

Most of the interferometric observations were executed in the mid-infrared (MIR) wavelength regime at 10 μm (N-band), a natural starting point, because the optical requirements to the accuracy of the VLTI infrastructure are lower at these longer infrared wavelengths. The observed GCIRS 3 is an outstanding source at 10 μm, being the most compact, brightest and isolated source at the GC. It bears significant signs of dust formation and will play a major role in understanding the dust formation and chemical properties of the local interstellar dust in the central parsec. The interferometric data of two observing seasons were interpreted together with different single telescope datasets. GCIRS 3 is known to be a very red luminous source, but no stellar spectrum could give away more detailed properties of the underlying source. I use a one-dimensional radiative transfer model to investigate the resolved dust shell properties, as observed with the 20 mas resolution of the VLTI at 10 μm. For the first time I can present results that show that the direct zone of dust formation around the deeply embedded star is observable. The temperature, derived from the spectral properties, and the spatial size, as derived from the high resolution interferometric dataset, show the cool star nature of the object.

Earlier spatially unresolved N-band spectroscopic observations found a significant increase of oxygen rich silicate absorption towards GCIRS 3, deeper than towards the neighboring stars. The spectral properties of the VLTI data show that the immediate dust shell, formed by IRS 3 is not responsible for this strong absorption and might be devoid of a significant amount of silicate, favoring GCIRS 3 being a cool supergiant of $\sim$ 3000 K stellar temperature, forming more carbon-rich dust. The main impact of this result on GC science is, that the silicate-poor dust formation of GCIRS 3 and its silicate-rich surroundings appear to be the best place to study the extraordinary enrichment of the GC dust with interstellar amorphous silicate molecules (Roche & Aitken 1985). The dust formation in the nucleus of a galaxy is important, since only a detailed understanding of its composition helps to interpret the observed spectra and spectral energy distribution of spatially unresolved dusty nuclei of other galaxies. Furthermore the confirmed existence of a second massive red supergiant so close to GCIRS 7, which is already known to be a red supergiant, challenges the theories of star formation in galactic nuclei.

Further currently possible VLTI-GC observations are presented in the following sections of Chapter 3. The dimensions of stellar bow-shocks are analyzed for the first time in the MIR to add information to the understanding of the kinematic features, which arise if massive stars with strong stellar winds ram into dense interstellar material. Such shock fronts can excite molecular hydrogen and add to the understanding of the excitation mechanisms in galactic nuclei (Pineau des Forêts et al. 2001). I show that such stellar bow-shocks are observable with the VLTI, and derive lower limits for their extension. Another set of first GC fringes was achieved in the near-infrared (NIR)

at 2 μm on GCIRS 7. In one section of this chapter I describe the special importance of this star for future interferometric phase-referencing experiments. Despite of the technical problems occurred, fringes were found on one of the observed baseline, proving the feasibility of a detailed interferometric study of this putative phase calibrator in the near future. Phase referencing will significantly increase the number of observable targets, as soon as the respective hardware will be implemented.

The following Chapter 4 reports on the first extragalactic sub-mm spectra of the innermost region in the Seyfert 2 prototype NGC 1068 with the new APEX telescope facility. The emission of the molecular rotational excitation lines CO(J=3-2) and HCN(J=4-3) were observed during the instrument testing phase. While the observations served for debugging the telescope operation, I prove that with dedicated data reduction already the current limited receiver capabilities are sufficient to measure broad extragalactic molecular line transitions in the sub-mm atmospheric transmission window. The observed lines are indispensable tracers of the warm and dense molecular gas (Papadopoulos & Seaquist 1999). The molecular gas is the major reservoir of matter in a galaxy, which supplies star formation and mass accretion onto the central SMBH.

In Chapter 5, I present the results of the search for rotational line transitions at 80 GHz, in particular the 1-0 transition of the HCN molecule. It traces gas densities larger than 10^4 cm^{-3} and is therefore a better quantitative tracers of the regions where star formation actually occurs than the stronger CO(1-0) transition, which correlates to the total amount of molecular gas which *could* be transformed into stars (Gao & Solomon 2004). The observed galaxies host a luminous quasar in their core. In nearby low luminosity AGN a relatively enhanced excitation of the HCN transition close to the central engine is observed (Usero et al. 2004). I investigate the hypothesis of an amplification and extension of this effect in high luminosity AGN from local nuclear to global galactic scales. Moreover the infrared luminosity ratios is used to trace global AGN dominance efficiently. Then the detectability of enhanced HCN intensities due to intense nuclear X-ray irradiation and ionization is investigated. The measured upper limits are consistent with both normal and relatively enhanced HCN excitation. Quantitatively my results show that the detection of the expected HCN intensities in a statistically valuable sample of quasar host galaxies is within reach.

In the last chapter, I analyze the physical properties of the radio jet in the radio loud quasar J1101+7225, which shows exceptionally far away from its nuclear origin (4 kpc) high relativistic motions. After a reanalysis of the cm-VLBI data, presented by Pott (2003), I include higher frequency data to follow the jet down to the hundred pc scale. The full analysis of the radio properties reveals an exemplary radio jet, which shows a complex inner structure including a possibly helical morphology. Far outside the nuclear region the jet rams into the host galaxy, which leads to a bending of the direction of propagation. Consequences for the galactic evolution of such interaction between the innermost accretion phenomenon and the surrounding host galaxy, which is typical for radio loud quasars, are not known yet.

The diversity of the observations and results obtained gives an impression of the wide range of possible interactions between supermassive black holes and their host galaxies as well as of the many ways to observe them. Most of the presented results are published in peer-reviewed journals and presented at several conferences.

Chapter 1

Astrophysical background

In the following, the stellar and extragalactic fundamentals are given, which are indispensable to understand the data and astrophysical results that are presented throughout the thesis. The presented information is given in the textbook of Carroll & Ostlie (1996), if not designated otherwise.

1.1 The fate of massive stars after the main sequence

The evolution of stars is based on the permanent attempt to stay in thermal and hydrostatic equilibrium. Stars lose energy usually via irradiation of light, but in later stages of massive stellar evolution, a huge amount of energy can also be released via neutrinos, produced in extreme nuclear processes. If a constant release of energy cannot be sustained anymore due to the lack of nuclear fuel, the star evolves into the next stage.

If assuming a negligible effect of magnetic fields and stellar rotation, the idea of stellar evolution can be summarized by the Russell-Vogt theorem:
The mass and composition of a star uniquely determine its radius, luminosity and internal structure, as well as its subsequent evolution.

Although several stars are shown to rotate rapidly, e.g. the rotation of the massive southern star Achernar and most recently of Vega is shown by means of optical interferometry (Domiciano de Souza et al. 2003; Peterson et al. 2006), the Russel-Vogt theorem is a good starting point for understanding stellar evolution and especially the famous Hertzsprung-Russel diagram (HR). After the gravitational collapse of a molecular cloud the hydrogen burning via the CNO-cycle in the center of the clouds ignites and the star populates the diagonal main sequence (MS) in the HR (Fig. 1.1), in which stellar temperature is plotted versus luminosity. The HR is divided into five luminosity classes (I-V), indicated as pink lines in Fig. 1.1. Each luminosity class describes a stage of stellar evolution. The stars spend by far the largest part of their lifetime on the MS, which accounts for the fact, that 80-90% of the observed stars in the galaxy are MS dwarf stars. The stellar lifetime itself and the position of a star in the HR along a given luminosity class is defined by its mass. The stellar mass scale ranges from about 0.08-100 $M_\odot$. The lower end is given by the critical mass density, required to start the hydrogen burning. Brown dwarfs and planets, having lower masses, do not reach this critical density. Above 90-100 $M_\odot$ strong thermal oscillations hamper stable nuclear energy generation in their centers, necessary for stellar life.

Denoting post-MS stars as giants, is based on the fundamental Stefan-Boltzmann law, which relates the bolometric luminosity of a black body to its size and temperature. If the stellar temper-
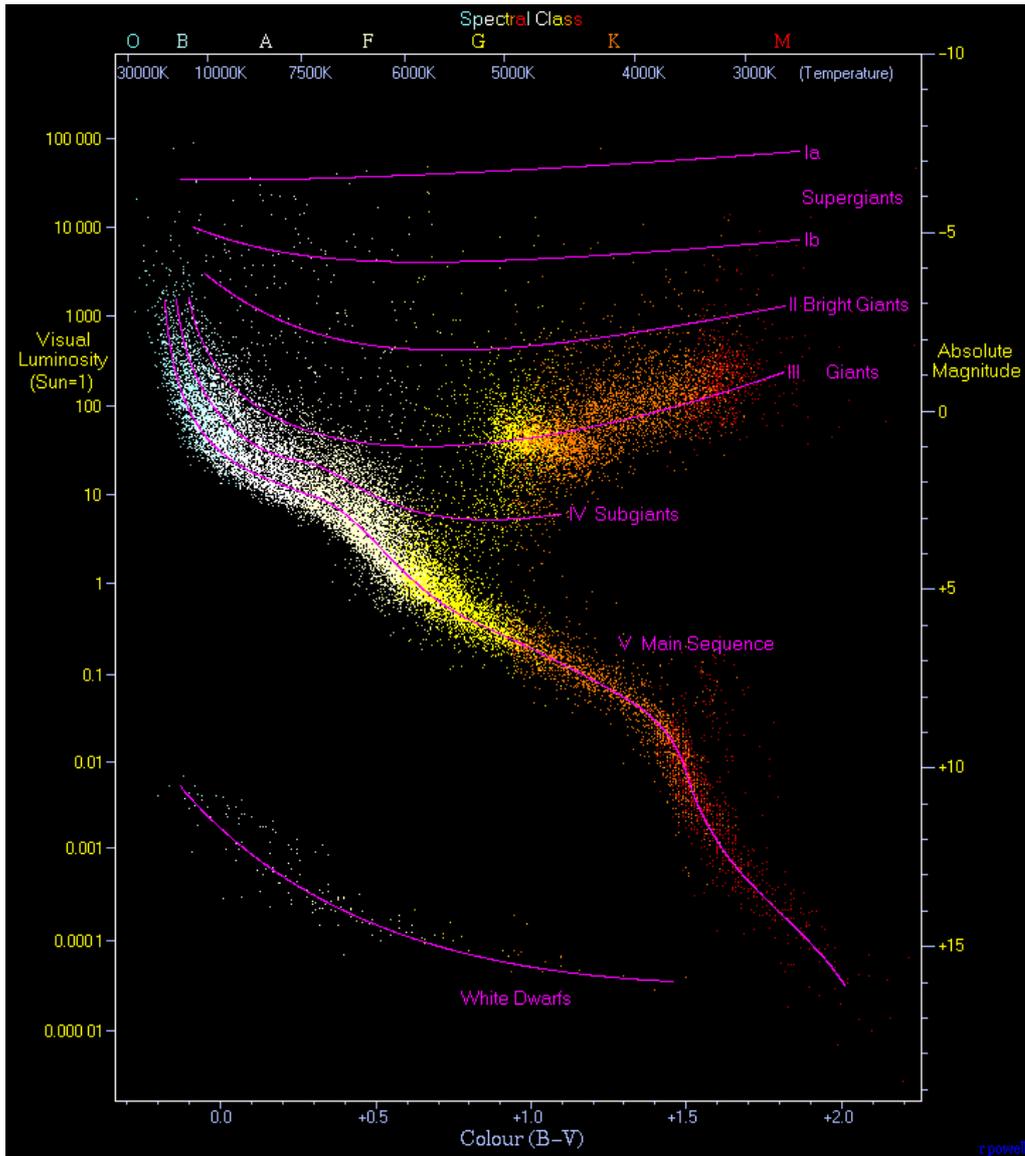
Figure 1.1: The Hertzsprung-Russell diagram, plotted of 22000 stars from the Hipparcos Catalog together with 1000 low-luminosity stars (red and white dwarfs) from the Gliese Catalog of Nearby Stars. While the main sequence is populated by ordinary hydrogen-burning *dwarf stars* of luminosity class V like the sun, the *giant stars* (class III) as well as the much rarer *bright giants* (class II) and *supergiants* of luminosity class I represents the post-MS stages above the MS. At the lower-left is the band of white dwarfs - these are the dead cores of old stars which have no internal energy source and slowly cool down over billions of years towards the bottom-right of the diagram. Courtesy of `http://www.atlasoftheuniverse.com`

ature is estimated from spectroscopy of photospheric lines, the radius is approximately given by
[1]

---

[1]The given T_e is the *effective* stellar temperature, which is noteworthy because a star as a big ball of gas and plasma has no final surface, and hence no definite surface temperature. While the effective temperature is defined to fulfill the Stefan-Boltzmann law, the respective radius describes the distance from the center to that stellar gas layer, which shows an optical depth of $\sim 2/3$, the so-called photosphere.

Figure 1.2: Stellar model parameters for different stellar masses: Given are the core temperature and density, T and ρ respectively, the mass M, luminosity $L_\odot$, and stellar radius $R_\odot$, and the timescale τ of the respective nuclear core burning phase until collapse (Table from Woosley et al. (2002)). Note that the current age of the sun ($\sim$ 5 Gyr) equals about 350 lifetime cycles of a 13 $M_\odot$ massive star. Massive stars die young!

			Hydrogen burning			
M_{initial}	T	ρ	M	L	R	τ
$M_\odot$	10^7 K	g cm^{-3}	$M_\odot$	10^3 $L_\odot$	$R_\odot$	Myr
1[a,b]	1.57	153	1.00	0.001	1.00	$\sim$11000
13	3.44	6.66	12.9	18.3	6.24	13.5
15	3.53	5.81	14.9	28.0	6.75	11.1
20	3.69	4.53	19.7	62.6	8.03	8.13
25	3.81	3.81	24.5	110	9.17	6.70
75	4.26	1.99	67.3	916	21.3	3.16
75[c]	7.60	10.6	75.0	1050	9.36	3.44

			Helium burning			
M_{initial}	T	ρ	M	L	R	τ
$M_\odot$	10^8 K	10^3 g cm^{-3}	$M_\odot$	10^3 $L_\odot$	$R_\odot$	Myr
1[b]	1.25	20	0.71	0.044	$\sim$10	110
13	1.72	1.73	12.4	26.0	359	2.67
15	1.78	1.39	14.3	41.3	461	1.97
20	1.88	0.968	18.6	102	649	1.17
25	1.96	0.762	19.6	182	1030	0.839
75	2.10	0.490	16.1	384	1.17	0.478
75[c]	2.25	0.319	74.4	1540	702	0.332

			Carbon burning			
M_{initial}	T	ρ	M	L	R	τ
$M_\odot$	10^8 K	10^5 g cm^{-3}	$M_\odot$	10^3 $L_\odot$	$R_\odot$	kyr
13	8.15	3.13	11.4	60.6	665	2.82
15	8.34	2.39	12.6	83.3	803	2.03
20	8.70	1.70	14.7	143	1070	0.976
25	8.41	1.29	12.5	245	1390	0.522
75	8.68	1.39	6.37	164	0.644	1.07
75[c]	10.4	0.745	74.0	1550	714	0.027

			Neon burning			
M_{initial}	T	ρ	M	L	R	τ
$M_\odot$	10^9 K	10^6 g cm^{-3}	$M_\odot$	10^3 $L_\odot$	$R_\odot$	yr
13	1.69	10.8	11.4	64.4	690	0.341
15	1.63	7.24	12.6	86.5	821	0.732
20	1.57	3.10	14.7	147	1090	0.599
25	1.57	3.95	12.5	246	1400	0.891
75	1.62	5.21	6.36	167	0.715	0.569
75[c]	1.57	0.434	74.0	1560	716	0.026

			Oxygen burning			
M_{initial}	T	ρ	M	L	R	τ
$M_\odot$	10^9 K	10^6 g cm^{-3}	$M_\odot$	10^3 $L_\odot$	$R_\odot$	yr
13	1.89	8.19	11.4	64.5	691	4.77
15	1.94	6.66	12.6	86.6	821	2.58
20	1.98	5.55	14.7	147	1090	1.25
25	2.09	3.60	12.5	246	1400	0.402
75	2.04	4.70	6.36	172	0.756	0.908
75[c]	2.39	1.07	74.0	1550	716	0.010

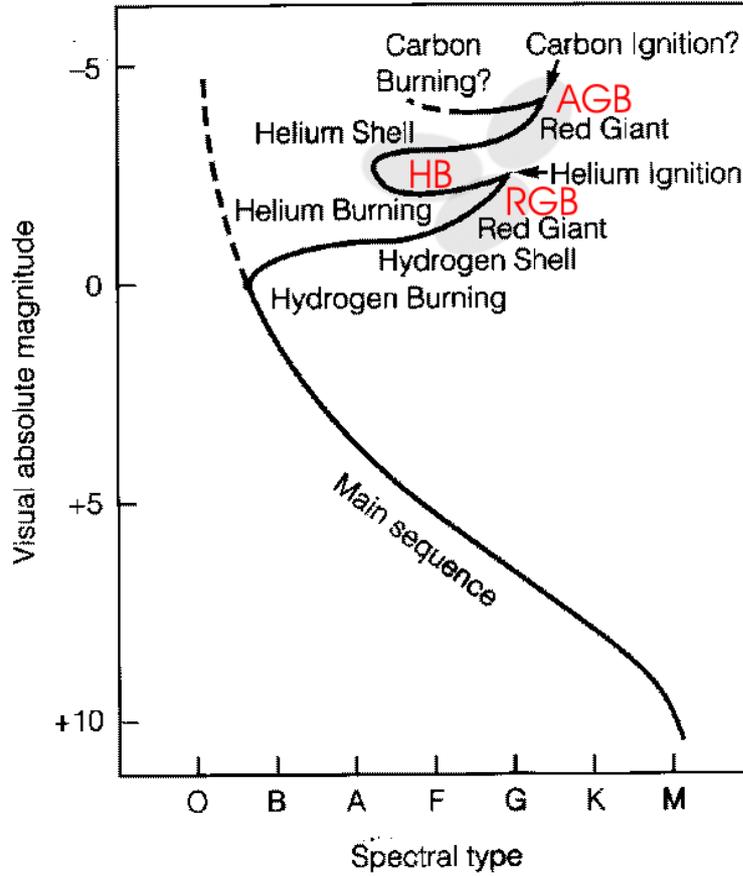|			Silicon burning			
M_{initial}	T	ρ	M	L	R	τ
$M_\odot$	10^9 K	10^7 g cm^{-3}	$M_\odot$	10^3 $L_\odot$	$R_\odot$	d
13	3.28	4.83	11.4	64.5	692	17.8
15	3.34	4.26	12.6	86.5	821	18.3
20	3.34	4.26	14.7	147	1090	11.5
25	3.65	3.01	12.5	246	1400	0.733
75	3.55	3.73	6.36	173	0.755	2.09
75[c]	3.82	1.18	74.0	1540	716	0.209

Figure 1.3: The stellar evolution phases. All stars with masses $M > 2\,M_\odot$ ignite He core burning and progress beyond the RGB (Chaisson & McMillan 2005). The post-MS giant stages, the Red Giant Branch and the Asymptotic Giant Branch, as well as the transition zone of the Horizontal Branch are highlighted. The respective nuclear burning processes are given. The supergiant phase is at the very top of the HR, and is reached only by massive stars beyond $8\,M_\odot$. A supergiant can reach a size of a thousand solar radii.

$$R = \frac{1}{T_e^2} \sqrt{\frac{L}{4\pi\sigma}} \, . \tag{1.1}$$

This implies that all stars lying vertically above the MS are larger than the respective stars on the MS of the same temperature. More precise radius estimates involve the stellar surface gravity and density, which change significantly over the post-MS stellar evolution (see e.g. Cox 2000, for an overview over these basic physical parameters of stars). In Chapter 3 I estimate the stellar type of the enigmatic GCIRS 3 to be a red supergiant by means of optical interferometry. By fitting radiative transfer models to data, which were obtained with optical interferometry, the temperature and stellar size was estimated. These properties were used to calculate the bolometric luminosity and to establish for the first time its supergiant nature.

While the hydrogen burning in low mass stars of solar type ($M \leq 1\,M_\odot$) lasts for more than 10^9 yr, more massive stars exploit their resources considerably faster with typical MS-lifetimes of

less than 10^7 yr at $M \geq 15\, M_\odot$, following roughly the rule

$$\mathrm{MS - lifetime} \propto \frac{M}{L} \propto \frac{1}{M^3}\,. \tag{1.2}$$

The MS lifetime is finished, when the core is cleaned out of hydrogen. The stellar core starts to cool and contract, to increase density and to heat up. As the core contracts and heats, the unexploited hydrogen resources in outer layers are heated to several million K. The phase of shell hydrogen burning is ignited. Now basically a sequence of nuclear shell and core burning of successively heavier elements takes place. It can reach up to iron for the massive stars only with stellar masses beyond $\sim 8\, M_\odot$. Only these stars can reach sufficiently high core temperatures and densities to ignite the nuclear burning process beyond the triple-alpha process of stellar fusion of helium. The sequence of nuclear core burning elements is

$$H \rightarrow He \rightarrow C \rightarrow Ne \rightarrow O \rightarrow Si \rightarrow Fe\,. \tag{1.3}$$
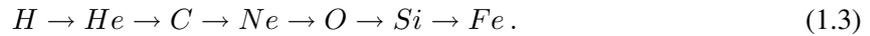
It stops at latest with iron which cannot release further energy by fusion with other elements.

During shell burning periods and especially before the start of a new core burning of a heavier element (Eq. 1.3), significant expansion of the star can occur, accompanied by convection of elements in the outer layers. During convection hot elements carry excess energy outward while cool elements fall inward. Especially freshly produced elements, results of the nuclear reactions in the core, can be dredged up to the surface, visible to the observer by photospheric emission lines. For example after the helium shell burning the so-called *third dredge-up* phase can appear in stars with masses exceeding $2\, M_\odot$. It enriches the surface with carbon atoms and creates a carbon star with a carbon-to-oxygen ratio larger then one and strong carbon emission lines. If the third dredge-up does not take place, the stellar photosphere is more oxygen rich because of the previous shell burning processes. In Chapter 3 the different optical properties (absorption, reflection, scattering) is used to probe whether carbon or oxygen dominates the dust shell[2]around GCIRS 3. Evidences will be found, which suggest that the third dredge-up occurred in GCIRS 3.

While the zones of the red giant branch (RGB), the horizontal branch (HB), and the asymptotic giant branch are passed by most stars until helium core and shell burning, only the massive stars experience the later post-AGB stages of stellar evolution.

In Fig. 1.3 the post-MS phases are indicated and correlated with the respective nuclear burning stages. In the RGB and AGB red giant phases, the stellar shells narrow, but radially expand rapidly while keeping its temperature, and the star moves vertically up in the HR. The horizontal motion along the HB is based on a temperature increase after ignition of helium in the core.

One significant phenomenon of the late stages of massive star evolution should be mentioned here, since it is an essential property of the massive stars in the GC, which I have observed: the mass-loss. The gravitational bounding of the expanded outer shells in the (super-)giant phases is reduced, while the radiation pressure is enormous. This leads to outward directed stellar winds and a significant amount of mass loss. The mass loss of massive stars is beside supernova explosions the most important process of enriching the galactic interstellar matter with heavier elements and dust particles (Zijlstra et al. 2006).

---

[2]In astronomy all particles flying around are called dust, if they are more complex than ions, atoms and molecules. The dust grains are made of heavier atoms (Si, C, O etc.), the grains can reach sizes of up to the micron scale, and they are formed in dense matter around newborn stars, mass-losing old stars and supernovae of dying stars. The heavier atoms itself are form during stellar evolution.

Typical stellar mass loss rates range from $10^{-7}\,M_\odot\,\mathrm{yr}^{-1}$ of MS-O stars, the hottest and most massive MS stars over $10^{-(6..4)}\,M_\odot\,\mathrm{yr}^{-1}$ for AGB stars up to $10^{-(5..4)}\,M_\odot\,\mathrm{yr}^{-1}$ of very extreme hot and massive Wolf-Rayet stars, a rare stellar evolution phase of some massive stars. Only about 230 galactic WR stars are known (van der Hucht 2001), among the 300 billions of stars in the Milky Way. Nevertheless an unusually large amount of WRs have been found in the central parsec of the Galaxy, e.g. most recently (Paumard et al. 2006). This underlines the special stellar structure of the GC.

The strong stellar winds, driving the mass loss, reach terminal velocities ν_∞ of a few tens of km s^{-1} for red AGB stars and up to an order of 1000 km s^{-1} for the blue and hot MS stars, WRs and supergiants. These winds most probably are responsible for many bow shocks seen in the dense gas and dust of the GC. Such bow shocks are visible in the thermal IR. The matter is compressed and heated by the ram pressure of stellar winds, ramming into denser interstellar material (Sect. 3.4).

Finally the star runs out of nuclear energy sources and is poised to undergo a catastrophic event, the Supernova explosion (Fig. 1.4).

1.2   Supergiants

Figure 1.4: An optical HST image of the remnant of the Type II supernova 1987a. The inner ring has a radius of 0.21 pc, i.e. $10^7\,R_\odot$! Courtesy of STScI.

Supergiants only evolve from massive stars, having ages of 6-15 Myr. Since two of the brightest and most prominent GC stars are red supergiants, I put together further background information about this rare stellar fate. My presentation is mainly based on the review of Woosley et al. (2002) and references therein, if not indicated otherwise.

The post-AGB evolution of stars depends strongly on the chemical composition and stellar mass.

The supergiants are very massive and luminous stars near the end of their lives. They are sub-classified as Ia or Ib, with Ia representing the brightest of these stars. These stars are very rare – one in a million stars is a supergiant. The nearest supergiant star is Canopus (F0Ib) 310 light years away. Some other examples are Betelgeuse (M2Ib), Antares (M1Ib) and Rigel (B8Ia).

Numerical models for supergiants typically show two types of supergiants. While all supergiants are dominantly powered by helium burning in core and shells, some appear to be *red* with a convective envelope of lower temperatures, higher opacities and significantly larger radii than the *blue* counterparts, which are dominated by radiative energy transport in their interior [3]. Intermediate supergiant colors appear to be thermally unstable, the ratio is known to change by an order of magnitude depending on the given metalicity Z [4]: from $B/R = 48$ at $Z = 0.03$ in the inner Milky Way to only $B/R = 4$ at $Z = 0.002$ in the metal-poor Small Magellanic Cloud (Langer & Maeder 1995).

The aforementioned WR stars are thought to represent a special late phase of massive stellar evolution, which is reached only by a very few massive progenitors driven by secondary[5] stellar properties. They have similar properties to blue supergiants, and in particular in the carbon rich version, they are known to be strong dust formers, at uniquely high mass loss rates. My VLTI target GCIRS 3, a deeply dust embedded star, was thought to be such a hot WR star because of the extraordinarily high amount of dust absorption along the line of sight, but the hot, effective temperatures of 2.5-$3 \cdot 10^4$ K of WR stars would have produced a significantly larger dust free zone around the star, than the one, which I observed.

Because the very late stages after helium core burning like carbon burning pass by rather quickly (Fig. 1.2 and 1.3), the surface evolution of a supergiant, which creates the observable appearance, cannot follow. Thus typically the star remains in its supergiant appearance for the observer, until the explosion.

In Fig. 1.4 the remnant of the renowned supernova SN 1987a is shown in an optical image. Although it exploded in a satellite galaxy of the Milky Way, the Large Magellanic Cloud, it is the closest and best studied supernova explosion of modern (telescope) times. The precursor star was identified to be a blue supergiant. Three hours before the optical light of SN 1987a reached the earth, strong neutrino radiation had been measured independently by a Japanese and a US American Cerenkov detector. These observations greatly confirm the stellar models of the very last phases of a supergiant, which state that a great part of the gravitational energy, freed after the last core collapse, which accompany the end of a nuclear burning phase, is released by neutrinos. The remaining mass after the supernova explosion of massive stars is large enough to form a neutron star or in the most massive cases a stellar black hole. The nature of the remnant of SN 1987a is still unclear, but observational upper flux limits exclude a bright pulsar (neutron star type) or a mass accreting black hole (Graves et al. 2005).

1.3   Interstellar dust extinction

Interstellar extinction describes the absorbing effect of interstellar matter on the intrinsic spectrum of an astrophysical phenomenon, if the matter is located between the event and the observer. It can

---

[3]Note the horizontal orientation of the supergiant region in the HR (Fig. 1.1). In reflection of Eq. 2.3, this tells immediately, that bluer, i.e. hotter, supergiants, have the same luminosity and therefore smaller radii then red ones.

[4]In astronomy, the *metalicity* is defined as the mass ratio Z between metals and all elements together. All elements heavier than Helium are called metals.

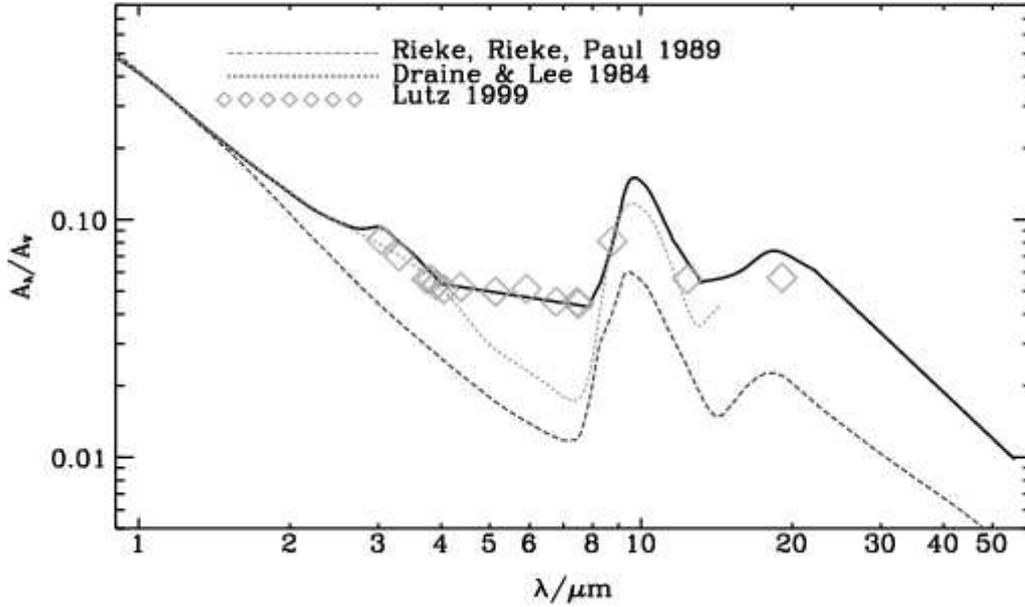[5]in contrast to the primary properties luminosity and mass

Figure 1.5: The extinction law of the line-of-sight towards the Galactic Center is shown as black solid line. I apply this law in Chapter 3. The classical law by Draine & Lee (1984, lower curve) shows already the broad silicate absorption at 10 μm, but at relatively less strength than indicated by the newer results of (Rieke et al. 1989, middle curve) and (Lutz 1999, diamonds). Interestingly it turns out that only the local diffuse dust around GCIRS 3 already creates an optical depth in the 10 μm silicate feature, which is comparable to the complete average interstellar silicate optical depth along the line-of-sight to all other stars in the central parsec. The solid line shows this average value. The figure is taken from Moneti et al. (2001).

be measured empirically via the observation of sources with a known intrinsic spectrum, at best stars with a strong continuum without significant spectral line emission in the respective spectral region. A more complex view of the radiation attenuation by interstellar molecules, which includes the reradiation of absorbed photons, is given in the next section. About 30% of the galactic starlight is absorbed and reradiated by dust (Bernstein et al. 2002). Describing only the absorption can however be sufficient to derive e.g. the intrinsic spectrum of a star at a given distance to the earth.

Mathematically the absorption is described by the optical depth τ (Rybicki & Lightman 1986)

$$I_\lambda(\tau_\lambda) = I_\lambda(0) \cdot e^{-\tau_\lambda} , \qquad (1.4)$$

with $I_\lambda(\tau_\lambda)$ being the radiation intensity at a given optical depth. The term *depth* derives from the fact, that a longer way S through absorbing material increases the optical depth

$$I_\lambda(s) = I_\lambda(s_0) \cdot e^{\underbrace{-\int_{s_0}^{s} \alpha_\lambda(s')ds'}_{\tau_\lambda}} . \qquad (1.5)$$

If the optical depth is one, the average photon of the intrinsic emission process has been absorbed. Media with an optical depth $\tau > 1$ are called optically thick, media with $\tau < 1$ are called optically thin. Similar to the optical depth, the extinction is defined by

$$A_\lambda = 2.5 \, log_{10}(\frac{F_\lambda^0}{F_\lambda}) . \qquad (1.6)$$

Thanks to this definition, the extinction can simply be subtracted from the observed magnitude to derive the intrinsic, unabsorbed magnitude of the source. The observed fluxes F are proportional to the radiation intensities I and optical depth and extinction are related via

$$A_\lambda = 2.5 \, log_{10}(e^{\tau_\lambda}) = 1.086 \cdot \tau_\lambda \,. \tag{1.7}$$

At best the spectral shape of the interstellar extinction can be estimated by observing two stars of the same spectral type, one with and one without extinction. The comparison of both spectral energy distributions (SED) on basis of Eq. 1.4 provides the wavelength dependent optical depth τ_λ.

It turned out that in the solar neighborhood, i.e. a few parsecs around the sun, the spectrum of the optical depth, or the so-called extinction law, has a fixed shape and scales with the extinction at a certain wavelength, e.g. with A_V at optical wavelengths. This indicates that the average chemical composition of the interstellar dust is constant, only the amount of absorbing material changes with line-of-sight and distance to the star.

Interestingly this general scaling law was shown to change partially for the Galactic Center (Roche & Aitken 1985). My MIDI data are obtained in the MIR atmospheric N-band window around 10 μm. This window mostly coincides with a broad absorption feature (Fig. 1.5), evoked by interstellar silicate molecules. Silicates are molecules, compound of silicon and oxygen of different fractions (Si_xO_y). Together with carbon based graphites they dominate the interstellar dust composition (Draine & Lee 1987). A study of the interstellar absorption towards the GC showed, that the relative strength of the absorption feature with respect to the continuum absorption is twice as deep as the relative depth in the solar neighborhood. This is an indication for a lack of carbon stars in the GC, resulting in less carbon enrichment and an increased relative optical depth of the oxygen based silicate feature. Naturally the extraordinarily deep silicate absorption towards GCIRS 3 was always interpreted to hint at an O-rich silicate dust forming star, but the new interferometric high-resolution data disprove strong silicate formation in the immediate dust shell of GCIRS 3 (see Chapter 3).

1.4   Radiative transfer in astronomy

Astronomy is constrained to measure the radiation of physical processes. After the invention of technical detectors for electromagnetic waves, step by step the full spectrum became observable, from long radio wavelengths over the classical optical regime, dominated by stars and visible by the unaided eye, to X- and γ-rays. But often the light rays encounter particles and interact with their surroundings on their way to the earth, which results in a significant change of the characteristic SED. The phenomenological approach of the interstellar extinction, described in the previous section, is a first step to account for this alteration of the intrinsic spectrum, which has to be known to correctly understand the radiation process observed.

In Chapter 3 the infrared light of a dusty star at the galactic center is analyzed. If the star is unresolved, the purely absorptive model of extinction is sufficient to derive the intrinsic spectrum, if the absorption is known. There are two reasons to go one step further and analyze the radiation extinction in detail.

Firstly, the extinction spectrum contains characteristic information about the extinction process, namely the absorbing and scattering particles. A dust shell around a mass-losing post-MS star attenuates the stellar emission spectrum in a characteristic way, depending on the chemical composition of the dust shell. The extinction of the interstellar matter between star and earth is dominated

by silicate and graphite molecules, but close to the star the dust composition can change dramatically, e.g. to a complete dominance of carbon rich molecules around carbon stars. Also the higher dust temperatures close to the star change its chemical composition and the optical properties of the dust (Ossenkopf et al. 1992).

Secondly, the dust does not only absorb a part of the passing radiation. Via the absorption process the dust is heated and emits itself thermal radiation. Furthermore a significant fraction of the radiation is not absorbed, but scattered. Thus after the stellar light has passed through the dust shell of a star, the SED consists of the sum of the absorbed spectrum, depending on the optical depth (Eq.1.4), and the spectrum irradiated by the dust.

This situation is described by the fundamental equation of radiative transfer

$$I_\lambda(\tau_\lambda) = I_\lambda(0) \cdot e^{-\tau_\lambda} + S_\lambda \cdot (1 - e^{-\tau_\lambda}) \,. \tag{1.8}$$

S_λ is the wavelength dependent emissivity of the dust. It depends on the shape, size, temperature, density and other properties of the dust particles.

To understand the observed dust extincted spectra, a solution for the radiative transfer function has to be found. Numerical codes can calculate solutions for the radiative transfer problems, leading to the effective optical depth of a given dust distribution. Usually a grid of different solutions is calculated for physically reasonable parameters, dust compositions and incoming radiation. The comparison with the observed attenuated spectrum leads then to the best set of parameters.

I analyzed the infrared light coming from the deeply dust embedded star GCIRS 3 by means of radiative transfer (RT). Since the MIDI data did not trace any significant deviation from circular symmetry, I apply the one dimensional code of Ivezic et al. (1999). The scattering is described by the Mie-scattering process, assuming spherically symmetric dust particles of sizes up to the wavelength of the incoming light. Due to the enormous luminosity, GCIRS 3 is most likely a supergiant star. These stars show a significant mass-loss, driven by the strong stellar winds. In a certain distance of several stellar radii, the temperature is low enough to enable the stable sublimation of dust particles. The applied RT code involves a calculation of the density of the dust shell, which typically falls exponentially with increasing radius. In the strong stellar radiation fields of AGB and post-AGB stars, the density distribution is not a free parameter anymore but can be estimated by hydrodynamical calculations for mass loss rates above $10^{-7} \, M_\odot \, \mathrm{yr}^{-1}$ (Netzer & Elitzur 1993). This situation occurs in the case of GCIRS 3.

1.5   The quasar phenomenon

Chapters 5 and 6 deal with astronomical observations of quasars. Quasar is an acronym for *quasi-stellar radio source*. They were discovered in the 1950s. Since in the optical they appear blue and stellar-like, they were thought to be nearby stars with extreme radio properties. Only optical spectroscopy of emission lines revealed cosmological redshifts and pointed to an extragalactic nature. The quasar 3C 273 was shown to reside at $z \approx 0.158$, an enormous redshift at those times (Schmidt 1963). Nowadays quasars are known to be active galactic nuclei (AGN) and often embedded in host galaxies.

The main properties of quasars as seen in the late 1960s are summarized by Peterson (1997):

- Star-like objects identified with radio sources

- Time-variable continuum flux

- Large UV-flux

- Broad emission lines

- Large redshifts

The large time-variability, which can occur on timescales of less than one day (Witzel et al. 1986), indicates small sizes of the emitting region via the light-/ information-travel argument. Sizes of order of a light day were derived, which equal 170 AU, the size of the solar system! This is the first indication of the SMBH accretion scenario, which today is believed to explain the tremendous energies emitted by quasars. The total quasar luminosity can easily exceed 10^{13} $L_\odot$ and outshine the stellar luminosity of a large galaxy. Together with the large distances that explains the difficulty to detect any signature of the host galaxy. The quasar appears to be a point-like star. The line emission of molecular gas however, which can make up about 10% of the total mass of the host galaxy, is observable at mm-wavelengths, where the luminosity of radio-quiet[6] QSO decreases. This enables meaningful detections of host galaxy properties of such QSO (Chapter 5).

Nowadays the quasar phenomenon is put in the broader context of active galactic nuclei (AGN) in general. Different types of AGN have been discovered. They deviate from the above given classical quasar definition by missing one or another property, or showing the property at lower strength. The immediate counterpart of quasars are the quasi-stellar objects (QSOs), which show similar luminosities and properties at all wavelengths, except the radio regime. The existence of radio-quiet counterparts underlines the fact, that some of the extreme radio properties of quasars are based on orientation effects. The non-thermal radio emission in quasars is caused by synchrotron processes, emitted by electrons, which are ejected at relativistic velocities from the nuclear region, and spiraling around magnetic fields. But the brightness of the synchrotron radiation is highly amplified, if emitted towards the observer, which is an effect of special relativity. Chapter 6 deals with these relativistic effects in the outflow of a quasar nucleus.

Within the larger frame of high-luminosity AGN, the extreme radio properties of quasars are seen as a special case. QSO and quasars are not differentiated as labeling different astrophysical phenomena anymore. Also throughout this thesis, both names are used synonymously. In all AGN the extreme luminosity emanating from a small volume in space can only be explained by mass accretion onto a supermassive black hole, often exceeding the mass of the black hole at the center of the Milky Way by several orders of magnitude. Today high luminosity AGN are detectable at redshifts larger than 6, which resembles only 7% of the current age of the universe (Jiang et al. 2006). In fact studying AGN and their cosmic evolution is a key object of observational cosmology. The number density of quasars per volume changes significantly over cosmological timescales. No strict borderline between *high* and *low* luminosity quasars can be given. In fact a smooth transition appears to be more probable. But at an absolute bolometric luminosity of $-23 \geq M_{\mathrm{bol}} \geq -24$ the nuclear luminosity clearly dominates the host galaxy, as derived for the BQS [7] (Schmidt & Green 1983). In the following such a bolometric luminosity is used as fair distinction between high and low AGN luminosity. In chapter 5 I study the dense molecular gas content of two such high luminosity quasars from the BQS.

---

[6] A standard division between *radio-loud* and *radio-quiet* is given by the radio power $P_{5\ \mathrm{GHz}}$, $\log_{10}[P_{5\ \mathrm{GHz}}(\mathrm{W/Hz/sr})] = 24$ (Goldschmidt et al. 1999).

[7]**B**right **Q**uasar **S**urvey, derived from the Palomar Green (PG) survey of blue stellar objects.

While in the immediate surroundings of the Milky Way no high luminosity QSO are found, their number density peaks in the redshift range of $2 \leq z \leq 3$ This was shown e.g. by Richards et al. (2006), who studied tens of thousands of quasars from SDSS[8]. Indications have been found that the quasar phenomenon might be related to galaxy merging events (e.g. Sanders et al. 1988; Bahcall et al. 1997).

During the first decades of quasar studies the focus was on the phenomenon itself, suggesting a SMBH as source of energy. Today the relation of the QSO to its host galaxy is a major field of research. Established connections between the host galaxy and a central SMBH, as the famous relation between the black hole mass and the mass of the galactic bulge (Magorrian et al. 1998), are critical tests for our understanding of galaxy formation and evolution. The study in Chapter 5 deals with the search for signatures in the hosts of high luminosity QSOs, which are related to the AGN itself.

---

[8]**S**loan **D**igital **S**ky **S**urvey, currently the largest optical sky survey covering about a quarter of the sky, which contains about a million galaxies and quasars. It is a unique basis for all statistical investigations, see `http://www.sdss.org`

Chapter 2

Overview over the central techniques applied

In this chapter I give an overview over the natural conditions and limitations observational astronomy has to deal with. In addition central properties of the applied technologies are presented to realize an insight in state-of-the-art astronomy. This chapter focuses on my observations, which are discussed in the subsequent chapters. Direct connections between a presented technology and a certain observation are highlighted. Apart from the style of presentation, the information given here is not my own creation. Nevertheless such introductory information may help all readers, who are not familiar with the applied techniques, to evaluate the technical complexity of modern astronomy. If not cited otherwise the following sections are backed by the textbook of Carroll & Ostlie (1996).

2.1 General aspects

The overall complexity of modern facilities, which reaches from constructing special purpose, non-commercial prototypes and instruments over state-of-the-art computing facilities to careful site selection, instrumental maintenance, and calibration, is needed to enable repeatable experiments and push several central properties of astronomical observations to the limit. In the following these central, critical properties are introduced.

Coverage of the electro-magnetic wavelength spectrum

Nowadays major fractions of the entire electro-magnetic spectrum, extending from meter waves in the MHz-radio regime to x- and $\gamma-$rays way beyond the optical, are observable by different, adequate detector systems. The reasons for the permanent attempt to increase the observable fraction of the electromagnetic spectrum are manifold:

- Different astrophysical processes dominate different wavelength regimes. E.g. the non-thermal synchrotron emission from the very nucleus of quasars peaks at cm-wavelengths (cf. Chapter 6), while the thermal emission of solar type stars are best studied in the optical.
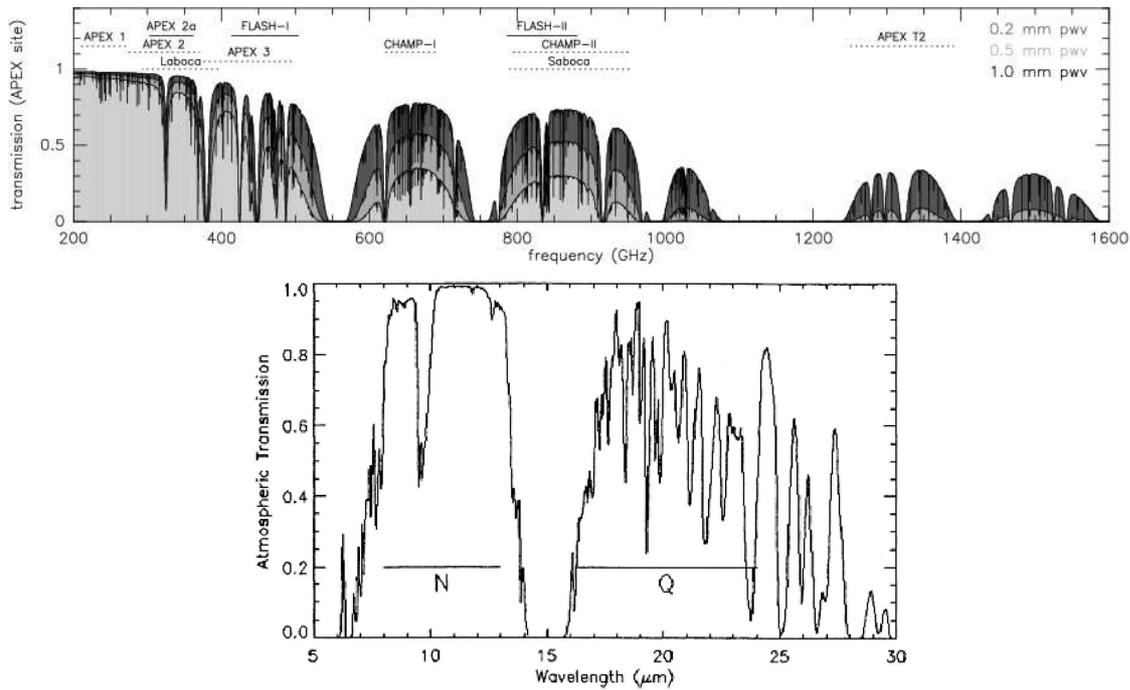
Figure 2.1: Left panel: Zenith transmission above the APEX telescope at the ALMA site in Chile (5100m above sea level). The different colors are indicating the dependency of the atmospheric transmission of the column of precipitable water, given in the upper right corner. The median water column is about 1.2 mm over the year, with the best 25% of the time having a column of 0.7 mm. During winter time, the cooler atmosphere contains less water and the median precipitable water column can decrease down to 0.4. While the deterioration towards shorter wavelengths is obvious, at good winter conditions frequencies up to 1.5 THz can be observed! The names refer to the instruments which will exploit the respective bands. Underlined names indicate instruments, which have already been commissioned. My data, presented in Chapter 4, have been taken with the APEX 2a facility receiver in the 350 GHz band (taken from Güsten et al. 2006). Right panel: Mid-infrared transmission at the VLT observatory atop Cerro Paranal. The reduced transmission near 10 μm due to ozone is deteriorates the data quality at these wavelengths (Chapter 3). Courtesy of ESO.

. The cosmological redshift shifts emission lines and peaks of spectral energy distributions towards longer wavelengths. This effect can help to find redshifted extragalactic emission lines which lie outside an atmospheric transmission window at local galaxies at $z \approx 0$ (for definition of z see Footnote 2 in Chapter 4).

. Absorption phenomena intrinsic to the source can block a certain wavelength, but reradiate the light at different ones. E.g. dust in star formation regions blocks most efficiently at uv-optical wavelengths but reradiates the light in the infrared, which makes excess emission at far infrared wavelengths a good tracer of star formation (SF), while the SF itself is not visible in the optical.

Despite of new detectors ground-based telescopes, as used throughout this thesis, always suffer from the absorbing and scattering atmosphere, which strictly limits the achievable wavelength coverage to so-called atmospheric windows of low opacity[1]. Here, I discuss transmission problems at the case of the recently inaugurated APEX sub-mm telescope, which I used during the Science

---

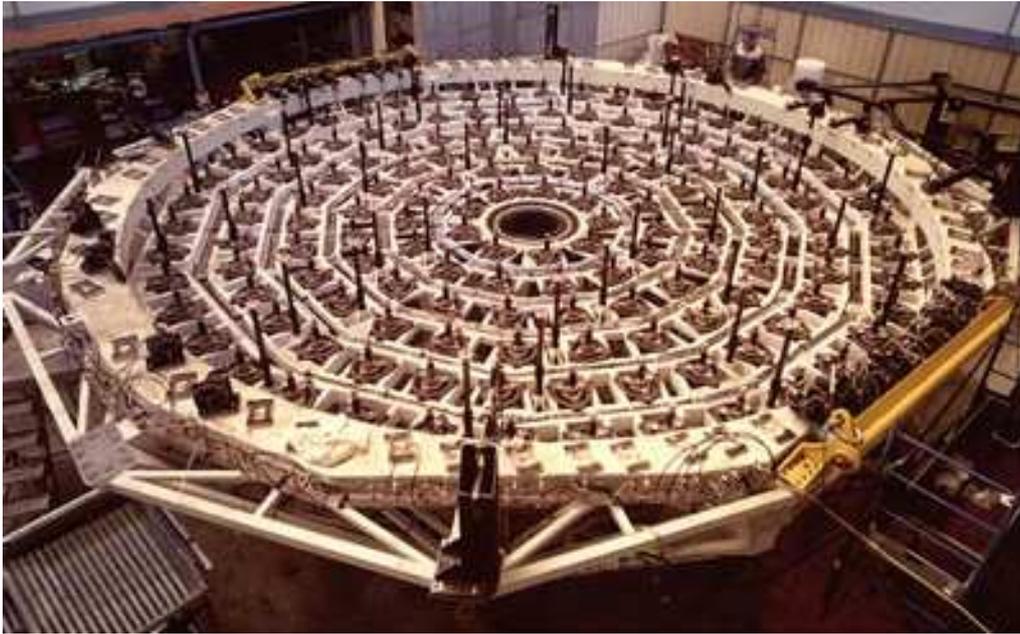[1]Opacity is a synonym for optical thickness, which is discussed in Sect. 1.3, 1.4

Figure 2.2: The actuators of one VLT primary mirror of 8 m diameter. The actuators are part of the active optics system stabilizing the shape of the monolithic mirror, which is made of the glass ceramics ZERODUR and has a surface accuracy of 50 nm, that is accurate to a tenth of the wavelength of visible light.
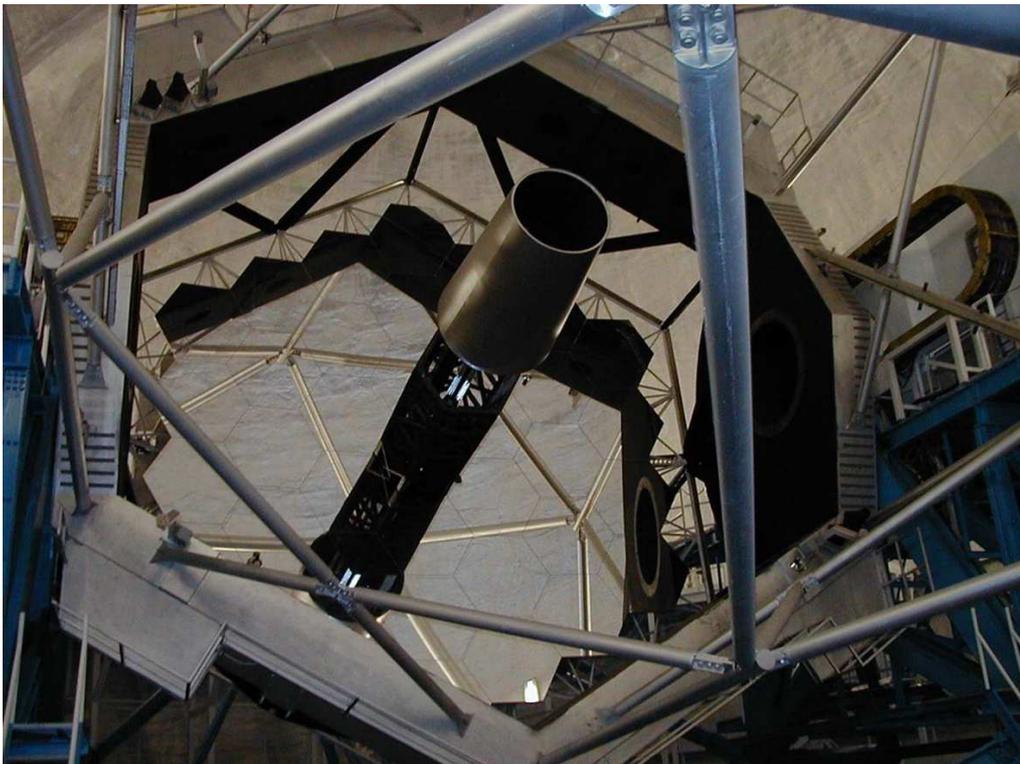

Figure 2.3: The 10 m primary mirror of the Keck observatory atop Mauna Kea, Hawaii. The hexagonal mirror segments, which enable the large diameter increasing the collecting area, is visible. For such segmented mirrors the active optics technique is indispensable. Courtesy of Keck observatory.

Verification phase[2]. Since the atmospheric transmission of sub-mm radiation is mainly constrained by the *amount* of water per unit volume along the line-of-sight, the transmission is optimized if the atmosphere is thin and dry. Thus, extensive site testing is necessary to enable optimum system performance of the instrument. The final location Llano Chajnantor was tested over six years, keeping in mind, that not only the APEX[3] telescope, but later on the giant ALMA[4] mm-array will be erected at the same site (D'Addario & Holdaway 2000). It is located above 5000 m in the Atacama desert, which guarantee dry and stable conditions to minimize the atmospheric deteriorations (Fig. 2.1).

For comparison the best European site for millimeter observations, the 3000 m Pico Veleta, near Granada, Spain (Chapter 5), show 4-7 mm precipitable water in summer, and down to 1 mm at best winter nights with respectively lower atmospheric transmission due to more water and the lower site. These numbers illustrate that efficient ground-based observations in the sub-mm domain are not possible at Pico Veleta. Thus, the extension of the observable wavelengths to the sub-mm domain requires sites like Llano Chajnantor and the many related technical challenges to operate modern technology at the low pressure and the extreme conditions of a 5000 m altitude site.

Angular resolution

The angular resolution α is a measure for the sharpness of the image. Typically it is given in radian measure and describes the minimal angular size of astrophysical phenomena discernable with the used telescope. The wave nature of light sets the ultimate diffraction limit,

$$\alpha_{[rad]} \approx 1.22 \frac{\lambda_{[m]}}{D_{[m]}} . \tag{2.1}$$

λ denotes the observing wavelength and D the diameter of the telescope. $\alpha_{[rad]}$ is determined by the circular aperture of a telescope. It can be interpreted as minimal resolvable binary separation distance and is known as the Rayleigh Criterion. The full width at half maximum (FWHM) of the point spread function (PSF) is comparable to $\alpha_{[rad]}$. While the PSF is the image of a totally unresolved point-like star, its FWHM gives a lower limit for resolvable source extensions. In the observed image the extended source is convolved with the PSF.

For many years larger optical telescopes did not provide the full increase of angular resolution with respect to radio telescopes, as could be expected due to the much shorter observing wavelengths. Reasons for this deviation from Eq 2.1 are temporal and spatial variability of the optical properties (diffraction and scattering of the light) of the atmosphere. They are increasing significantly with frequency (see also Sect. 2.2.2). This results in the *seeing* effect, which corrugates the wavefront of the incoming light, blurs the imaging process and unsharpens the astronomical image way beyond the theoretical diffraction limit. Only real-time adaption of the shape of the reflecting mirrors can account for this effect, if fainter objects shall be observed. Such *adaptive optics* (AO) systems were developed and applied to the currently largest optical 8-10 m class telescopes in the recent decade, enabling for the first time deep diffraction limited imaging at such diameters.

The FWHM of a seeing limited PSF degrades proportional to the wavelength (Quirrenbach 2000)

$$\alpha_{\text{seeing}} \propto \lambda^{-\frac{1}{5}} . \tag{2.2}$$

---

[2] Chapter 4 and `http://www.eso.org/science/apexsv/apex2asv/pott.html`

[3] **A**tacama **P**athfinder **EX**periment, more information under `http://www.apex-telescope.org`

[4] **A**tacama **L**arge **M**illimeter **A**rray

In contrast to the diffraction limit (Eq. 2.1), the seeing limited resolution gets better with longer wavelengths and is independent of the telescope diameter. This holds as long as D is larger than the Fried parameter r_0, which itself describes the scale lengths over which the optical properties of the atmosphere remain stable and the rms [5] of the atmosphere-induced phase fluctuations is smaller than one radian. r_0 scales as $\lambda^{6/5}$ and is at optical wavelengths less than 25 cm, i.e. larger telescopes without AO correction gain only in sensitivity, not in angular resolution.

α_{seeing} reflects the atmosphere-induced wavefront- (i.e. image-)distortions. Because α_{seeing} decreases with wavelength, the respective AO requirements are alleviated at longer wavelengths. This leads to best AO performances with limited wavefront correction at near- to mid-infrared wavelengths (1-10 μm). Longwards of 10 μm the diffraction limit of constructible telescopes outrivals the seeing effect. I used the AO system of the VLTI and discuss in Chapter 3 that for the VLTI still at MIR wavelengths as long as 10 μm the use of higher-order AO leads to a recognizable improvement of the data quality. The interferometric beam combiner instruments are fed by AO corrected telescope beams (Donaldson et al. 2000), which is essential for stabilizing the flux throughput and enabling continuous fringe detection of the VLTI.

The other limitation to the achievable diffraction limit is given by the requirements on the quality of the shape of the primary mirror of the telescope. To fulfill the prerequisites for Eq. 2.1, the shape of the primary mirror must resemble the ideal parabolic form with an accuracy better than the observing wavelengths. Again this requirement is much harder in the optical than in the radio regime. At large diameters typically a trade-off has to be achieved between a heavy, stiff construction, necessary to keep the form at different telescope orientations, wind and temperature[6] conditions, and a light construction, which is still efficiently movable. The actual technical limit, reached with the help of shape-stabilizing active optics, is given for monolithic mirrors with a diameter of about 8 m (like the VLT[7]; Fig. 2.2) and for segmented mirrors with about 10 m (used at the Keck telescopes[8]). Currently project studies are underway to investigate concepts of Extremely Large Telescopes (ELT), which shall combine all image and atmosphere correcting techniques described to enable a (segmented) primary mirror of 30 m diameter, thus increasing the collecting area and thereby the sensitivity by an order of magnitude[9].

The alternative technique to increase the angular resolution, beyond the currently available single telescope limits, is the interferometry that combines the light of different, individually complete telescopes. The angular resolution, achievable with interferometry, can also be described with Eq. 2.1, if the single telescope diameter is replaced by the maximum separation distance between the used telescopes. I have used well established radio interferometers at cm-wavelengths to study relativistic effects in extragalactic radio jets at mas resolution scale (Chapter 6). And the Galactic Center studies (Chapter 3) are based on observations with the infrared counterpart, the VLTI project of ESO. An introduction to radio interferometry is given in my diploma thesis (Pott 2003). Although the general physical concept is similar, the new techniques and strategies necessary to enable beam interference at infrared wavelengths is described in a separate section below (Sect. 2.2).

---

[5]**R**oot-**M**ean-**S**quare is used as synonym for the standard deviation of a randomly distributed quantity.

[6]Noteworthy about 50% of the total power consumption of the Paranal Observatory is used to aircondition the primary mirrors of the telescopes at day time to avoid shape deformations driven by temperature changes

[7]**V**ery **L**arge **T**elescope of ESO at Cerro Paranal, `http://eso.org/paranal/insnews/vlt_overview.html`

[8]`http://keckobservatory.org`

[9]More information about the most progressed ELT studies of the European and North American astronomical community are given at `http://eso.org/projects/e-elt` and `http://www.gmto.org,http://tmt.ucolick.org`

Sensitivity

The sensitivity of ground based telescope systems, limiting the observability of faint targets, depends on the collecting area of the telescope, the atmospheric transmission at the observatory and the length of the integration times at equal conditions. Again the straight forward tactic of increasing the integration times is most easily applicable at radio wavelengths, due to the much reduced atmospheric influence and variability, as well as due to the relaxed accuracy requirements thanks to the longer observing wavelengths. During my search for HCN molecular line emission at 80 GHz, I could finally create a single dataset out of several successive days of observations, which included about 20 hrs of on-source integration time (Chapter 5). Such a long integration is only effective if the atmospheric conditions do not change significantly over the integration time, which is usually not the case for optical observations.

If the data is affected by statistically changing noise factors following a Gaussian distribution, simple (noise weighted) averaging of the data increases the signal-to-noise ratio proportionally to the square root of the increased total integration time. This effect was essential to search for non-Gaussian, systematic errors in the APEX datasets (4.2) at 0.9 mm, a part of which suffered from strong systematic baseline problems.

All the fundamental qualities of any astronomical observation discussed above have an immediate, individual influence on the quality of the observation, but they are also connected to each other. Increasing the observing frequency decreases the diffraction limit, but for example it shifts the astrophysical focus from radiating dust in the infrared to naked stars in the optical wavelength regime. Or increasing the angular resolution due to the application of AO also increases the point source sensitivity by better concentrating the flux in the center of the PSF. This effect is quantified by the Strehl-ratio, which is commonly used to characterize the actual AO performance during the observation. The results of this thesis could only be achieved due to the use of modern telescopes pushing the discussed criteria to the technical limits.

In the following sections I give an introduction to the major challenges of optical interferometry and their solutions (Sect. 2.2), motivated by the very new capabilities of optical long baseline interferometers and by my extensive VLTI observations, presented in Chapter 3. Furthermore, an overview of the heterodyne receiver technique is set out in Sect. 2.3. Heterodyne receivers are crucial for the cm-/mm- and sub-mm observations with the EVN (Chapter 6), IRAM 30 m telescope (Chapter refch:hcn), and APEX (Chapter 4).

2.2 Optical interferometry – challenges and concepts

In this section the basic principles and techniques of optical interferometry, focused on the observables of my MIDI experiments are presented. MIDI combines the light of two telescopes in the astronomical N-band and is therefore a minimal two-element interferometer.

2.2.1 Interferometric imaging? Yes please, but how?

If not cited otherwise, I base this section on (Lawson 2000). Every interferometric measurement aims at simulating a big telescope with large diameter by connecting several smaller, but technically (and financially) more feasible telescopes. The sensitivity of a big primary mirror, which increases with the square of the diameter, cannot be reached with an array of smaller telescopes,
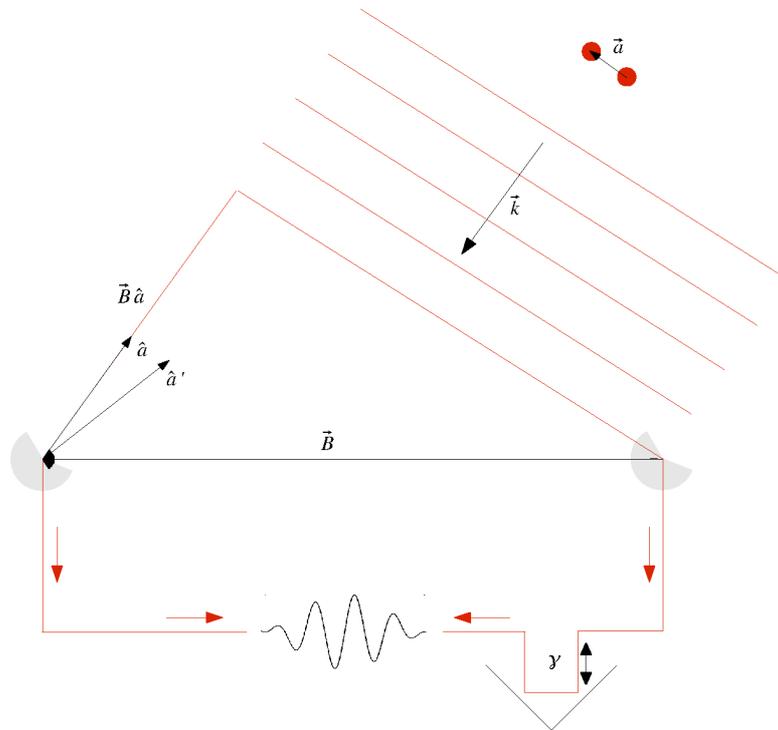
Figure 2.4: Basic principle of a two-element interferometer as VLTI/MIDI. The geometric delay $\vec{B}\hat{a}$ is shown, which derives from the orientation and length of the baseline vector $\vec{B}$ between the two telescopes and the normalized vector $\hat{a}$ pointing to the (phase) center of the source. The geometrical delay vanishes if the source is in Zenith. $\hat{a}'$ symbolizes an extended brightness distribution resolvable by the interferometer. Light coming from $\hat{a}'$ has an additional OPD with respect to the geometric delay, which is measured by the interferometer. $\hat{a} - \hat{a}'$ equals the angular distance $\vec{a}$ and $\vec{k}$ depicts the wavenumber of the incident waves. A typical pupil plane fringe pattern of a MIDI observation is shown, achieved by continuously varying the optical path length γ of one light beam. Courtesy of Th. Ratzka.

because all of the individual elements must detect the source individually. If however the single telescope is not much larger than the interferometer elements the interferometer can be more sensitive to point sources, if the respective point source is embedded in a significant amount of diffuse flux [10].

Many astronomical objects have a brightness observable by modern optical interferometers. Especially the combination of 8 m class telescopes at the VLTI and the KI projects[11] increased the number and type of observable targets significantly, bringing stellar interferometry step by step away from a single purpose instrument, which is build to measure the radii of nearby stars, to a multi purpose instrument, capable to detect stellar discs and shells as well as the dust around AGN (e.g. van Boekel et al. 2004; Jaffe et al. 2004).

---

[10]Note: this effect did *not* dominate the MIDI observations of GCIRS 3 and was only mentioned here for the sake of completeness. In the case of GCIRS 3, the single telescope could well detect both the diffuse and the compact emission (Fig. 3.21), but the single elements of the interferometer were not sensitive enough to record the diffuse part. Thus there was nothing measured which could be resolved out by the interferometer.

[11]**VLT I**nterferometer in Chile: `http://eso.org/projects/vlti` and Keck Interferometer in Hawaii `http://planetquest.jpl.nasa.gov/Keck`

PA: 154°, Length: 9m, Elev.: 0°   PA: 109°, Length: 28m, Elev.: 20°   PA: 105°, Length: 46m, Elev.: 40°

PA: 106°, Length: 58m, Elev.: 60°   PA: 110°, Length: 62m, Elev.: 76°   PA: 119°, Length: 55m, Elev.: 60°

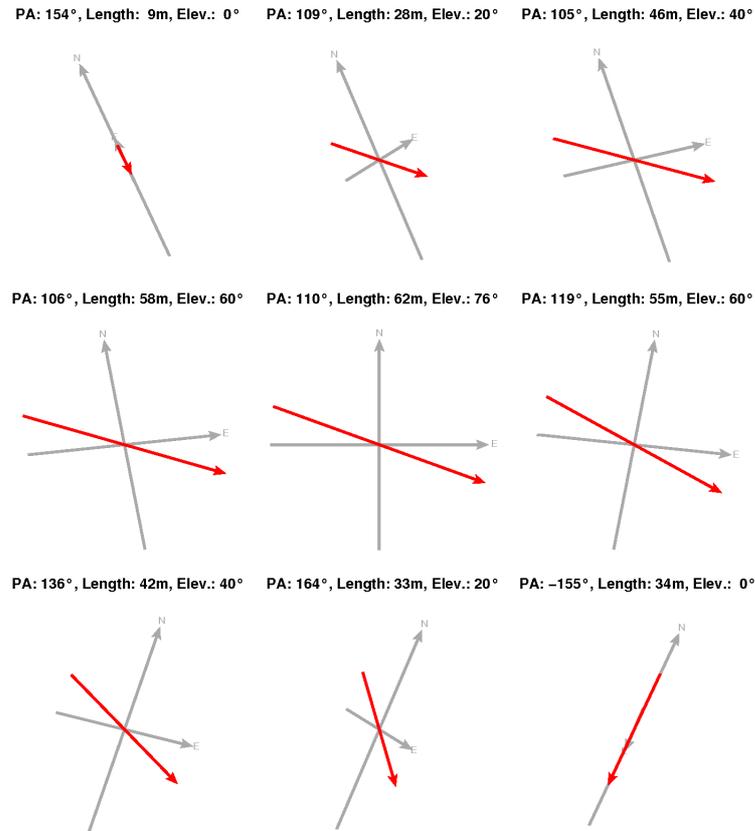PA: 136°, Length: 42m, Elev.: 40°   PA: 164°, Length: 33m, Elev.: 20°   PA: −155°, Length: 34m, Elev.: 0°

Figure 2.5: The continuous change of the baseline projection over the night is shown by projecting the VLTI baseline UT3-UT4 (62 m) onto a star at Declinate -11.5°. The grey North-East cross defines the platform of Paranal. The perpendicular orientation of the platform in the first and the last image panel cannot be reached observational, since the source can only observed down to an elevation of 30°. The red line gives length and orientation of the baseline as seen from the star, or projected onto the sky. The elevation of the star is given, the star culminates in the central plot, where the Paranal-platform is not distorted. Courtesy of Th. Ratzka.

Chapter 3 deals with the analysis of interferometric data of an optical two-element interferometer. Is such a minimal interferometer capable of measuring images at the interferometric resolution, as we are used to from radio interferometer arrays? The short answer is *no*. But indeed critical source properties *can* at the high angular resolution, which would have been unknown without stellar interferometry.

An astronomical image can be separated in the total flux F of the source, and the normalized brightness distribution $I(\alpha, \delta)$. During the imaging process of a single telescope the full information F and I is measured at the given angular resolution. But simple brightness distributions, such as the two points of an unresolved binary system or circularly symmetric distributions contain only a small amount of image information, which is measured redundantly by the imaging process of a monolithic telescope. The *amount* of image information can be characterized by the Fourier transformation, i.e. by the number of different sine functions necessary to create the image by superposition of the sine functions. The frequence and phase of such sine waves can be efficiently measured with an interferometer, even more they are the primary measurable of any interferometric observation.

The mathematical basis of such a signal decomposition is the two-dimensional spatial Fourier transform of the flux normalized intensity, or couched by the van Zittert-Zernike theorem,

$$V(u, v) = FT(I(\alpha, \delta)); \quad V \in \mathbb{C}. \qquad (2.3)$$

In analogy to the Fourier analysis of 1-dimensional signal waves (sound, radio etc.), the complementary Fourier coordinates are called *spatial frequencies* or in IF slang simply *u,v* coordinates. One visibility $V(u, v)$ is a complex quantity, consisting of the visibility modulus and the visibility phase[12], which describe together with the spatial frequencies u, v exactly one of the mentioned sine waves.

The contrast of the interference or fringe pattern, produced by a two-element interferometer, is a measure for this visibility. The phase and intensity of a perfect fringe pattern is correlated to phase and modulus of the visibility. Fig. 2.4 shows the concept of a two element optical interferometer like VLTI/MIDI. Here the incoming light waves are sketched as plane waves coming from a distant source and neglecting the disturbing effects of the atmosphere. In optical interferometry the incoming wave cannot be recorded and correlated afterwards, as in radio interferometry. Thus direct beam overlap and interference is required. This makes the very long baselines, known from radio interferometry, impossible at optical wavelengths. The transmission losses are too high, and the required accuracy of the optical path cannot be made available at baselines exceeding a few hundred meters. Currently investigations are underway to push this limit by connecting the telescopes with optical fibers[13]. The geometrical delay describes the different arrival times of the same stellar wave front at the two telescopes, if the star is not in the zenith. Further optical path differences (OPD) are typically introduced by atmospheric turbulence. If OPD is corrected for properly, the light rays can interfere coherently and produce the fringes. In pupil plane interferometers like MIDI, the OPD is modulated systematically, which creates a temporal fringe pattern (Fig. 2.4) on the detector. It is described by the fundamental equation at a given wavelength λ

$$\text{Interference flux} = \underbrace{2 \cdot \sqrt{F_1 \cdot F_2} \cdot (V(\lambda) \cdot cos(2\pi OPD/\lambda + \phi)}_{=:\text{correlated flux}} + 1). \qquad (2.4)$$

$F_{1,2}$ are the flux contributions of the individual telescopes. In reality the cosine function is damped by a sinc envelope due to the finite width of the spectral channel. The linear flux term is filtered, while the object's visibility equals the amplitude of the cosine variation. Thus a power spectrum of the detector signal reveals immediately the visibility modulus. ϕ is a phase shift, which can be evoked by a source displacement, away from the phase center (Eq. 2.10), or by atmospheric and instrumental effects. The MIDI data, presented in this work, cannot distinguish the intrinsic phase of the source from atmospheric contributions.

---

[12]A word about terminology: Up to now, the major part of interferometric observations in the optical-infrared wavelength regime probes stellar properties due to the lack of sensitivity for extragalactic observations. Thus an optical/infrared interferometer is often called a *stellar* interferometer. This *stellar* only refers to the given sensitivity limits, which confine the observable targets to be bright and compact objects. It does not denote a special kind of interferometry, e.g. in contrast to a hypothetic *galactic* interferometer. Furthermore the primary measurable of a single baseline interferometer like VLTI/MIDI is the visibility modulus, because the phase information is not calibrateable against atmospheric disturbances. And if the situation is clear, often (also throughout this thesis) the visibility modulus is simply called visibility.

[13]see the 'Ohana project on Mauna Kea plan to combine light at a maximum baseline of 800 m, http://lesia.obspm.fr/astro/interfero/pages/ohana.html

A complex brightness distribution cannot be described by a single measurement, which determines the amplitude of one spatial sine wave only. The experience with radio interferometers show, that consistent astronomical images can be obtained by non-linear algorithms exploiting the van Zittert-Zernike theorem, if a limited number of complex $V(u,v)$ are measured. The required number depends on the complexity of the brightness distribution and of the intended quality of the final image, but an array of four telescopes can be seen as a very minimum. Each telescope pair of an array, the so-called baseline, contributes one $V(u,v)$ at a time, and several $V(u,v)$ over the course of a night, since the baseline orientation with respect to the target, which defines u,v, changes due to the earth rotation (Fig. 2.5).

Interferometric imaging theory shows further, that the phase information of the complex visibility is indispensable for deriving reliable images (Thompson et al. 2001). Only point-symmetric brightness distributions have real Fourier transforms without any visibility phases. The visibility phase is encoded in the phase of the interferometric fringe. Unfortunately typical path length fluctuations due to the turbulent atmosphere are on the order of 5-10μm, which translates to more than a radian even at the 10 μm observing wavelength of MIDI, resulting in a loss of the phase information at each interferometer element and in a random visibility phase. A standard trick in interferometry to overcome this problem is the measurement of so-called closure phases. But since this technique requires the simultaneous combination of three beams, it cannot be applied to MIDI. Thus due to the lack of an absolute phase reference, complex imaging with VLTI/MIDI is not possible, but I will demonstrate in the following paragraphs, that nevertheless an important amount of imaging information can be measured.

The fringe measurement results in one visibility measurement at a given spatial frequency (u,v), which itself are given by the projection of the used baseline onto the sky. Note that the visibility at (u,v) is only defined by the brightness distribution of the source (Eq. 2.3), and the spatial frequency is given by the position of the telescopes. That is, large apertures of the individual interferometer elements have no other influence on the interferometric measurement, than yielding higher SNRs. The interferometric angular resolution is only determined by the baseline used, and it is not increased by larger apertures.

The van Zittert-Zernike theorem suggests, that the true brightness distribution can only be recovered by a Fourier back transform, if all spatial frequencies are measured, which is impossible. The amount of observed spatial frequencies is described by the u,v-coverage (e.g. Fig. 3.12). Thanks to the earth rotation (Fig. 2.5), already several measurements at a few baselines of a small array can yield a significant uv-coverage within a given uv-radius, which defines spatial resolution of the combined dataset. And VLTI/MIDI offers six different VLT baselines.

Since the Fourier transform of a real function is hermitian and the intensity distribution I is the power of the electrical field E, the visibility modulus is always point symmetric

$$\text{Pointsymmetry}: \quad I = E \cdot E^* \in \mathbb{R}^{\geq 0} \quad \rightarrow |V(u,v)| = |V(-u,-v)|. \qquad (2.5)$$

For the analysis of visibility data and the most efficient design of an interferometric observation,

the basic properties of the Fourier transform have to be known

$$\text{Linearity}: \quad FT(\sum_k f_k \cdot I_k(\alpha, \delta)) \quad = \sum_k f_k \cdot V_k; \quad \text{with} \sum f_k = 1 \quad (2.6)$$

$$\text{Similarity}: \quad FT(\widetilde{I}(a \cdot \alpha, d \cdot \delta)) \quad = V(\frac{u}{a}, \frac{v}{d}); \quad \text{with} \widetilde{I} = |ab| \cdot I \quad (2.7)$$

$$\text{Convolution}: \quad FT(I_1 \star I_2) \quad = V_1 \cdot V_2 \quad (2.8)$$

$$\text{Gauss} \rightarrow \text{Gauss}: \quad FT(e^{-\frac{\alpha^2 + \delta^2}{2 \cdot (a^2 + d^2)}}) \quad \propto e^{-2\pi^2 \cdot (a^2 + d^2) \cdot (u^2 + v^2)} \quad (2.9)$$

$$\text{Spatial} \rightarrow \text{Phaseshift}: \quad FT(I(\alpha - \alpha_0, \delta - \delta_0) \quad = V(u, v) \cdot e^{2\pi i \cdot (\alpha_0 \cdot u + \delta \cdot v)}). \quad (2.10)$$

These properties are indispensable to understand the partial imaging information of the visibilities. In my MIDI project (Chapter 3), I cover over the course of two nights a well sampled annulus in the u, v-plane with two orthogonal baselines, probing the circular symmetry of the visibility and of the brightness distribution under the assumption of vanishing phases. It is instructive to combine Eq. 2.7 and 2.9. Circumstellar spherical dust shells typically have a Gaussian shaped brightness distribution. That means, that the visibilities will also decrease like a Gaussian with increasing baseline lengths, and a few measurements are necessary only to fit the shape of a Gaussian to the visibility data, thus defining via Fourier back transform the FWHM of the intrinsic source distribution. The similarity law now specifies the fact, that increased extension results in a decreased visibility at a given spatial frequency. This is e.g. a background idea for Sect. 3.3.3. In Sect 3.3.3.4 I create step by step a toy model to explain the measured visibilities, which is as simple as possible, but as complex as necessary. More realistic radiative transfer models like the one presented in Sect. 3.3.4.5 can be used to give such toy models a physical meaning.

2.2.2 Atmosphere and stellar interferometry

The degree of complexity of atmospheric disturbances of the single telescope imaging process can be described by the number of Zernike polynomials needed to estimate the wavefront corruption (Born & Wolf 1999). They consist of a set of orthogonal polynomials, which distinguish the different imaging errors like tip-/tilt, astigmatism, etc. The first Zernike polynomial calculates the piston, i.e. the atmospheric phase shift, between the telescopes of a two-element interferometer. The wavefront sensor of an AO system measures a certain number of Zernike modes. The Zernike polynomials can be factorized in a radial and an angle dependent factor. Thus the complexity of atmospheric disturbances are scaling with the size of the telescope aperture: The bigger the telescope, the more complex AO system is needed to enable diffraction limited images. In principle a two-baseline interferometer, the basic element of any interferometer, only has to correct for the first Zernike mode or piston between the two light rays before combination, independent of the baseline length. Thus increased angular resolution can be reached without the necessity to correct for more Zernike modes in contrast to larger telescopes.

On the other hand, the phase noise of the individual beam increases and exacerbates the piston correction with increasing baseline lengths, if, as in the case of the VLTI, the single element of the interferometer has again a diameter significantly larger than r_0 (the scale size of atmospheric turbulence) and spatial filtering is applied. AO correction at the individual interferometer elements reduces this phase noise (Tubbs 2004). Thus from the point of view of correcting atmospheric disturbances, the VLTI is positioned somewhere between a 100 m single telescope and an interferometer with 100 m baselines and small primary mirrors.
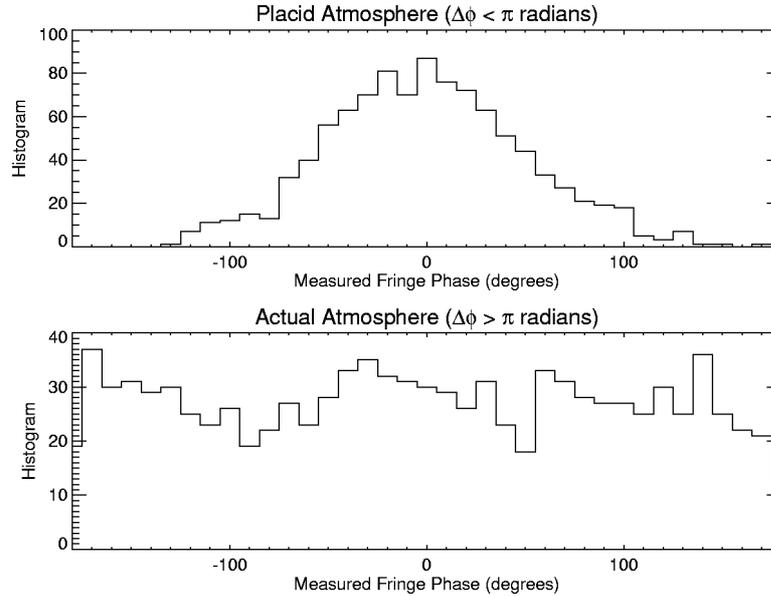
Figure 2.6: If the rms of statistic phase variations is smaller than 1 rad, coherent integration of successive fringes will lead to a fixed and calibrateable atmospheric phase contribution (upper panel). However in the infrared larger phase variations occur, and without a clear phase reference phases of 0 and 2π cannot be distinguished. The phase histogram resembles white noise (lower panel). The atmospheric phase contribution cannot be calibrated and the intrinsic phase information is lost. Figure from Monnier (2000).

As mentioned before, the typical piston noise at infrared wavelengths is larger than 1 radian. Thus phase wrapping occurs, and the single interference scans cannot simply be averaged to get rid of this noise (Fig. 2.6). Nevertheless coherent fringe averaging is possible for the spectrally dispersed MIDI data, bearing the promise of higher sensitivity at low SNR, as discussed in the next section. Beside the imaging limitations, fringe data of random phase have a further disadvantage. If in the single MIDI data frame, which usually is measured in a few ms to minimize thermal noise, the fringe contrast is too low to clearly identify the sine pattern, one cannot blindly integrate subsequent frames to increase the SNR as in normal imaging experiments. The time-varying phase will destroy any fringe contrast during averaging.

2.2.3   Coherent and incoherent integration of MIDI data

The thermal noise in mid-infrared data can easily be three orders of magnitude stronger than the science signal. This leads to very short detector integration times and several individual frames. In fact this necessity to observe thousands of single frames to achieve a decent SNR is used to ease the fringe detection. Periodically the OPD varies from frame to frame. Following Eq. 2.4, this results in a defined flux variation in each spectral channel (Fig. 2.7). MIDI measures dispersed fringes at a spectral resolution $R = \lambda/\Delta\lambda = 30$ or 230. Thus again following Eq. 2.4, in spectral direction each single scan shows a sinusoidal fringe pattern. Topic of this section is the way of how to average the single scans of a measurement.
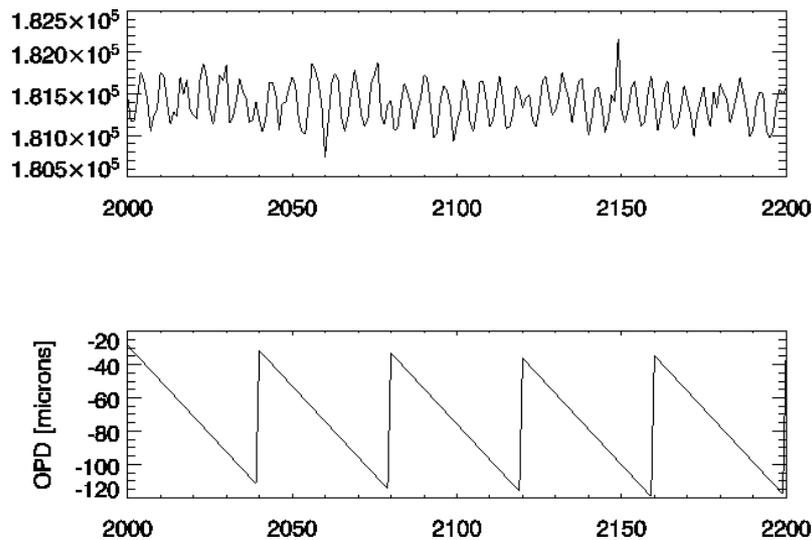
Figure 2.7: A part of a MIDI fringe measurement is shown. The abscissa gives the frame number. In the lower panel the periodically varied OPD is shown. The upper panel shows one spectral channel. The intensity varies sinusoidal following the OPD change, the shallow envelope is given by the narrow spectral band of one channel. Courtesy of W. Jaffe.

Incoherent integration

The incoherent method is depicted in Fig. 2.8. The fringe contrast or amplitude in each OPD scan is the correlated flux, which can be estimated by calculating the power spectrum of each scan along the OPD variation (Eq. 2.4, Fig. 2.7). The mean of the correlated fluxes of all scans is the average looked for. I have used this method to approximate the uncertainty of the correlated flux measurement by calculating the standard deviation over the observed scans. It turned out, that this error contribution is usually significantly smaller than other ones (Sect. 3.3.2.2).

The typical draw back of such power spectrum analyses is the always positive noise contribution to the signal, which systematically affects the result in case of low SNR. In the standard incoherent reduction of MIDI data, an average noise power contribution is estimated and subtracted. It is estimated away from the signal and for scans, which apparently do not contain any fringe.

Coherent integration

The idea of coherent integration is to estimate for each scan the OPD and phase $\phi(\nu)$ and change the measured fringe contrast according to Eq. 2.4 to a common OPD and phase. Then the individual scans can be averaged minimizing the noise contribution. This can be realized with MIDI data despite of the mentioned atmospheric phase corruption, because in the N-band the phase corruption changes dominantly linear with the frequency (Tubbs et al. 2004). And this linear trend can be estimated and rejected together with a fixed phase offset in each scan by analyzing the MIDI spectrum, which shows a sinusoidal frequency dependence with an amplitude corresponding to the current OPD.

Of course after removal of this linear trend, any linear spectral dependence of the intrinsic phase is removed as well, but the resulting differential phases of each scan are dominated by source properties and are not changing anymore by more than a radian over the scans. Now the scans
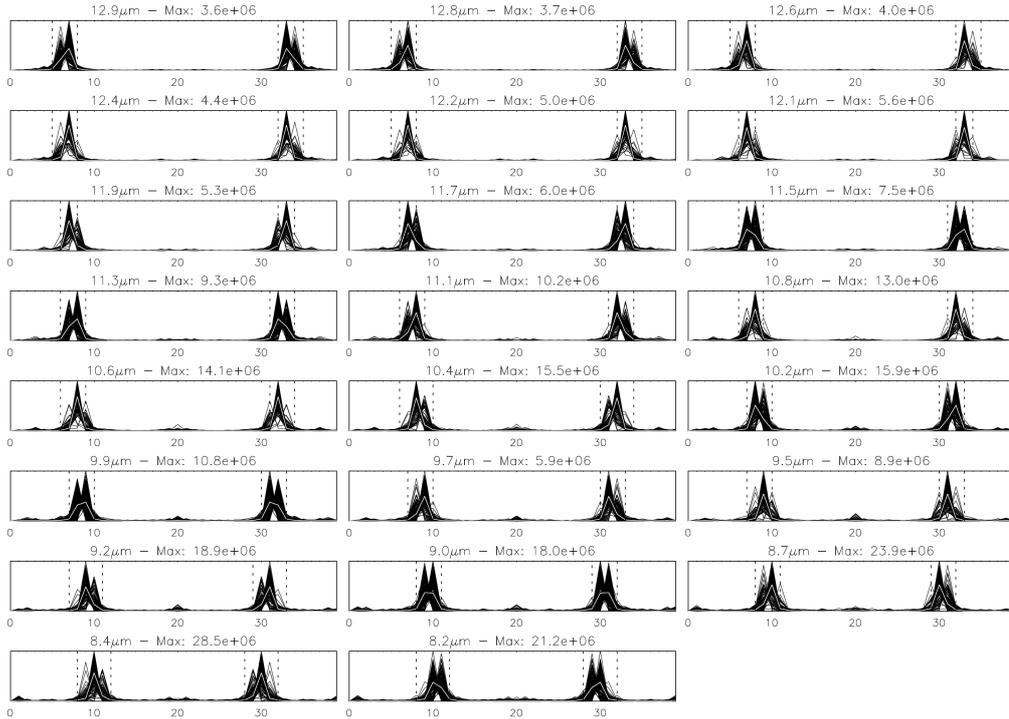
Figure 2.8: The power spectra of all 23 channels of a typical MIDI measurement at $R \sim 30$. Each power spectrum is calculated along one scan, the spectra of different scans are overplotted, the white curve in each panel is the mean power spectrum. The central wavelength of each spectral channel is indicated, the dashed vertical lines show the channel bandwidth in the Fourier space. The integrated flux between both dashed lines is proportional to the correlated flux. Due to the calculation of power spectra, any phase information is ignored. Abscissa coordinates are arbitrary, but centered around 20, right between the two arms of the cosine Fourier transform. Note the different ordinate scaling as indicated by the maximum value given on the top of each figure. Courtesy of Th. Ratzka.

Figure 2.9: A laboratory image a single MIDI scan showing the sinusoidal fringe pattern of one interferometric channel, which enables the group delay calculation. Courtesy of ESO.

can be averaged without separate estimation of the noise level as necessary for the incoherent averaging. The remaining noise contributions are minimized by the coherent algorithm. Details and formulae of coherent integration are given in (Jaffe 2004).

A part of my detailed analysis of the accuracy of MIDI data in Sect. 3.3.2.2 consists of a direct comparison of the results of both methods. Since the MIDI data of the Galactic Center is close to the sensitivity limit, a significant improvement by the coherent method could have been expected. But my results show, that the noise contributions to the results of the incoherent reduction can be estimated with sufficient accuracy. Rather the parallel reduction with both methods and comparison of the results revealed differences which changed statistically from dataset to dataset. Thus such a comparison of the differently reduced correlated fluxes leads to a more realistic approximation of the achievable reduction accuracy of one dataset.

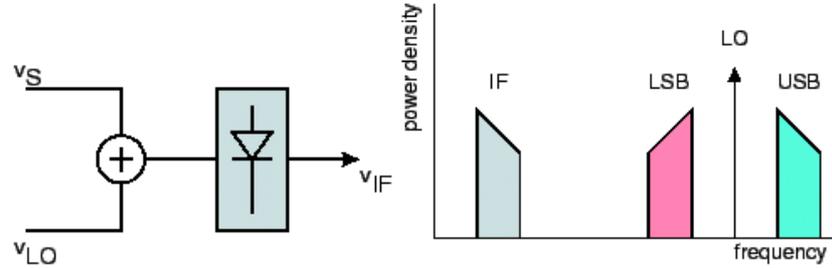## 2.3 Heterodyne receivers – outsmarting wave nature of light

Figure 2.10: Schematic frequency conversion in a heterodyne receiver. The left diagram shows the two building blocks of heterodyne mixing: The superposition, symbolized by the plus sign, of the interesting signal at sky frequency ν_S and the signal of the local oscillator at know frequency ν_{LO}. And the non-linear device, symbolized by the diode sign, with an appropriate output filter centered around the intermediate frequency ν_{IF}. Usually one of the two sidebands (USB,LSB in right panel) is suppressed before mixing (Dutrey 2000).

Technical basis of all the observations at cm-, mm-, and sub-mm wavelengths, which are presented in the Chapters 4, 5, and 6, respectively, are heterodyne receivers. Although nowadays, the heterodyne technique is very common and in use since many years, I give a short introduction for mainly two reasons. First its application in all radio interferometers is one of the major differences between radio and optical interferometry. And second, the special setup of the IRAM 30 m telescope, which I used to conduct the observation of chapter 5 is only understandable in the by drafting the heterodyne technique:

In the heterodyne receiver the typically weak signal of the celestial source (U_S)is added to a relatively strong monochromatic signal, called the local oscillator (U_{LO}). The sum is passed through a *non-linear* device, the output of which can be described by Taylor polynomials in ($U_S + U_{LO}$). We concentrate on the quadratic term, the others are suppressed at the output of the receiver

$$U_{S/LO}(t) = V_{S/LO}\,cos(2\pi\,\nu_{S/LO}t + \phi_{S/LO}) \tag{2.11}$$

$$\text{non} - \text{linear mix}: I(t) = a_0 + a_1(U_S + U_{LO}) + a_2(U_S + U_{LO})^2 + ... \tag{2.12}$$

$$= ... + a_2 V_S V_{LO} cos(2\pi\,(\nu_S \pm \nu_{LO})t + \phi_S \pm \phi_{LO}) + ... \tag{2.13}$$

$$filter(\underbrace{|\nu_S - \nu_{LO}|}_{\nu_{IF}}): I(t) \propto V_S V_{LO} cos(2\pi\,(\nu_S - \nu_{LO})t + \phi_S - \phi_{LO}); \, USB \tag{2.14}$$

$$or: I(t) \propto V_S V_{LO} cos(2\pi\,(\nu_{LO} - \nu_S)t + \phi_{LO} - \phi_S); \, LSB. \tag{2.15}$$

If U_S and U_{LO} are simply superposed, both sidebands (Fig. 2.10) are contained in $I(t)$, which is usually accounted for by filtering one sideband before mixing[14]. The signal has several good properties. It is proportional to V_S, thus tracing the original spectrum. But it is also proportional to V_{LO}, thus being amplified by the local oscillator. And of course the output signal now beats at ν_{IF}, which is usually significantly lower than ν_S. Actually the complete signal processing at a radio telescope can involve up to four heterodyne down mixing conversions.

The heterodyne mixers transform the intrinsic frequencies of the sky signal to MHz frequencies, which can easily be processed via standard high frequency (HF) electronics. The difference between radio and infrared sky frequencies is the fact, that the observable bandwidth $\Delta\nu$ is given

---

[14]As noted e.g. in Sect. **??**, the I have used such singe sideband receivers.

by the HF-spectrometer, which is fed with the down-mixed $I(t)$. Since the spectrometers do not offer more than a few GHz, the relative bandwidth $\Delta\nu/\nu_S$, which is proportional to astrophysical widths, shrinks with increasing sky frequency, down to extremely small spectral bandwidths at infrared wavelengths. This reduces the sensitivity and applicability to cover typical line widths in the optical-to-infrared. E.g. the THIS heterodyne mixer [15] offers in its standard version a bandwidth of 1.4 GHz, which equals a bandwidth of less than 15 km/s at 10 μm, whereas typical stellar lines show widths of tens of km/s. Thus the heterodyne option has to be omitted for most applications. That is the reason, why most stellar interferometers take the effort to combine the light directly, although also an infrared heterodyne interferometer has been realized [16]. The plus in bandwidth of direct interferometry at infrared stellar interferometers has to be paid by the technical difficulty of instantaneous optical path length correction at accuracies of a fraction of the observing wavelength. And very long baselines up to thousands of kilometers, like in radio VLBI (Chapter 6) cannot be achieved without heterodyne technology, since only the down-mixed signal can be recorded with loss of phase information, which is indispensable for the interferometric measurement.

The other reason, why I mentioned the heterodyne technique, is, that the observations of Chapter 5 were only possible by exchanging the local oscillator of the 3 mm receiver of the IRAM 30 m telescope. The cosmological redshifts beyond $z \sim 0.1$ of the observed quasars let the 88 GHz rest frequency of the observed HCN transition appear below the standard observing limit of 80 GHz, which is given by the frequency tuning range of the used local oscillators.

---

[15]**T**uneable **H**eterodyne **I**nfrared **S**pectrometer, a modern heterodyne infrared mixer developed at the Universität zu Köln, `http://www.ph1.uni-koeln.de/workgroups/astro_instrumentation/this/index.html`
[16]Infrared Spatial Interferometer Array `http://isi.ssl.berkeley.edu/index.htm`

Chapter 3

First fringes on the Galactic Center

In this chapter I report about three seasons of VLTI observations. These are the first successful interferometric observations at infrared wavelengths of sources, which are located closer then 0.5 pc to the very center of the Milky Way, a supermassive black hole. The observations show that optical long baseline interferometry (OLBI) at the GC offers a new tool for research at very high angular resolution. After an overview of the many fields of Galactic Center (GC) science (Sect. 3.1), I give a personal presentation of the GC as testbed for modern stellar interferometers (Sect. 3.2). The VLTI as most cutting-edge optical interferometer is right in the process of construction. Many upgrade phases still have to be implemented, and I outline several aspects, which can be studied by GC observations in the respective test and commissioning phases.

Then the results of the extensive MIR VLTI observation campaign is described in Sect. 3.3 & 3.4, with significant contributions to solving the enigmatic nature of GCIRS 3. As outlook to the near future, my new NIR-VLTI project is presented at the end of the chapter in Sect. 3.5, which has started about half a year ago.

3.1   Astrophysics at the Galactic Center

The GC is a huge scientific pit, with all kinds ores, which make up astrophysical research. The observations probe our understanding of star formation just as well as the formation of the nucleus of a late type galaxy. The distance from the earth to the core of the Milky Way has recently been estimated to be ~ 7.6 kpc or $25 \cdot 10^3$ ly (Eisenhauer et al. 2005), making the GC by far the closest center of a large spiral galaxy. Its astrophysical properties can be studied at a unique angular scale of ~ 40 mpc/arcsec, which equals 1.5 light months per arcsec. This is two orders of magnitude smaller than the angular scale at the nucleus of M31, the next comparable galaxy (McConnachie et al. 2005).

High resolution imaging observations of the central stars orbiting the location of the non-thermal strong radio source SgrA* gathered over the past decade compelling evidence for the existence of a supermassive black hole at the position of SgrA* (Fig. 3.1; Eckart & Genzel 1996; Ghez et al. 2000; Schödel et al. 2002). This opens the exciting possibility to observe and investigate star formation and the kinematics of the central stellar cluster under the direct influence of the gravitational potential of such a mass monster of $\sim 3.6 \cdot 10^6 \, M_\odot$ (Eisenhauer et al. 2005). General relativistic effects may be observable with the μas resolution of the new generation of interferometric instruments (Rubilar & Eckart 2001).
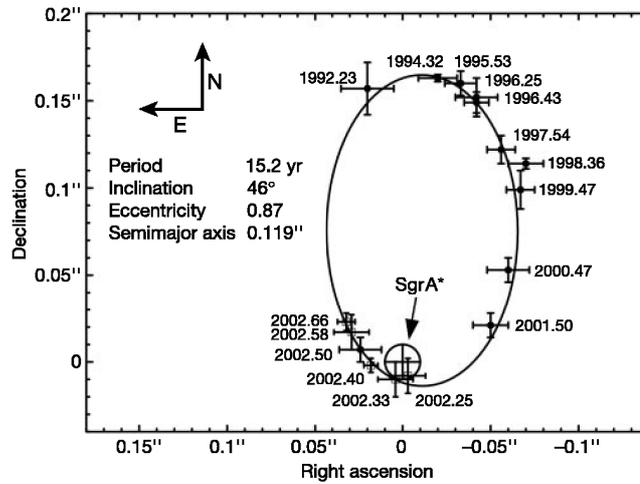
Figure 3.1: Orbit of the massive star S2 around SgrA*, which constrains the mass and location of the dynamic mass center, as indicated by the crossed circle. The time of the respective observation is indicated (Schödel et al. 2002).
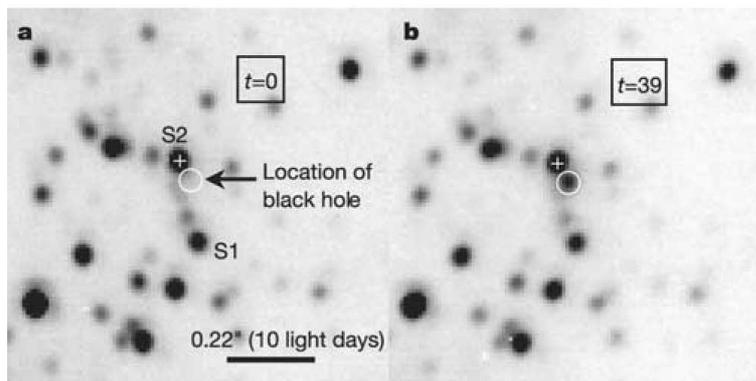

Figure 3.2: A NIR flare, emitting from the accretion disc around the SMBH at SgrA* (Genzel et al. 2003a). H-band AO-image is shown with 40 mas angular resolution. The time indicated in the boxes is in minutes and gives a flaring time scale. North is up and east is to the left.

The variety of experiments and obtainable resolution of the observations grows together with the technical progress and the inauguration of new instruments. Eisenhauer et al. (2005) use the new adaptive optics-assisted integral-field spectrometer SINFONI on the ESO VLT to observe the spectral imprint and position of stars within the central 30 lt-days. Polarized flares of the ongoing weak accretion onto the black hole can be regularly observed since a few years (Fig. 3.2; Genzel et al. 2003a; Eckart et al. 2004a, 2006). The sensitivity of the new mid-infrared VISIR instrument of the VLT enables first investigations of the photometry and infrared SEDs of more than 60 point-like sources, far beyond the number of known photometric MIR measurements at the GC (Viehmann et al. 2006). VISIR was shown most recently to be sensitive enough to detect the SgrA* in a flaring state (Schödel 2006a).

The unusually large number of massive, young stars in the stellar cluster at the GC (e.g. Krabbe et al. 1995; Genzel et al. 2003b; Eckart et al. 2004b; Moultaka et al. 2004) are indicative of an

active star formation history despite the tidal forces exerted by the gravitational potential of the central SMBH. The presence of numerous stars in short-lived phases of their development, such as dust-producing Wolf-Rayet (WR) stars, indicates that the most recent star formation episode took place not more than a few million years ago. This "paradox of youth" (Ghez et al. 2003) is still unsolved, but an inward spiraling of stellar clusters into the immediate vicinity of SgrA* is a possible option (Gerhard 2001). The strong tidal shear forces appear to suppress lower mass star formation (Morris 1993). The recent comprehensive reviews of Eckart et al. (2005) and Melia & Falcke (2001) present further up-to-date information of the Galactic Center.

At the present point, the angular resolution of the VLTI already allows to resolve the dust envelopes of some stars in the GC. A structural analysis on the scale of tens to hundreds of AUs would open the way for a detailed study of stellar properties, as well as for investigating the interaction between a star and the GC environment. The dust formation and ionization properties of a stellar cluster are dominated by the brightest and most massive stars, which are typically well suited for interferometric observations. Interferometry with the Very Large Telescope Interferometer (VLTI) will allow imaging of the Galactic Center at an angular resolution of a few milliarcseconds with the 2nd generation beam combining instruments. Thus the VLTI will be a prime instrument to study the immediate environment of the massive black hole at the center of the Milky Way in the upcoming years.

3.2 The Galactic Center as testbed for optical interferometry

While in the previous section I emphasize the prospects of high resolution observations of the GC, here I want to present a number of points, which show that the GC is not only a region of extraordinary astrophysical interest. Furthermore, the unique properties of the central stellar cluster are an ideal, challenging testbed for numerous tasks and applications of modern stellar interferometry with large telescopes. Most of the observational experience in stellar optical interferometry as well as the commissioning and science demonstration phases of the 1st generation VLTI instruments are based on nearby, isolated bright stars, the easiest targets for optical interferometry. However the GC offers many possibilities to probe the actual performance of the instruments under more challenging conditions. While the aspects discussed below apply to all optical interferometers, which can observe the GC, often I focus the discussion on the VLTI as an exemplary modern stellar interferometer.

Sensitivity

There is little experience made with observing fainter targets with AO assisted stellar interferometry. While totally dark in the optical, the GC offers in a central small field of about 30" diameter targets of large range of brightnesses. The brightest ones are already observable with the currently implemented modes of the 1st generation beam combining instruments, and for all planned further modes, which will increase the sensitivity, stars at the respective sensitivity limit are given (e.g. Fig. 3.35 for a NIR image).

In particular, a wide range of brightnesses can be observed in the same small region of the sky under exactly similar observing conditions due to the density of the central stellar cluster. Thus sensitivity dependent interferometric performance can be studied in great detail.
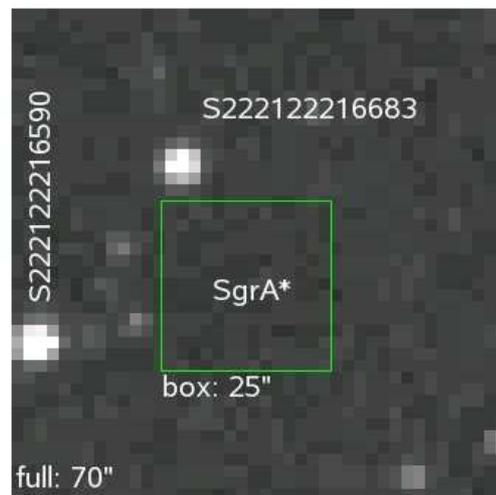
Impact of AO

Figure 3.3: Optical image from the Digitized Sky Survey of the central arcmin. The box, centered at SgrA*, highlights the central 25 arcsec, which contain my VLTI targets. Both named stars are suited as optical AO guide stars with a B magnitude of ~ 15. The GC itself is hidden by the high optical extinction.

A number of scientifically interesting targets (deeply embedded young or evolved stars, active galactic nuclei) are too faint in the optical wavelength regime to enable the use of Adaptive Optics to correct the incoming wavefronts. In these cases typically wavefront monitoring of an off-axis guide star is the alternative. The current AO system of the VLTI has an optical wavefront sensor. It has to be investigated how the achievable interferometric accuracy depends on the usage and distance of such an off-axis guide star.

Fig. 3.3 shows, that the GC offers two such optical guide stars. The closer (20" to SgrA*) is by 0.6 mag dimmer than the more distant one (30" to SgrA*). Since both brightness and distance affect the AO performance, both are equally well suited. Because the distance between both guide stars is comparable to the GC distance of both stars, even the expected Strehl ratio[1] at the GC can be approximated by estimating empirically the Strehl ratio of the second guide star, not used for the AO loop.

The dependence of the quality of interferometric GC observations on the AO performance can be investigated by the comparison of "off-axis" GC observations with "on-axis" calibrator observations. Typically the interferometric infrared calibrator stars also are in the optical bright enough to enable on-axis guiding.
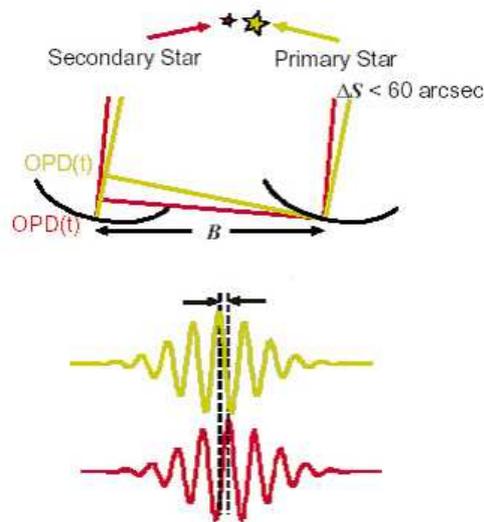
Figure 3.4: Visualization of the crowded field problem. If two nearby stars are bright and compact enough to produce fringes, their fringe patterns peak at a slightly different OPD. The indicated maximum distance of 60" are constrained by the field-of-view of the VLTI and depend on the interferometric infrastructure. Figure courtesy of ESO.

Crowded fields

High stellar density within the field-of-view of the interferometric science instruments or the fringe tracker may bear difficulties for the observability and the applied fringe tracking mechanisms.

Fig. 3.4 depicts the situation. If two close stars produce fringes, the fringe tracker has to be able to distinguish between both fringes. An error of the fringe tracking algorithm due to fringe blending decreases the visibilities and the accuracy of the OPD estimation. Also in case of clearly separated fringes it has to be assured that always the same fringe is monitored, if two nearby stars are in the interferometric field-of-view. The difficulty of this process also depends on the OPD noise induced by the atmosphere. Since this OPD noise increases with airmass, the GC is an ideal fringe tracking testbed for the VLTI, because the GC culminates at Paranal close to the zenith in the summer months and the full airmass dependence can be studied.

Several resolvable groups of massive bright stars exist in the inner 25", which have a number of stars concentrated within a diameter of $\sim 2''$ (IRS 16SW and IRS 13E; Lu et al. 2005; Schödel et al. 2005). Such dense stellar fields are not only challenging the complex acquisition and fringe tracking procedures of an optical interferometer. They are also prime targets for the first true imaging experiments.

Pointing accuracy

How feasible is efficient pointing on (faint) science targets with a very small field-of-view, which is a characteristic of all stellar interferometers? Again due to the extraordinary stellar density of the central parsec, as outlined in the previous paragraphs, numerous target cases at all sensitivity levels

---

[1]The Strehl ratio describes the quality of the wavefront correction by comparing the difference between the ideal diffraction limited PSF and the real one. The Strehl ratio is one, if the PSF is completely recovered.

can be found to probe the pointing accuracy. Especially in the MIR wavelength regime, diffuse dust emission is ubiquitous at any sensitivity level due to thermal dust radiation (Fig. 3.36). This can further hamper the acquisition procedure. The full range from isolated point sources to fully diffuse extended emission exists in the central parsec at MIR wavelengths.

All the aforementioned items constitute the suitability of the central parsec of the Galaxy for advanced testing of sensitive OLBI facilities. In the next section a scientific study with the currently available VLTI is presented, which is only possible with the angular resolution of the VLTI.

3.3 Peering to the enigmatic GCIRS 3 at highest angular resolution

GCIRS 3 is the most prominent MIR-source in the central parsec. NIR spectroscopy failed to solve the enigma of its origin. The properties and peculiarities of extreme individual objects of the central stellar cluster contribute to our knowledge of star and dust formation close to a supermassive black hole. I conducted an unprecedented interferometric experiment to understand the nature of GCIRS 3 and investigate its properties as spectroscopic and interferometric reference star at 10 μm. VLT/VISIR imaging resolves the compact emission[2]. The VLTI/MIDI instrument was used to measure spectroscopically resolved visibility moduli of this compact emission at an angular resolution of $\sim$ 10 mas. Recent NIR/MIR photometry data were added to enable simple SED- and full radiative transfer-modeling of the data.

The luminosity and size estimates show that IRS 3 is a cool supergiant enshrouded by an inner and a distinct outer dust shell. Blackbody temperatures were derived for both components in different ways. The coinciding interpretation of single telescope and interferometric data confirm the existence of both components. The interferometric data resolve the inner rim of dust formation. Despite the observed deep 10μm-silicate absorption towards GCIRS 3 I favor a carbon rich circumstellar dust shell. The silicate absorption most probably takes place in the outer diffuse dust, which is mostly ignored by MIDI measurements, but well observable in complementary VLT/VISIR data. This indicates physically and chemically distinct conditions of the dust depending on its distance to GCIRS 3. The results of this section have been submitted to a peer-reviewed journal for publication.

3.3.1 Introduction

The active history of star formation despite the tidal forces of the SMBH becomes manifest in the existence of numerous massive, young stars in the central cluster (Krabbe et al. 1995; Genzel et al. 2000; Eckart et al. 2004b; Moultaka et al. 2004). The 7 most luminous ($L > 10^{5.75}\,\mathrm{L_\odot}$), moderately hot blue supergiants ($T < 10^{4.5}$ K) provide about 50% of the flux ionizing the region (Blum et al. 1995; Krabbe et al. 1995; Najarro et al. 1997). Schröder et al. (2003) have shown, that a few tens of carbon rich supergiants can produce about 50% of the mass-loss of a large stellar sample with solar neighborhood characteristics. Thus, similarly to the ionizing flux, the mass loss and dust formation properties of a stellar cluster can be dominated by a few prominent stars. These facts underline the importance of studying individual extreme objects like GCIRS 3 [3] to understand properties of the entire surrounding stellar environment.

The recent advent of mid infrared[4] (MIR) instruments at 8 m class telescopes enables us to study

---

[2] The data reduction of the VISIR data was done by Rainer Schödel.
[3] in the following IRS 3
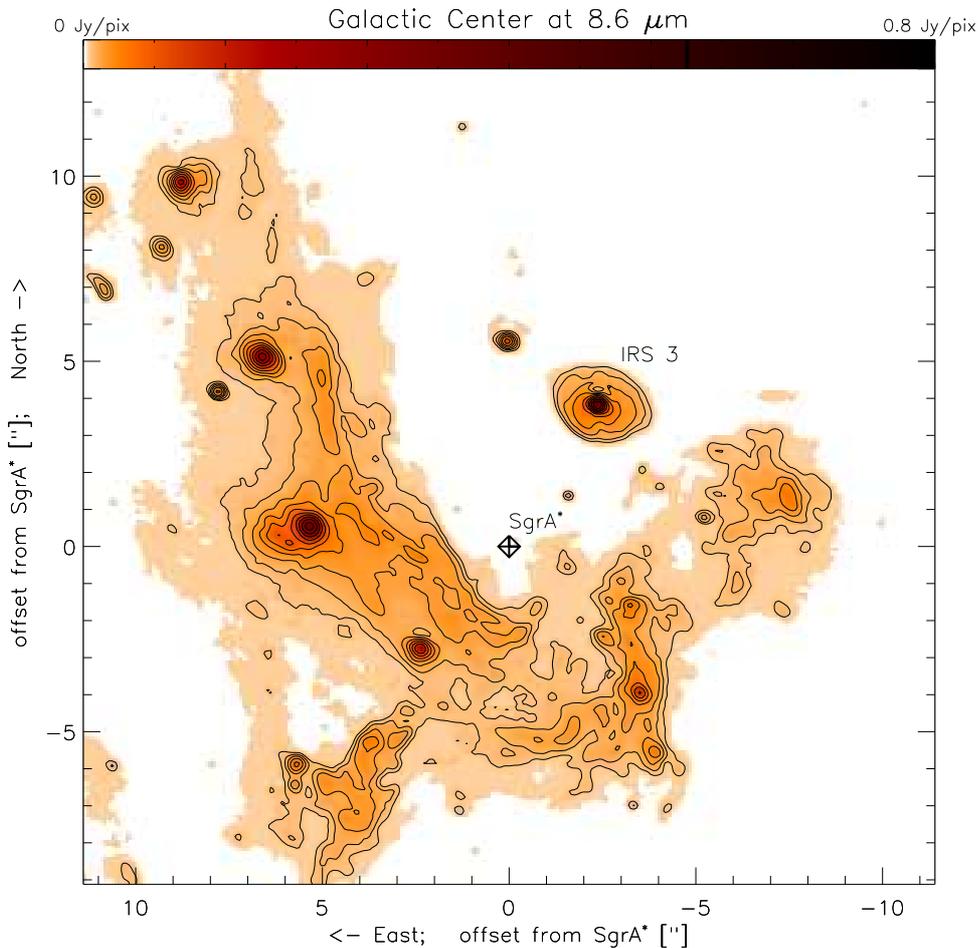[4] 3-20 μm covering the atmospheric L, M, N, and $Q-$windows

Figure 3.5: A flux calibrated Lucy-Richardson deconvolved image at 8.59 μm is shown, after restoration with a 250 mas Gaussian beam[2]. The logarithmic contours levels are $1.6^n \cdot 7$ mJy. The flux scale is given on top. IRS 3 and Sgr A* are highlighted. The data reduction was kindly provided by R. Sch$\acute{}$odel.

in detail the thermal dust at the Galactic Center (GC) at unprecedented angular resolution. The investigation of the circum- and interstellar dust distribution at the GC uncovers stellar mass loss, zones of wind interaction, formation history, evolution and kinematics.

Photometric and spectral properties of dusty stars at the GC have recently been published by Moultaka et al. (2004) and Viehmann et al. (2005, 2006). Despite an average optical extinction of $A_V \sim 25$ (Scoville et al. 2003b; Viehmann et al. 2005), infrared spectroscopy and imaging reveal the nature of the underlying dust embedded stars in most cases, since the dust extinction is wavelength dependent and decreases towards longer wavelengths.

This section focuses on the most prominent of the MIR bright dusty sources, the deeply embedded stellar source IRS 3, which still eludes any spectral classification (Paumard et al. 2006; Tanner et al. 2006). It is located within the central 20". A recent state-of-the-art N-band image with an angular resolution of only 250 mas is shown in Fig. 3.5. The extended and diffuse dust emission surrounding IRS 3 is visible at unprecedented angular resolution in this image.

NIR extinction studies reveal a spatial variation of only $\sim$10% ($A_K \approx 3$) of the interstellar extinction over this region (Scoville et al. 2003b; Moultaka et al. 2004; Schödel 2006b). In contrast,

narrow-band N-band photometry and spectroscopic observations are interpreted to indicate a significant amount of *additional* silicate absorption along the line of sight towards IRS 3 with respect to other parts of the central 20" (Becklin et al. 1978; Roche & Aitken 1985; Viehmann et al. 2006). The published intrinsic optical depths of order $\tau_{9.8}$(IRS 3) ~ 1 in addition to the average $\tau_{9.8}$(GC) ≈ 3.5 (e.g. Roche & Aitken 1985) still underestimate the true value due to confusion problems. While the high-resolution VISIR data clearly indicates that more than 50% of the N-flux is diffuse, extended emission at 0.3" resolution, a byproduct of the MIDI observations are calibrated low resolution spectra, which show $\tau_{9.8}$(IRS 3) to be much larger than the value given above.

Rieke et al. (1978) found the spectro-photometric MIR properties of IRS 3 to resemble either young stars near or within HII regions or OH/IR stars. The former interpretation is supported by the lack of radio emission, the latter is opposed by the lack of OH-maser emission. With a MIR color temperature of ~ 400 K, the central emission of IRS 3 was found to be (together with the nearby GCIRS 7) the hottest and most compact of the sources dominating the thermal dust irradiation from the GC (Rieke et al. 1978; Gezari et al. 1985; Smith et al. 1990). Extended dust emission around IRS 3 interacting with external stellar winds has been found in recent $L-$ and $M-$band observations (Viehmann et al. 2005). While hot star hypotheses are given by some authors (Krabbe et al. 1995; Tanner et al. 2003), the lack of ionizing gas leads Roche & Aitken (1985) to the assumption of IRS 3 being a cool dust enshrouded star.

Within the past two years I collected a unique dataset of OLBI data of IRS 3 at 10 μm. These constitute the first successful OLBI observation of an object within the central parsec of our galaxy, opening the window to NIR/MIR GC observations at highest angular resolution (Pott et al. 2005a). In this sections I show that the OLBI data strongly support the former hypothesis of a cool dust enshrouded star. Furthermore the results shed light on the amount and spectral shape of the interstellar 10 μm extinction towards IRS 3 at unprecedented angular resolution. Since MIDI is a relatively new instrument, the achievable precision of visibility measurements of such distant, challenging targets is not common knowledge yet. In Sect. 3.3.2 I describe the observations, the extensive data reduction and calibration efforts, and the evaluation of different data reduction techniques in some detail. Then the immediate observational results are given (Sect. 3.3.3), followed by a detailed discussion of the results in the astrophysical context (Sect. 3.3.4) and the conclusions in Sect.3.3.5.

3.3.2   Observations and data reduction

In summer 2004 I started an observing campaign to study the brightest MIR-excess sources in the Central Parsec with MIDI at the highest angular resolution available today. The Mid-infrared interferometric instrument (MIDI) combines the light of two 8.2m unit telescopes of the ESO Paranal Observatory in Chile (Leinert et al. 2003). I used the standard 0.5"×2" slit and dispersed the light over the entire $N-$band (8-13 μm) with the prism providing a spectral resolution of $R \sim 30$. The first MIR fringes of IRS 3 were recorded successfully on the night of 7 Jul 2004. The whole dataset comprises 14 independent visibility measurements of IRS 3 with interlaced calibration measurements (Table 3.1).

3.3.2.1   Interferometric calibrator stars

In Table 3.2 I list the used calibrators with their main features. The angular diameter estimates result from fitting ATLAS9 and MARCS model atmosphere spectral energy distributions (SEDs)

Table 3.1: Log of observations of IRS 3. The wavelength dependent transfer function has been estimated for each night on basis of regularly conducted calibrator measurements, typically about once per hour(Sect. 3.3.2). The number of calibrators used per night is given, the applied parameters are given in Table 3.2. The projected baseline length (PB) and position angle (PA) are given for the beginning of the fringe measurement. The last column gives the median relative uncertainty obtained for the calibrated visibility outside the low-flux region of the silicate absorption.

Baseline	PB	PA	Airmass	accuracy
	[m]	[deg E of N]	[1]	[%]
#1 night: 2004-07-07	-	5 calibrators		
U2-U3	45.7	46	1.03	12
U2-U3	42.3	52	1.16	12
U2-U3	37.0	55	1.45	12
U2-U3	26.4	53	2.63	14
#2 night: 2004-07-08	-	8 calibrators		
U2-U3	44.9	11	1.38	19
U2-U3	43.5	50	1.11	14
#3 night: 2005-05-25	-	7 calibrators		
U3-U4	45.8	89	1.36	14
#4 night: 2005-06-23	-	4 calibrators		
U3-U4	45	89	1.39	23
U3-U4	46.8	90	1.33	16
#5 night: 2005-06-27	-	4 calibrators		
U3-U4	54	139	1.29	11
#6 night: 2005-07-20	-	7 calibrators		
U3-U4	58.6	101	1.07	22
U3-U4	59.6	124	1.08	22
#7 night: 2005-08-23	-	2 calibrators		
U3-U4	62.5	112	1.00	20
U3-U4	54.9	136	1.25	21

to optical and NIR photometry. The used models (Kurucz 1992, 1994; Plez et al. 1992) adopt solar metalicity. Details of the model fitting are given in van Boekel (2004, Chapter 5). The modeled $12\mu m$ flux densities listed in Table 3.2 are consistent within $\lesssim 5\%$ with the work of Cohen et al. (1999), who presented a list of absolutely calibrated infrared spectra. Furthermore none of the used calibrators shows an MIR-excess, defined as having a measured $12~\mu m$ flux density more than $3~\sigma$ above the synthetic spectra fitted to the optical-NIR data. Such a MIR-excess would indicate the existence of (extended) dust shells. Dust shells, which can be expected to exist around K-M giants, radiate the stellar flux at longer wavelengths and decrease the visibility amplitudes of the entire object, i.e. they deteriorate the calibrator properties. The absence of a MIR-excess makes all visibility calibrators usable as potential photometric calibrators too, down to the 5% uncertainty, which is often not reached due to atmospheric and instrumental variability. The photometric variability and the fitting uncertainty of the angular diameter of all used calibration stars in Table 3.2 affect the accuracy of the derived transfer functions by less then 1% at all VLTI baselines (≤ 200 m).

Table 3.2: Parameters of the calibrators used for estimating the transfer function. The last column gives the night in which the calibrator has been used.

Name	Spectral type	Diameter [mas]	Flux dens. [Jy @12μm]	night
HD107446	K3.5III	4.42±0.03	22.0	4
HD109379	G5II	3.25±0.02	15.1	1
HD123139	K0IIIb	5.34±0.03	36.4	3
HD134505	G8III	2.50 ±0.01	8.4	4
HD142804	M1III	2.79±0.04	8.0	7
HD152820	K5III	2.62±0.01	7.5	3,4
HD160668	K5III	2.28±0.01	5.7	3,5
HD165135	K0III	3.48±0.02	15.5	1-7
HD169767	G9III	2.16±0.01	5.9	3
HD169916	K1IIIb	4.00±0.03	20.1	4
HD173484	M4III	3.43±0.04	11.9	5,6
HD177716	K1IIIb	3.76±0.03	17.1	2
HD178345	K0II	2.49±0.01	7.6	5-7
HD188512	G8IV	2.07±0.01	5.9	1-3
HD192947	G6/G8III	2.33±0.02	7.5	1
HD213009	G7III	2.08±0.02	5.9	5
HD218594	K1III	3.18±0.02	12.4	3
HD220704	K4III	3.45±0.02	13.2	7
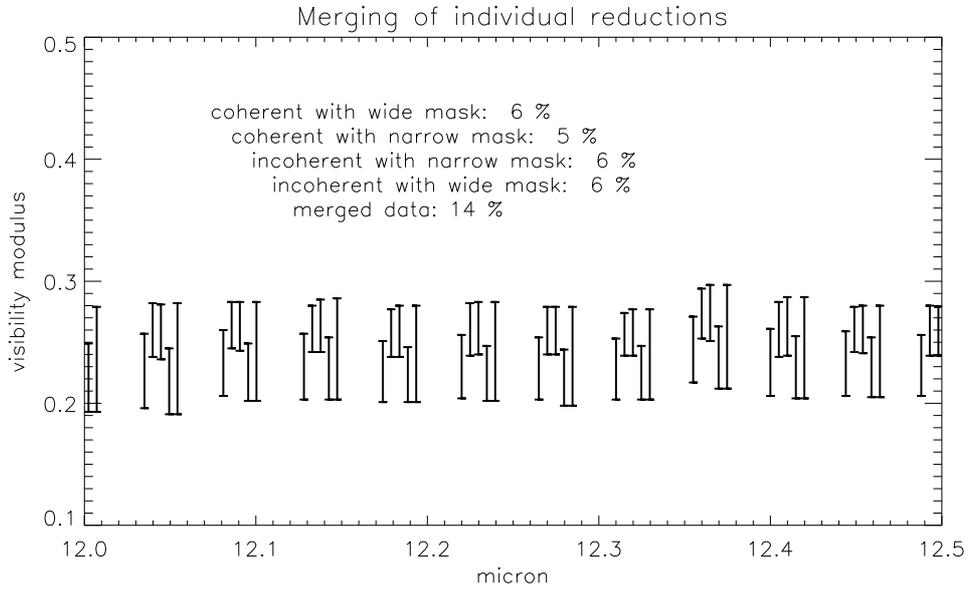
Figure 3.6: A part of the science data taken on 2005-05-25 is shown. To clearly demonstrate the differing results of the different reduction methods (coherent and incoherent fringe averaging and static and dynamic detector apertures), they are overplotted with increasing shifts in wavelength. The method and its intrinsic relative error, if applied on the given data set, is indicated with similar shifts. The position of the narrow dynamic detector mask was optimized for each measurement to match the brightest pixels. The rightmost error bars present the merged, maximum error bars. I based my analysis on these merged data.
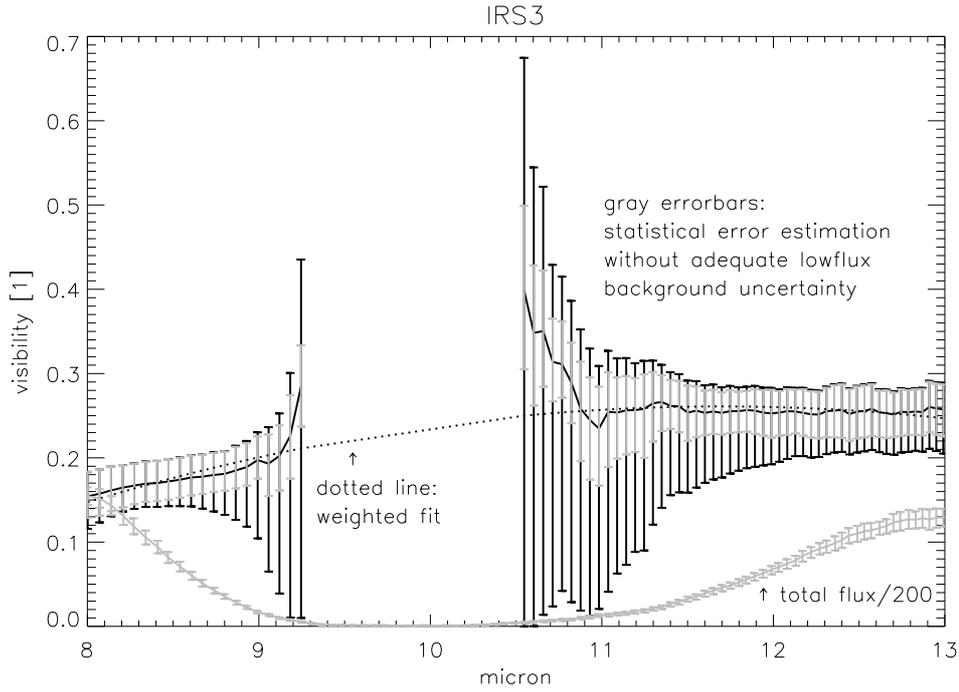
Figure 3.7: Influence of faulty background estimation on the final accuracy, the night of 2005-05-25 is shown here. The standard reduction (gray) of this dataset suggests a significant deviation from the smooth visibility spectrum, which is shown by the dotted line (weighted quadratic fit over the silicate absorption feature). E.g. the visibility increase, suggested by the gray data points, short-wards of 11 μm towards the absorption center, cannot be confirmed if I consider the impact of background subtraction errors (black error bars). Thus it might be an artefact of the data reduction algorithms run at the sensitivity limit. Indeed not all datasets are showing such an increase after the standard reduction. To demonstrate the flux dependence of the importance of background accuracy, I overplotted the total flux spectrum (in Jy).

3.3.2.2 Calibration and absolute accuracy

The immediate measurand, the raw visibility V_{raw}, is the ratio of measured correlated (F_{C}) and total flux (F_{T}). The final quantity of interest is the calibrated visibility (V_{cal}), which is computed by dividing the raw visibility (V_{raw}) by the interferometric transfer function (TF) of the observation. Propagation of errors relates the uncertainties Δ to each other

$$V_{\mathrm{calib}} = \frac{V_{\mathrm{raw}}}{TF} \qquad \rightarrow \quad \left(\frac{\Delta V_{\mathrm{calib}}}{V_{\mathrm{calib}}}\right)^2 \;=\; \left(\frac{\Delta V_{\mathrm{raw}}}{V_{\mathrm{raw}}}\right)^2 + \left(\frac{\Delta TF}{TF}\right)^2 \qquad (3.1)$$

$$TF = \frac{V_{\mathrm{raw}}}{V_{\mathrm{ideal}}}\bigg|_{\mathrm{calibrator}} \quad \rightarrow \quad \left(\frac{\Delta TF}{TF}\right)^2 \;=\; \left(\frac{\Delta V_{\mathrm{raw}}}{V_{\mathrm{raw}}}\right)^2\bigg|_{\mathrm{calibrator}}. \qquad (3.2)$$

The TF is derived from the V_{raw} measurement of a calibrator star and its intrinsic visibility (Eq. 3.2). The uncertainty of the diameter of the calibrator usually is too small to affect ΔTF (Table 3.2). Thus $\Delta V_{\mathrm{calib}}$ suffers twice from the accuracy of the estimation of V_{raw} (Eq. 3.1). This central accuracy can be estimated by means of the following considerations and investigations of calibrator data sets:

All constant defects of V_{raw} are corrected for by multiplication with TF and thus have only minor influences on the final accuracy. E.g. the time delay between the measurement of F_{C} and F_{T} is
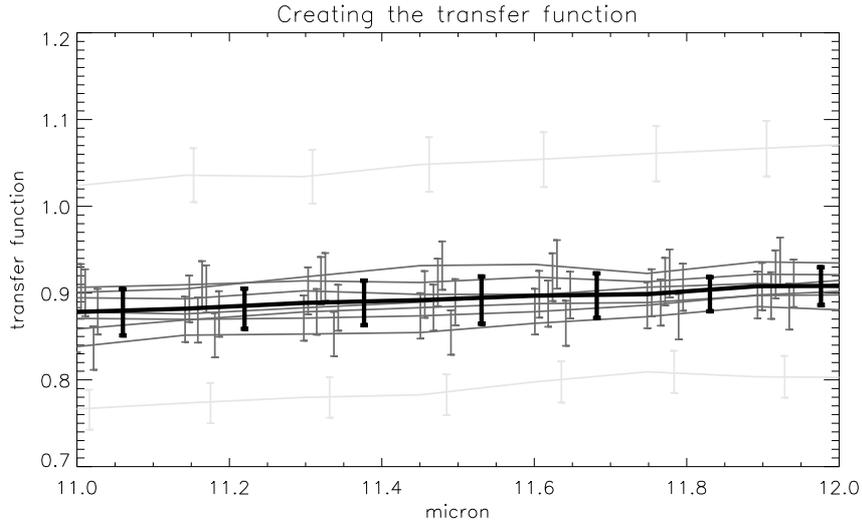
Figure 3.8: The transfer functions are shown in gray, derived from the individual calibrator measurements of 2005-05-25. The error bars of order 5% indicate the statistical error of the single data frames of one measurement, which is slightly smaller than the absolute variation of the TF over the night. The mean TF, which I use for this night, is overplotted in bold solid black style with the standard deviation. This standard deviation should be smaller, if the uncertainty of a single TF is only 5% (Sect. 3.3.2.2). The two light gray TF were rejected from calculating the mean because of abnormal behavior relative to the average of the good TF.

only a few minutes in the high-sensitivity mode of MIDI used. This reduces the variation of atmospheric transmission in the thermal infrared, due to airmass difference and temporal fluctuations, to such a level that a small and time-constant impact on the quotient F_C/F_T can be assumed. I prove this by the following test, visualized in Fig. 3.9. If the atmospheric and instrumental flux transmission change randomly at a significant level between the F_C and F_T measurements, the orders of magnitude of V_{raw} and the resulting TF are affected and the absolute accuracy of the calibrated visibility is worse than the relative spectral accuracy. To derive this spectral accuracy I linearly normalize each individual TF of a night by dividing through the integral over a fixed part of the N-band and estimate the maximum scatter in each spectral channel. If this scatter is significantly smaller than the scatter of the normalization factors, a strong transmission variability has been observed (assuming constant intrinsic visibility). Fig. 3.9 shows that this is not the case.

Faulty and unequal background suppression during reduction of both data sets also does not vary on a significant level for the bright calibrator stars. The influence of background noise for faint science targets is discussed at the end of the section.

As a matter of fact Leinert et al. (2004) states that the accuracy of V_{raw} is dominated by the accuracy of the overlap between the interfering beams , which critically relies on the wavefront corrections during observations. This is difficult to quantify and thus cannot be easily incorporated in the TF. Usually the quality of the beam overlap does not vary *statistically* during one observation. This means that there is no *mean* overlap accuracy which correctly describes a single observation and that the TF, if derived from one calibrator measurement, may not be applicable to a subsequent science observation. I confirm this on the basis of my dataset. A single observation of both F_C and F_T consists of several frames which are averaged during data reduction. I estimate the standard deviation of the subsequent scans and analyze the background in chopped photometry data to derive a statistical uncertainty for each measurement of V_{raw}. The resulting total statistical
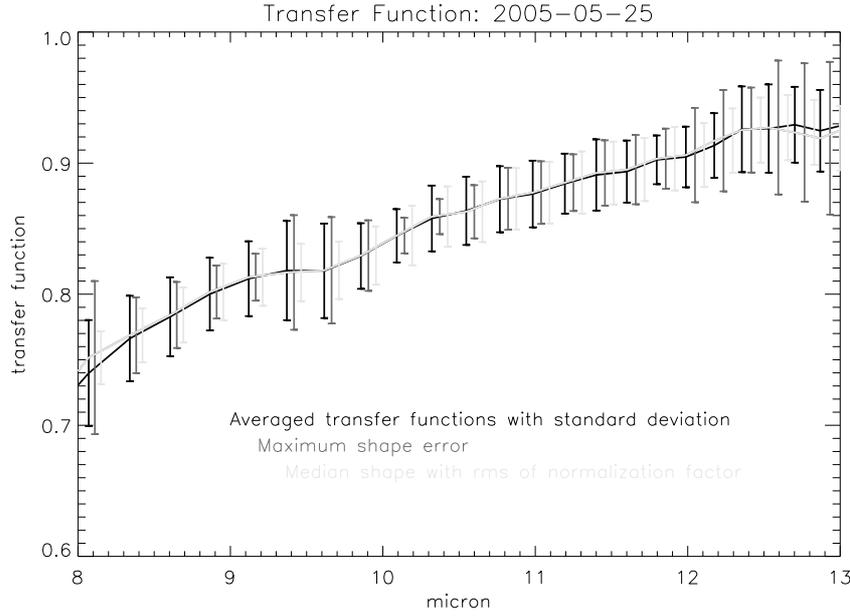
Figure 3.9: Different analyses of the transfer functions, derived from the calibrator measurements at 2005-05-25 are shown. To increase the clarity of the plot, the wavelengths of the two gray overplots are shifted, as indicated by the labeling in the figure. Black line and error bars are the result of averaging (mean & standard deviation) of the individual TFs. Both gray curves are averaged in normalized space, created by dividing the individual TF by their integral. The dark gray errors indicate the maximum differential fluctuation between adjacent spectral channels, thus presenting a conservative maximum of the spectral shape error of TF. The light gray errors however are reflecting the standard deviation of the normalization factor, thus representing the order of magnitude of the variability of transmission between the F_C and F_T measurement. Note the increase of the shape error around the atmospheric ozone absorption band at 9.7 μm and at the borders of the N-band, where the applicability of simple linear normalization decreases.

uncertainty $\sigma(V_{\mathrm{raw}})$ is similar for the individual calibrator observations, but it cannot fully explain the larger scatter of individually estimated TF over the respective observing night (Fig. 3.8). That means that the absolute accuracy of the visibility measurement can change significantly with every new pointing.

Furthermore the overnight scatter of TF is significantly reduced in the 2005 data due to the more stable VLTI feeding by the higher-order AO-system MACAO instead of the earlier tip-tilt only correction of the STRAP units (Arsenault et al. 2003). This also confirms the dominating influence of varying beam overlap and flux concentration between different pointings on the visibility accuracy.

The above given tests and considerations underline the origin of the accuracy of the V_{raw} measurement and motivate that the accuracy of a single measurement can only be given by the TF statistics of *several* calibrator measurements. I calculate the mean and standard deviation of the different TF to quantify TF and ΔTF. Note that the estimation of errors presented even holds for an extended calibrator with visibilities significantly less than one, provided that the diameter of the calibrator is known at sufficient precision. Although $V_{\mathrm{raw, calibrator}}$ will systematically change over the night with changing projected baseline length, this effect is annihilated by calculating TF (Eq. 3.2).

Since the number of calibrators per night is typically around 8, one TF strongly deviating from

the others can influence mean and standard deviation significantly. To avoid this situation I did not use the median, but rejected manually the anomalous TF (on average one per night, Fig. 3.8). This has the advantage that the mean and standard deviation of the resulting sample better represents the spectral shape of the TF reducing the probability of artificial spectral features in the calibrated visibility spectrum.

To complete Eq. 3.1 I have to know the relative uncertainty of V_{raw} of the measured target. Qualitatively the origin is similar, as discussed above for the calibrators, but the flux of the science targets can be significantly smaller than the calibrator fluxes. Since my calibrators cover a range from 5-35 Jy, I searched for any flux dependence of ΔV_{raw} on basis of my data. I checked for every night, whether on average the scatter of the TF of the fainter calibrators is larger than the scatter of the TF of brighter ones, but did not find any such flux dependence. Thus I assume a flux-independent relative uncertainty of V_{raw} resulting in the uncertainty of the calibrated visibility

$$\frac{\Delta V_{\mathrm{calib}}}{V_{\mathrm{calib}}} \quad = \quad \sqrt{2} \cdot \frac{\Delta TF}{TF} \,. \tag{3.3}$$

 This estimation might still underestimate the relative accuracy of the final calibrated visibility of the science target, since IRS 3 was observed with an off-axis AO-guide star, which decreases the AO performance with respect to the on-axis guiding on the calibrators. I compared the PSF of the photometric data of IRS 3 with the calibrator measurements and specified three datasets with calibrator-like PSF. These are highlighted throughout the analysis and provide the tightest constraints to my interpretation of the data (cf. Sect. 3.3.2.4, 3.3.3).

If the correlated flux drops significantly below 5 Jy and approaches the sensitivity limits, an increase of the relative uncertainties will probably occur due to the increased influence of noise, but outside the deep silicate absorption the correlated spectrum of IRS 3 is above this limit. Furthermore, imperfect background subtraction has an increasing influence on the final accuracy with decreasing source flux. To account for this I estimate the background level by reducing sky-frames without the source. Typically the background randomly varies between zero and a value close to F_{bg}, where F_{bg} is the sum of the mean and standard deviation of all spectral channels of the background frames. This leads to a maximum background induced error interval

$$V_{\mathrm{raw,bg}} \in \left(\frac{F_{\mathrm{C}} - F_{\mathrm{C,bg}}}{F_{\mathrm{T}}}, \ \frac{F_{\mathrm{C}}}{F_{\mathrm{T}} - F_{\mathrm{T,bg}}} \right) \,. \tag{3.4}$$

which dominates the flanks of the strong silicate absorption towards IRS 3. A putative increase of visibility towards the absorption center, which appears to be present after applying the standard reduction, cannot be verified after incorporating the background uncertainty (Fig.3.7).

3.3.2.3   Data reduction

I used the data reduction package MIA+EWS provided by the MIDI consortium[5]. This package offers two different methods to reduce the data: *incoherent* averaging of the fringe power in each spectral bin over several scans, and *coherent* averaging of the single dispersed scans. In the $N-$band the latter method can provide the differential phase information in addition to the visibility amplitude, if the atmospheric and instrumental delay and dispersion have been properly removed. A more detailed description of both methods and their realization in MIA+EWS

---

[5]See the ESO web pages for general information and links (`http://www.eso.org/instruments/midi`). Currently the data reduction package is provided on: `http://www.strw.leidenuniv.nl/~nevec/MIDI`.

is given by Leinert et al. (2004) and Jaffe (2004), respectively. Since noise contributes always positively to the power spectrum, it is not automatically reduced by averaging incoherently over several scans. In contrast the coherent integration reduces the statistical noise of the fringe data by averaging, which makes this method favorable at very low correlated flux (below about 1 Jy) and low SNR. Correlated fluxes down to 0.1 Jy could be estimated by this method (Jaffe, private communication). Since my MIDI data is usually well above this limit I found consistent results of both reduction algorithms throughout the complete dataset (Fig. 3.6).

The constantly changing baseline projection due to earth rotation limits the integration times of the T_C measurement. To reduce the noise level, which is intrinsically high in the thermal infrared, only the pixels with the highest SNR should be considered by the reduction algorithm. This is achieved by detector aperture masks, which can lead to reduced SNR if the chosen aperture is too large, too small or misplaced with respect to the incident source photons. This effect is strongly enhanced by beam distortions and motions only partially corrected by the AO system, which holds especially for my data since I had to lock the AO on an off-axis guide star 35" away from the GC. Therefore I reduced the full dataset four times: with both coherent and incoherent fringe averaging and by applying two different apertures (or detector masks), a wide standard one with fixed location and a narrower one which is chosen dynamically for the PSF of every observation to trace the beam maximum and to have an optimized size.

After calibrating the data and estimating its accuracy as described in Sect. 3.3.2.2 the four spectra ($V_{\text{calib}} \pm \Delta V_{\text{calib}}$) were averaged. To estimate the accuracy conservatively, I select a maximum ΔV_{calib} including all four uncertainty intervals (Fig. 3.6).

Note that the apparent correlation between systematically higher visibilities and the use of the narrower mask in this figure is not a general systematic effect, but depends on the data set. Other data show an apparent correlation between visibility and averaging method, independent of the chosen mask. Consequently I do not prefer one single reduction method to another but use the merged data. Note further that the differences are *significant* with respect to the intrinsic uncertainties, resulting in clearly increased uncertainties of the merged data. The mean final relative accuracy of each merged scientific dataset is given in Table 3.1.

3.3.2.4 Photometric Calibration

MIDI observations provide the astronomer with spectra of the total flux of the target in addition to the visibility modulus. I flux-calibrated the spectra on the basis of the regularly observed interferometric calibrator stars, typically late type giants (Sect. 3.3.2.1). I fitted an airmass-dependent system response to the calibrator measurements of each night to flux calibrate the science data (for a more detailed description see van Boekel et al. 2005). Spectra that were obviously faulty were not taken into account. Such a time-independent system response model makes it possible to use all good calibrator measurements of the night, which is especially favorable if the broad band spectrum of the science target is not known. Furthermore the airmass dependence can minimize the impact of larger distances between the calibrators and the target. In some nights only one star was closer than $10°$ to the target due to scheduling requirements. On normal nights the incorporation of airmass-dependence reduces the calibration uncertainties by up to 5%. But then the model includes uncertainties due to varying atmospheric transmission and the instrumental throughput over the night, resulting in final photometric accuracies of about 5-10%, which dominate the intrinsic uncertainties of the used calibrator spectra.

The Gaussian detector masks (Sect.3.3.2.3), that are typically applied, do not affect the visibility

calculation but only the photometry. If the science target is not completely unresolved by the single telescope PSF (Fig. 3.20) or if such a weighting mask is not well centered on the brightest pixels, the measured flux is decreased. I reduced the photometry separately without applying any mask to take care of any such bias. Furthermore it turned out that a lot of datasets on the target have at least one beam of significantly lower quality than the other one. Since the calibrator measurements do not show such a strong beam variation, this effect is assumed to result from the use of an off-axis AO guide star during the observations of IRS 3, decreasing the accuracy of the wave-front correction (Sect.3.3.2.3). A manual selection of good datasets facilitates a final photo-spectrometric accuracy of less than 10%, which is decreased towards low fluxes due to the remaining background. The result is shown in the lower spectrum in Fig. 3.15).

3.3.3   Results

In this section I present the direct results of my interferometric measurements

3.3.3.1   Visibility moduli

Table 3.3: The measured mean visibility moduli below and above the silicate absorption, which is centered at 9.8 μm. PB and PA stand for projected baseline length and position angle and characterize the interferometric resolution at the time of the observation.

Julian date	PB	PA	Visibility	
	[m]	[deg E of N]	8-8.7 μm	11.8-13 μm
#1 night: 2004-07-07				
2453194.7	45.7	46	0.17 ± 0.05	0.27 ± 0.04
2453194.7	42.3	52	0.20 ± 0.06	0.28 ± 0.04
2453194.8	37.0	55	0.24 ± 0.07	0.34 ± 0.04
2453194.9	26.4	53	0.47 ± 0.19	0.53 ± 0.10
#2 night: 2004-07-08				
2453195.5	44.9	11	0.22 ± 0.06	0.32 ± 0.06
2453195.7	43.5	50	0.22 ± 0.05	0.26 ± 0.04
#3 night: 2005-05-25				
2453516.6	45.8	89	0.17 ± 0.03	0.25 ± 0.04
#4 night: 2005-06-23				
2453545.5	45	89	0.10 ± 0.05	0.18 ± 0.05
2453545.5	46.8	90	0.11 ± 0.04	0.22 ± 0.04
#5 night: 2005-06-27				
2453549.8	54	139	0.13 ± 0.02	0.22 ± 0.03
#6 night: 2005-07-20				
2453572.5	58.6	101	0.10 ± 0.04	0.21 ± 0.05
2453572.7	59.6	124	0.08 ± 0.03	0.18 ± 0.04
#7 night: 2005-08-23				
2453606.5	62.5	112	0.05 ± 0.02	0.15 ± 0.04
2453606.6	54.9	136	0.05 ± 0.02	0.12 ± 0.04

In Table 3.3 the measured visibility moduli are given. Following Sect. 3.3.2.2 I did not find within the uncertainties any deviation from a smooth visibility slope over the full $N-$band. Since no
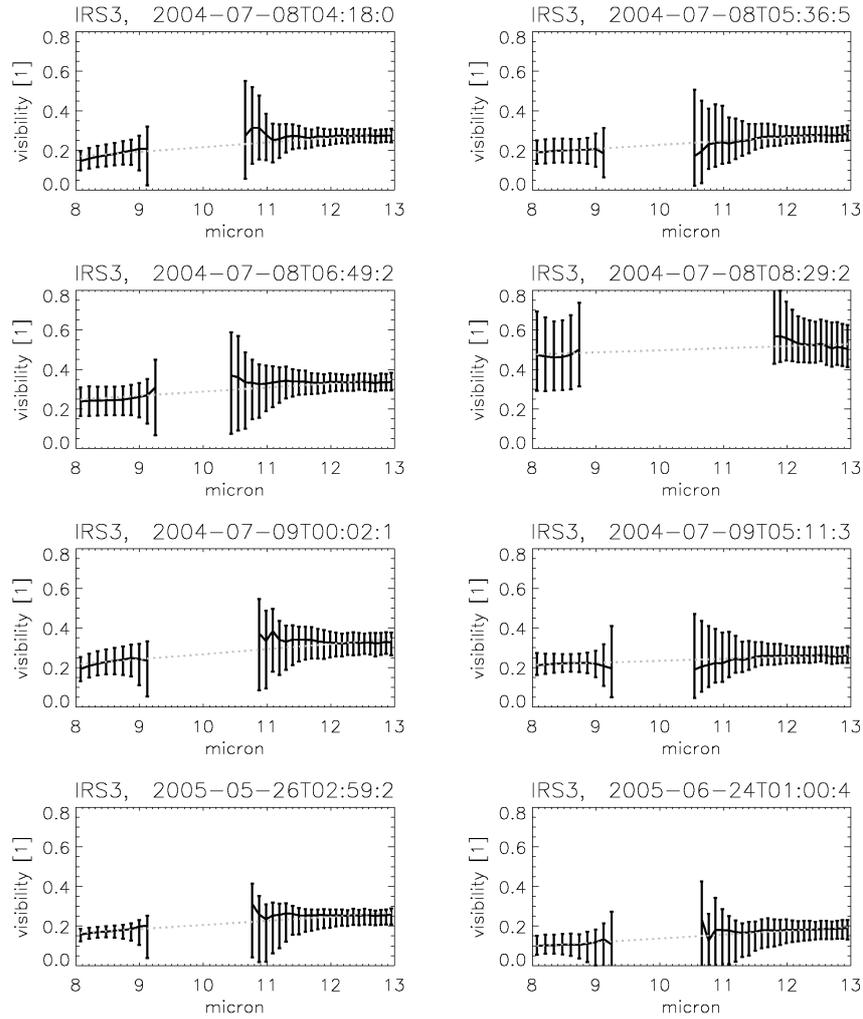
Figure 3.10: The calibrated visibility spectra with identical scaling in all plots. The observing time is indicated. Furthermore the gray dotted line shows the linear interpolation over the deep silicate absorption, where I do not have reliable data. If necessary I used the interpolated data, but only in the central wavelength interval without error bars.

correlated fluxes have been measured at the center of the silicate absorption, I give the mean visibility and its accuracy for two adjacent wavelength intervals in Table 3.3. The fully calibrated visibility spectra are shown in Fig. 3.10.

3.3.3.2   Probing the circular symmetry in uv-space

Circular symmetry in uv-space implies circular symmetry of the brightness distribution. To probe the variation of the measured visibility, I compared our data at a given uv-radius. Since I observe a smooth continuous visibility spectrum over the $N-$band apparently free of spectral line features within the uncertainties, no spectral channel is biased towards a certain dust layer bearing such a line emission or absorption. Thus the size scale of the brightness distribution of the dust should be constant or increase only slightly with wavelength, due to the lower temperatures of larger, outer dust components dominating at longer wavelengths. By fitting a wavelength-independent
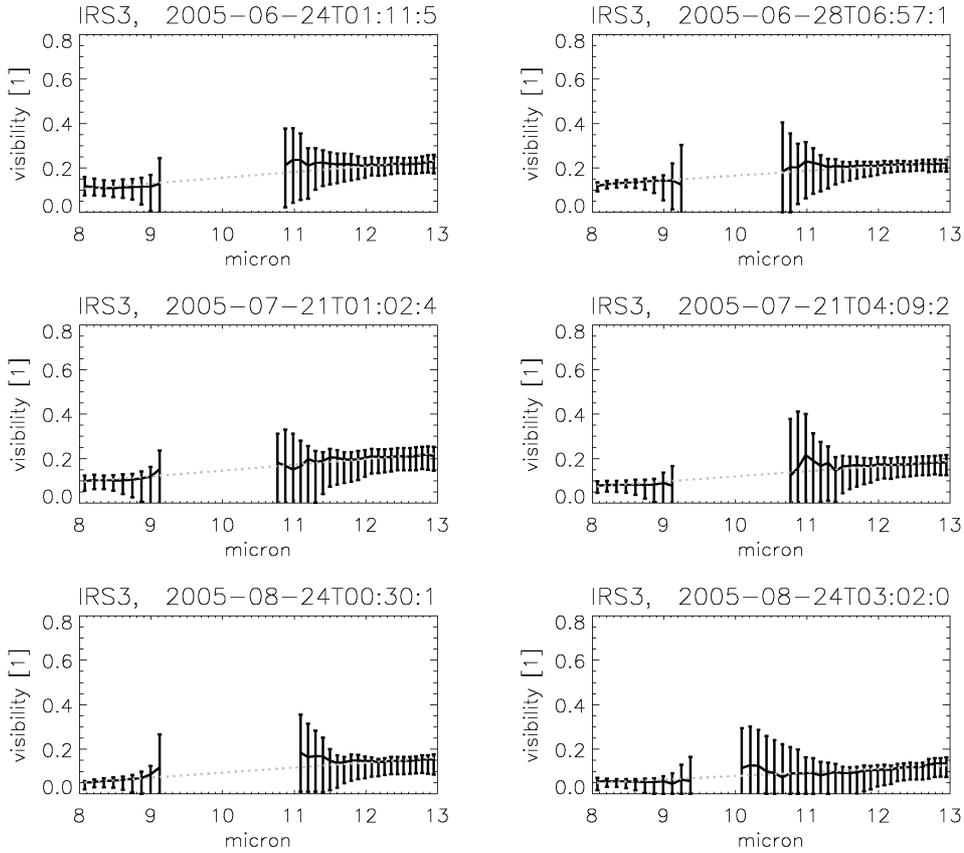
Figure 3.11: Continuation of Fig. 3.10

brightness distribution, I in fact average over such slight size increases with wavelength, and at the same time I greatly enlarge the uv-dataset at a given uv-radius, since I can use all spectral channels together.

In Fig. 3.12 I show the uv-coverage of the entire dataset, overplotted with a ring of constant uv-radius (5 Mλ). The uv-radius gives the angular resolution and should show similar visibilities at different position angles (PA) in case of circular symmetry. In Fig. 3.13 the mean visibilities at $R_{uv} = 5$ Mλ of each dataset are plotted. The overplotted horizontal indicates that the full dataset still conforms with total circular symmetry. Although some data points do not perfectly coincide with circular symmetry, it has to be remembered that the shown error bars of single measurements may be underestimated, since their estimation relies on averaging several calibrator measurements of the observing night leading to an average uncertainty which may be exceeded in individual cases.

On the other hand the drawn horizontal shows that a slight deviation from circular symmetry is possible. The values around PA=(120$\pm$30°) appear to lie on average below the values at smaller PA. Possible reasons for such circular asymmetry are discussed in Sect.3.3.4.4. But it has to be mentioned that the data points with the best photometric quality (used to fit the horizontal in Fig. 3.13) have nearly identical visibilities at different PA. And a comparison with the uv-coverage (Fig. 3.12) shows that the longer wavelength spectral channels have been considered at those PA with a tendency towards lower visibilities (Fig. 3.13), i.e. the possible deviation from circular
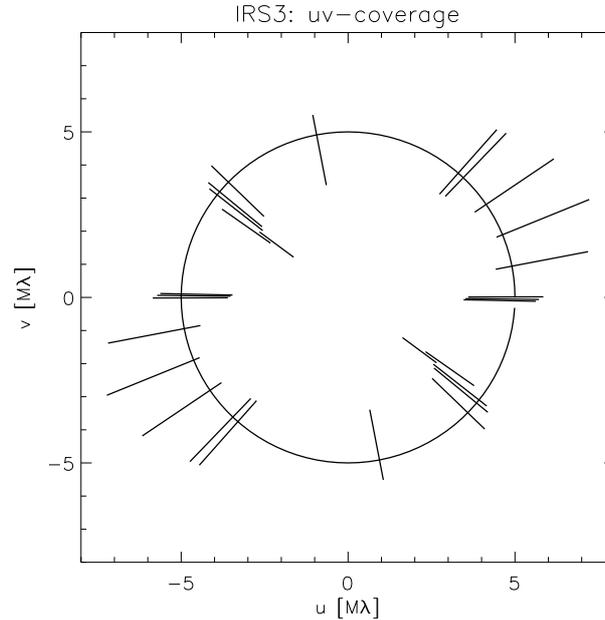
Figure 3.12: uv-coverage of all used observations. The overplotted ring indicates a uv-radius of 5 Mλ. I have investigated the degree of circular symmetry along this annulus (Fig. 3.13).
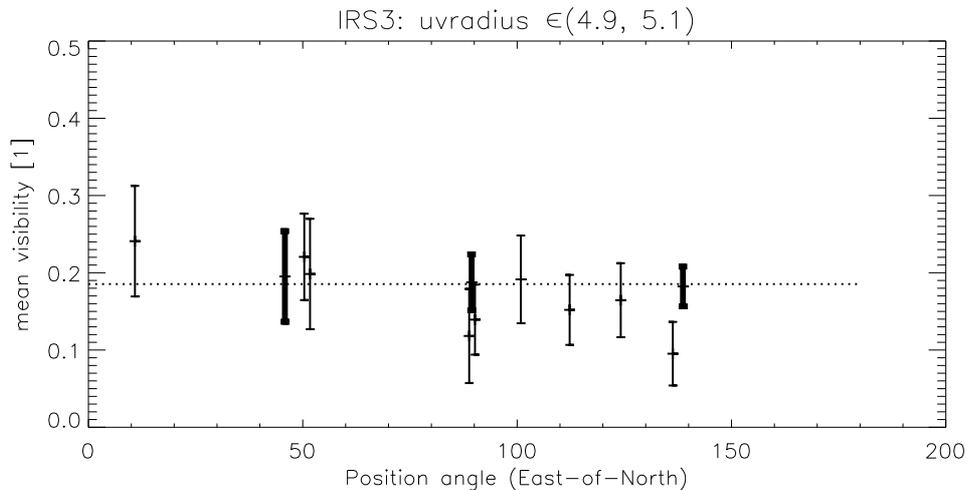
Figure 3.13: The measured visibilities at a uv-radius of 5 Mλ are shown. To guide the reader's eye I have overplotted a horizontal representing total circular symmetry, which was fitted to the data of best photometric quality in both beams (three thick error bars). If a linear correlation with arbitrary slope is fitted to the full dataset, a negative slope shows a $\sim 10\%$ smaller reduced χ^2, which could indicate asymmetry or a wavelength dependent size (Sect. 3.3.3.2).

symmetry in Fig. 3.13 might in fact be an artefact of the assumption of wavelength-independent size. This interpretation is further backed by a slight increase of size with wavelength indicated by the wavelength dependent analysis of the data (Sect. 3.3.3.4.2).

Based on the circular symmetry found I show the PA-averaged data plotted over the uv-radius in Fig. 3.14. Similar to Fig. 3.13, a wavelength-independent brightness distribution has been
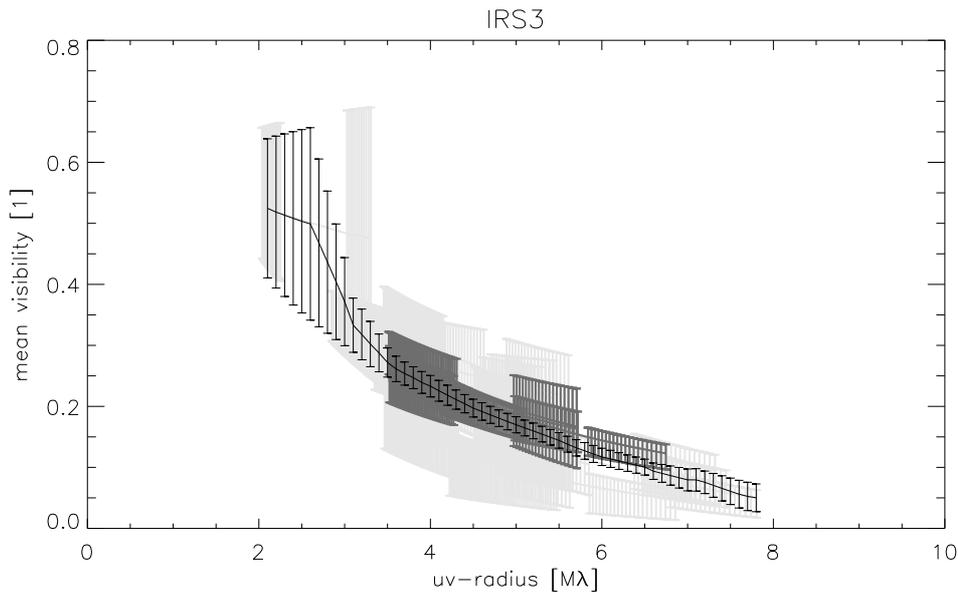
Figure 3.14: The azimuthal and spectral average plotted over uv-radius (black solid line and error bars). The measured visibilities are overplotted (error bars in light gray). The three datasets with best beam quality are highlighted in dark gray. To calculate the average, I interpolated linearly over the silicate absorption where necessary.

assumed to merge all datasets. The three datasets of highest photometric quality are highlighted. This suggests that beyond $\sim 6\,\mathrm{M}\lambda$ the averaged uv-data (black solid line) indicate visibilities, that are too low since they lie below the best data.

3.3.3.3 Photo-spectrometry

In Fig 3.15 the flux-calibrated spectrum of IRS 3 is shown based on the reduction described in Sect. 3.3.2.4. Only the data of best photometric quality and AO correction have been taken into account. The resulting three data sets, observed in July 2004, May 2005, and Jun 2005 do not show significant photometric variability beyond the general uncertainties. This agrees with the study of flux-variable sources in the GC by Ott et al. (1999), who find no variability for IRS 3.

3.3.3.4 Morphological interpretation of the visibility data

In this section I explain the MIDI data by a model for the brightness distribution, which is as simple as possible, but as complex as necessary. Although the results cannot compete with detailed radiative transfer models, they summarize the average order-of-magnitude properties in terms of morphological shape, size and flux. Such a heuristic model is therefore an important check and starting point for further analysis, discussion and interpretation of the data (Sect. 3.3.4). Thanks to the large multi-wavelength data set I get a non-trivial model of the dust distribution around IRS 3.

3.3.3.4.1   General structure   I assume a circularly symmetric brightness distribution of wavelength independent size (Sect. 3.3.3.2). The full dataset is shown in a radial uv-plot in Fig. 3.14.
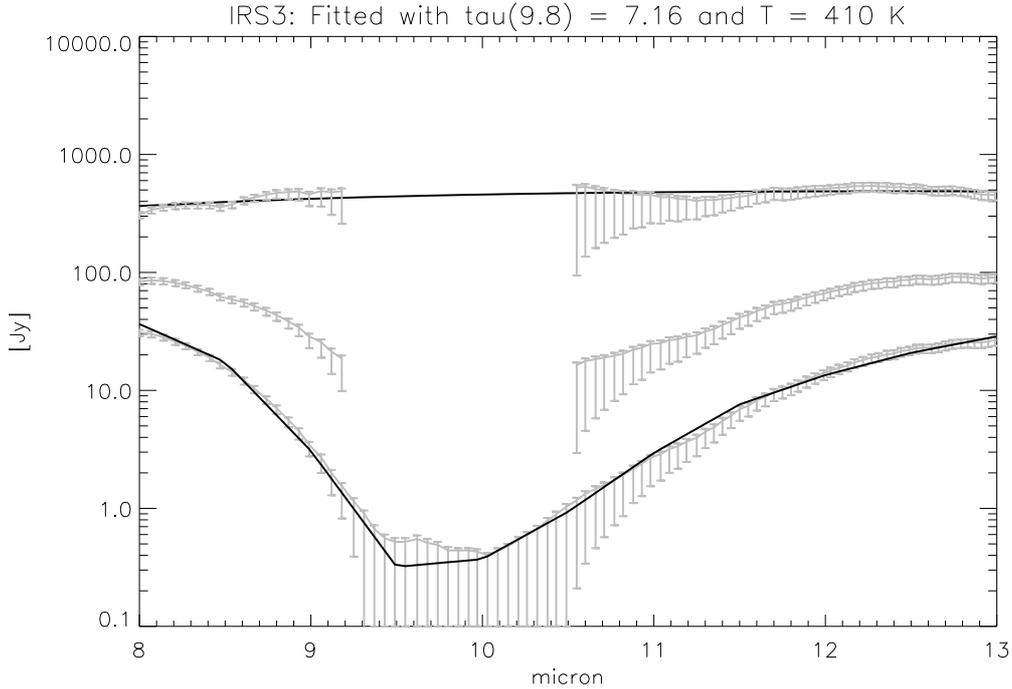
Figure 3.15: The flux calibrated and dereddened photometry. The upper spectrum is dereddened with $\tau_{9.8} = 7.2$, its error bars indicate the wavelength intervals used to fit the temperature. The middle spectrum is dereddened with $\tau_{9.8} = 3.3$, which corresponds to the standard average optical extinction of A_V=25 towards the central parsec, assuming the extinction law by Moneti et al. (2001). The lower spectrum is the extincted measured spectrum. The black solid lines show the extincted and dereddened χ^2-minimized temperature fit of T=410 K.
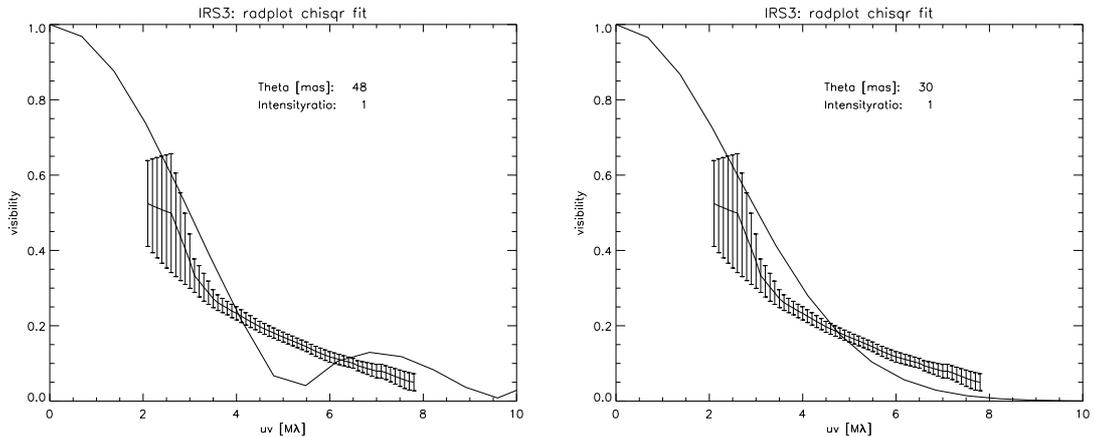
Figure 3.16: Best-fit models of the brightness distribution with a *single* component model; left panel shows a uniform disc, right panel shows a Gaussian. The angular diameter is indicated.

The two simplest circularly symmetric brightness distributions are a uniform disc and a Gaussian. Fig. 3.16 demonstrates that the visibility moduli cannot be explained by a single component. Despite the conservative error estimates neither of both models can reproduce the data even approximately.

In contrast, *two* superposed components of different size and intensity ratio are sufficient to model
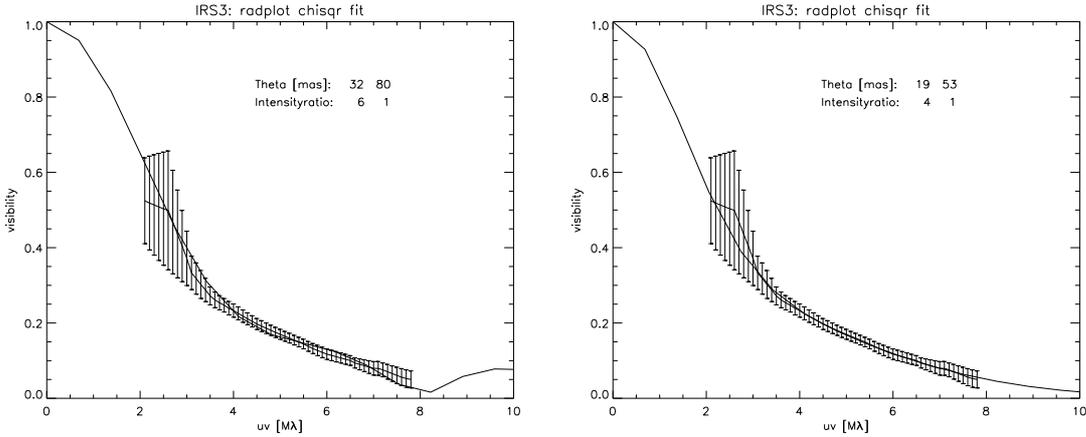
Figure 3.17: Best-fit models of the brightness distribution with a *two* component model. Left: two uniform disc components; right: two Gaussian components. The error bars are the azimuthally averaged data (Fig. 3.14, Sect. 3.3.3.4.1). Both models fit the error bars satisfactorily, but the Gaussians are closer to the measured data: the reduced best-fit χ^2 is about ten times smaller for the two-Gaussians model.

the data (Fig. 3.17). With the given dataset both two uniform discs and two Gaussians are possible. However, the data reduction indicates that the visibility at low uv-radii (~ 2.5 Mλ) is probably overestimated, and should be expected to lie in the lower half of the indicated error bars. This would favor a Gaussian shape for the larger component. At longer uv-radii the smaller component dominates. A closer coincidence with the data suggests a Gaussian shape for the smaller component, too. But the final distinction between Gaussian and disc shape of the smaller component requires additional data at longer baselines. In case of a uniform disc the visibility would increase again around ~ 10 Mλ as indicated by the overplotted model in Fig 3.17 (left panel). I investigated the uv-space ≥ 12 Mλ with the longest UT-baseline (UT1-4: 130m) without fringe detection. This might support a Gaussian shape for the smaller component. But it is also possible that the visibility increase, indicative of a uniform disc shape of the inner component, was too small to be detected with the long baselines used.

3.3.3.4.2 Wavelength dependence The spectroscopically resolved MIDI data allow the investigation of wavelength dependent properties of the general model of the previous section. I fit intensity and size of two superposed Gaussians to the data (Fig. 3.18). I bin the data to a 0.5 μm sampling, using error-weighted visibility averages. The unreliable data around the center of the silicate absorption are interpolated using a χ^2-fit of a quadratic curve to the spectral channels of good SNR. In Fig. 3.10 the individual fit regions are indicated by error bars. The interpolated data are used in the central wavelength interval devoid of error bars.

In Fig. 3.18 the resulting best-fit parameters are shown. Using χ^2-minimization, the uncertainties of the fit are of the order of the scatter of the data around the overplotted linear correlations. A slightly larger systematic uncertainty might be introduced by the estimated errors of the individual data points. To address this, I re-fit the data with increased weighting of the three datasets of best photometric quality. The overall trends are similar, but the size of the larger component may be underestimated in Fig. 3.18 by 5-10 mas, θ_s, the FWHM of the smaller component, may show a slight size-increase with wavelength by about 3 mas, and the flux ratio increases towards the smaller component ($F_s/F_l \sim 0.7$). This increased flux ratio can be understood by lower photometric quality, typically decreasing the average visibility due to imperfect beam overlap.
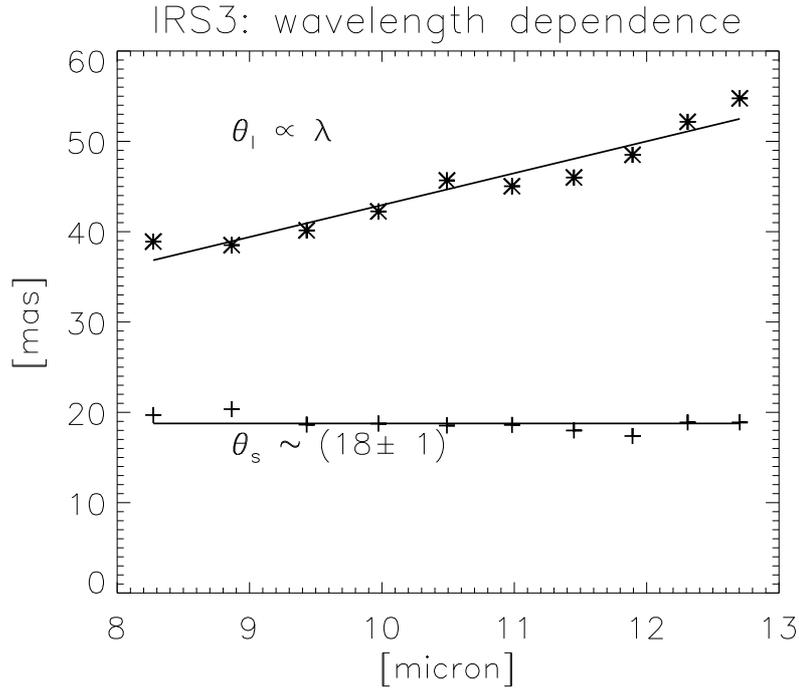
Figure 3.18: Wavelength dependent model consisting of two Gaussians. The inner component shows stable size over the N-band, an indication for carbon rich dust shells (Ivezic & Elitzur 1996b). The trends are discussed in the text. Around 10 μm, the Gaussians are fitted to the interpolated data points. See also Fig. 3.19

But a decreased visibility means increased *relative* brightness of the larger component. Thus, probably a few of the data sets of lower photometric quality show too small visibilities, favoring the larger structure.

The most intriguing result is that the smaller component (θ_s) shows a roughly constant full width at half maximum (FWHM) of about 18 mas, while the larger shows a significant linear size increase with wavelength. This is an indication that I directly resolved the inner zone of dust formation at all wavelengths, which has a fixed size, and that the dust shell might be carbon rich (Ivezic & Elitzur 1996b,cf. Sect. 3.3.4.5).

Furthermore the relative flux contribution of the larger component increases with wavelength, suggesting that the larger component is an outer, cooler dust shell around the central object. Temperatures and luminosities of both components are derived in Sect. 3.3.4.3 purely based on the interferometric data.

3.3.4 Discussion

3.3.4.1 Interstellar absorption and the composition of the circumstellar absorbing dust

Following the most recent published results, I assume a spectral profile of the interstellar absorption towards the GC as published by Moneti et al. (2001) and an average visual extinction of $A_V = 25$ towards the GC (Scoville et al. 2003b; Viehmann et al. 2005). Moneti et al. (2001) incorporated into their model that the mean interstellar dust towards the GC region shows a relatively
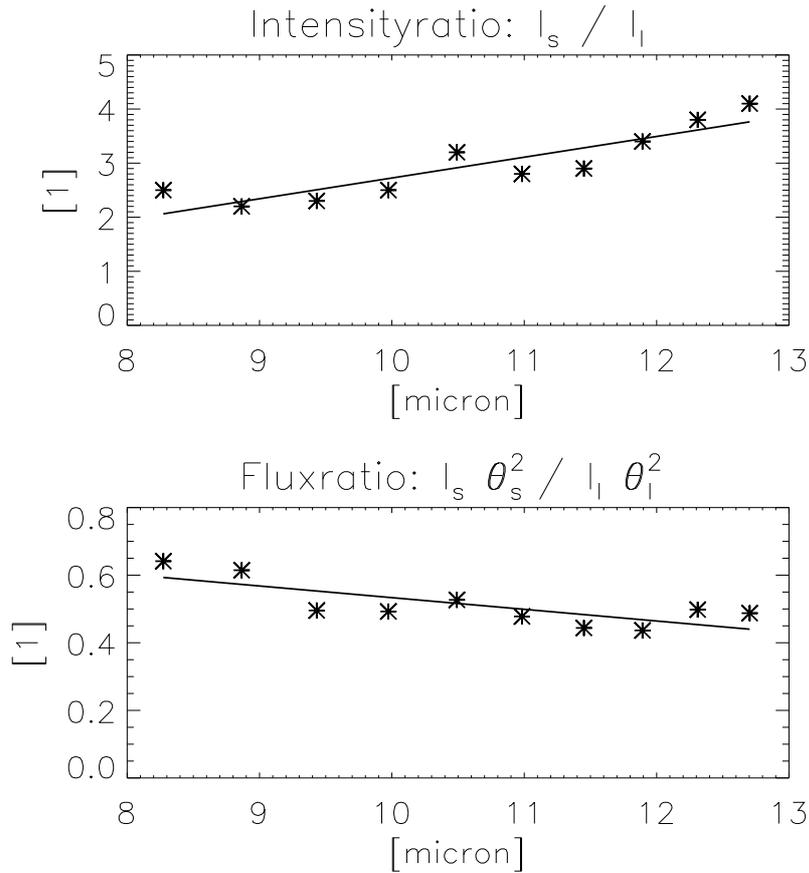
Figure 3.19: Continuation of Fig. 3.18. The wavelength dependent model consisting of two Gaussians. $I_{s/1}$ denote the intensities (in arbitrary units) and $\theta_{s/1}$ denote the FWHM of the smaller and the larger component, respectively. The flux ratio calculates as $(I_s \theta_s^2)/(I_1 \theta_1^2)$. In Sect. 3.3.4.5 the physical properties of the inner component are analyzed by RT calculations.

stronger silicate absorption than in the solar neighborhood (Roche & Aitken 1985).

While no strong increase of the interstellar extinction towards IRS 3 is found in the NIR (e.g. most recently confirmed by Schödel 2006b), several authors claim silicate absorption along the line of sight to IRS 3 intrinsic to the source. (e.g. Roche & Aitken 1985; Viehmann et al. 2006).

A first glimpse of the probable location of this additional extinction is given by the high resolution single telescope N-band imaging with the new VLT/VISIR instrument. In Fig. 3.21 the complete emission of IRS 3, unresolved by earlier imaging, is clearly resolved into a diffuse and a compact component. Although the total diffuse flux is even larger than the compact flux, its surface brightness is very low and hidden in the noise of all MIDI data. Thus most of the diffuse flux is not included in the single telescope MIDI photometry ($F_{T,\lambda}$), although it is observed at similar spatial resolution to the VISIR data. The two components fitted to the interferometric data (Sect. 3.3.3.4) and discussed in the following sections, together make up the unresolved emission in the right panel of Fig. 3.21. To clarify the situation, I speak of *local, interstellar* silicate absorption in addition to the GC average, if the absorbing silicate is located in the dust, which radiates the diffuse emission. In contrast, absorption in the inner dust components, resolved by the MIDI flux and visibility estimates, is labeled as *intrinsic, circumstellar* absorption.
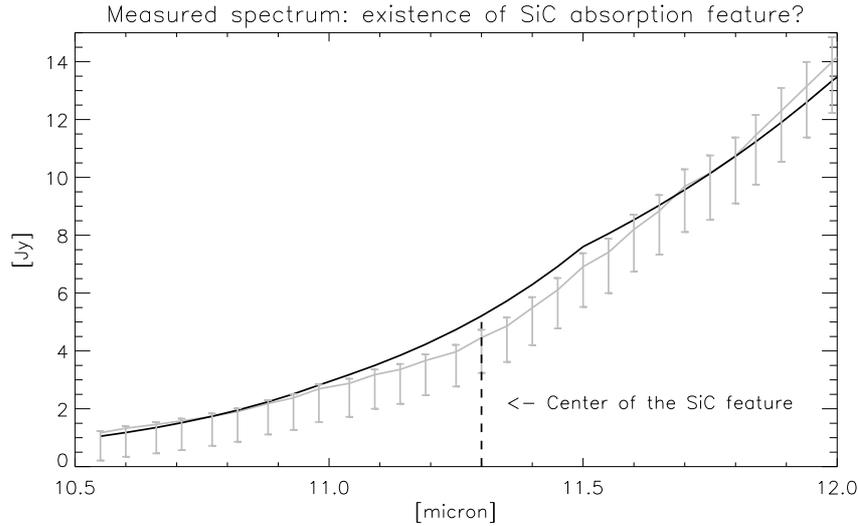
Figure 3.20: A zoom of the lower spectrum in Fig. 3.15 into the wavelength interval of the 11.3 μm feature of SiC. The measured data is plotted in gray, the black solid line represents the best-fit extincted blackbody SED of $T = 410$ K. The existence of SiC in absorption is suggested, but the low sampling of the applied extinction law, which does not contain the SiC feature, may hamper a better fit to the data.
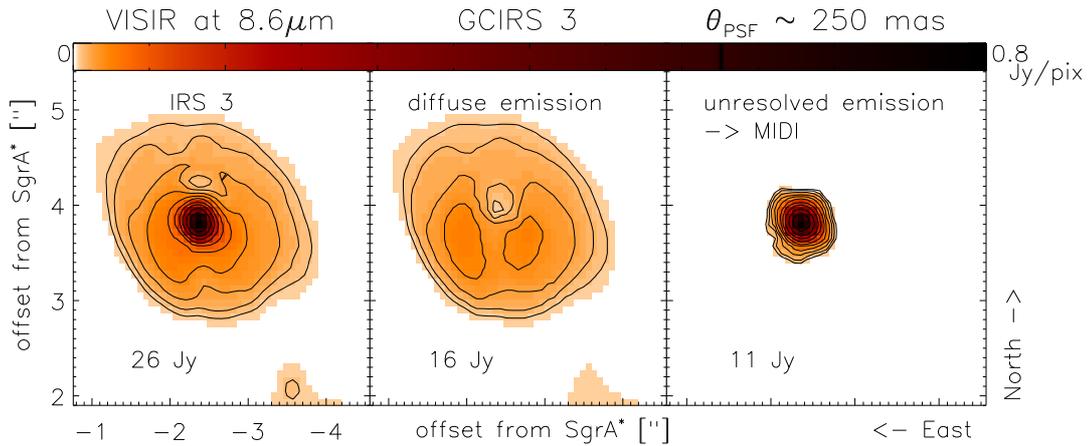

Figure 3.21: The VISIR 8.6 μm imaging data of a 4" field of view centered on IRS 3. Left: A zoom of Fig. 3.5. Middle: The diffuse emission with subtracted PSF. The respective full field-of-view of VISIR is shown in Fig. 3.36. Right: The flux calibrated PSF, i.e. the unresolved emission. The data reduction is detailed in (Schödel 2006a). All images have the same color coding as indicated at the top and the same contour lines for better comparability. The logarithmic contours levels are $1.6^{n} \cdot 7$ mJy. The flux of the different components is given in the figures. Note that the diffuse flux peaks below 40 mJy/pix. Although VISIR and the MIDI photometry have similar resolution, the complete diffuse flux, shown in the middle panel, is hidden in the noise of the MIDI photometry due to the shorter integration times. Therefore the flux calibrated MIDI F_{T} spectrum (Fig. 3.15) fits to the unresolved flux shown in the right panel. Further, the two dust components, derived from the interferometric data (Sect. 3.3.3.4) constitute together the unresolved component shown here, since the single telescope observations provide an angular resolution of about 250 mas.

The MIDI spectro-photometry confirms the existence of a broad 9.8 μm silicate absorption feature remaining in the data after correction for standard GC extinction. I show the measured spectrum

in Fig. 3.15 (lower curve). For the dereddening of the spectrum I used the μCep emission profile of the silicate feature, as realized in the extinction law by Moneti et al. (2001) for lines of sight to the GC. Several authors state that this profile matches both the local ISM absorption and the GC interstellar silicate absorption profile best (although at different relative optical depth; Roche & Aitken 1984, 1985; Chiar & Tielens 2006).

The IRS 3 spectrum of a spectral resolution of $R = 30$ shows this coincidence perfectly. I reddened a single blackbody of variable temperature with an absorption spectrum of the normalized shape of the silicate feature seen in emission towards μCep (see Moneti et al. 2001) and a variable optical depth $\tau_{9.8}$. The shapes of the observed and dereddened spectra coincide with the spectra shown by Roche & Aitken (1985) (Fig. 3.15). The best χ^2-fitted parameters are a blackbody temperature of $T = (410 \pm 30)$ and $\tau_{9.8} = (7 \pm 0.5)$. This temperature resembles other $N-$band measurements (e.g. Gezari et al. (1985) found a color-temperature of about 400 K), but is below the 800 K derived from $K-$ and $L-$band data (Moultaka et al. 2004). This indicates that a single blackbody may not be appropriate to describe the complete NIR-MIR SED. Although the hotter component, dominating the $K-$ and $L-$band, cannot be resolved against the cooler outer dust shell by the single telescope spectrum or image at 10 μm with additional SED information, the interferometric 10 μm data alone can resolve it (Sect. 3.3.4.3).

Since the center of the absorption feature is hidden in the noise of the background subtraction, there remains a certain level of uncertainty in the estimation of $\tau_{9.8}$, but the spectrophotometric quality of the wings is good enough to exclude $\tau_{9.8} \leq 6.5$. Assuming $A_V = 25$, this means $A_V/\tau_{9.8} \leq 4$. This is a remarkable result, since it doubles the silicate MIR optical depth towards IRS 3 with respect to the average of the GC region ($(A_V/\tau_{9.8})_{GC} \approx 8\text{-}10$; Roche & Aitken 1985), which itself is twice as deep as $A_V/\tau_{9.8}$ in the solar neighborhood. This is shown by the middle spectrum in Fig. 3.15, which is the measured spectrum corrected for standard values of extinction ($A_V = 25$ and $(A_V/\tau_{9.8})_{GC}$). The remaining silicate absorption is obvious. The aforementioned authors quantify for the first time an additional $\tau_{9.8} \approx 0.8$ for IRS 3. Although the spectral resolution of both datasets is comparable, the spatial resolution of the MIDI photometry data[6] is increased by at least an order of magnitude.

In addition, at 11.3μm a significant drop of the data below the fit is obvious (Fig. 3.20), even at the logarithmic scale shown in Fig. 3.15. This further absorption feature, in addition to the dominating broad silicate absorption, can be attributed to SiC, which is not included in the applied extinction law. SiC peaks around 11.3 μm and has a much narrower spectral width than the interstellar silicate feature. If I exclude the data of the wavelength region around 11.3 μm for the χ^2 minimization, the discrepancy between data and fit around the center of the SiC feature becomes even stronger, although the fitted temperature and $\tau_{9.8}$ remain constant in the given interval of uncertainties. This further supports the existence of a SiC absorption feature towards IRS 3, but the sampling of the applied extinction law is with 0.5 μm at MIR wavelengths not high enough to sample properly the SiC feature. Thus a definitive answer regarding its existence cannot be given.

Arguments against a circumstellar intrinsic silicate absorption in the dust in the immediate environment of IRS 3, which could be evoked by a thick O-rich dust shell, are:

- Most silicate-rich dust shells show the silicate feature in emission. Similarly the SiC feature is typically found in emission in the dust shells of evolved stars. Since our estimated optical depth $\tau_{9.8}$ is already very deep, an even larger amount of absorbing dust would be necessary to overcome the circumstellar emission and result in such strong features as observed.

---

[6]which is the VLT 10 μm resolution of ~ 250 mas, not the interferometric resolution

- The spectral shape of the observed silicate absorption perfectly coincides with the interstellar absorption features. No indications of circumstellar crystalline silicates are found, although spectroscopic data with higher SNR and spectral resolution covering the full $N-$band are needed to further investigate the spectral shape in more detail.

Thus a circumstellar dust shell free of a significant amount of silicates appears to be a reasonable assumption for the immediate environment of IRS 3. This is confirmed by the visibility data, which do not show any spectral feature coinciding with the broad shape of the 9.8-silicate feature at any baseline length.

Such a lack of an intrinsic, circumstellar silicate-rich dust shell and the deep interstellar silicate absorption would favor the bright IRS 3 to be the primary target for estimating the true spectral shape of the interstellar absorption in the $N-$band towards central GC sources at the high spatial and spectral resolution now available at ground based 8 m class telescopes.

3.3.4.2 Dust temperatures from the spectral energy distribution
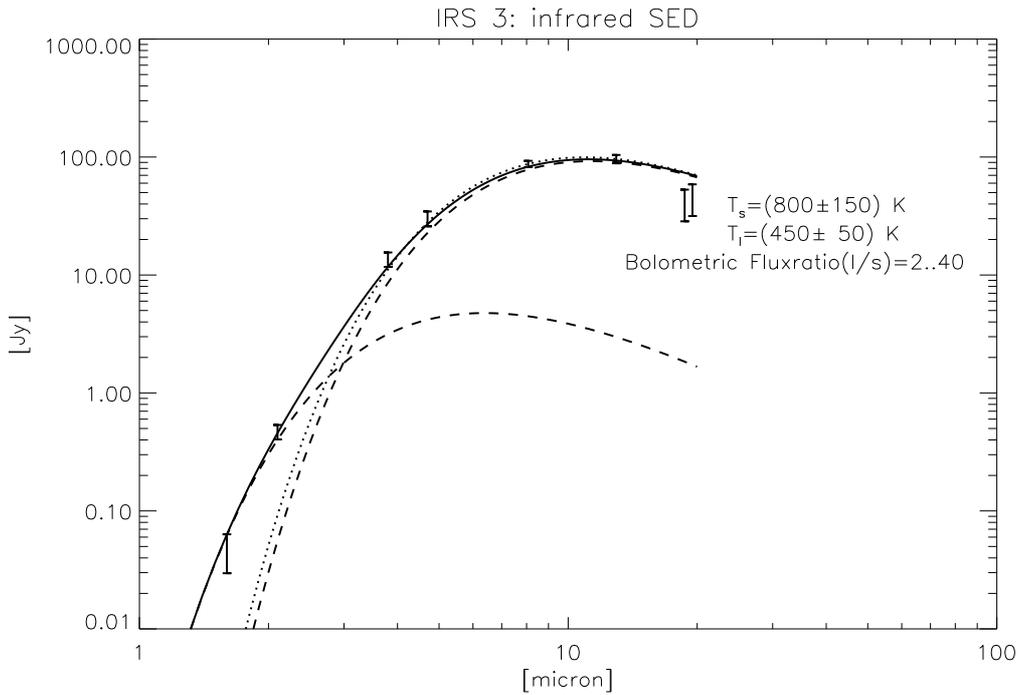
Figure 3.22: SED temperature fit shows two components. The black solid line is the superposition of two spatially unresolved blackbody SED, plotted individually as dashed lines. The dotted line close to the cooler and presumably larger T_l component shows a blackbody SED of $T = 410$ K, which was fitted to the N-band spectrum alone (Sect. 3.3.4.1). The range of the possible bolometric flux ratio, given in the plot, is rather large and is better constrained by the MIDI visibility estimates (Sect. 3.3.4.3). Data are taken from Viehmann et al. (2005,$H-$, $K-$, $L-$, $M-$bands) and Viehmann et al. (2006,$Q-$band). Additional corrections to the published $H-$ and $Q-$band data are mentioned in the text. The $N-$band data was taken from the MIDI observations at 8 and 13 micron, outside the silicate absorption feature. The data was extinction corrected by A_V=25.

The MIR regime is dominated by thermal dust emission. I have shown in the previous section that the $N-$band spectrum of IRS 3 can be fitted convincingly by a reddened blackbody. But published

studies of stellar dust shells show that the full infrared photometric information is required to describe the optical and physical properties of the shells.

I have investigated the full infrared wavelength range from 1.6-20 μm, available at sufficient spatial resolution to distinguish IRS 3 from other sources. The corresponding SED is shown in Fig. 3.22.

A second star close to IRS 3 was recently classified as a Wolf-Rayet star (Paumard et al. 2006). It is unresolved in the published medium resolution NACO data (Viehmann et al. 2005), but I confirm this secondary star on high resolution NACO images, showing about 30% and less than 10% of the IRS 3 H- and K-band fluxes, respectively. For the SED fit in Fig. 3.22 I used the accordingly reduced published H magnitude. Since the companion is located by about 120 mas east of IRS 3, its MIR flux could also contribute to the MIDI data. But a significant contribution should show up as a binary pattern in the visibility data (Sect. 3.3.4.4), which was not observed. Thus I assume negligible contamination of the flux of IRS 3 long-ward of 2 μm by the WR-star, which is further supported by the bluer NIR SED of the secondary.

To account for the uncertainties in the amount of interstellar silicate absorption towards IRS 3 (Sect. 3.3.4.1), I used for the MIR-SED only the fluxes at 8 and 13 μm outside the 9.8 μm absorption feature. All data were dereddened with the Moneti extinction law scaled to A_V=25. Similarly to the N-band, a broad interstellar silicate absorption feature is located in the $Q-$band. At 20 μm only narrow-band photometry inside the silicate absorption was available. I dereddened this data by scaling the interstellar absorption to fit the measured $N-$band optical depth, exceeding the average GC values. At least the plotted SED data for $\lambda \leq 13 \, \mu$m should be free of any significant contribution of the diffuse VISIR component, because of its low surface brightness and presumably cool temperature. Only the Q-band data may contain a fraction of the diffuse flux, although similar to the MIDI spectra, these VISIR Q-band data do not reach the low noise level of the 8.6 μm imaging data.

I could successfully fit the extinction-corrected SED with *two* blackbody spectra. The lower temperature, which I attribute to the outer component ($T_l = (440 \pm 50)$ K), coincides with the single blackbody temperature fitted to the $N-$band spectrum (Sect.3.3.4.1). This single blackbody SED is overplotted (dotted line) in Fig. 3.22, which shows immediately, that for $\lambda \leq 5 \mu$m additional flux by hotter dust is required to explain the measured infrared SED. This is consistent with the findings of Moultaka et al. (2004), who fitted a blackbody temperature of 800 K to their 2-4 μm data.

The calibration of the $Q-$band emission, apparently too faint to fit the model, was very difficult and the deviations can fully be attributed to calibration errors (Viehmann, private communication) including the uncertain amount of interstellar silicate extinction in that band. Alternatively at least a part of these deviations might reflect model errors due to the simple blackbody approach. The RT model calculations show better SED fits (Sect. 3.3.4.5).

I can state, summarizing these considerations, that no further blackbody component is needed to explain the full infrared SED. In particular this excludes any significant stellar contribution to the NIR fluxes of the SED, emerging from IRS 3 itself or a second star inside the PSF. This leads to two possible interpretations: either the inner and hotter dust component is optically thick at NIR wavelengths avoiding any direct detection of stellar light or the enshrouded star has a very hot continuum emission. The absence of any stellar photospheric lines in NIR spectra of IRS 3 (Tanner et al. 2006) support the optical thickness of the circumstellar dust at these wavelengths.

Table 3.4: Temperatures derived from the interferometric $N-$band data on the basis of the size estimates of the two-Gaussian model. I used each fitted FWHM θ as diameter of a spherical thermal dust shell. The temperature T_{sphere} of such a shell is given by its flux and size. For comparison temperatures T_{Fratio} are derived from the 8-13 μm flux ratios only. The good coincidence of the results of both approaches within the uncertainties justifies that these simple calculations are order of magnitude estimates of the dust temperatures involved. The individual component fluxes and sizes have uncertainties of about 15% and 10%, respectively.

	inner		outer	
	8 μm	13 μm	8 μm	13 μm
F [Jy]	35	32	55	66
θ [mas]	18	18	40	55
T_{sphere} [K]	(640±80)	(725±125)	(480± 50)	(400±050)
T_{Fratio} [K]	(620±190)		(470±110)	

3.3.4.3 Dust temperatures from the interferometric data

In contrast to the previous section, here I present the derivation of temperatures from the *spatially resolved* MIDI observations in MIR as a further step to interpret such interferometric data.

The simplest morphological interpretation of the data consists of two circular symmetric Gaussian components enshrouding the same central object (Sect. 3.3.3.4). One-dimensional radiative transfer calculations confirm bell-shaped brightness distributions of circumstellar dust shells (Ivezic & Elitzur 1996b). That I can observe both dust components suggests the outer being optically thin and physically separated. That is, the observed total flux simply constitutes of the sum of the flux of both components. From the observed total fluxes and flux ratios I calculate the component fluxes as

$$F_{\text{tot}}^{\text{d}} = F_{\text{s}} + F_{\text{l}} = (R+1) * F_{\text{l}}. \qquad (3.5)$$

$F_{\text{tot}}^{\text{d}}$ is the total dereddened flux (Sect. 3.3.4.1) and R is the flux ratio between the inner and the outer dust shell. All measurable quantities in Eq. 3.5 are supposed to be wavelength-dependent. In other sections I present strong indications for the absorbing silicate not to be located in the circumstellar dust (Sect. 3.3.4.2, 3.3.4.5). Nevertheless, here I confine the calculation to the edges of the $N-$band outside the silicate feature to minimize the possible corruption of the results by faulty correction for the interstellar extinction.

In Table 3.4 the component fluxes and FWHM-sizes for the two-Gaussian model of Sect. 3.3.3.4 and the derived temperatures are given. T_{sphere} is the temperature of a spherical blackbody of radius $\theta/2$ at GC distance emitting the observed flux. T_{Fratio} is the blackbody temperature solely derived from the 8-13 μm color of each component. I find:

- a reasonable increase of temperature of the inner component with respect to the outer one. This perfectly coincides with the infrared SED. The MIR-interferometric data already show the inner, hotter dust component in contrast to spatially unresolved $N-$band photometry alone, but its physical properties are better confined by the complete IR-SED (Sect.3.3.4.2) and by more detailed radiative transfer models (Sect.3.3.4.5)

- The interferometric data confine the bolometric flux ratio between the two components to $F_{\text{o/i}} \approx 2$, greatly reducing the uncertainties of the SED-based analysis (Fig. 3.22).

. $F_s = e^\tau \cdot F_{s,0}$ in Eq. 3.5 might only be a fraction of the intrinsic flux $F_{s,0}$, attenuated by the optical depth τ of the outer shell, which would increase the estimated inner shell T_{sphere} temperatures (Table 3.4). But although in fact the RT calculations lead to higher temperatures for the inner component, no strong arguments for a significant optical depth have been found. Rather the best RT SED fit of the inner component shows significant deviations from the blackbody shape assumed here. The uncertainties of the estimation of T emphasize the zeroth-order characteristics of this simple approach, but physically consistent properties of the dust structures have been derived.

3.3.4.4 Circular symmetry
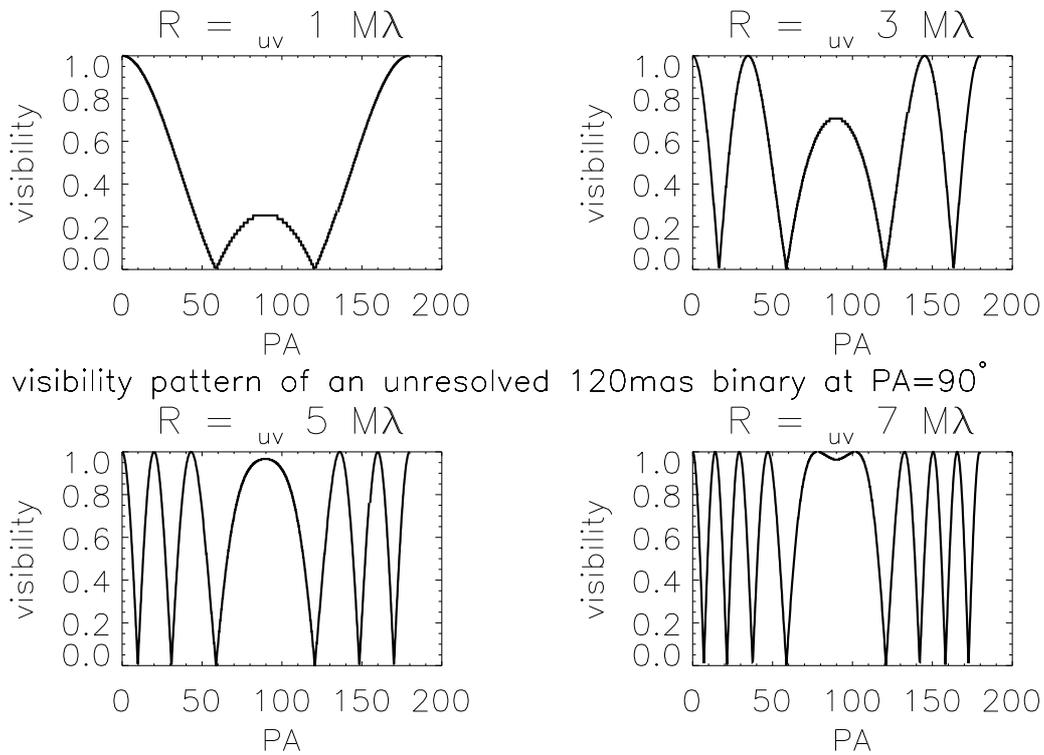
Figure 3.23: Visibility patterns for a 120 mas east-west binary at several uv-radii. The individual components are not resolved.

In their spectroscopic survey of the Central cluster, Paumard et al. (2006) classified the star IRS 3E, only 120 mas east of IRS 3, to be a Wolf-Rayet star of type WC 5/6. Since Wolf-Rayet stars of this spectral type are known to be (often strong) dust formers, it is possible that IRS 3E is still visible in the $N-$band. Additionally its spectral classification as carbon rich WC-star does not conflict with my interpretation of the spectral data in terms of lack of silicate emission.

The visibility pattern of such a binary system with 120 mas separation and east-west orientation is shown in Fig. 3.23 for several R_{uv}. The shown pattern has been calculated for two stars of equal brightness, and both being individually unresolved by the interferometer. IRS 3 *is* resolved by MIDI, which would decrease the amplitude of the variation shown in Fig. 3.23, but the variation per PA is defined by the binary separation only. I.e. the imprint of a 120 mas binary system should show several ripples over 180° rotation, which cannot be confirmed with the data

(Fig. 3.13). Furthermore I did not observe photometric variability beyond the calibration uncertainties (Sect. 3.3.3.3).

The simplest deviation from circular symmetry is an elliptical morphology, or more generally a brightness distribution of different apparent extension in orthogonal directions. The analysis of Fig. 3.13 (Sect. 3.3.3.2) allows such an interpretation: Towards $PA = 120\ ^\circ$ the measured visibilities appear to be slightly lower than in orthogonal direction, necessitating a larger extension of the brightness distribution in this direction, respectively. Such a lateral contraction could be evoked by the strong stellar wind of a nearby star, but more probably this deviation from circular symmetry is an artefact of the creation of Fig. 3.13 (cf. Sect. 3.3.3.2).

3.3.4.5 Radiative transfer models

Table 3.5: Best parameters of the cool star scenarii, the respective radiative transfer model calculations are shown in Fig. 3.24, 3.25. For the model calculations, the dust shell was confined to end at a radius of $10^4\,R_i$. The brightness distribution of the favored C-rich model is shown in Fig. 3.28. T_* denotes the stellar effective temperature, T_{dust} the dust temperature at the sublimation zone, visible as ring of radius R_i in Fig. 3.28 and resolved by MIDI. Further $R_{i/*}$ denotes the size ratio of the stellar and dust sublimation radius and $L_{*,bol}$ labels the bolometric luminosity of the embedded star.

T_* [K]	T_{dust} [K]	Comp.	$\tau_{8.0, 9.8, 13.\ \mu m}$	inner radius R_i [AU/mas/$R_{i/*}$]	$L_{*,bol}$ [$L_\odot$]
3000	900	amC [a]	0.5,0.4,0.3	65/9/18	$4.5{\cdot}10^4$
3000	1000	Sil[b]	1,6.7,1.8	55/7/16	$4.0{\cdot}10^4$

[a] 100% amorphous Carbon grains (Hanner 1988)
[b] 100% warm amorphous silicate grains (Ossenkopf et al. 1992)

I confronted the rather simplistic model of two Gaussians with a physically self-consistent radiative transfer (RT) model to further investigate the probability of the existence of two distinct dust components surrounding IRS 3 and estimate their physical properties.

Due to the circular symmetry of the source I used the one-dimensional code DUSTY (Ivezic et al. 1999). Since IRS 3 appears to be very luminous, isolated, and surrounded by a lot of dust, it is most reasonable to assume that IRS 3 is a post main-sequence star with strong stellar winds and massive dust formation. I followed a heuristic approach and calculated four distinct scenarios spanning the space of possible stellar parameters: *hot* and *cold*, realized by stellar effective temperatures of $T_{*,hot} = 2.5 \cdot 10^4$ K and $T_{*,cold} = 3 \cdot 10^3$ K; *C-rich* with C/O abundance ratios beyond 1, realized by a domination of the circumstellar dust by amorphous carbon grains and *O-rich* with dust composition dominated by warm amorphous silicates.

I applied radial density profiles dominated by radiation pressure of the star (Ivezic & Elitzur 1995). While the chemical composition and temperatures of the dust have important influences on the infrared spectrum, the stellar effective temperatures T_* and the luminosity L_* scale the physical size of the system in dependence of T_{dust}, the temperature of the sublimation zone, where dust formation initiates. For the grain size distribution I used a power-law distribution as published by Mathis et al. (1977) and an upper limit on the grain size of $a = 0.25\ \mu m$, which was successfully applied in similar experiments. The main parameters of the model to be tested are T_{dust} at the inner boundary of the dust shell, and the optical depth related to the amount of irradiated dust.

A proper fit to find the best set of parameters should include detailed variation of all ingoing parameters like the density profile, chemistry (e.g. existence and amount of SiC, crystalline olivines)
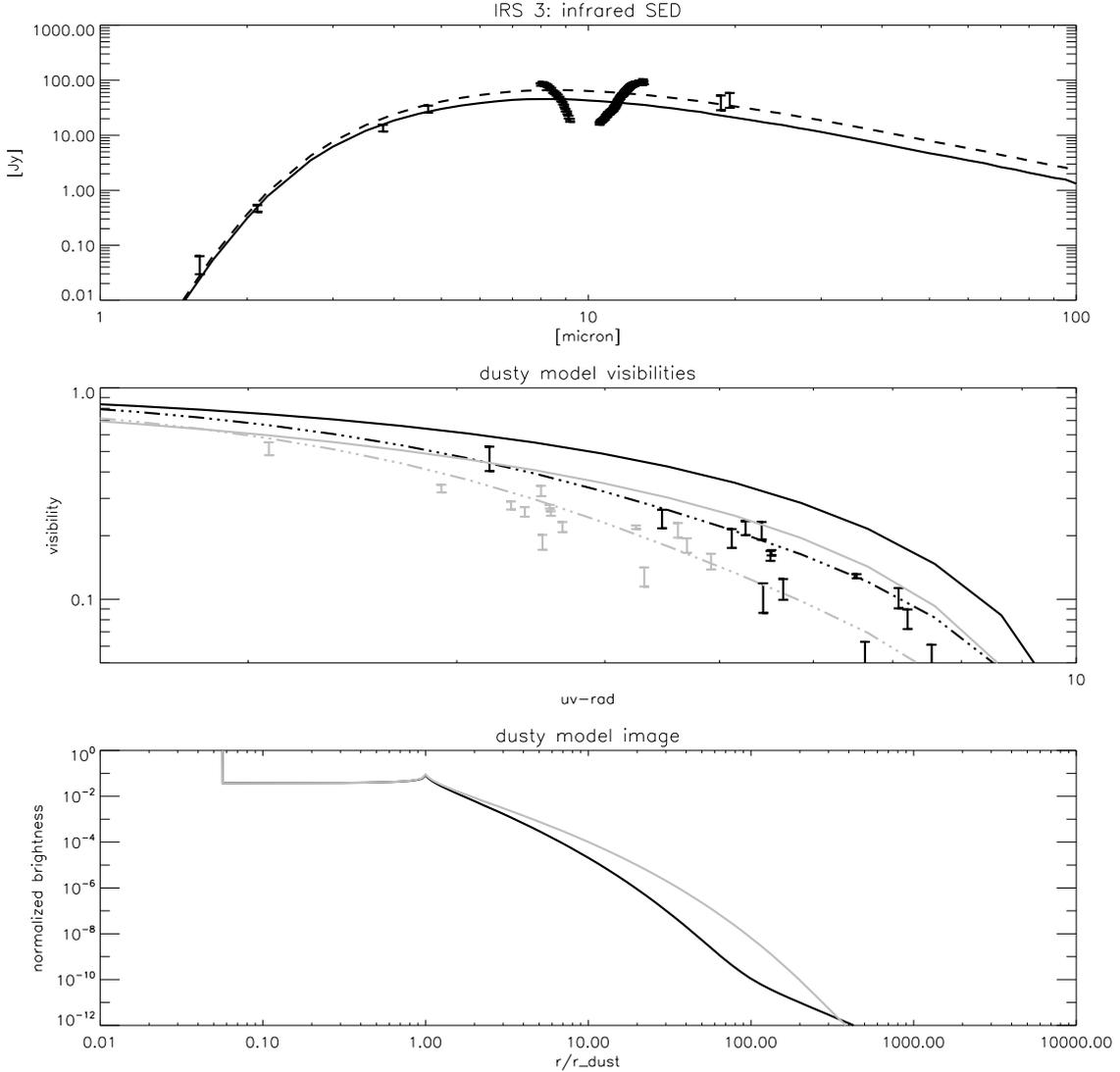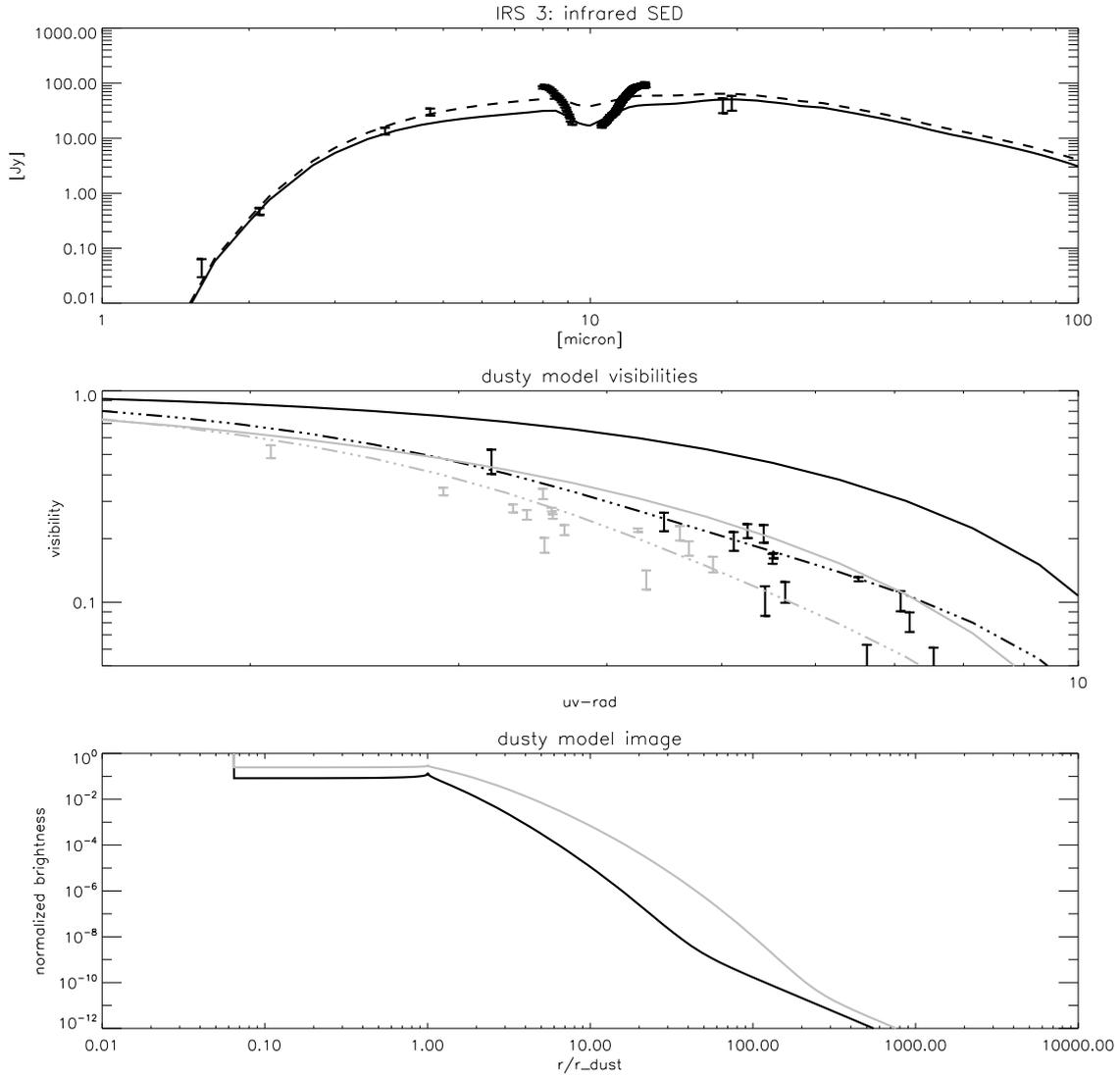
Figure 3.24: The best-fit C-rich cool star model. Detailed physical parameters are given in Table 3.5. Black and gray refer to 8.2 μm and 13 μm, respectively. The solid lines are the single component RT model of the inner circumstellar dust, the dashed line shows the superposition of this RT model with a second outer component, modeled by a Gaussian brightness distribution (FWHM 40 mas) and a blackbody SED of 540 K. Upper panel: spatially unresolved SED; middle panel: visibility moduli versus uv-radius (Mλ); lower panel: radial brightness profile versus R_i.

etc. I dismissed this approach, because the interstellar extinction of both the SED in general and the $N-$band in particular towards IRS 3 is not known at sufficient accuracy to model the circumstellar dust with RT calculations in great detail (Sect. 3.3.4.1). The parameters cannot be fine-tuned unambiguously by comparison with the dereddened stellar spectrum.

Since the depth of the interstellar silicate absorption is unclear, I excluded the data around 9.8 μm from the fitting process. The investigation of the four model scenarios by variation of the remaining free parameter T_{dust} lead to the following coinciding results:

- The comparison of the modeled infrared SEDs with the data constrains T_{dust} of C-rich models to 650 K$\leq T_{\mathrm{dust}}^{fit} \leq$950 K. O-rich dust requires systematically about 10-20% higher

Figure 3.25: The best-fit O-rich cool star model. Detailed physical parameters are given in Table 3.5. Black and gray refer to 8.2 μm and 13 μm, respectively. The solid lines are the single component RT model of the inner circumstellar dust, the dashed line shows the superposition of this RT model with a second outer component, modeled by a Gaussian brightness distribution (FWHM 40 mas) and a blackbody SED of 530 K. Upper panel: spatially unresolved SED; middle panel: visibility moduli versus uv-radius (Mλ); lower panel: radial brightness profile versus R_i.

temperatures than C-rich dust to match the SED at similar accuracy.

. Best-fitting O-rich dust models are optically thick at 9.8 μm, supporting the earlier reported hypothesis of intrinsic silicate absorption. Due to the strong silicate features, the largest differences between O-rich and C-rich models are apparent at 10 and 20 μm. A precise knowledge of the interstellar extinction at these wavelengths would lead to the capability to distinguish between both scenarios.

. The photometry data alone can be fitted convincingly by *single*-shell models of both hot *and* cold stars
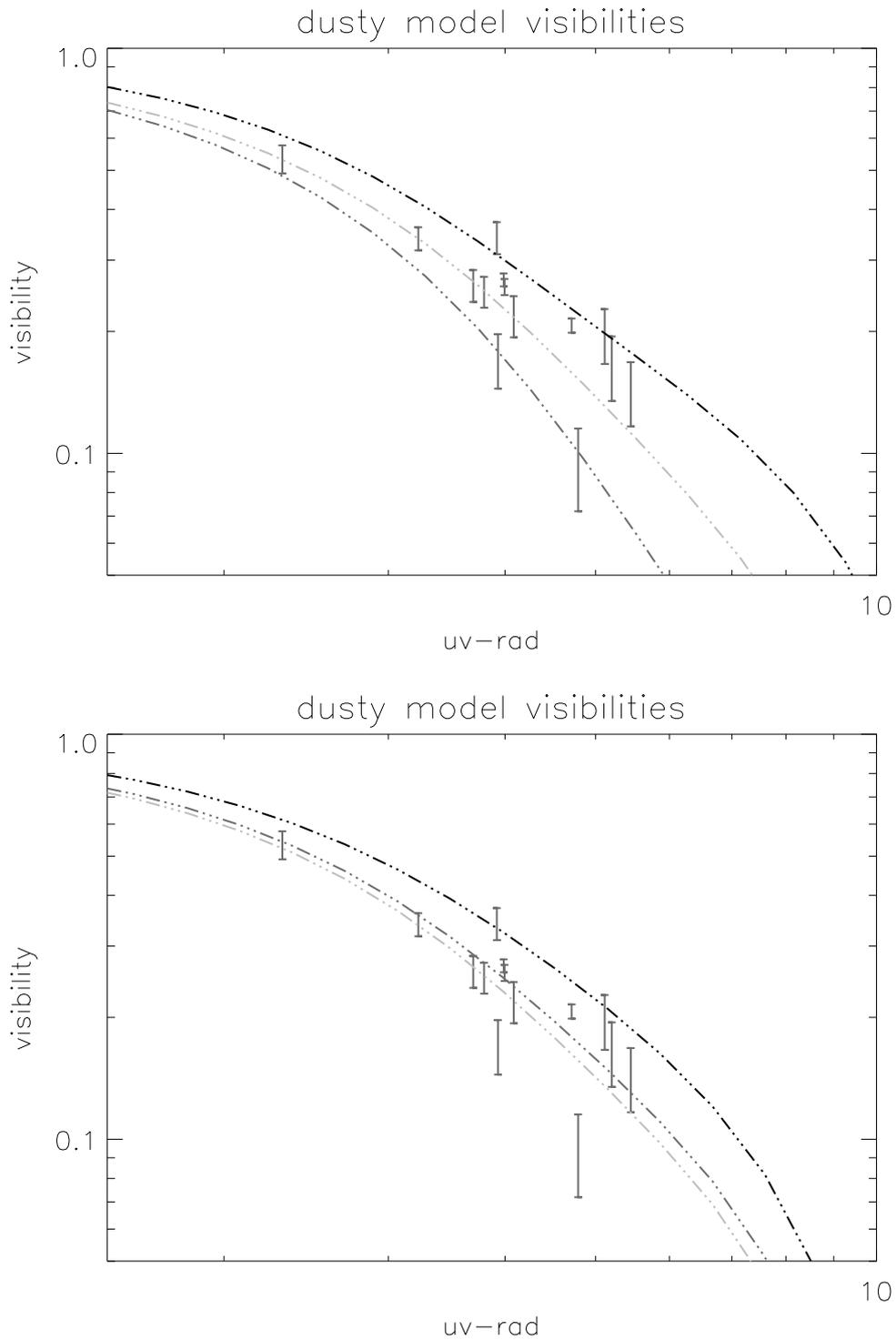
Figure 3.26: Dot-dashed lines are RT-model plus second Gaussian component as in Fig. 3.24&3.25. Upper panel: O-rich; Lower panel: C-rich; black: 8.2 μm, dark gray: 11.5μm; light gray: 12.7 μm; only the data taken at 11.5μm overplotted. Lower panel shows a comparison of the N-band optical depth of the inner component of both models. See also Fig. 3.27
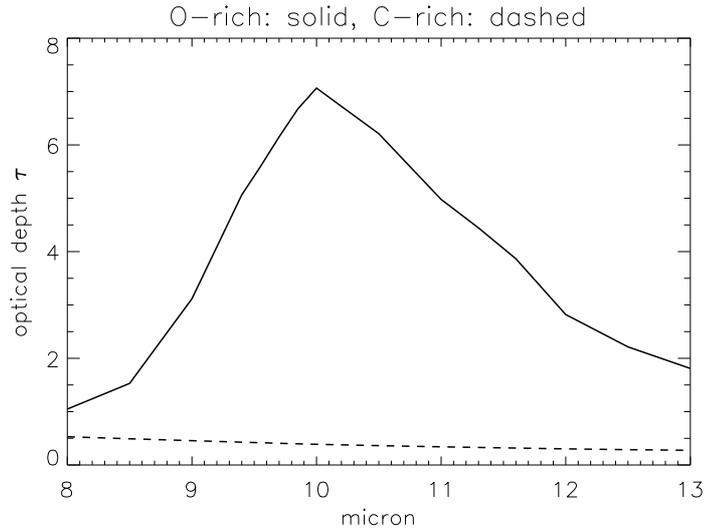
Figure 3.27: A comparison of the N-band optical depth of the inner component of both models shown in Fig. 3.26.

This aforementioned ambiguity of T_* is resolved by the interferometric data. The R_i of hot stars with T_{dust}^{fit} are much too large to model the measured visibilities. Increased T_{dust} solves this size problem, but significantly underestimates the MIR flux. A second cooler dust shell could account for the missing flux, but again decreases the visibility. Thus for the first time I can present a strong experimental indication for the exclusion of any hot star scenario.

Cool stars have sufficiently smaller R_i at a given T_{dust}. In any case, the shallow shape of the visibility curve around 5 Mλ requires the superposition of such a small R_i dust shell with a larger, cooler outer component to match the MIR fluxes, the low visibilities, and the shallow shape simultaneously. I realized such a second shell by superposing a Gaussian brightness distribution with a blackbody SED onto the RT model. It should be noted however, that the apparent existence of such a second component may be an artefact of the relatively simply RT models. Similar multi-component dust shells around the well-studied cool carbon star IRC+10216 could be resolved into one complex dust shell by more detailed modeling (e.g. Ivezic & Elitzur 1996a; Men'shchikov et al. 2001).

The best-fit C-rich and O-rich cool star models are presented in Fig. 3.24&3.25 at 8 and 13 μm. The fitted T_{dust} is in good agreement with the SED-only fitted temperatures. A realistic approximation of the uncertainty of the estimation of T_{dust} within my approach is about $\pm$100 K, keeping in mind possible systematic imperfections by the RT calculations. The parameters of the the second shell are constrained to an accuracy of $\sim$10-15 mas for the FWHM and of $\sim$50-100 K for the blackbody temperature.

The calculated photometry and visibilities of the competing O-rich and C-rich dust compositions are too similar at 8 and 13 μm, far away from the central silicate absorption, to favor one model over the other with respect to the estimated uncertainties of the data. But this situation changes along the wings of the silicate absorption due to the increasing optical depth of the O-rich atmosphere:

The optical depths of the O-rich models at 9 and 11-12 μm create larger brightness distributions with decreased visibilities at these *silicate wing* wavelengths. This effect is strongest at 10 μm
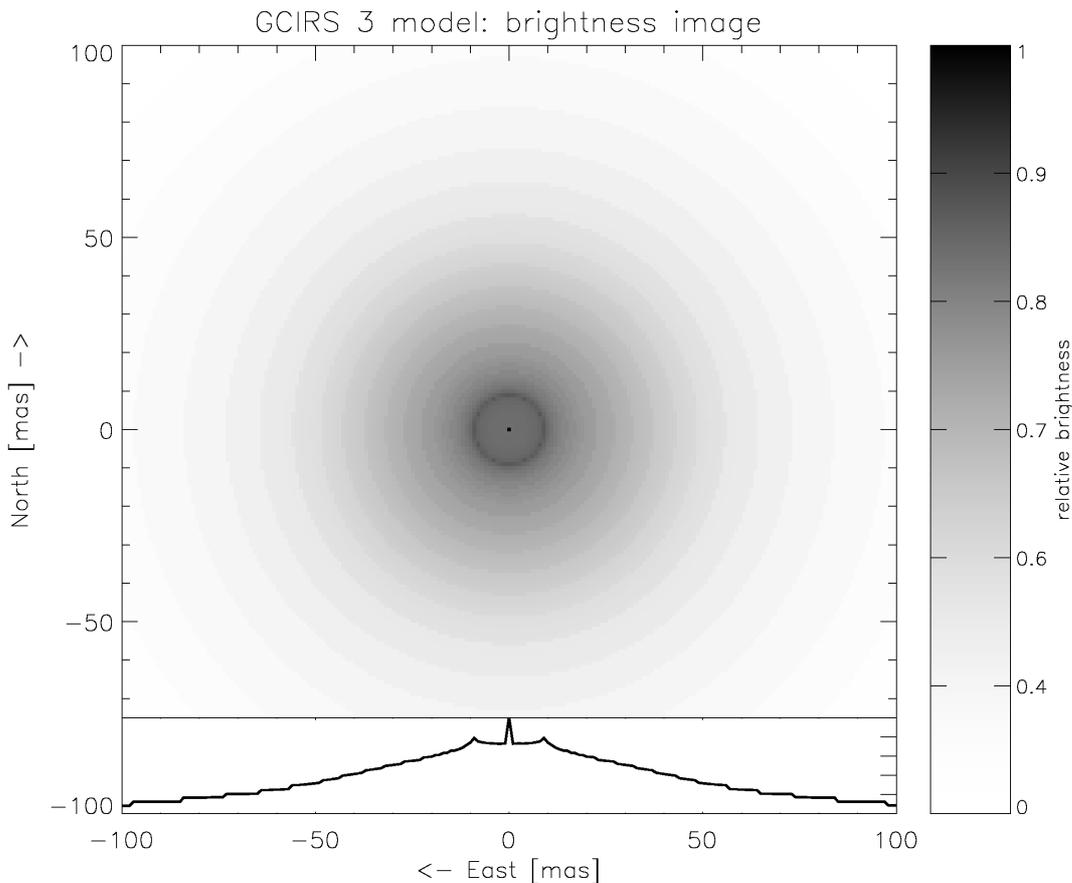
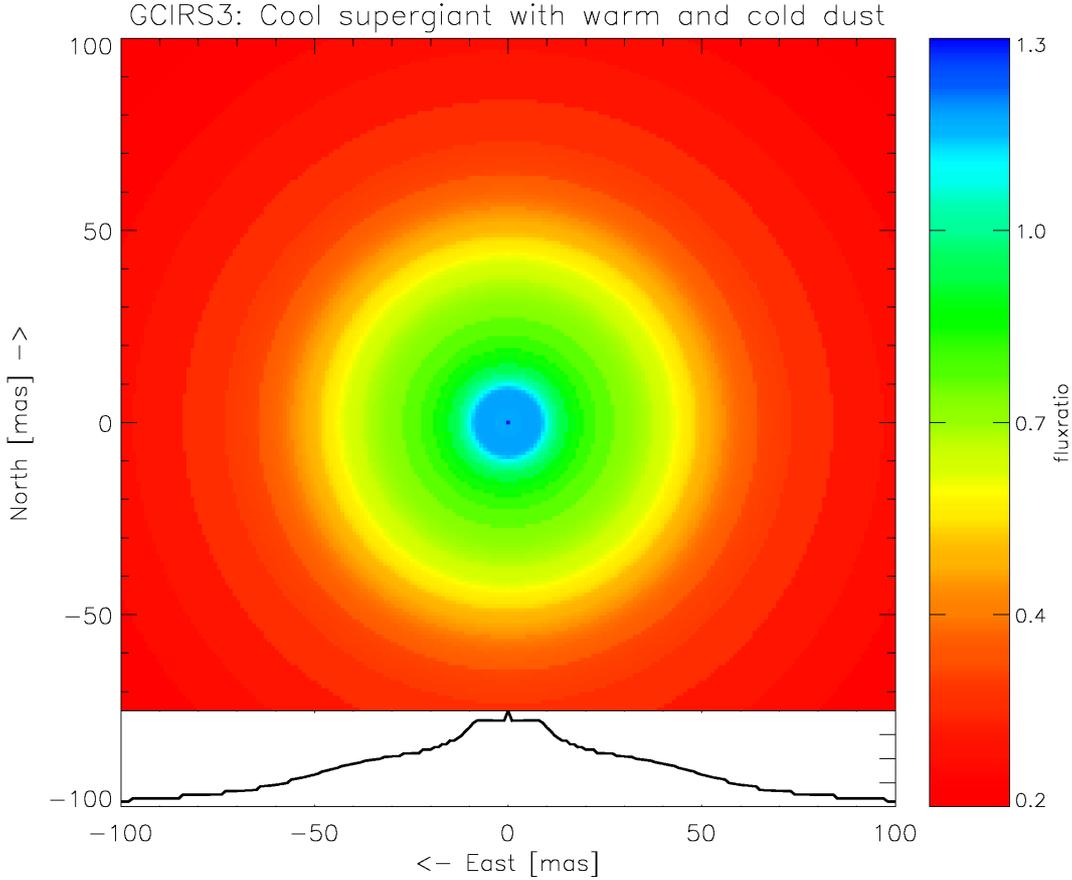Figure 3.28: The brightness distribution of the cool star model of IRS 3. The results of the C-rich RT calculations are superposed with the outer dust component of 40 mas FWHM. The panel shows the mean N-band brightness distributions. The inner rim, the sublimation zone of dust formation, is visible as an annulus. The radius of 9 mas is resolved by my MIDI observations. At the bottom the radial intensity profile of the image is shown. Image and the radial plot are scaled in the same way. Note the logarithmic intensity scaling. See also Fig. 3.29

but still significant at the aforementioned wing wavelengths. This effect of apparent size increase, or any other spectral visibility feature, clearly coinciding with the silicate feature, has not been observed, which is demonstrated in Fig. 3.26, where the measured data at 11.5 μm are shown with overplotted modeled visibility spectra.

In Fig.3.28 I plotted a mean N-band brightness distribution of the best-fit C-rich cool star model together with a flux ratio map between 8 and 13 μm in Fig.3.29. The shown model distributions include the superposed outer component of 40 mas. I assume a similar chemical composition of both components, but a significantly lower density, temperature, and optical depth of the outer one. Since the inner component itself has an optical depth of ∼0.4 (Fig. 3.26), a possible attenuation of the flux emanating from the inner component by a significant optical depth of the outer component was not considered.

In the intensity map, the inner rim of dust sublimation at a radius of 9 mas is clearly visible. Higher flux ratio, related to the net temperature differences between both components, highlights the entire inner part. Outside, a smooth decrease of the temperature with increasing radius coincides with the expectations for circumstellar dust shells.

Figure 3.29: The cool star model of IRS 3. The results of the C-rich RT calculations are superposed with the outer dust component of 40 mas FWHM. In the panel the flux ratio between the brightness distribution at 8 and 13 μm is shown, indicating the trend to increasing flux dominance by the outer component due to the lower temperature at larger radii. At the bottom, the radial intensity profile is shown. Image and radial plot are scaled in the same way.

Summarizing the RT analysis of the data, I find the cool star scenario with carbon dominated dust shells the most probable one. The huge estimated stellar luminosity (Table 3.5) points to a cool supergiant similar to the nearby IRS 7 and IRS 19 in the GC (Blum et al. 1996b).

The reasonable assumption of a stellar wind driven dust density distribution, valid for windy post-main sequence stars, enables to calculate the mass loss $\dot{M}$, terminal outflow velocity v_∞ and an upper limit on the stellar mass M_* (Ivezic & Elitzur 1996a). I obtain the following results for the carbon rich cool star set of parameters (cf. Table 3.5), which describes the observations best. The calculations are based on a gas-to-dust mass ratio of 200 and a dust grain bulk density of 3 g cm^{-3}

$$\dot{M} = 5 \cdot 10^{-5} \, M_\odot \, \mathrm{yr}^{-1}; \quad v_\infty = 20 \, \mathrm{km \, s}^{-1}. \tag{3.6}$$

The inherent uncertainties are discussed by Ivezic et al. (1999).

The respective optical depth of the carbon rich dust shell in the NIR is $\tau_{2\,\mu\mathrm{m}} = 5$, confirming that the circumstellar dust is optically thick in the NIR, as already suggested by the analysis of the spatially unresolved SED (Sect. 3.3.4.2). Thus photospheric CO band-heads, typical for (super$-$)giant NIR spectra, cannot be observed, which explains the impossibility of spectral classification of the central object as described by many authors (most recently Tanner et al. 2006).

3.3.5   Conclusions

I have presented new high resolution 10 μm data of the enigmatic IRS 3 object in the immediate vicinity of SgrA*. The analysis and interpretation of the data contribute to the understanding of both the nature of the embedded star and the location of the unusually strong interstellar silicate absorption towards IRS 3. The new high resolution VISIR imaging data clearly resolve IRS 3 into a compact and a diffuse emission component for the first time. Most probably the deep silicate absorption towards IRS 3 partially takes place in the local interstellar dust, which is responsible for the substantial diffuse MIR emission.

The interferometric data bear convincing evidence for IRS 3 being a cool star within a carbon rich dust shell without circumstellar silicate absorption. The imprint in the circularly symmetric interferometric data of a second, distinct circumstellar dust shell data was shown. A one dimensional radiative transfer model can successfully explain the complete available near and mid infrared data, unresolved by single telescope measurements, if an outer, optically thin dust shell of about 40 mas diameter and 540 K is added. The inner rim of incipient dust formation has a radius of 65 AU and a temperature of $\sim$ 900 K.

With a bolometric luminosity of 4.5 $\cdot 10^4$ $L_\odot$ and a stellar temperature of order 3000 K of IRS 3 appears to be a cool supergiant, most probably in the helium core burning phase. Its supergiant-like properties, similar to the nearby IRS 7, set a lower mass limit of 8 $M_\odot$ and an age of about 5-15$\cdot 10^6$ yr, depending on the true stellar mass (Woosley et al. 2002). The existence of several supergiants shows, consistently with the unusually large number of found Wolf-Rayet stars, the extraordinary stellar properties of the GC with respect to ordinary stellar clusters. The importance of mass-losing massive stars and their supernova ending for the enrichment of their environment is well known.

In addition to the interstellar silicate absorption I find indications for SiC absorption. For the first time the new generation of MIR spectrometers at 8m class telescopes offer the possibility to study in detail the spectral properties of the interstellar absorption towards GC stars at sufficient angular resolution to account for source confusion and substantial diffuse emission in this outstandingly dense and dusty region. Since a C-rich circumstellar dust shell is free of any silicate feature and IRS 3 is embedded in an exceptionally large amount of ISM, the resulting deep absorption of a smooth continuum is perfect to study the detailed shape of the interstellar absorption towards the GC. The absorption profile depends on the chemical composition and is needed to accurately correct for the ISM extinction, yielding the intrinsic spectra of all GC sources.

On basis of my results I propose to build such a new study of the interstellar silicate absorption towards the GC on IRS 3 and other stars free of silicate-rich dust shells. Furthermore a longterm MIR variability study is proposed to investigate periodical dust formation, suggested by the two circumstellar dust shells found. The region around IRS 3 appears to be ideal to investigate the extraordinary silicate-enrichment of the interstellar dust at the GC in the area of gravitational influence of the SMBH.

3.4   VLTI/MIDI measurements of extended bowshocks in the Galactic Center

In addition to IRS 3, I investigate with MIDI the extension of all other dusty mid-infrared excess sources (IRS 1W, IRS 10W, IRS 2, IRS 8) in immediate vicinity to the black hole (BH) at

the GC, which can be observed with the instrument. The observations were conducted with the UT2-UT3 baseline on the nights of the 7th and 8th July 2004. The instrumental setup is already described in Sect. 3.3.2. All sources are too extended, and the respective low visibilities were not detected. I derive 3σ upper limits of the correlated fluxes of the sources and combine the results with published NIR data.
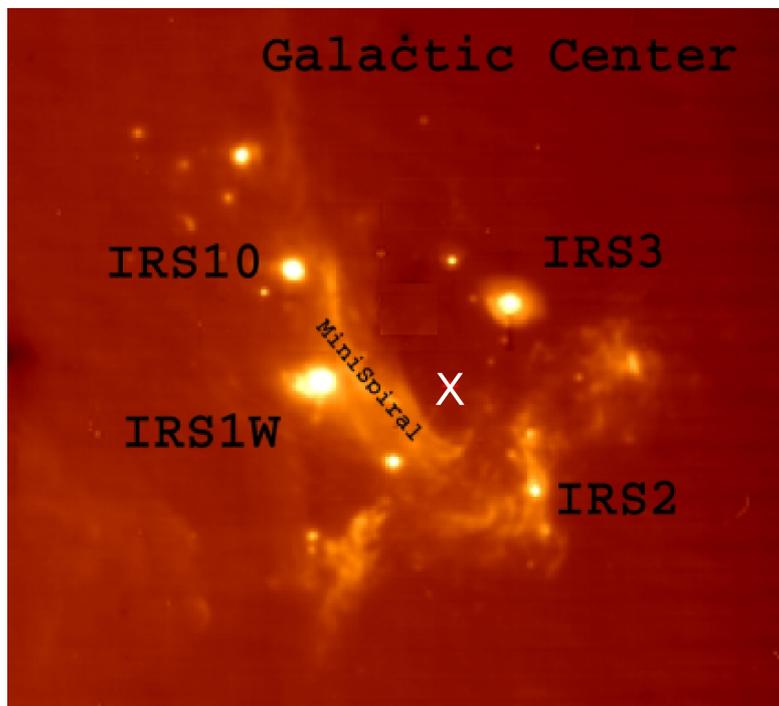
3.4.1 The sources - stellar bowshocks

Figure 3.30: The GC region in the N-band, the angular scale is given in the image. The bowshocks as well as the Nothern Arm (Mini-Spiral) and IRS 3 are labeled for orientation, SgrA* is indicated in the center by a star. From the commissioning data of VISIR. IRS 8 is about 30" North of SgrA*. The figure was kindly provided by T. Viehmann.

The featureless infrared excess sources within the MiniSpiral (e.g. IRS 1W and IRS 10W, see Fig. 3.30 for orientation) only a few arsec away of SgrA* could indicate young stellar objects, still embedded in their natal matter. But recent near infrared AO supported imaging suggested a different explanation for these sources. After subtraction of the point spread function of the central stellar object clear bow-like morphologies could be imaged (Tanner et al. 2005, Fig. 3.31). A more thorough analysis revealed that these bows can be explained by heated dust which is shocked through the interaction of a strong stellar wind ($v_\infty \sim 1000\,\mathrm{km\,s^{-1}}$) from a massive star (most favourable of Wolf-Rayet type) ploughing through the dense matter of the Mini-Spiral. Also IRS 3 shows at 5 μm such a shock zone (Viehmann et al. 2005). The size, stand-off distance and compactness at 10 μm would add to the published NIR results and further constrain the bow shock scenarii and the corresponding stellar wind paramters.
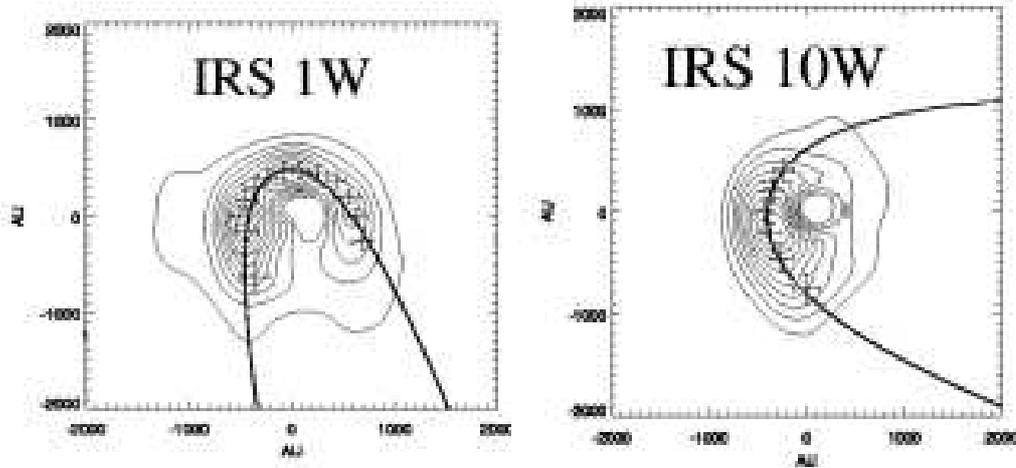
Figure 3.31: These are the NIR bowshocks, resolved by AO observations with the Keck telescope (Tanner et al. 2005). The central point sources have been subtracted to outline the bowshock strength. I have scaled the width these bow shock models to fit the upper limits of the MIDI data.

Table 3.6: Upper correlated flux limits give lower limits of the source size at 10 μm. For IRS 2 and IRS 8 no visibiltiy limits are given, due to the lack of consistent uncorrelated fluxes. IRS 8 is located about 30" north of SgrA*, therefore it lies outside of Fig. 3.30.

Sources with existing bow-shock models:		IRS 1W	IRS 10W
Total flux at 8.6micron (VISIR), (extinct. Av=25)	[Jy]	4.6	2.7
Upper limit of the correlated flux density	[Jy]	< 0.3	< 0.25
Visibility limits	[1]	< 0.06	< 0.09
Width of bow-shock models	[mas/AU]	> 30/240	> 20/160
Sources without existing bow-shock models:		IRS 2	IRS 8
Upper limit of the correlated flux density	[Jy]	< 0.4	< 0.35

3.4.2 Results

MIDI provides internal fringe tracking on the basis of group delay fringe tracking very similar to the coherent data reduction technique (Sect. 2.2.3). The group delay is estimated by the Fourier transform of the dispersed interferometric spectrum. An optical path difference (OPD) between the two interfering light beams results in a cos-pattern in the interferometric spectrum as long as the OPD is shorter than the coherence length.

No fringes of the embedded sources in the MiniSpiral (1W, 2 and 10W) were detected. I use the MIDI fringe search and track data to estimate upper limits on the correlated flux of the sources. Since no technical failure of the VLTI is apparent and fringes on calibrator sources and IRS 3 were regularly found throughout the night, I interpret these non-detections of the correlated flux as due to low visibilities. Nevertheless at the single telescope resolution (250 mas) no clear asymmetry, in particular now bowshock structure as in the NIR, is observable. This corresponds to the NIR bow shock size scale of ∼50-100 mas. That is, the sources are too extended and upper limits on the correlated flux are leading to lower limits on the extension of the bow-shocks at the observing wavelengths.
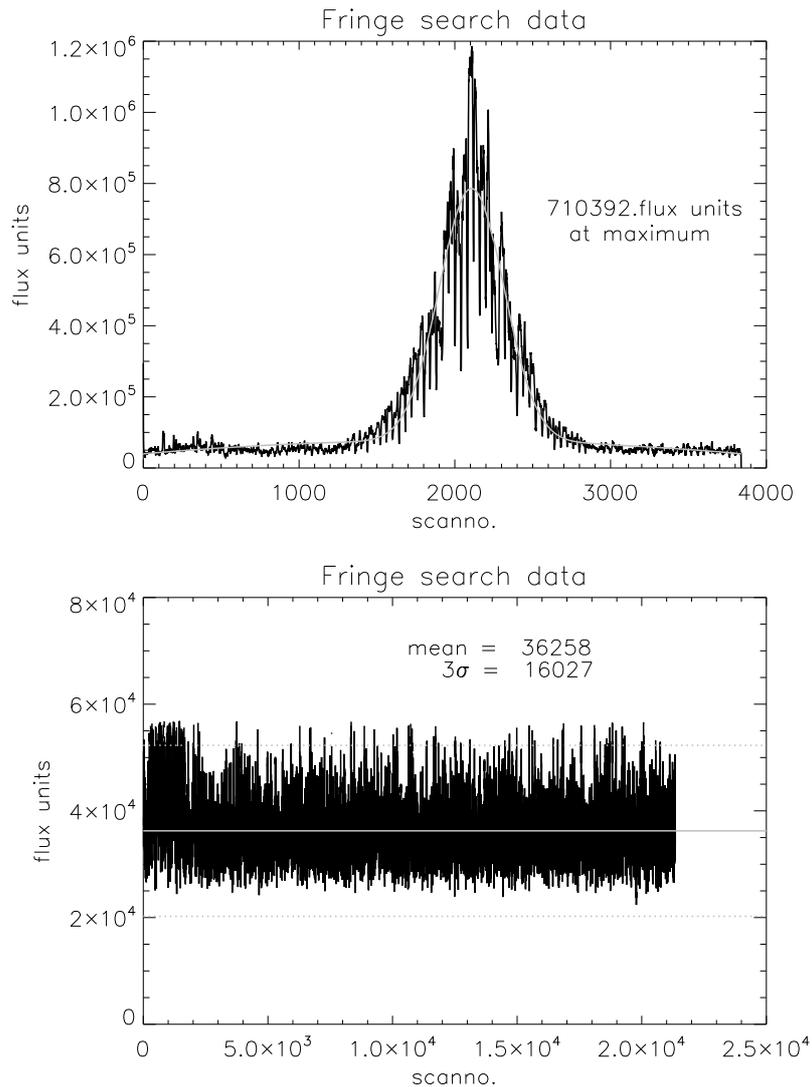
Figure 3.32: Both figures show the maximum Fourier amplitude of the MIDI fringe search data. A fringe detection is indicated by a significant peak (upper panel: visibility calibrator HD165135). This peak is well above the 3σ level of the search data of IRS 1W as indicated by the two horizontal lines in the lower panel. Note the reduced ordinate-scale in the lower panel.

The peak of the Fourier transform along the wavelength dependence of the spectrally dispersed interferometric data indicates the group delay. Its amplitude is proportional to the correlated flux of the source, if the group delay is zero and the amplitude is maximum over the scanned optical path difference range. We used this maximum Fourier amplitude of a calibrator source to flux-calibrate the fringe search data of the bow-shocks (Fig. 3.32).

To transform the thus estimated correlated flux limits into lower limits on the bow-shock size, I add to the NIR bow-shock model of Tanner et al. (2005) a one-dimensional parameter, which scale the radial FWHM of the bow-shocks. This is a reasonable model for the brightness distribution at $10\,\mu$m, although in the NIR an additional compact emission is apparent. But the acquisition images of the MIDI experiment does not show significant flux contributions of the compact sources at the MIR (Fig. 3.33). Nevertheless at the single telescope resolution (250 mas) no clear asymmetry, in
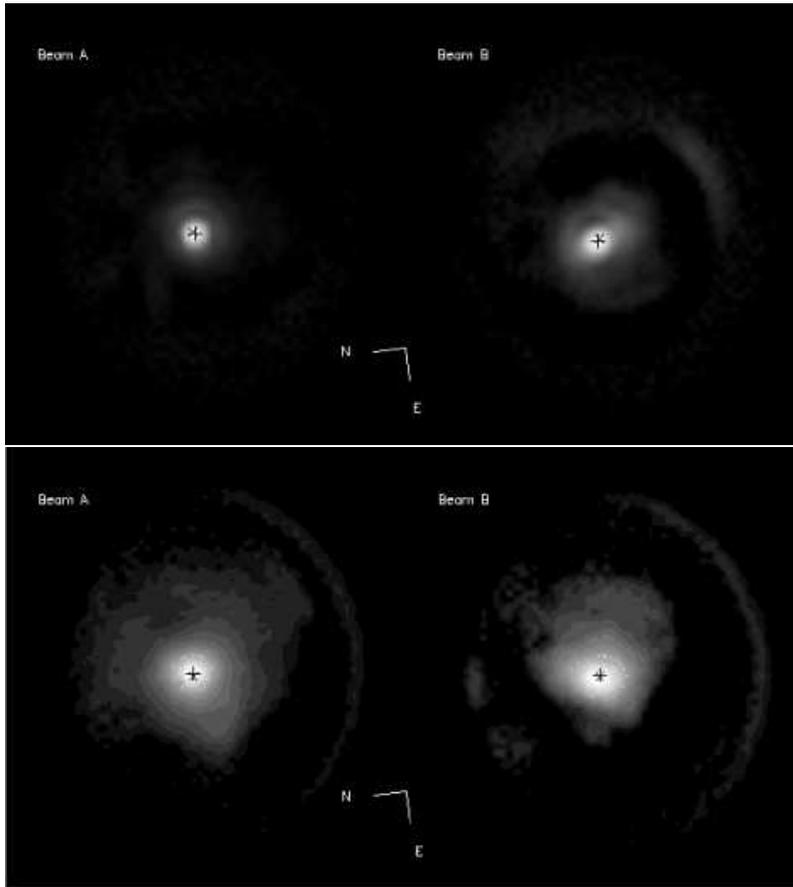
Figure 3.33: MIDI acquisition images of the fringe calibrator HD165135 (upper panel) and GCIRS 1W (lower panel). The unresolved calibrator shows the point spread function of the VLT Unit Telescopes. In comparison, the image of GCIRS 1W is much more extended, a possible flux contribution of an unresolved point source is of minor importance.

particular now bowshock structure as in the NIR, is observable. In part this is due to the limited sensitivity of the MIDI acquisition images, but it also corresponds to the NIR bow shock size scale of $\sim$50-100 mas.

Comparing the visibility moduli of these scalable bow shock models to the measured upper limits results in lower limits of the width of two bow-shocks at 10 μm (Table 3.6). Furthermore I derive an overall extension of IRS 1W by deconvolution of the acquisition image (Fig. 3.33). The PSF is obtained by calculating the median of all calibrator acquisition images over the night. The entire bow shock structure immediately related to IRS 1W extends to $\sim$350 mas and indicates a significant increase of the MIR emitting bow-shock with respect to the NIR findings.

Despite of the fact that no fringes were detected, the results are encouraging for a future MIDI study of the bowshocks. The new higher order adaptive optics system MACAO has improved the stability of the beams and concentrates more light into the interferometric field-of-view, as I showed with the IRS 3 dataset in Sect. 3.3.2.2. The bowshock widths found in the NIR are of the order of the lower limits presented here. Therefore positive fringe detection is within reach already without the external fringe tracker FINITO and the dual feed facility PRIMA, which will further increase the the VLTI sensitivity and are the motivation for the next section.

3.5   GCIRS 7: phase referencing at the GC
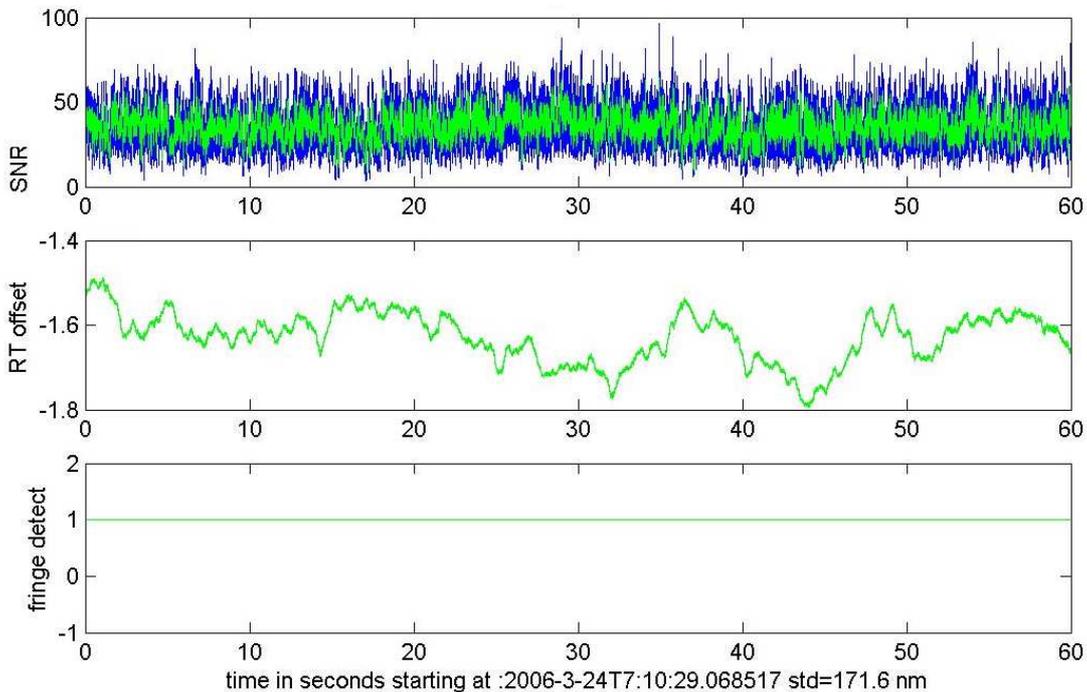
Figure 3.34: Successful closed loop fringe trakcing on the sky with FINITO and two Auxiliary Telescopes of the VLTI. The time is given in seconds. From top to bottom: SNR of the fringe measurement, the calculated OPD, and the boolean value of successful fringe detection. Courtesy of ESO.

In this section I shortly present a new VLTI GC project, which I started in April 2006. This project will be the basis for future VLTI observations of fainter targets, or re-observations of the bow shocks of the previous section. Phase referencing can be regarded as AO for interferometry. In Sect. 2.2, I discussed the fact, that the loss of phase information hampers the interferometric imaging, but it also limits the sensitivity. If no instantaneous phase reference of a calibrator source is given, the fringes of the science target must be detected permanently, because of the strong and fast atmospheric OPD variations in the infrared. If the fringes are not detected in the single scans, the SNR cannot be increased by averaging over several subsequent scans, since the random phase of the individual fringes, hidden in the noise of each scan, would destroy the signal due to destructive interference. Only coherent integration of low SNR fringe measurements can increase the SNR.

Two facilities are necessary to reach this goal. (i) an external fringe tracker, which permanently feeds the delay line system in closed loop with on-sky OPD measurements to keep the rms of the OPD fluctuations below 1 radian; (ii) a dual-feed device which splits the very narrow 2" field-of-view of the VLTI infrastructure in two parts. Each part contains the light of two different patches of the sky within the isoplanatic patch. One field contains the phase reference source, guided to the fringe tracker, and the other field contains the faint science source. Also high precision astrometry measurements with ten micron accuracy can finally be reached with such a VLTI upgrade.

While the dual-feed facility PRIMA[7] is still under construction, the VLTI external fringe tracker

---

[7]**P**hase-**R**eferenced **I**maging and **M**icro-arcsecond **A**strometry,
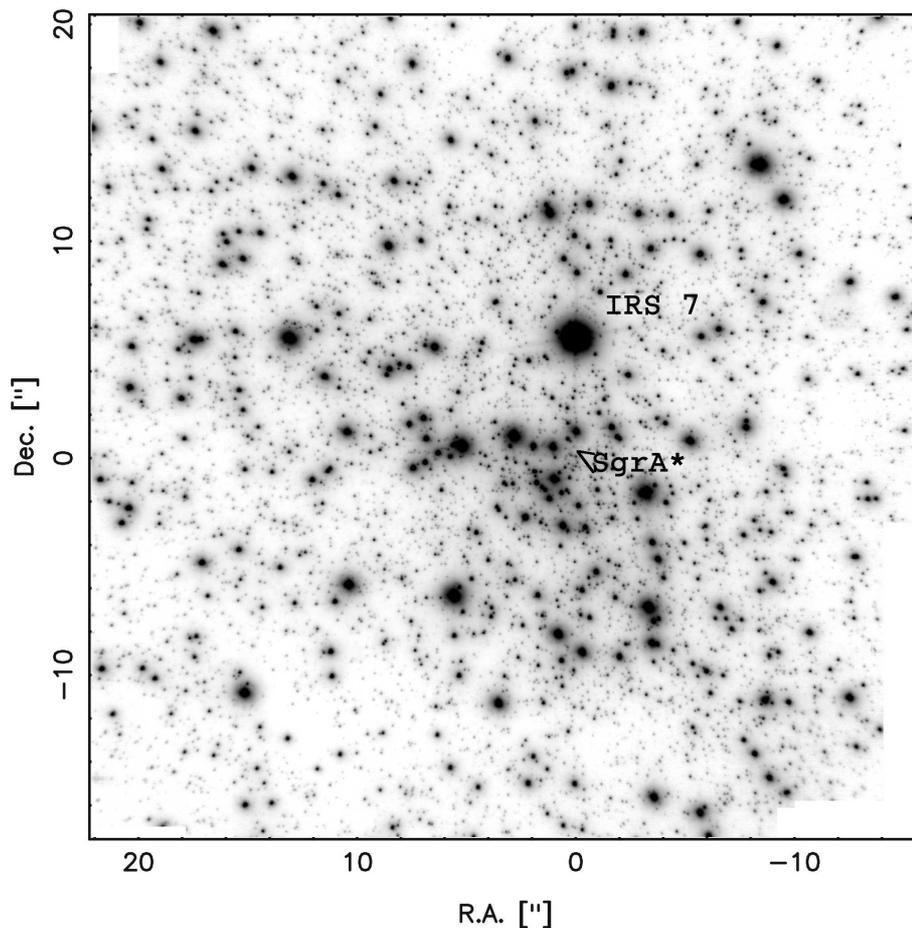`http://www.eso.org/projects/vlti/instru/prima/index_prima.html`

Figure 3.35: A NACO K-band image of the Galactic Center. It shows the numerous infrared sources in the GC as well as the unique brightness of IRS 7. The location of SgrA* is indicated.

undergoes intensive commissiong at the moment. The recently achieved on-sky performance is very encouraging, fringes were tracked for more than a minute (Fig. 3.34). That is the reason for that I started a campaign to characterize experimentally the putative prime candidate for future phase referencing experiments at the GC: GCIRS 7 [8]. The NIR-brightest GC source (Fig. 3.35) is a red supergiant and expected to be unresolved at AMBER resolution, thus being a prime candidate for phase referencing experiments. The proximity to SgrA*, $\sim$ 6", minimizes phase referencing errors and enables to investigate the infrared emission of SgrA* itself at highest possible accuracy. Already with FINITO [9] alone, locked on IRS 7, all sources within the 2" field-of-view of the VLTI can be investigated and probed for binarity, extension and stellar nature. Classical single-telescope imaging/spectroscopy of this region suffers from blending by the nearby IRS 7 itself (Fig. 3.35).

For phase referencing and high-precision astrometry, a reference source is needed, constrained to be *bright*, *compact* and *spherically symmetric* with respect to VLTI baselines and *close* to the science targets to be observed. In the GC region the only star beeing brighter than K=7 is the near infrared brightest source IRS 7, a supergiant M1 type star at a distance of about 6" to SgrA* (Blum et al. 1996b). This star is the infrared AO-guiding source of the continuous NACO observations

---

[8] in the following IRS 7

[9] The external fringe tracker of the VLTI systems is called **F**ringe-tracking **I**nstrument of **NI**ce and **TO**rino and is described in (Gai et al. 2003)
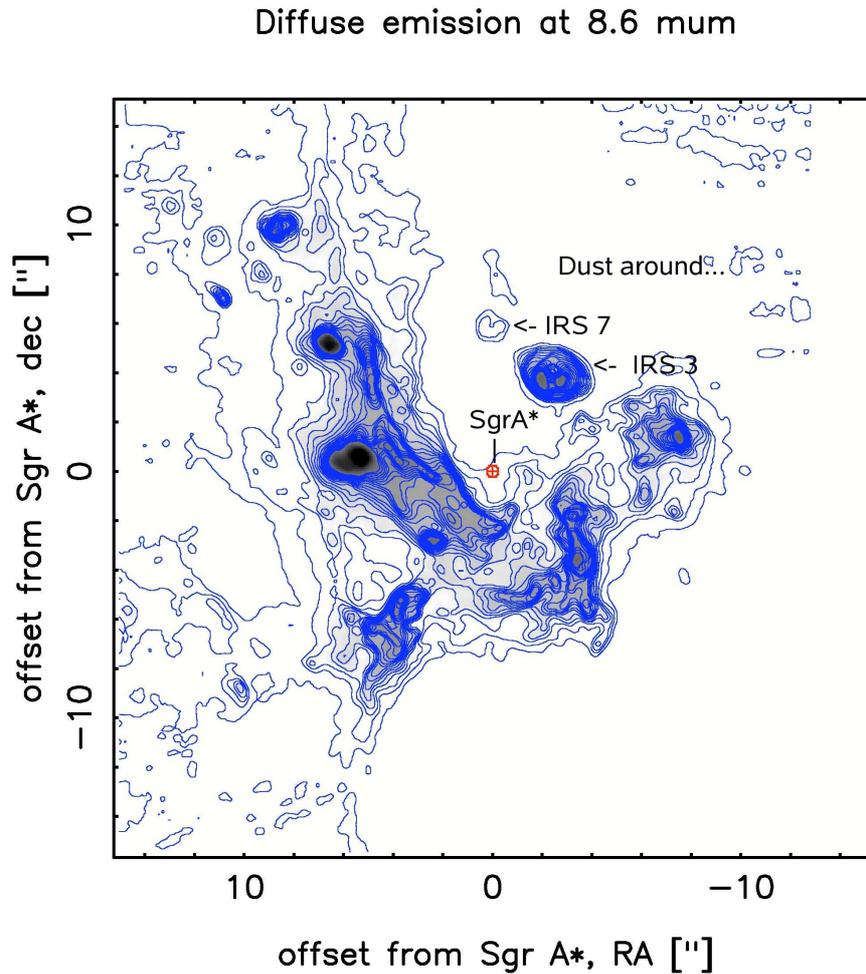
Diffuse emission at 8.6 mum

Figure 3.36: The diffuse emission at 8.6 μm (VISIR data) is shown after point source (i.e. adequate PSF) subtraction. The contour lines are linearly spaced in 1.5 mJy steps starting at 1.5 mJy. The existence of weak diffuse emission around IRS 7 is indicated by the contours. The location of IRS 3 and SgrA* is given for orientation. A zoom on IRS 3 is shown in Fig 3.21. Courtesy of R. Schödel.

of the GC region and of the NIR-flares of the accretion disc around SgrA*. Similarly to IRS 3, it belongs to the few cool supergiants of the GC. IRS 7 is the only star, which perfectly fulfills all criteria for a VLTI reference source in immediate vicinity to the GC.

Extension: Blum et al. (1996b) estimate the spectral class of type M1I and give $T_{eff} = 3600$ K. This leads to a stellar radius of about 0.5 mas at the distance to the GC, still unresolved for the VLTI (a 50 m projected baseline length gives an angular resolution of 8mas at 2μm and a linear 60AU at the GC.). Further Blum et al. (1996a) find no infrared excess below 4 μm. This indicates the lack of warm circumstellar dust which could evoke an infrared extension of up to hundreds of stellar radii. In contrast high resolution MIR data show clear indications for a significant amount of dust surrounding IRS 7. In Fig. 3.36 the diffuse thermal dust emission around IRS 7 is shown. I also could measure with MIDI the N-band spectrum and visibility (Fig. 3.37). Especially at the VLTI resolution of MIDI we found 60-80% of the emission to be extended. This dust might be too cold to significantly contribute to the NIR fluxes, but the existence of an inner hot component, still unresolved by single-telescope observations, is possible.

IRS 7: MIDI photometry spectrum (lambda/dlambda = 30)

dust emission ->

IRS 7: MIDI visibility

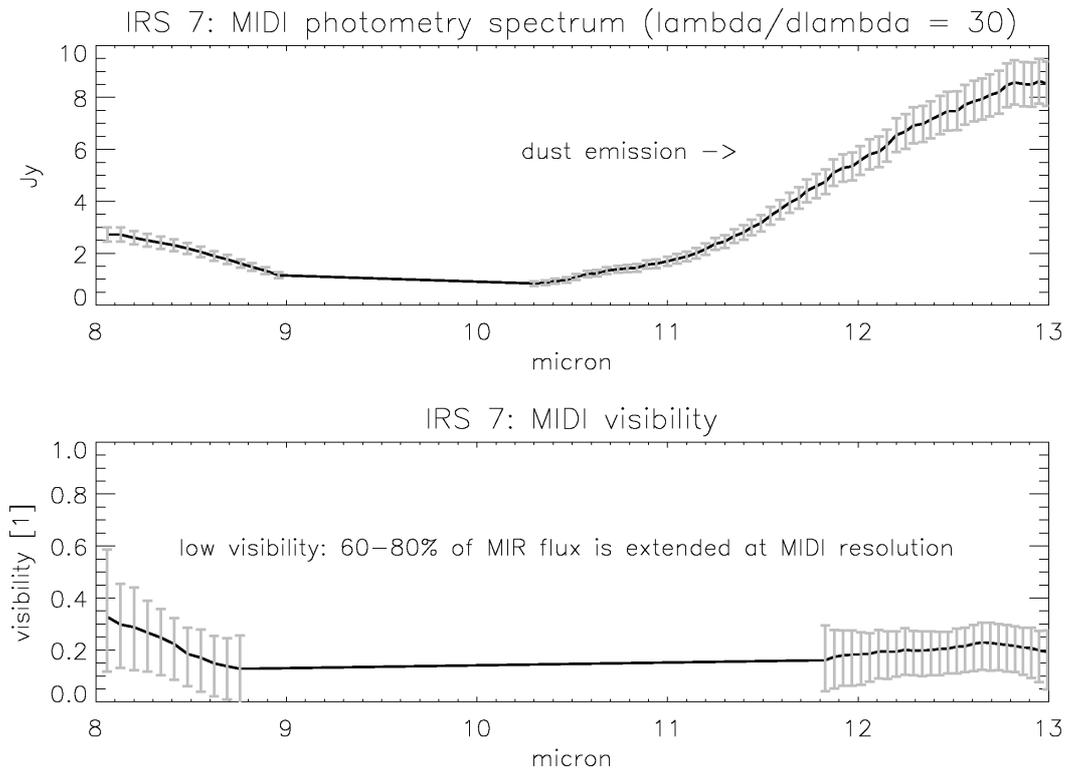low visibility: 60−80% of MIR flux is extended at MIDI resolution

Figure 3.37: Results from the MIDI observation in summer 2006. Upper panel: the N-band spectrum suffers from the broad silicate absorption, but a cool non-stellar dust contribution is obvious due to the strong longwavelength part. Lower panel: The dispersed visibility moduli show, that 60-80% (depending on the morphology of the dust distribution) of the MIR emission is extended at the short U23 baseline (47m $\rightarrow \sim 40$ mas resolution) in contrast to spatially less resolved VISIR data (Fig 3.36), which show extension only at the mJy level. Where no errorbars are plotted, the data were not reliable due to too few flux and I linearly interpolated the spectra.

Long Period Variability of IRS 7: Blum et al. (1996a) and Ott et al. (1999) found a long-term variability of several years reaching its minimum luminosity of K= 6.6mag around 1998 and classifying IRS 7 to be a Long Period Variable (LPV). Alvarez et al. (2000) present an extensive optical and near-infrared spectrophotometric study of such evolved stars. The mechanism evoking the variability in such systems is still unknown. It has to be investigated if the long-period variability has a measurable influence on VLTI experiments due to an expanding shell as probable origin.

Summarizing IRS 7 is the most favorable candidate for future phase-referencing and off-axis fringe tracking experiments, but its extension at VLTI baselines has to be investigated.

I was awarded VLTI/AMBER telescope time for this project. AMBER[10] is the NIR VLTI beam combining instrument (Petrov et al. 2003). AMBER can combine the light of three telescopes. It can measure the closure phase, which is a direct measure of the symmetry of the source, unaffected by atmospheric turbulences. One calibrated AMBER visibility and closure phase dataset with UT1-3-4 can show: (i) if the source is indeed unresolved at all UT baseline lengths (ii) if it is spherically symmetric (circular symmetric amplitudes in the uv-plane and closure phase zero), and (iii) if these properties change over the HK band.

---

[10]**A**stronomical **M**ulti-**BE**am combine**R**; http://www.eso.org/instruments/amber/

Fringes were detected at the baseline triple UT1-3-4, but at the time of the observations, the delay line model of the VLTI was not precise enough to continuously keep the fringes at all baselines. Thus at the moment no statement can be derived from the obtained dataset because of low SNR. The delay line model is an empirical model, which presets and tracks the coarse position of the delay lines, while the star is moving over the sky. AMBER only measures an additional offset between these preset delay line positions and the true OPD. The required accuracy of the delay line model is especially high at the low spectral resolution mode, which I had to use to get enough flux per spectral channel. As discussed in the introductory sections, the sinc envelope of the fringe pattern becomes narrower with increasing widths of the spectral channel. Thus in case of a fringe measurement with low spectral resolution, the delay line preset must be more precise to keep AMBER within the coherence length, where fringes can be measured. Nevertheless short fringe detections were possible, and I plan new observations.

In this chapter different currently feasible applications of the VLTI in the GC were presented. The first results are promising and suggest that the time of OLBI-GC research has just begun.

Chapter 4

The first extragalactic APEX observations at 350 GHz – Warm molecular gas in the nearby Seyfert NGC 1068

Seyfert galaxies are the low-luminosity counterparts of QSOs (Peterson 1997). NGC 1068 is the archetypal and best-studied Seyfert galaxy of activity type 2. The unified AGN-model declares type 2 AGN as dust absorbed type 1. It is widely accepted to explain overall successfully many observational findings. It was inspired by the detection of weak, polarized, broad optical emission lines of a few 1000 km s^{-1} line widths towards NGC 1068. Such broad emission lines had been observed only towards type 1 nuclei until then (Antonucci & Miller 1985). A major topic of actual AGN research is to understand the feeding processes of the final accretion onto the central SMBH, thought to be responsible for the enormous luminosity of the AGN.

The central dense gas distribution in a galaxy is the prime candidate for AGN feeding. It is best studied by observing the molecular gas. Except for the most abundant H_2, several other abundant molecules like CO and HCN show line emission in the (sub-)mm wavelength range. This wavelength range is favorable due to significantly reduced interstellar dust extinction with respect to optical and near-infrared wavelength bands. High-resolution mm-observations of NGC 1068 confirmed the capability to observe that part of the molecular gas, which is directly associated with the nucleus. Observational and theoretical efforts like the international NUGA[1] project are initiated to investigate in detail the role, which plays molecular gas in feeding the central engine around nearby low-luminosity AGN (García-Burillo et al. 2003).

With a distance of only 15 Mpc, corresponding to its spectroscopic redshift[2] of $z = 0.0038$, NGC 1068 is relatively nearby and can be observed at high linear resolution. Mapping of the ^{12}CO(1-0) and ^{12}CO(2-1) rotational transition lines[3] of the central 40" revealed two distinct morphological structures (Schinnerer et al. 2000). The circumnuclear disc (CND) dominates the inner

---

[1]**NU**clei of **GA**laxies

[2]The spectroscopic redshift is defined as $z = \frac{\Delta\lambda}{\lambda_{\mathrm{rest}}} = \frac{\lambda_{\mathrm{observed}} - \lambda_{\mathrm{rest}}}{\lambda_{\mathrm{rest}}} = \frac{\Delta\nu}{\nu_{\mathrm{rest}}}$; the Hubble law relates the spectroscopic redshift (for values much smaller than 1) to the linear distance to the galaxy: $D_{\mathrm{[Mpc]}} = \frac{c_{\mathrm{[km\,s^{-1}]}} * z}{H_0}$. Throughout this work I assume the Hubble constant H_0 to be 75 km s^{-1} Mpc^{-1}. Recent studies of the cosmic background radiation field give a slightly smaller value $\sim$ 71 km s^{-1} Mpc^{-1}.

[3]All molecular line transitions in this and the following Chapter 5 are rotational line transitions between different

5", close to the resolution limit of the IRAM[4]PdBI[5] at mm-wavelengths. Two emission peaks of different redshift reveal the disc structure of the very central molecular gas. The outer star burst ring (SBR) hosts a significant amount of the molecular gas, probably connected to the CND via a bar-like structure. The problem of the high-resolution interferometric studies is that due to the lack of short baselines extended flux is lost, which makes sensitive single-dish observations an indispensable complement to trace the full gas content. The angular resolution of the used APEX telescope at sub-mm wavelengths suffices to distinguish between both morphological structures (Fig. 4.2).

The sub-mm transitions of CO(3-2) and HCN(4-3) had already been observed successfully towards the center of NGC 1068 with the JCMT[6]. The estimated line intensity ratios suggest a selective depletion of gas-phase oxygen in the dense molecular clouds of the central narrow-line region (Sternberg et al. 1994). A central concentration of dense ($n_{H_2} \sim 10^5 \, cm^{-3}$), warm ($T \geq 70$ K) molecular cloud cores without low-density envelopes could explain the HCN data (Tacconi et al. 1994). The calculation of large velocity gradient (LVG) models are used to constrain the molecular gas properties (relative abundances, excitation temperatures, optical depth) by fitting the parameters to the observed line ratios. While normally one average molecular gas phase is sufficient to explain the line ratios of a galaxy, the intense radiation from the star-burst in NGC 1068 appears to strongly excite a significant amount of the diffuse molecular gas. In this case a second gas phase is required to explain the line ratios (Papadopoulos & Seaquist 1999). A necessary ingredient to such studies of highly excited and warm molecular gas are the sub-mm emission lines.

I could convince the science verification team of the new APEX facility, that NGC 1068 is one of the best targets to probe the APEX capabilities in observing broad extragalactic emission lines. The publications on the observed CO(3-2) emission serve as an ideal basis for a detailed comparison to investigate the quality of APEX 350-GHz spectra and their calibration. A positive evaluation enabled further observations of the HCN(4-3) transition, which had never been observed before in the SBR away from the nucleus. The complete results of my these APEX observations are presented in the next sections.

4.1   Observations

The observations were carried out in August 2005 within the ESO Science Verification phase of the new APEX 12m telescope at the Llano Chajnantor in Chile (Fig. 4.1). I have used the facility receiver *APEX 2a*, a double sideband heterodyne receiver installed in the Nasmyth Cabin A (Belitsky et al. 2006). The Fast-Fourier-Transform-Spectrometer was executed as backend at full 1 GHz bandwidth and 0.5 MHz sampling. I observed the CO(3-2) and HCN(4-3) rotational line transitions in the 0.9 mm atmospheric transmission window at nine different pointings around the nucleus of NGC 1068. More observational details are given in Table 4.1. Table 4.2 list the confirmed telescope efficiencies. The directly measurable antenna temperature of APEX is transformed into the theoretically frequency independent main-beam temperature, which is proportional to the luminosity of the source, via: $T_{mb} = \eta_f / \eta_{mb} * T_A^*$.

---

levels of the rotational quantum number J. That is, why I usually omit the J and abbreviate the full annotation. ^{12}CO(1-0) means ^{12}CO(J=1-0) etc.

   [4]**I**nstitut für **R**adio**A**stronomie im **M**illimeterbereich; `http://www.iram.fr`

   [5]the IRAM **P**lateau **de B**ure **I**nterferometer: `http://www.iram.fr/IRAMFR/index.htm`

   [6]**J**ames   **C**lerk   **M**axwell   **T**elescope   on   Mauna   Kea,   Hawaii;   more   information   under `http://www.jach.hawaii.edu/JCMT`

Figure 4.1: The APEX telescope at the Llano Chajnantor, the ALMA site at an altitude of 5100 m above sea level.
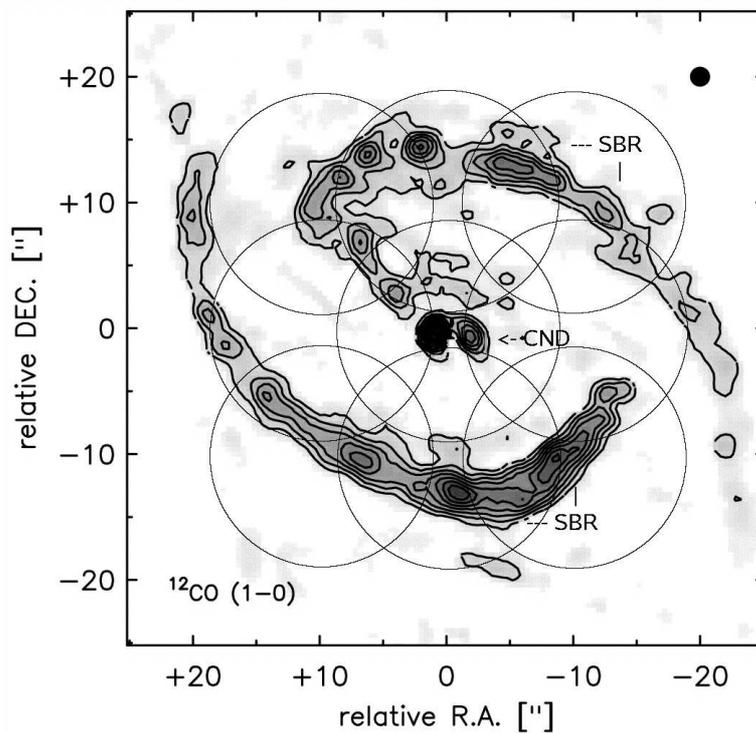

Figure 4.2: The nine observed pointings are indicated as circles of a diameter of 18" (the FWHM of the telescope beam at the observed sky frequencies). They are overlayed over a CO(1-0) high-resolution map of PdBI data (Schinnerer et al. 2000). The two distinct morphological features are indicated as circumnuclear disc (CND) and star-burst ring (SBR).

Table 4.1: The observations of NGC 1068 were conducted at 20th-22th Aug. 2005. The offsets are relative to the radio position of the nucleus (cf. text).

offsets		CO(J=3-2) at 345.796 GHz [a]; LSB		HCN(J=4-3) at 354.505 GHz [a]; LSB	
RA / Dec. ["]		$t_{\rm source}$ [s]	$T_{\rm sys}$ [K]	$t_{\rm source}$ [s]	$T_{\rm sys}$ [K]
10/	10	76	149	135	170
0/	10	38	147	176	167
-10/	10	37	152	151	171
10/	0	56	146	59	168
0/	0	115	154	642	198
-10/	0	102	150	140	161
10/	-10	115	153	170	164
0/	-10	94	150	77	185
-10/	-10	56	146	119	160

[a]from the Cologne Database for Molecular Spectroscopy (CDMS, cf. Müller et al. 2001). NCG 1068 is redshifted by $z = 0.0038$ (from NASA/IPAC Extragalactic Database (NED))

Table 4.2: APEX telescope efficiencies (from Güsten et al. 2006)

ν[GHz]	$\theta_{\rm mb}$ ["]	$\eta_{\rm f}$	$\eta_{\rm mb}$	$S/T_{\rm mb}$ [Jy/K] [a]	Receiver
352	17.3	0.97	0.73	30.3	APEX-2a
464	13.3	0.95	0.60	31.2	FLASH-I
812	7.7	0.95	0.43	32.0	FLASH-II

[a]For a Gaussian source and beam size, and a source much smaller than the beam: $S_{\rm [Jy]}/T_{\rm mb,\,[K]} = 8.18 \cdot 10^{-7} * \theta_{\rm mb,["]}^2 * \nu_{\rm [GHz]}^2$ (Rohlfs & Wilson 1996)

I observed nine grid points of a regular grid of 10" separation. The offsets correspond to the putative position of the nucleus: $\alpha_{2000} = 02^{\rm h}42^{\rm m}40^{\rm s}.71$, $\delta_{2000} = -00°00'47.9''$. It was estimated at cm-radio wavelengths with the British long baseline interferometer MERLIN[7], which enables at the observing frequency of 5 GHz an angular resolution of better than 50 mas. Muxlow et al. (1996) give the position uncertainties of the location of the nucleus of NGC 1068 with ±20 mas.

The pointing positions have been chosen to observe the complete central morphology of NGC 1068. A beam overlap by nearly 50% of the FWHM of the telescope beam of 18" at 350 GHz guaranteed a smooth dataset. While the central pointing matches the entire CND, the SBR is covered by the surrounding 8 pointings. Fig. 4.2 shows the pointing positions. The FWHM are overlayed as circles over a high-resolution map of PdBI data of the CO(1-0) line tracing the total molecular gas content (by Schinnerer et al. 2000). For comparison, the 1.4" beam of the map of the interferometer is indicated in the upper right corner.

4.2 Data reduction

For the data reduction I have used the CLASS/GILDAS[8] software, a dedicated package for single-telescope and interferometric (sub-)mm observations. At the time of the observations, no sec-

---

[7]**M**ulti-**E**lement **R**adio **L**inked **I**nterferometer **N**etwork; more information under http://www.merlin.ac.uk

[8]The **C**ontinuum and **L**ine **A**nalysis **S**ingle-dish **S**oftware is a part of the **G**renoble **I**mage and **L**ine **D**ata **A**nalysis **S**oftware, developed at IRAM; more information under http://www.iram.fr/IRAMFR/GILDAS
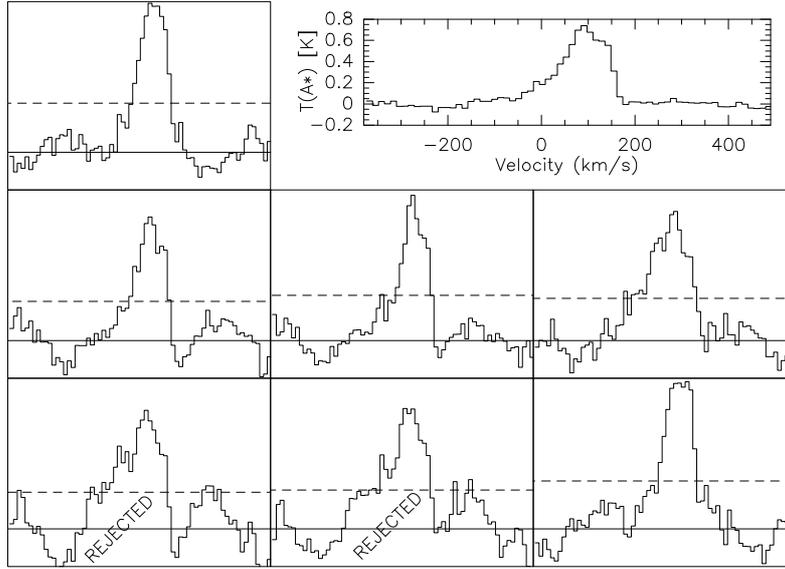
Figure 4.3: Illustration of the scan selection with the data at offset (-10,0)": The solid line in each single scan spectrum marks the 0 K baseline level, the dashed line indicates 33% of the maximum intensity. Baseline ripples outside the expected line emitting region without any source flux, which show amplitudes close or above this 33% limit, are regarded as *strong* and the respective scan is not included in the average shown in the upper right corner and in Fig. 4.4

ondary mirror with beam switching capabilities (*wobbler*) was installed. That is, why in this early phase of instrument commissioning the biggest observational problems consists of so-called baseline ripples and temporal changes of the baseline quality, which hampers especially the presented extragalactic observations of broad (several hundreds of km s^{-1} !) emission lines.

If the baseline imperfections are of random character, sufficiently long integration times can diminish their influence, but in addition to random ripples and non-linear baseline corruptions, in several scans appeared a strong sinusoidal pattern of technical origin, which was too strong and phase-constant to vanish after averaging over the applied total integration time. I tried to apply sinusoidal baseline fits to these scans, but the subtraction of such baselines leads to variable, ungaugeable subtraction of source flux, because the width and strength of the emission line to be observed were too similar to the sinusoidal pattern. I reject those scans, with an amplitude of the baseline variation of order 30% or more of the peak line emission (Fig. 4.3).

In all used CO(3-2) scans the line peaks with a SNR of $\sim$10 at an adequate sampling. Since the major goal of this project was the detection of the line transitions, I did not subtract other than linear baselines. The remaining baseline imperfections become manifest in uncertainties of the line shape. The error on single channel flux densities can reach 30%. After linear baseline subtraction the integrated line flux can be estimated at higher precision ($\sim$15%), because typically the baseline imperfections are varying randomly over the wide transition lines (see Fig. 4.3 for an example).

The weaker HCN(4-3) transition is not apparent in the single scans. This exacerbates significantly the manual reduction scheme outlined above. I refused all scans with any indication for non-linear baselines outside the region, where CO(3-2) was detected. Furthermore I rejected all scans which show *systematic* baseline errors. The selection criterion for the characterization of such systematic

baseline errors is based on the radiometer formula (e.g. Burke & Graham-Smith 2002, Chapter 3),

$$\Delta S \;\; \propto \;\; (B\,\tau)^{-1} . \tag{4.1}$$

It describes the connection between channel bandwidth B, total integration time τ and rms-uncertainty of the flux estimation in this channel, ΔS. The bandwidth can be varied by changing the spectral binning. The integration time depends on the number of used scans, each of which consisted of an individual integration time of $\tau_0 \approx 20\ s$. The individual scans were summed with an rms-weighting, where the rms-flux uncertainty of a single channel was estimated by comparison of several neighboring channels in a part of the spectrum, which is supposed to be free of any line emission. If after an increase of B or τ the flux noise ΔS was *not* reduced according to Eq. 4.1, the scan was declared to be dominated by non-random, systematic uncertainties which would systematically affect the finale sum. Those scans were rejected.

The total on-source integration time t_{source} of all scans used is reported in Table 4.1.

4.3   Results

4.3.1   Spectra of the CO(J=3-2) rotational line transition
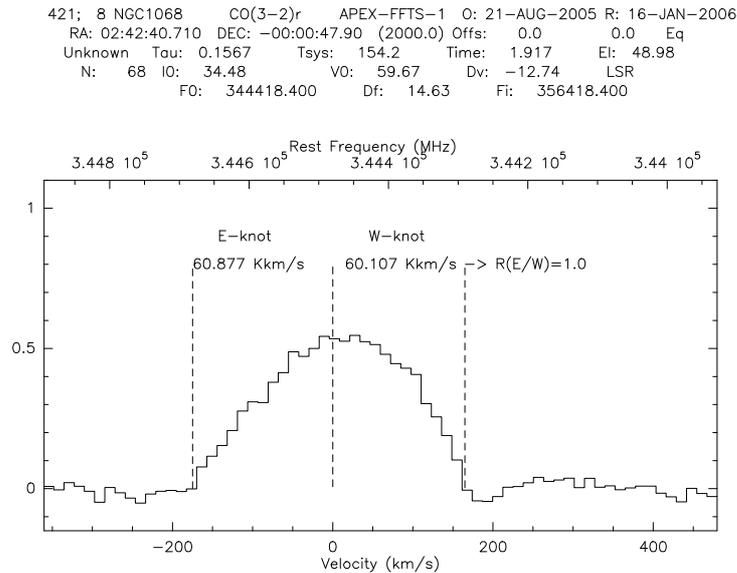
Figure 4.4: Spectrum of the nucleus with the full data information provided. The nomenclature of the knots follows Usero et al. (2004) and distinguishes between two major components of the CND in the nuclear CO distribution . The integrated line widths are indicated. Both knots appear to have equal brightness (Ratio(E/W) = 1).

CO(3-2) was detected at all nine pointing positions. The integrated line intensities are given in Table 4.3.

A map of the extended CO(3-2) emission was presented by Papadopoulos & Seaquist (1999). The principle investigator of the aforementioned article kindly provided me with their JCMT data to enable a detailed comparison of the results. After resampling and convolution to a common resolution of 18", I could overplot the individual spectra to compare intensity and spectral shape.
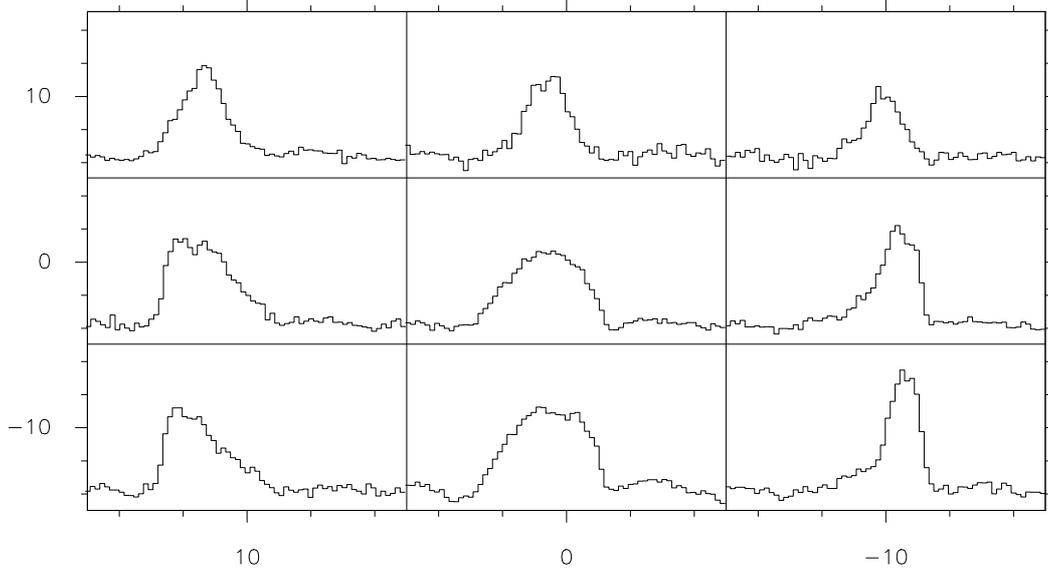
Figure 4.5: The reduced CO(3-2) spectra at nine different pointings, as indicated in arcsec offsets. Offset (0,0) is the pointing on the nucleus respectively the CND. These spectra are corrected for linear baselines only, the remaining baseline imperfection do not affect the integrated line intensities as given in Table 4.1 significantly. The scales are similar to Fig. 4.4. North is up and East is to the left.

Table 4.3: The measured line intensities of the CO(3-2) rotational line transition, integrated over the indicated velocity width between the zero flux densities. Intensity scale is T_A^*

CND	SBR			
units: (offset [“]): Int.Intensity [K km s^{-1}]; FWZI [km s^{-1}]				
(0/0)”: 121; 344	(10/10)” 95; 330	(0/10)” 75; 290	(-10/10)” 55; 240	
	(10/0)” 120; 340		(-10/0)” 90; 330	
	(10/-10)” 100; 330	(0/-10)” 145; 360	(-10/-10)” 95; 320	

Table 4.4: Comparison of published JCMT data and my APEX observations at the position of the nucleus (offset: 0/0”).

	JCMT [a,b]	APEX [a]	JCMT [c]	APEX [d]
FWHM(beam)	14”	18”	16”	18”
CO(J=3-2)	44 K	57 K	430 mK	435 mK
HCN(J=4-3)	3.1 K	< 5.5 K [e]		

[a]line-center brightness temperatures in the T_{mb}-scale, corrected for a Gaussian source size of 2”
[b]from Sternberg et al. (1994).
[c]T_{mb} averaged over Δv = 950-1300 km s^{-1} read out from the map by Papadopoulos & Seaquist (1999)
[d]T_{mb} averaged over Δv = 950-1300 km s^{-1} at the central pointing, not source size corrected
[e]3 σ upper limit, on basis of $3\sigma(T_{mb,HCN})$ = 50 mK per channel at a spectral resolution of 40 km s^{-1}

The result is shown in Fig. 4.6. The JCMT data have a spectral resolution of 8 km/s, whereas my spectrum are binned to a resolution of 13 km/s, both spectral channel widths are far below the width of the emission lines.

The comparison of the spectra confirms the capabilities of the standard APEX data calibration and my executed manual data reduction. Despite of the severe problems in defining the spectral
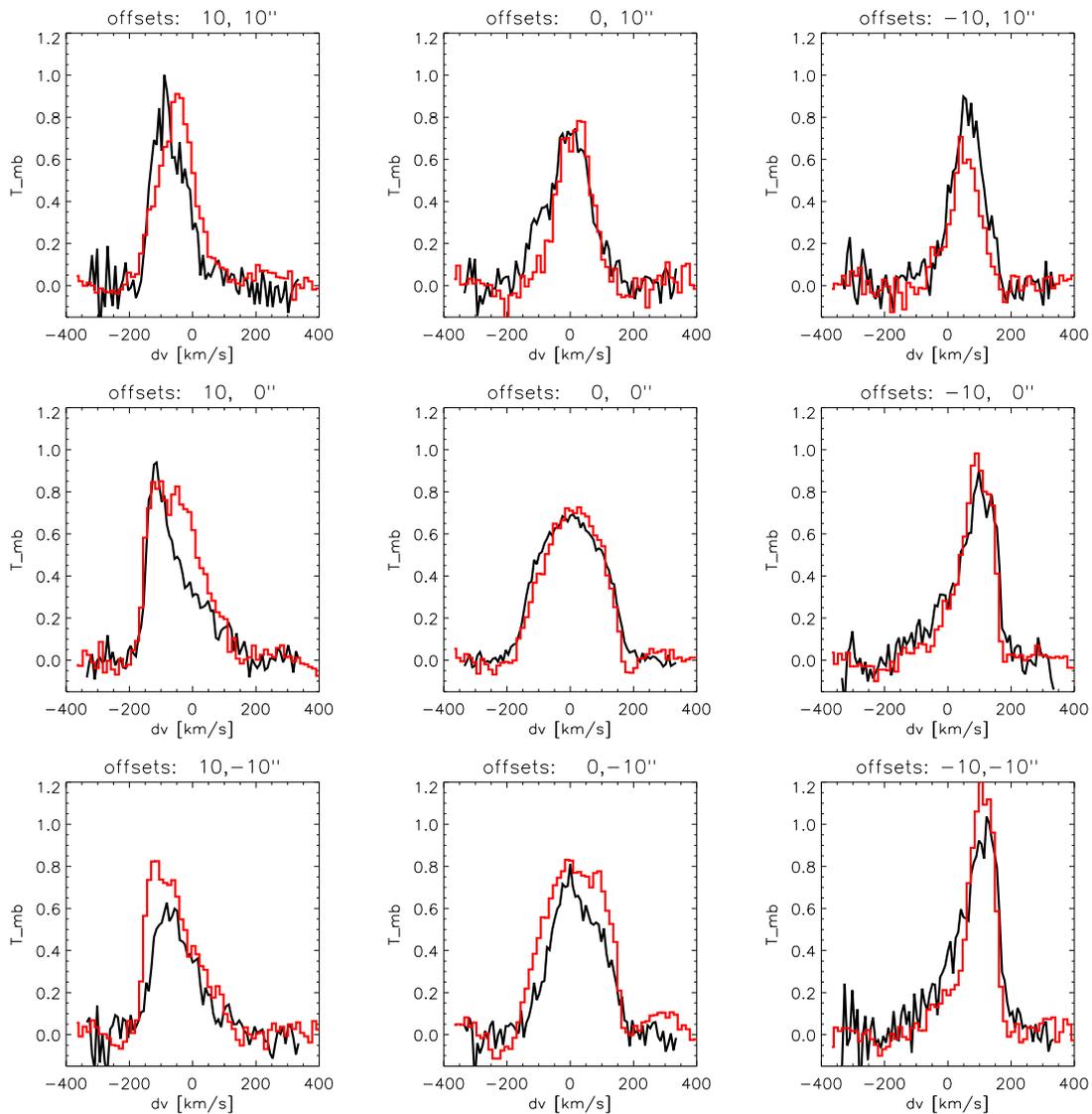
Figure 4.6: The JCMT-spectra are shown in black, my APEX spectra in red solid lines. The spectral resolution is given in the text, the intensity is plotted in the main-beam temperature scale T_{mb}. The offsets to the nucleus are indicated in the individual plots.

baseline, the intensity and shape of both datasets coincide within the given uncertainties. The remaining differences do not clearly correlate with the total integration times (cf. Table 4.1). This indicates, that systematic uncertainties may still be present in the reduced data. E.g. pointing $(0/-10)$" [9] was observed about 1.5 min on-source, which is a medium integration time with respect to the other pointings and should show less random uncertainties than spectra of less total integration times. But the (0/-10)"-offset spectrum still have significant remnants of the sinusoidal baseline artefacts outside the emission line. These remnants apparently widens the shape of the line itself (Fig. 4.6). On the other hand pointing errors and original beam-size differences between the APEX and JCMT datasets can also account for the slightly different results of both observing runs due to the complex distribution of the molecular gas in the center of NGC 1068 (Fig. 4.2).

---

[9]This pointing nomenclature always lists the offset in Right Ascension first.
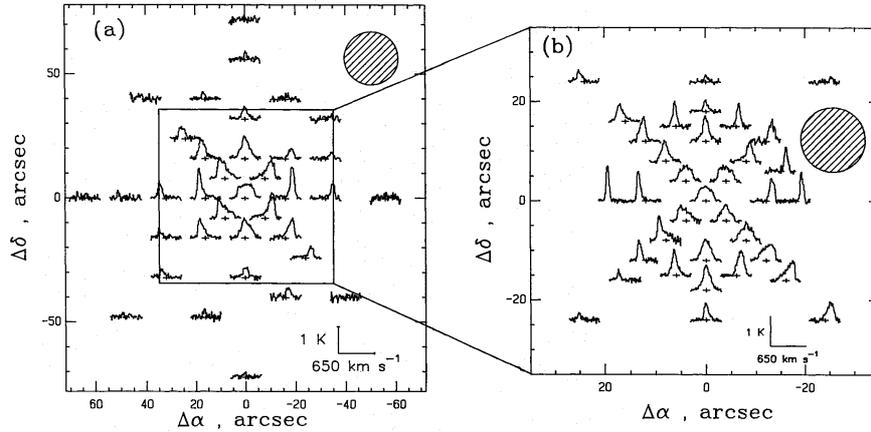
Figure 4.7: CO(1-0) (left) and CO(2-1) (right) rotational line emission towards NGC 1068. The line-center is indicated by the cross, the units are given in the lower right corner of each panel. Taken from (Planesas et al. 1989)

Here I would like to outline, that I did *not* tune in no way the manual scan selection to produce spectra, which match as good as possible the JCMT spectra. The scan selection was purely based on the criteria discussed in Sect. 4.2.

Tacconi et al. (1994) and Sternberg et al. (1994) published the detection and the peak flux density of CO(3-2) and HCN(4-3) at the nucleus. They corrected the measured main-beam temperature for a Gaussian source size of FWHM $\theta_s = 2''$

$$T_{s,corr} = T_{mb} * \frac{\theta_{tel}^2 + \theta_s^2}{\theta_s^2} .$$
(4.2)

I apply the same correction to my data leading to a difference of about 30% (Table 4.4). The results still coincide within the errors, because here the peak fluxes are compared and I estimated a conservative general uncertainty of 30% per spectral channels (i.e. also for the peak flux), mostly based on systematic errors. But in the particular case of the nuclear spectrum, a smaller error appears to be more adequate for my APEX data. The spectral shape of my nuclear spectrum appears to be rather smooth without spectral artefacts on the order of 30%. And the difference to the nuclear JCMT spectrum of Papadopoulos & Seaquist (1999) is 10-15% only. Thus there is strong evidence, that the differences between the source size corrected peak fluxes are real.

One possible explanation for the shown disagreement of the peak fluxes derives from the larger APEX beam. It may collect additional flux contributions from the SBR with respect to JCMT, but the beam overplotted over the high-resolution map does not suggest a large contribution of this effect.

A more probable explanation comes from the single-dish data themselves. Since the JCMT telescope beam has a FWHM of 14" at 350 GHz, which is significantly smaller than the APEX beam size, such a different peak flux after the correction for the source size can indicate a wrongly assumed source size. The true source size can be estimate with Eq. 4.2

$$\theta_s^2 = \frac{T_{mb,JCMT} * \theta_{JCMT}^2 - T_{mb,APEX} * \theta_{APEX}^2}{T_{mb,APEX} - T_{mb,JCMT}} = 17'' .$$
(4.3)

Sternberg et al. (1994) derived the $\theta_s = 2''$ from PdB interferometric measurements. The higher resolved data presented more recently by Schinnerer et al. (2000), show in fact, that the nuclear

molecular gas emission is divided in two distinct sources of the CND, each of which being even smaller than the assumed θ_s. This would confirm the assumed $\theta_s = 2''$ as a reasonable average in the lower resolved maps, but still disagree with the APEX data.

The channel maps published by Papadopoulos & Seaquist (1999) also indicate a more realistic single dish source size of the order of 20", in close agreement with Eq. 4.3. The much larger $\theta_s = 17''$, derived from the direct comparison of the different single dish measurements indicates, that the interferometer is missing a significant amount of diffuse molecular line emission due to missing short baseline coverage. That is, the 2" source size correction, derived from the interferometric maps, is not applicable to single dish data, since a significant amount of flux is resolved out by the interferometer.

A further check of the quality of the reduced APEX data can be done invoking the observed spectral shapes. The spectral shape is created by the kinematics of the molecular gas distribution. Assuming that most of the regions emitting the molecular transition lines are contributing at similar ratios to each transition line intensity, the spectral line shapes of different transitions should coincide.

Planesas et al. (1989) observed CO(1-0) and CO(2-1) with the IRAM 30m telescope, thus measuring all diffuse flux emission. Fig.4.7 shows for the comparison of the line shapes of the spectral lines different rotational line transitions of CO at the same pointing positions of my APEX observations. Despite of the baseline instabilities the spectral shapes of the APEX CO(3-2) transitions coincide with respective CO(1-0) and CO(2-1) 30m spectra very well.

4.3.2 Searching for the HCN(J=4-3) emission
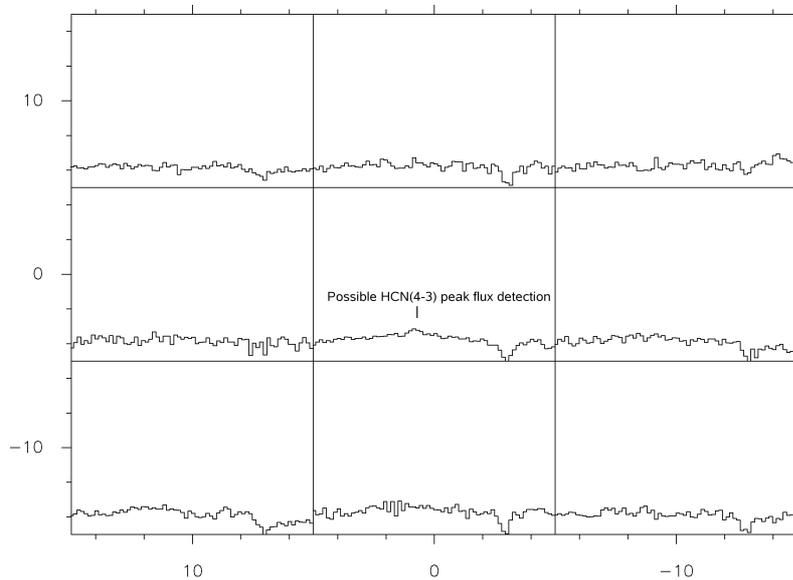
Figure 4.8: The reduced HCN(4-3) spectra at the nine pointings, as indicated in arcsec offsets. Abscissa and ordinate are given in km s^{-1} and T_A^*, respectively. The scaling is identical to Fig. 4.4. The spectra have been corrected for linear baselines and are shown at a spectral resolution of 12 km s^{-1}
. The expected line center at the nucleus is indicated.

The positive results of the CO(3-2) observation, presented in the previous section, convinced the ESO Science Verification committee to spend more time on NGC 1068. I have tried to observe the

HCN(4-3) emission from the nuclear region as well as from unprecedented off-nuclear pointings towards the SBR only. The given observing time (Table 4.1) was not sufficient to detect this transition (Fig. 4.8). Nevertheless the measured upper limit coincides with the source size corrected peak flux intensity from Sternberg et al. (1994) as shown in the last row of Table 4.4.

If I apply the single-dish source size $\theta_\mathrm{s} = 17''$ derived in the previous section, both values are equal

$$\theta_\mathrm{s} = 17'' \rightarrow T_\mathrm{s,corr,JCMT} = 0.1\ K;\ T_\mathrm{s,corr,APEX} \leq 0.1\ K\ . \tag{4.4}$$

This coincidence of my $3\ \sigma$ upper limit on the peak flux with the published value suggests, that at the central pointing the line detection was nearly achieved. In fact, the central spectrum in Fig. 4.8 corroborates this finding. A slide peak at the central position is visible, but I could not confirm this with conservative error estimates, since too many data sets had to be rejected because of systematic baseline errors. The reduction was exacerbated due to the fact, that the red side of the emission free part of the spectrum, which is needed to estimate a good baseline over the broad emission line, shows an absorption feature.

The $3\ \sigma$ peak flux limits of the SBR pointings are of the same order of magnitude as the central one.

4.4 Conclusions

The actual instrumental setup of the APEX telescope for 350 GHz observations systematically affect the spectroscopic baseline of the datasets. The non-linear baseline distortions can be much stronger than all other thermal noise contributions. In case of galactic narrow emission line observations of widths of up to a few tens km s^{-1} this should not be problematic and the subtraction of low-order baseline polynomials lead to reliable data sets.

But this standard data reduction is not sufficient to observe broad extragalactic emission lines. Nevertheless I could show, that dedicated data reduction based on manual scan selection and a theoretical approach to find and reject those scans with very large systematic, non-thermal errors can successfully be applied to produce scientifically valuable datasets.

A detailed comparison with published data was presented. Both the intensity and the spectral line shape of the reduced CO(3-2) emission line could be confirmed. The comparison have shown, that despite severe baseline corruption the conservative estimate of a spectral channel uncertainty of $\sim 30\%$ indeed is adequate to characterize the reduced APEX data. This level of uncertainty was derived from the data reduction process itself, The 30% may still be dominated by remaining non-random systematic errors, which vary from scan to scan, but also pointing differences and different observing beam-sizes could be responsible for the remaining differences to the comparative dataset. The comparative spectra also have a channel-to-channel uncertainty of 10% (Papadopoulos & Seaquist 1999), which further alleviates the differences. The quality of the central pointing towards NGC 1068 itself was even good enough to derive a reasonable single-dish source size of the nuclear line emission.

This source size of 17" can be applied to recalculate published source-size corrected data. It verifies that the detection of HCN(4-3) at least towards the nucleus with the current APEX without any improvements is already possible within less then 1 h on-source observing time.

Chapter 5

Search for dense molecular gas in two QSO host galaxies

The HCN(J=1-0) rotational line transition traces the dense ($n_{H_2} > 10^4\,\mathrm{cm}^{-3}$) fraction of the molecular gas typically located in star-forming (SF) regions. Its rest frequency of 88.6 GHz (Müller et al. 2001) makes it observable from the ground through the 3 mm transmission window of the atmosphere. Observed correlations between the CO-, HCN-, and FIR luminosities in nearby non-active, star-burst, and low-luminosity active galaxies represent the physical connection between star formation and molecular gas as its fuel.

In addition to the SF connection, HCN(1-0) shows an interesting interlink to the AGN phenomenon. Namely, an abnormally high HCN/CO line ratio close to AGNs may indicate the conditions of an X-ray-dominated region. But this effect has typically been observed only towards low-luminosity Seyfert galaxies yet (Kohno et al. 2003; Usero et al. 2004). HCN(1-0) has hardly been investigated in nearby high-luminosity AGN within this context. I initiated a project to investigate the HCN(1-0) line emission from high-luminosity AGN hosts with the IRAM 30m facility. A successful detection of HCN towards such galaxies would open the window of high-resolution follow-up studies with the Plateau-de-Bure Interferometer to constrain and maybe resolve the AGN dominated zone of the dense molecular gas in the host.

The aim of my initial, spatially unresolved single telescope study is to compare the HCN luminosity with published CO and IR luminosities to investigate the role of SF in the observed QSO host galaxies. HCN(1-0) has not yet been systematically detected in relatively nearby ($z \sim 0.1$) standard optically luminous QSO host galaxies, which underlines the recentness of my observations.

I estimate upper limits on L_{HCN}, which agree with the known correlations and do not show strong excess abundance or excitation of the HCN due to the luminous active quasar nucleus. The star-burst origin of the far-infrared luminosity in the observed QSO hosts cannot be proven unambiguously by these upper limits. I find that the IR/FIR ratio indicates independently of L_{IR} if a significant amount of AGN heated dust is present. Most of the content of this chapter has been published in a peer-reviewed journal (Pott et al. 2006).

5.1 Introduction

The evolutionary sequence from ultra-luminous infrared galaxies (ULIRGs; $L_{IR} \geq 10^{12}\,L_{\odot}$) to quasars has become a popular, though controversial, theory (e.g. Sanders et al. 1988; Sanders

2003). Common IR properties tracing active galactic nuclei (AGN) and star formation (SF) in the respective galaxies support such evolutionary schemes. (Sub-)mm photometry and spectroscopy have very recently revealed that optically luminous quasars already show in the early universe ($z > 1$) indications for vigorous star formation, ULIRG-like FIR/CO luminosity ratios, and HCN-emission (Cox et al. 2005; Solomon & vanden Bout 2005, and references therein). The dust emission appears to trace the evolutionary history of quasars (Haas et al. 2003). Optically selected standard quasars (e.g. the Palomar-Green (PG) quasars; Schmidt & Green 1983) have NIR-MIR luminosities dominated by the AGN with negligible stellar light contributions at wavelengths shorter than 5 μm. Nevertheless SF seems to be present in quasar hosts (Surace et al. 2001).

Haas et al. (2003) discuss the possibility of quantifying the star burst (SB) contribution to the infrared luminosities of PG quasars on the basis of sensitive ISO SEDs. The radio-FIR correlation known from SB galaxies (Condon 1992) appears to be fulfilled for the radio-quiet PG quasars, while the IR brightest ($L_{FIR} \geq 10^{12} L_{\odot}$) radio-loud counterparts do not clearly indicate the importance of SB contribution to the FIR. In these IR-brightest quasars, the FIR component might simply constitute the Rayleigh-Jeans tail of the SED of the AGN-heated dust, normally dominating only the MIR emission of the quasar hosts.

Recent CO studies of QSOs (e.g. Evans et al. 2001) have revealed large amounts of molecular gas by applying the adequate conversion factors between L_{CO} and the total molecular gas mass. The QSOs show systematically higher infrared-to-CO luminosity ratios compared to the majority of galaxies with similarly high infrared luminosity, but no visible AGN. Evans et al. (2001) conclude that their selected sources show either a strong AGN-heated dust contribution to L_{IR} or an increase in star formation efficiency (SFE), i.e. star formation rate (SFR) with respect to the total amount of molecular gas available.

Solomon et al. (1992) and Gao & Solomon (2004, hereafter G04) studied the HCN content in 65 nearby galaxies, covering three orders of magnitude of L_{IR} up to the ULIRG regime and established that the *dense* gas tracer HCN is tightly correlated to the SFR. Furthermore, the global HCN/CO line-intensity ratio appears to be a strong star-burst indicator. By applying this putative SB indicator to their entire sample, including the most infrared luminous objects, the far-infrared luminosity could be mostly assigned to star-burst activity, with only an insignificant contribution from AGN heated dust.

The question of the SB contribution to the total L_{IR} is still unanswered for infrared-bright QSO+host-galaxy systems, which harbor a strong AGN. Their FIR may comprise a major SB contribution and follow SB-induced FIR/CO and FIR/HCN correlations. To probe the latter correlation initially in two PG QSO hosts, I was awarded observing time at the IRAM 30m mm telescope in Granada, Spain. With single-dish telescopes the HCN emission will be spatially unresolved at $z = 1$ (Sect. 5.2). But due to the dominance of the AGN in the UV/optical it is well possible that also the weak global HCN fluxes of QSOs might be significantly enhanced by direct AGN excitation. The results of this search are presented in Sect. 5.3 In Sect. 5.4 the findings are discussed and compared with published data. The conclusions are summarized in Sect. 5.5.

5.2 Observations and source selection

The observational details are given in Table 5.1. The weather conditions were good with system temperatures of 150-250 K and zenith opacities of $0.05 \leq \tau_{zen} \leq 0.1$ at the sky frequencies. Because the observing frequencies fall outside the standard tuning range of the receivers, the local oscillators were exchanged (Sect. 2.3). To verify this non-standard procedure, I conducted a

Table 5.1: Source list and parameters of the observing run in June 2005 with the IRAM 30m-telescope. At 80 GHz, the telescope properties are: HPBW: 31"; Beam efficiency: 0.8; Forward efficiency: 0.95; S/T_{mb}: 4.95 Jy/K

Source	R.A. (J2000)	Dec. (J2000)	z_{CO}	D_L [a] [Mpc]	transition	Sky freq. [GHz]
PG0838+770	08 44 45.36	76 53 09	0.132	540	HCN(J=1-0)	78.296
PG1415+451	14 17 00.84	44 56 06	0.114	470	HCN(J=1-0)	79.562

			$\log L_{\mathrm{IR}}$ [b] [$\log L_\odot$]	$\log L_{\mathrm{FIR}}$ [b] [$\log L_\odot$]	$F_{CO}^{average}$ [mJy]	L'_{CO} [a] [K kms^{-1}pc^2]
PG0838+770			11.48	11.15	37	2.1·10^9
PG1415+451			11.39	10.83	66	1.5·10^9

[a] from Evans et al. (2001)

[b] calculated from the IRAS flux densities as published by Sanders et al. (1990) using the standard IRAS conversion formulae (e.g. presented in Table 1 in Sanders & Mirabel 1996). L_{IR} covers 8-1000 μm and L_{FIR} covers 40-500 μm.

frequency tuning test on the giant molecular cloud Sgr B2, which were successfully. Pronounced lines like ^{13}CH$_3$OH, H^{13}CCCN, and EtCN were found to coincide with the findings of the molecular line survey of Turner (1989, 1991) of similar spectral resolution.

Each line was resolved by 1MHz-filter bank backend, while the data was smoothed to a velocity resolution of about 25 km s^{-1}. Frequent observations of continuum sources provided a pointing accuracy of 3-5". I used single-sideband SIS receivers and the wobbler with a switch cycle of 2 s and a beam throw of 110". At least four times per hour, a chopper wheel calibration was performed. Baselines were flat, and only linear polynomials were used for correction.

I selected the two sources from a sample of 13 PG quasars with known CO fluxes (Evans et al. 2001; Scoville et al. 2003a) that show the brightest average CO flux density (line-flux/linewidth; Table 5.1).

5.3 Results – upper limits on the HCN luminosity

Table 5.2: The observational results.

Source	Δv_{FWHM} [a] [km s^{-1}]	$S_{\mathrm{HCN}}\Delta v$ [b] [Jy km s^{-1}]	L'_{HCN} [b] [K km s^{-1} pc^2]	$L'_{\mathrm{HCN}}/L'_{\mathrm{CO}}$ [a]
PG0838	90	< 0.67	< 7.2 · 10^8	< 0.34
PG1415	50	< 0.84	< 6.9 · 10^8	< 0.46

[a] Δv_{FWHM} and L'_{CO} from Evans et al. (2001)

[b] 3σ flux and luminosity limits are calculated with $\sigma(S_{\mathrm{HCN}}\Delta v) = \sigma(S_{\mathrm{chan}}) \cdot (2\,\Delta v_{\mathrm{FWHM}}\Delta v_{\mathrm{chan}})^{1/2}$, assuming a triangular line shape; $\sigma(S_{\mathrm{chan}})$ and velocity resolution Δv_{chan} are given in Fig. 5.1

The observational results are presented in Fig. 5.1 and Table 5.2. The spectra in Fig. 5.1 are smoothed to a resolution adapted to the CO data, which are presented by Evans et al. (2001) assuming a similar width of the HCN line. Under the same assumption, I calculated 3σ upper limits to the luminosity of the HCN(J=1-0) rotational line transition (Table 5.2). Accounting for
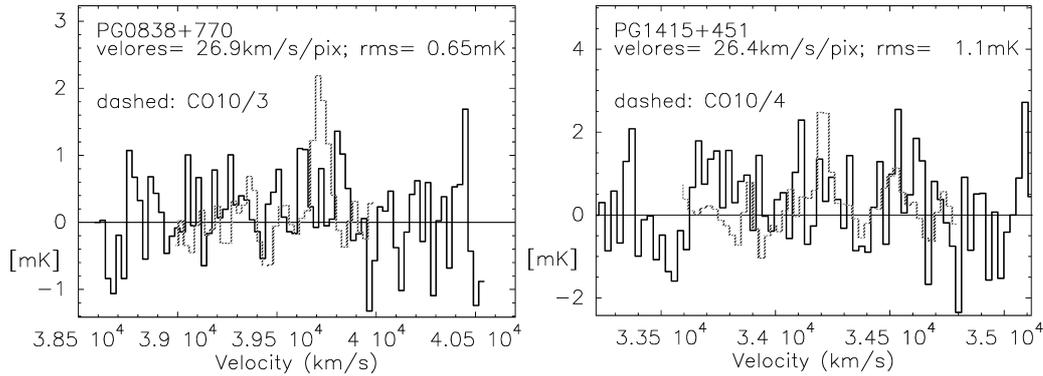
Figure 5.1: The spectra of the two QSO hosts towards which I searched for the HCN(1-0) emission. The velocity scale follows the optical convention $v = cz$. The flux density is given in the T_{mb}-scale. The spectra are smoothed to a resolution of 14 MHz with a 7 MHz sampling. The derived 3σ-upper limits are given in Table 5.2. The CO(1-0) spectra from Evans et al. (2001) are over-plotted after conversion to the 30m-T_{mb}-scale assuming that the QSOs had not been spatially resolved by their interferometric observations.

the weak expected line fluxes, the σ are lower by a factor of five than the average rms on the 30m line fluxes achieved by G04.

5.4 Discussion of the results

In the following, the observational results are compared to published CO and FIR luminosities and the resulting ratios are discussed.

5.4.1 HCN/CO line ratio

The upper limits on the HCN luminosity lead to HCN/CO line ratios of less than ~ 0.46. These global ratios are around the highest ratios measured close to low-luminosity AGN (e.g. Helfer & Blitz 1995, they report HCN/CO ≈ 0.6 in the nucleus of the Seyfert 2 prototype NGC 1068). Kohno (2005) reports that ratios above 0.2 can appear in the nuclei of some Seyferts most probably due to intense X-ray irradiation by the AGN. Such X-ray dominated regions (XDRs) appear to be confined to the innermost regions ($\lesssim 100$ pc), in general without significant contributions to the global HCN luminosity in gas-rich host galaxies (Kohno et al. 2003; Usero et al. 2004).

Although the spatially unresolved IRAM 30m observations can only probe the global L_{HCN}, the outstanding nuclear activity in quasars might also contribute significantly to the global HCN excitation. Thus the upper limits on the global line ratios can exclude a strong global HCN/CO excess in the QSO hosts beyond the values found in low-luminosity active nuclei. But since the upper limits are above 0.3, it cannot be ruled out that a significant part of the total HCN is XDR-like excited by the AGN itself.

A comparison of the reached sensitivities (Fig. 5.1) with the respective HCN/CO line ratios in both observed QSOs might suggest, however, that the higher HCN/CO upper-limit of PG 1415+451 derives from the lower sensitivity reached only in this observation.
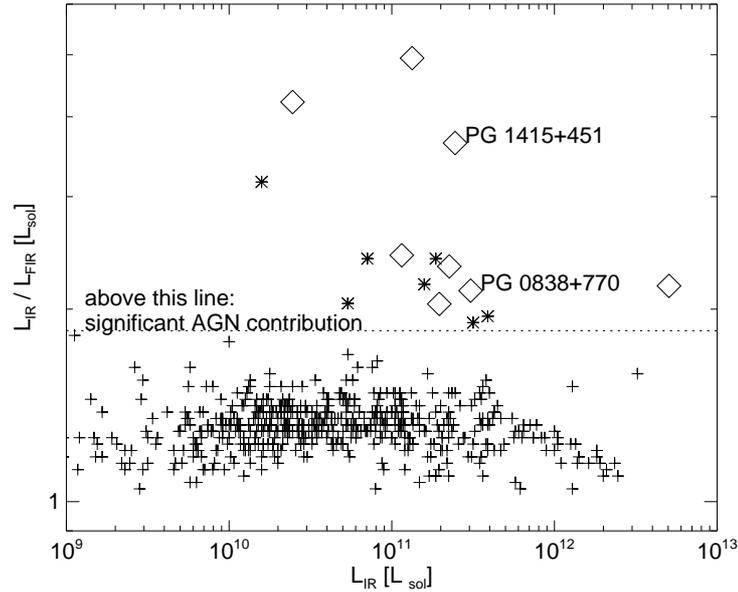
Figure 5.2: The IR/FIR ratio is shown as a diagnostic to reveal significant AGN-contribution to the total infrared luminosity of a galaxy. The IRAS Revised Bright Galaxy Sample (Sanders et al. 2003) is plotted, including virtually all galaxies from G04 (crosses). The dotted line represents IR/FIR = 1.85 and is arbitrarily chosen to guide the reader's eye. All radio-quiet PG quasars (including those observed here; the IRAS flux densities taken from Sanders et al. 1990) are above the line and indicated by diamonds. The stars above the line are active galaxies of Seyfert type. There are no quiescent / SB galaxies above the line. I suggest using such a plot as a diagnostic to find significant AGN-contributions to the IR luminosity of a galaxy (see Sect. 5.4.2). The size of the symbols reflect the order of magnitude of the luminosity uncertainties.

5.4.2 Probing the FIR origin

In infrared luminous QSO host galaxies, the IR is reprocessed UV-optical irradiation that is emitted by the AGN itself (AGN-scenario) and by massive stars (SF-scenario). Multi-wavelength information is required to investigate which scenario dominates the global properties of a specific galaxy, or whether neither dominates.

In Fig. 5.2 I plot the IR/FIR luminosity ratio of a large flux-limited sample of galaxies – the IRAS bright galaxy sample (IBGS) includes normal, star-burst, active, and ultra-luminous IR galaxies (Sanders et al. 2003) – together with the radio-quiet subset of PG quasars (Sanders et al. 1990). Nearly all galaxies of the G04-sample are included in the IBGS, which comprises all levels of star-burst activity. The vast majority of the galaxies populates a continuous band around IR/FIR ~ 1.3 over several orders of magnitude of total IR luminosity, whereas all quasar hosts, including the observed ones and a few Seyferts, are located well above this value.

This demonstrates that the AGN dominates the global L_{IR} in the selected quasars. Thus I decide to concentrate on the FIR wavelength regime in the following. The central question is: How strong is the FIR luminosity (Table 5.1) affected by the AGN? One can investigate the AGN-powered fraction of the FIR (FIR$_{\mathrm{AGN}}$) by a comparison with the molecular gas luminosities.

The FIR/CO- and the FIR/HCN-luminosities of the G04-sample are plotted in Fig. 5.3 (upper and lower panel, respectively). I probe for linear correlations by χ^2-fits to slopes in log-space. The estimated slopes are given in Fig. 5.3. Indeed slopes of *one* for the quasars and the G04-subsample ex-
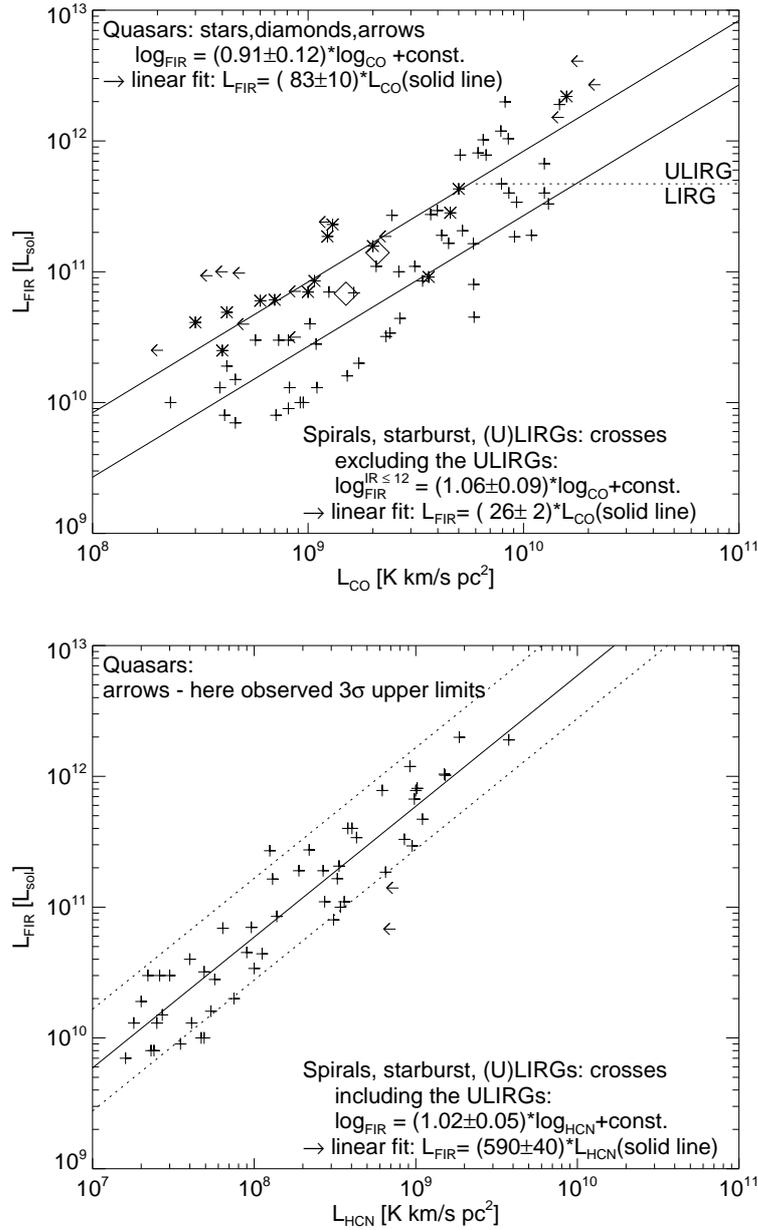
Figure 5.3: The correlation plots of G04 extended by quasar hosts with known CO luminosities (Alloin et al. 1992; Evans et al. 2001; Scoville et al. 2003a,the two investigated quasars are highlighted as diamonds) (upper panel) and the estimated upper limits (arrows) on L_{HCN} (lower panel). Linear correlations are given (solid lines), resulting from a fit in log-space, where the slope was fixed to one. The dotted lines in the lower panel show the expected FIR/HCN correlation for quasars in case of the AGN-scenario (Sect. 5.4.2), for global HCN/CO ratios of 0.05 (upper line) and 0.3 (lower line). In contrast, the SF-scenario implies that the quasars are predicted to follow the given FIR/HCN correlation. Note that the less sensitive upper HCN-limit (PG1415) is further away of the standard FIR/HCN correlation. Individual uncertainties are 30-50%.

cluding ULIRGs for the FIR/CO correlation are found. The IR/gas correlations, published by G04, translate into similar FIR/gas correlations, reflecting the luminosity-independent IR/FIR ratios of the sample (Fig. 5.2). With respect to the linear correlation given in Fig. 5.3 ($L_{FIR} = 26\,L'_{CO}$),

the quasars show an FIR excess by a factor of 2.6 (PG0838) and 1.7 (PG1415). These excesses can limit FIR_{AGN}, if I assume (i) normal SFE (i.e. $FIR_{SF} \geq 26\,L'_{CO}$) and (ii) that the detected CO is predominantly fueling SF.

The FIR/CO ratio of the quasars is similar to or below the ratio of most ULIRGs. Since G04 argued that the increased FIR/CO ratio in ULIRGs could be evoked entirely by an increased SFE without significant FIR_{AGN}, the lower limit of FIR_{AGN} is zero. Summarizing, I can constrain FIR_{AGN} to: $0 \leq FIR_{AGN}(PG0838) \leq 40\,L'_{CO}$ and $0 \leq FIR_{AGN}(PG1415) \leq 20\,L'_{CO}$.

Furthermore, the quasars with published L_{CO} show a linear FIR/CO correlation themselves (upper solid line in Fig. 5.3, upper panel). If I include the ULIRGs in the quasar sample assuming that they are dust-enshrouded quasars, the logarithmic slope increases to (1.07±0.09); i.e. a linear correlation is still within the uncertainties. I include neither the ULIRGS nor the quasars with upper limits on their CO luminosities in the fits. Since they appear to be equally distributed above the considered quasars in Fig. 5.3, a significant change of the logarithmic *slope* is not to be expected from incorporating these objects. On the other hand, most of the ULIRGs are located above the linear correlation plotted in Fig. 5.3. This indicates a logarithmic slope steeper than one if more ULIRGs with similar properties as the measured ones were included. But together with the CO-upper-limit quasars, a linear correlation shifted towards higher L_{FIR} is possible, too.

On the basis of this linear correlation, I can assume FIR_{AGN} of an average QSO to fulfill: $0 \leq FIR_{AGN} \leq 57\,L'_{CO}$ following the above argumentation. Thus a global AGN dominance of the entire IR of the quasar host is possible. This AGN-scenario can lead to two different expectations for the global FIR/HCN ratio of quasars, depending on the global HCN/CO ratio. Using the linear correlations given in Fig. 5.3, an HCN/CO ratio of 0.05 (G04) would shift the FIR/HCN relation upwards to FIR=1660 HCN (upper dotted line). On the other hand, global AGN-dominance could imply a significant increase in the global HCN/CO ratio (cf. Sect. 5.4.1). Assuming an increased HCN/CO ratio of 0.3 would lead to FIR=280 HCN (lower dotted line).

If the SF-scenarios holds ($FIR_{AGN} \sim 0$) instead, the quasars are expected to follow the standard correlation (solid line). Since even the more sensitive upper limit (PG0838) on FIR/HCN does not exclude any range of the expected FIR/HCN, more sensitive HCN data are needed to better constrain the FIR/HCN ratio in quasars.

Furthermore, the dotted lines in Fig.5.3 are at the borders of the G04-sample. Since a similar scatter is to be expected for QSOs, only a statistically significant sample of HCN-detected quasars could establish the existence of a non-standard FIR/HCN correlation for quasars.

5.4.3 Size scales of the emitting region

In this section I present a simple black body approach to derive an order-of-magnitude size of the dust distribution, emitting the infrared radiation in the quasar hosts. I assume a thermal origin of the observed infrared radiation of the quasars hosts, justified by the fact, that it is mostly reprocessed UV/optical light of the massive stars and the AGN.

Basis of the following calculations is the assumption, that the emitting dust heated by star bursts or the AGN, is distributed spherically symmetric. Most star-bursts are located in the inner ~ 1 kpc of a galaxy (Carroll & Ostlie 1996, Chapter 24). This radius can be regarded as upper limit on R_e, especially if the dust is primarily heated by an AGN. R_e constitutes a reasonable size scale of the IR emitting region, although a significant deviation from the assumed symmetry would result in a larger average distance between the radiating dust and the center of the galaxy.
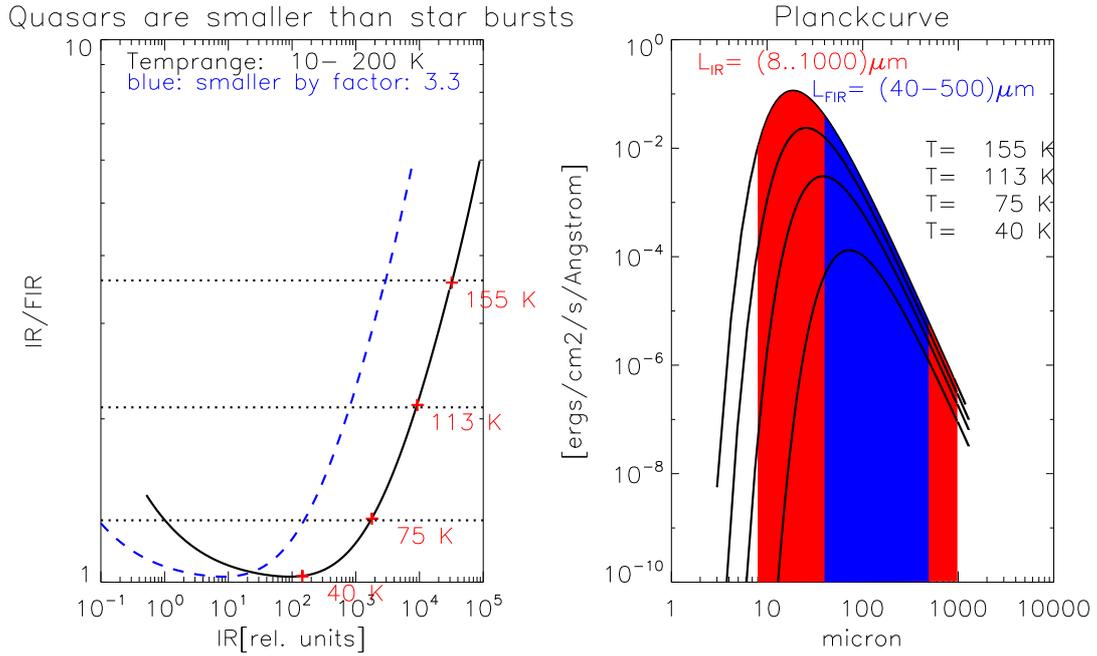
Figure 5.4: Left panel: The IR/FIR luminosity of spherical black body is plotted. Four temperatures of the black body spectrum are indicated. Above 40 K the ratio defines unambiguously the temperature. The blue dashed line is similar with a reduced radius of the emitting surface with respect to the black solid line. The ratio of both radii is indicated in the top of the figure. Certain ratios and temperatures, discussed in the text, are highlighted. Right panel: The black body flux at the surface of the emitting region is given for the respective temperatures. The IR and FIR bandwidths are indicated. If the temperature is know from the IR/FIR ratio, the radius of a spherical emitting region can be estimated if the flux is distance to the source is known.

Also if the distance to the quasar is known, $R_{\rm e}$ cannot be directly derived from the observed fluxes, since the spectral black body luminosity L_λ of a radiating sphere depends on both the temperature and the size (e.g. Carroll & Ostlie 1996, Chapter 3)

$$L_\lambda \, d\lambda = \underbrace{4\,\pi\,R_{\rm e}^2}_{surface} \cdot \underbrace{\pi}_{intensity \to flux} \cdot \underbrace{\frac{2\,h\,c^2}{\lambda^5 \left(e^{\frac{h\,c}{\lambda\,k\,T}} - 1\right)}}_{B_\lambda(T)} \, . \tag{5.1}$$

with $B_\lambda(T)$ being the Planck formula for the intensity of a black body radiation field which has to be multiplied by π to yield the respective flux density. Conventionally h, c, and k, denote Planck's constant, the speed of light and Boltzmann's constant, respectively.

But Fig. 5.4 demonstrates, that the IR/FIR ratio, discussed in the previous section can be used to derive unambiguously the average dust temperature $T_{\rm d}$, if it is above ~ 35 K, which is reasonable for star-forming and active infrared bright galaxies. The dotted lines in the left panel of Fig. 5.4 give the ratios of 1.3 (average of the star-burst galaxies), 2.1 and 3.6, the latter being the measured ratios of PG0838 and PG1415, respectively. The respective temperatures are also given in the plot.

As a primary result, this calculation shows that normal, star-burst and low-luminosity AGN have similar average thermal dust temperatures around (75±15) K. Only the AGN dominated quasar hosts show significantly hotter dust temperatures above 100 K. Furthermore, as indicated by the

blue dashed line, an increased IR/FIR ratio, without an increased infrared luminosity requires a decrease in size. E.g. R_e for an average QSO IR/FIR=3 is about a third of the respective R_e of a star-burst galaxy with IR/FIR=1.3, but of similar infrared luminosity. That is, the dust in quasar hosts appears to be significantly more concentrated.

The linear R_e can be calculated from the infrared luminosities as:

$$R_e(T) = \sqrt{\frac{L_{\mathrm{IR}}}{4\,\pi} \cdot \frac{1}{\int_8^{1000} \pi\, B_\lambda(T)\, d\lambda}} = \sqrt{\frac{L_{\mathrm{FIR}}}{4\,\pi} \cdot \frac{1}{\int_{40}^{500} \pi\, B_\lambda(T)\, d\lambda}} \qquad (5.2)$$

$$\hookrightarrow R_e(PG0838) = 33\ pc; \quad R_e(PG1415) = 16\ pc\,.$$

As mentioned before, the resulting radii are lower limits and match only the reality, if indeed the radiating dust is smoothly distributed over a sphere.

5.5   Conclusions

I present firm upper limits on the HCN (J=1-0) rotational line emission of the host galaxies of two optically selected nearby standard QSO hosts from the PG sample. The derived upper limits on the global HCN-CO ratios of $\lesssim 0.4$ cannot rule out significant direct HCN excitation by the AGN in XDRs in the observed hosts.

Furthermore, I put the HCN upper limits in the context of previous statistical studies, investigating the molecular gas and IR properties of nearby spiral, SB and low-luminosity active galaxies. I propose to derive a significant AGN-contribution to the total infrared luminosity of a galaxy from an IR/FIR ratio significantly larger than 1.3 (as found in the observed quasars).

My limits on FIR/HCN are consistent with the standard $L_{\mathrm{FIR}} - L_{\mathrm{HCN}}$ correlation of quiescent and SB galaxies, as well as with hypothetic correlations for AGN-dominated FIR to HCN in QSO hosts. In this chapter I show that proving the existence of a HCN-FIR correlation in evolved quasar hosts is within observational reach.

The IR/FIR ratio was transformed to an average dust temperature applying a black body approach. This leads to dust temperatures of about 75 K for all considered infrared bright galaxies, independent of the infrared luminosity. Only strongly dominated AGN hosts show a significantly increased dust temperature and therefore smaller sizes of the emission region with respect to similarly luminous star-burst galaxies. The effective radius R_e gives a lower limit on the size of the infrared emitting region. I calculate radii of 16 pc and 33 pc for the observed QSO host galaxies.

Chapter 6

Relativistic jet motion in the core of the radio-loud quasar J1101+7225 (Vol.2)

This chapter deals with the properties of the relativistic radio jet in a quasar. The presented results continue an initial investigation presented in my Diploma thesis (Pott 2003). In order to avoid significant duplication of information, I only briefly introduce to the topic here. For more details I refer to the Diploma thesis. The final results presented are published in a peer-reviewed journal (Pott et al. 2005b).

Quasars or QSOs are the high-luminosity counterpart of the AGN phenomenon. Radio jets in quasars often extend far into the host galaxy and show a direct physical outflow connection from the AGN to its host. A part of the molecular gas of the quasar host, studied in the previous chapter of this thesis, is thought to represent a host-AGN connection in the other direction. The innermost and densest molecular gas in AGN represents the fuel for the accretion onto the central SMBH, which finally accounts for the huge optical-UV quasar luminosity. The radio jet outflow is necessary to fulfill the laws of conservation of energy, because it can remove a significant amount of kinetic energy and angular momentum from the innermost accretion region. Only if the kinetic energy is lost, the remaining matter can finally surpass the event horizon of the accreting black hole.

My cm-VLBI data traces out-flowing knots as far as $\sim$ 8 kpc from the center, while lower resolved VLA[1] observations reach even further (Xu et al. 1995). Analysis of the (relativistic) kinematics of non-thermal radio sources gives important physical insight into the inmost regions of an active galactic nucleus (AGN). The ejection of radio jet components and the jet kinematics are most probably related to the process of accretion onto the nucleus itself. Quantitative estimates of physical properties, such as magnetic fields and source sizes, can be derived, too. In the Diploma thesis I presented a first analysis of a 1.66 GHz EVN[2] dataset and the spatially unresolved spectral energy distribution of the quasar J1101+7225. Now I will discuss multi-wavelength, multi-epoch VLBI data including a new reduction of the EVN data. Further the final results on the jet geometry and kinematics are given. A partial overlap with the respective sections in my diploma thesis could not be avoided.

---

[1]**Very Large Array** is a local radio interferometer offering an angular resolution of up to 40 mas at 43 GHz; `http://www.vla.nrao.edu`

[2]**European VLBI Network**; `http://www.evlbi.org`

6.1   The source

Table 6.1: General properties of J1101+7225.

property	value	reference
IAU ^{a} / other name:	J1101+7225 / [HB89] 1058+726	
R.A. (J2000)	11h 01m (48.8054 ± 0.0001)s	B02
Decl. (J2000)	$+72°25'(37.1183 \pm 0.6 \cdot 10^{-3})$''	B02
redshift	1.46	Jackson & Browne (1991)
abs. magnitude	-27.3 mag$\approx 10^{46.4}$ erg s^{-1}	Véron-Cetty & Véron (2001)
1.4 GHz radio cont	(1451 ± 30) mJy	White & Becker (1992)

^{a}International Astronomical Union

The radio-loud quasar J1101+7225 is a source of the Very Long Baseline Array (VLBA) Calibrator Survey VCS1 for phase-referencing observations (Beasley et al. 2002,in the following B02). I observed this source as a calibrator source within a larger experiment, that was focused on imaging faint Seyfert galaxies of the NUGA project. It turned out that J1101+7225 shows a complex source structure, which makes it physically interesting but, on the other hand, also less suitable as a calibrator. So far very little information is available for individual sources of the VCS1.

My analysis of the outer jet kinematics is based on the comparison of the new 1.66 GHz Very Long Baseline Interferometry (VLBI) map from the data obtained in 2002 with the available maps of past observations (a 1.66 GHz map by Thakkar et al. 1995, in the following T95, and a 2.3 GHz map by B02). Further data from a multi-epoch study at 5 GHz of the central 5 mas of J1101+7225 were used to determine the source structure of the central region, unresolved at lower observing frequencies.

In Table 6.1 the general properties of J1101+7225 are summarized to introduce the quasar. B02 estimated the position of J1101+7225 with (sub)mas-accuracy (Table 6.1), which is necessary for high-sensitivity phase-referencing experiments. In Sect. 6.2 details are given concerning the VLBI observations that are the basis for this work. Flux densities, the resulting maps, and a kinematical analysis of the mapped structure are presented in Sect. 6.3.1. Finally the results are discussed and summarized in Sect. 6.4.

6.2   Observations

Table 6.2: Details of the observing schedule of the EVN observation with eight antennae of J1101+7225.

date of observation	obs. frequency	bit rate & type of samp.
13 Feb 2002	1630.49MHz	256 Mbps & 2 bit
No. & bandwidth of IF	polarization	system and correlator:
4 DSB-IFs & 16 MHz	LCP	MKIV at MPIfR, Bonn

The observations were conducted during the period 13-14 Feb 2002, 21h-09h UT, while the scans of J1101+7225 typically lasted for three minutes at a total observing time of 1.6 h. This project was observed at 18 cm with the 100m antenna of the Max-Planck Institut für Radioastronomie (MPIfR) at Effelsberg, Germany, the 76m antenna at Jodrell Bank, UK, the 32m antenna at Medicina,

Italy, the 25m antenna at Onsala, Sweden, the 25m antennae at Shanghai and Urumqi, China, the 32m antenna at Torun, Poland, and the 14x25m antenna array at Westerbork, the Netherlands. Details concerning the observing mode are given in Table 6.2. After the observations, the data were correlated at the VLBI correlator of the MPIfR in Bonn, Germany, and imported into the Astronomical Image Processing System (AIPS) via the MK4IN program (Alef & Graham 2002). The data were fringe-fitted and calibrated in a standard manner with the AIPS package and imaged using the DIFMAP VLBI package (Pearson et al. 1994).

Further I use 5 GHz VLBI maps of J1101+7225, obtained in VLBA and global VLBI observations as part of a multi-epoch VLBI study (the Caltech-Jodrell Bank flat-spectrum sample CJF Taylor et al. 1996; Britzen 2002). These observations aimed at a statistical investigation of the kinematics of a complete sample of AGN (Britzen 2002,Britzen et al. in prep.). The sources were observed in 5.5 minute snapshot observations to determine the position and motion of jet components in the central 5 mas. The data were recorded over 32 MHz total bandwidth broken up into 4 baseband channels with 1-bit sampling. The recorded data were correlated in Socorro, USA.

In the analysis of Sect. 6.3.2 I include the VLBI-maps of J1101+7225 published earlier to analyze the evolution of the structure found. T95 observed the quasar with global VLBI at 1.66 GHz in the CJ1 survey which later on became a part of the CJF sample. The other map at 2.3 GHz was reduced from VLBA data via automatic imaging using the Caltech DIFMAP package (B02).

6.3 Radio properties of the quasar J1101+7225

6.3.1 Flux densities

The flux density of J1101+7225 has been measured occasionally during the last two decades. In Table 6.3 I summarize the measurements at the various frequencies. Based on these data I calculated the spectrum, shown in Fig. 6.1. The single-dish observations show a curved radio spectrum with a steep spectrum at low MHz frequencies ($\alpha_{\text{single}}^{38-178\,\text{MHz}} \sim -0.8$; $S \sim \nu^{\alpha}$) and considerable flattening towards higher frequencies ($\alpha_{\text{single}}^{1.4-5\,\text{GHz}} \sim -0.4$; $\alpha_{\text{single}}^{5-22\,\text{GHz}} \sim 0$). The spectral trend of the VLA measurements follows the single dish measurements. The slightly flatter shape ($\alpha_{\text{locIF}}^{1.4-8.4\,\text{GHz}} \sim -0.3$) plotted in Fig. 6.1 may overestimate the real spectrum, because only the peak brightness is published at 1.4 GHz.

In contrast with the EVN I measured a core flux density of (396 ± 20) mJy at 1.66 GHz. In combination with the core flux densities obtained at 5 GHz and the lower flux density limits given by the peak brightnesses of B02, this confirms a flat spectral shape (within the scatter due to different observations and epochs) at GHz-frequencies, which is shown as a dotted line in Fig. 6.1. These findings indicate that the continuous flattening of the single-dish spectrum is evoked by superposition of spectrally steep components, still unresolved with local interferometry but fully resolved and/or separable at VLBI resolution, and by the flat VLBI core, which is still nearly unresolved at the observing frequencies of 1.66 GHz and 2.3 GHz. Konigl (1981) calculated such flat GHz-spectra of compact synchrotron sources, involving optical thickness for the synchrotron radiation due to synchrotron self-absorption. Thus most of the central radio emission of J1101+7225 at these frequencies is emitted by a compact, unresolved core.

A significant fraction (up to 50%) of the single-dish flux density of the whole galaxy is radiated by the inmost region, still unresolved by interferometric observations. Models dealing with *relativistic beaming* explain the extraordinary luminosity of radio-loud cores with unresolved radio-jet

Table 6.3: Measured radio flux densities or peak brightnesses of J1101+7225, obtained with single-dish telescopes, local interferometers, and VLBI. The VLBI flux densities are the fitted core flux densities as presented in Tables 6.4 & 6.7
References and comments: (a) Rees (1990), catalogue revised by Hales et al. (1995); (b) Gower et al. (1967); (c) White & Becker (1992); (d) Kuehr et al. (1981); (e) Gregory et al. (1996); (f) Teräsranta et al. (2001); (g) Xu et al. (1995) gave this peak brightness of a map, which was convolved to a circular beam of 1.5" FWHM; (h) Patnaik et al. (1992) found this peak brightness to be 80% of the total flux density of 436 mJy;
The values are plotted over frequency in Fig. 6.1. For the interferometric observations 5% flux density errors are given.

obs.type	freq. [GHz]	flux dens. [mJy]	
single-dish	0.038	$(1.41 \cdot 10^4 \pm 800)$	(a)
single-dish	0.178	(3900 ± 600)	(b)
single-dish	1.4	(1451 ± 30)	(c)
single-dish	2.7	(1070 ± 35)	(d)
single-dish	5	(858 ± 76)	(e)
single-dish	22	(820 ± 100)	(f)
local interf.	1.4	(748 ± 40)/beam	(g), res $\sim$1.5"
local interf.	8.4	(349 ± 20)/beam	(h), res $\sim$0.2"
VLBI	1.66	(396 ± 20)	EVN Feb 2002
VLBI	2.3	(520 ± 25)/beam	B02, res $\sim$3 mas
VLBI	5	(139 ± 7)	- 1991.4 -
VLBI	5	(282 ± 14)	- 1993.4 -
VLBI	5	(337 ± 17)	- 1996.6 -
VLBI	5	(439 ± 22)	- 1999.9 -
VLBI	8.4	(383 ± 20)/beam	B02, res $\sim$1 mas

components approaching nearly along the line of sight at relativistic velocities (e.g. Blandford & Konigl 1979,and see Sect. 6.3.4). One consequence of these models is a straightforward explanation of variability of the core flux density by small variations in the jet orientation with respect to the observer. This variability is still observable with single-dish observations in case of core-dominated GHz emission. In fact I observed such a core-dominated variability in single-dish radio flux densities at 5 GHz (Pott 2003). The underlying variability of the VLBI core flux density was observed at 5 GHz (Table 6.3) and shows the same minimum at around 1992. Therefore only the later measurements were taken in Fig. 6.1 to approximate the spectral index of the VLBI core. The observed flux density variability of the core component strongly supports the concept of beamed radio emission, which can be confirmed in Sect. 6.3.4.

6.3.2   High apparent superluminal motion outside the central 10 mas

In Fig. 6.2 I present the map made from the EVN observation in February 2002. Clearly two extended regions are visible beside the core with more than 4.8% and 1.2% of the core peak brightness. They are labeled with *A* and *B*, respectively. More information about the underlying source structure can be retrieved by fitting circular and elliptical Gaussians to the visibility data and optimizing the fit to the amplitudes and closure phases (Pearson 1995). The structure in 200 mas distance to the core in N-NE direction could be confirmed neither by applying different taper to the uv data nor by a respective model component. The best model of the source structure
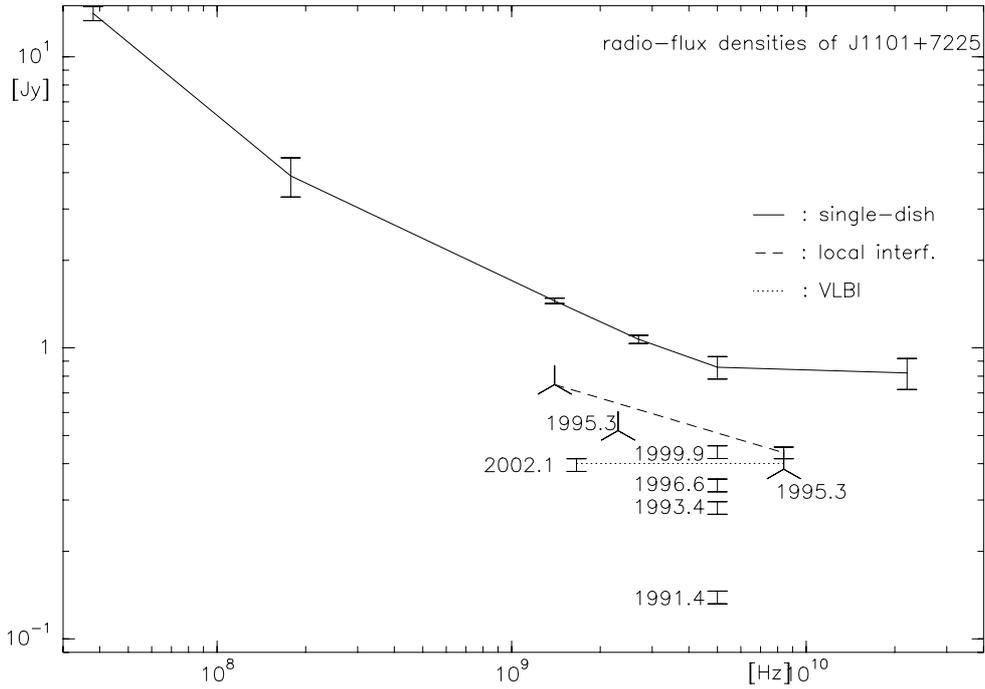
Figure 6.1: The radio spectrum of J1101+7225 at different angular resolutions, corresponding to Table 6.3. All VLBI measurements are labeled with the observing date. While the flux densities are plotted with error bars, the stars indicate peak brightnesses. Because the peak brightnesses may underestimate the flux densities, the corresponding spectra are dotted / dashed (see Sect. 6.3.1, partially presented in Pott (2003)).

Table 6.4: The best-fit Gaussians as mentioned in the text. *a* labels the major axis of elliptical Gaussians. *A*, *B1*, and *B2* were only fitted by circular Gaussians, because the locations of components of lower flux density can be fitted more reliably with less degrees of freedom. The flux density errors are $\sim 5\%$, the uncertainties of the location, and size of the Gaussians range between 0.2-0.5 of the beam size depending on the respective flux density.

	Flux dens.	location		size	
	(mJy)	r (mas)	ϑ (deg)	a (mas)	Axial ratio
Core	396	0	0	2.88	0.41@9.4°
C	149	3.3	14.1	1.83	0.39@-89.4°
A	54	23.3	21.0	3.62	1
B1	16	47.4	17.7	6.22	1
B2	7	62.8	18.5	4.21	1

is given in Table 6.4 and the corresponding map is inserted in Fig. 6.2. The measurement errors on the model parameters flux density, relative position, and source size are given in the respective tables. Their estimation is based on the comparison of different model fits, as described by Gómez & Marscher (2000). A more theoretical approach (Fomalont 1989) based on the dynamic range of the map gives comparable magnitudes.

This analysis shows that the extended *B* component from the cleaned map is a blend of at least two components (*B1*, *B2*). Furthermore within the central 5 mas a significant fraction of the flux density is radiated by an extended source beside the dominating unresolved core at a distance of a few mas to the core (see Sect. 6.3.3). This region close to the limit of resolution of the 1.66 GHz observations is studied in more detail in the next section (6.3.3) at higher frequencies.
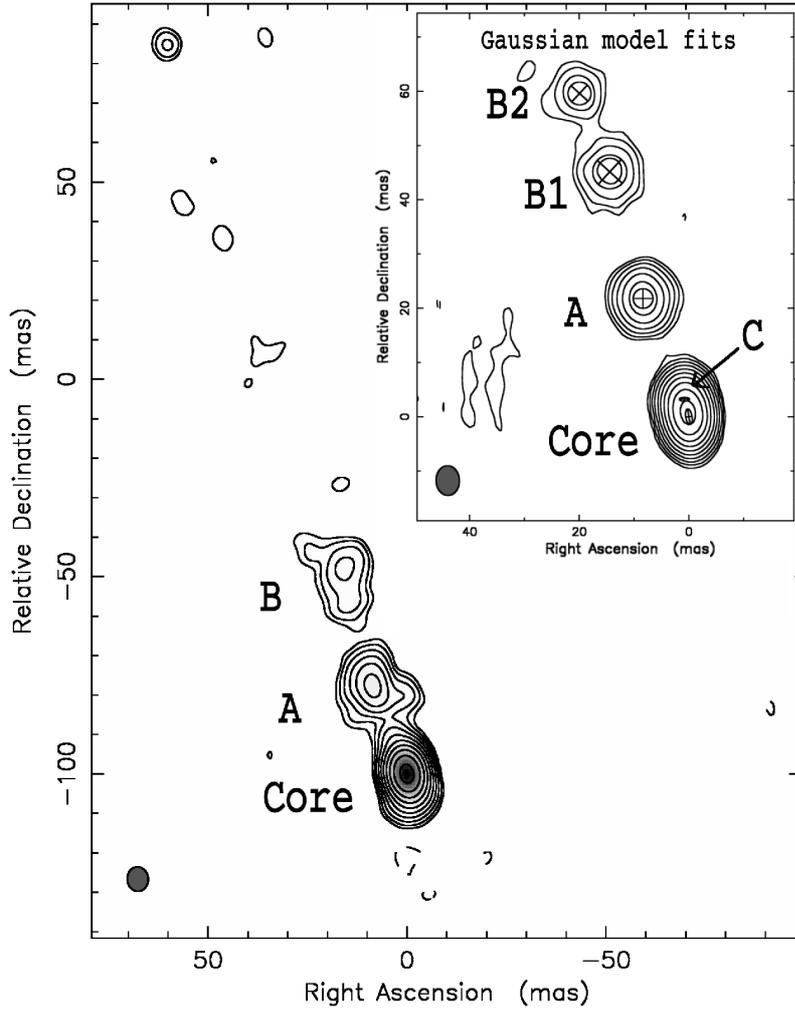
Figure 6.2: Cleaned map of the EVN observation of J1101+7225 at 1.66 GHz. The map shows a peak brightness of 407 mJy/beam. The contour levels are -0.15, 0.15, 0.3, 0.6, 1.2, 2.4, 4.8, 9.6, 19.2, 38.4, 76.8% of the peak brightness, and the beam size is 6.22×5.28 mas at position angle (PA) of 4°. In the upper right corner the Gaussian model fit representation of the VLBI image is given (with the same contour levels, but now with respect to a 399 mJy/beam peak brightness), obtained by fitting Gaussian components to the visibility data (beam: 5.5×4.3 mas at PA 2°). By this technique the extended structure at ∼ 50 mas distance to the core could be clearly resolved into two components.

Table 6.5: The angular distances between the core and the fitted Gaussian jet components (or their flux density weighted mean; cf. text). The errors reflect uncertainties in the fitting process and increase with decreasing component flux density, while derivation of the apparent velocities is described in the text. The position angles of the components did not change significantly during the observing epochs and were omitted. In the last column the read out values from a map by B02 are given for comparison, but cannot be included in the calculations due to lack of a Gaussian model fit.

epoch & freq. [GHz]:	Sep 1991 at 1.66 [T95]	Feb 2002 at 1.66	Apr 1995 at 2.3
components:	Distances in Fig. 6.3 [mas]		Dist. in Fig. 6.3 [mas]
Core-A	(19.6 ± 0.5)	(23.3 ± 0.5)	(21.5 ± 3)
Core-B	(53.7 ± 1)	(52.1 ± 1)	(52 ± 5)
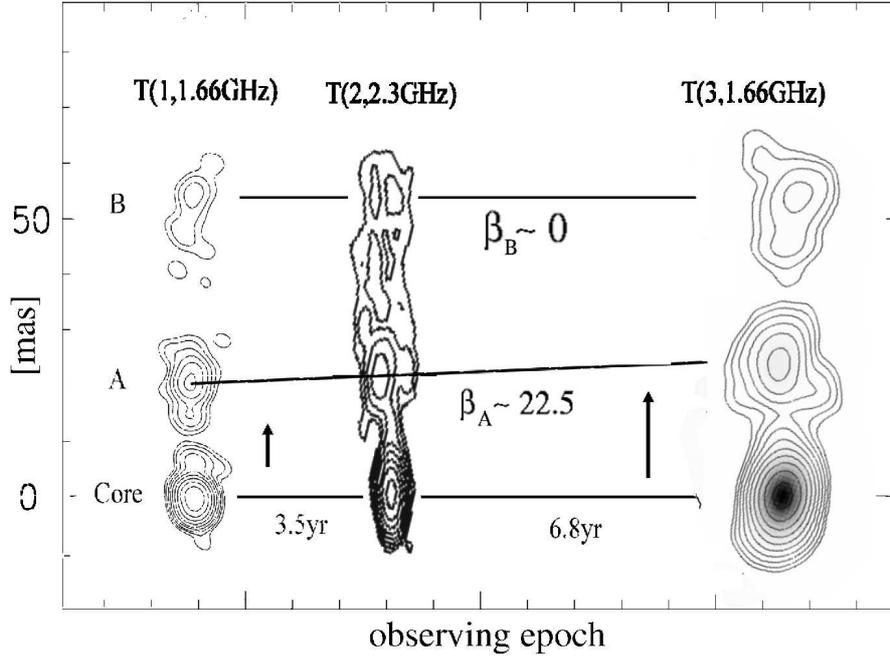
Figure 6.3: The cleaned maps are aligned vertically (rotation about -20°), which is justified by the fact, that no significant change of the position angle of the jet axis was observed. The apparent linear velocities of the fitted Gaussian components (cf. Table 6.5) are given. The first map by T95 at T(1,1.66 GHz) shows a peak brightness of 476 mJy/beam, the contour levels are -2, -1, 1, 2, 4, 8, 16, 32, 63, 127, 253 mJy/beam, and the beam size is 4.2×3.2 mas at PA 90°. The second map by B02 at T(2,2.3 GHz) shows a peak brightness of 520 mJy/beam, the contour levels are -3, 3, 6, 12, 24, 48, 96, 192, 384 mJy/beam, and the beam size is 3.3×6.7 mas at PA 20°. The beam PAs given here refer to the unrotated coordinate system.

Table 6.6: The measured mean apparent transversal angular velocity μ and the respective dimensionless linear velocity β as defined in the text.

components	$\mu[\mathrm{mas\,yr}^{-1}]$	$\beta_{\mathrm{app};h=0.71}$ [a]
Core-A	(0.36 ± 0.07)	(22.5 ± 4)
Core-B	0 [b]	0

[a]For the calculations I used $H_0 = 71^{+4}_{-3}\,\mathrm{km\,s}^{-1}\,\mathrm{Mpc}^{-1}$ and a deceleration parameter $q_0 = 0.1$.

[b]No significant propagation of the *B* component was found with respect to the errors.

T95 detected both *A* and *B*, too. A detailed comparison of my data with the Gaussian component model of T95 reveals a high separation velocity of the *A*-component at an unusually large de-projected distance to the core. In contrast to Table 6.4, T95 were able to fit three elliptical Gaussian components to the region around *A* and one to the *B* region. Because the angular extensions of both regions (*A* and *B*) are close to the limit of resolution, I prefer the *blend* interpretation of this situation. My *A* component does not correspond to *one* of the three fitted components of T95 but does correspond to a flux density-weighted mean of *all* three components; and vice versa, the mean of my *B1* and *B2* components corresponds to the one component of that region fitted by T95 to their visibility data. Although the full width at half maximum (FWHM) of the circular Gaussians *B1* and *B2* (cf. Table 6.4) do not overlap, the modeling process showed that due to their low flux densities, the sizes of the *B* components are insecure up to a factor of two. It is also possible that a third component exists, slightly too weak to be fitted. Thus the used flux density-weighted mean

appears to be the most adequate presentation.

Therefore I determine the apparent motion of the radio jet structures *A* and *B* with respect to the core (Table 6.5), where in case of several fit components the labels refer to the flux density-weighted mean of these. Angular velocities μ are presented in Table 6.5 on the right side. They are confirmed by the snapshot VLBA map at 2.3 GHz of B02 (last column in Table 6.5). I did not directly include these data in the velocity calculation. The introduced uncertainties due to the different observing frequency and the lack of a Gaussian model fit would annihilate the increased calculation accuracy. To demonstrate the apparent angular motion, I show the three VLBI maps in one figure in Fig. 6.3 on a common angular scale and rotated by about $-20\,°$.

The dimensionless linear equivalents β_{app} are calculated via

$$\beta_{\mathrm{app}} = \mu \frac{z}{H_0(1+z)} \left[\frac{1 + \sqrt{1 + 2q_0 z} + z}{1 + \sqrt{1 + 2q_0 z} + q_0 z} \right]$$

(cf. Pearson & Zensus 1987). The measured apparent superluminal *transverse* motion can be transformed via special relativity[3] into a minimal intrinsic velocity, expressed as

$$\beta_{min}^A \approx 0.9990^{+0.0003}_{-0.0005} \ \ at \ \ \vartheta_{min}^A \approx 2.54°\,^{+0.55}_{-0.38}. \tag{6.1}$$

The 22 mas distance to the core at $\vartheta = 2.5°$ can be de-projected to a large linear distance of about $4\,\mathrm{kpc}\,(\mathrm{at}\ z = 1.46,\ q_0 = 0.1)$. It turns out that the uncertainties in the estimation of β_{app} and the Hubble parameter are affecting β_{min}^A by less than 0.1%. The more distant *B*-component was found to be stationary within the errors at a mean angular distance of 52.9 mas.

6.3.3   Resolved structure in the central 10 mas

Table 6.7: The best-fit circular Gaussians of the 5 GHz data over four epochs. The flux density errors are $\sim 5\%$, and the uncertainties of the location and size of the Gaussians range between 0.2-0.5 of the beam size depending on the respective flux density.

epoch		Flux density	location		size
		(mJy)	r (mas)	ϑ (deg)	diam (mas)
1991.4	Core	139	0	0	0.57
	C1	132	1.81	0.2	1.01
	C2	133	3.38	11.3	0.85
1993.4	Core	282	0	0	0.51
	C1	113	2.47	4.9	0.57
	C2	61	3.76	10.7	0.20
1996.6	Core	337	0	0	0.40
	C1	97	2.32	6.0	1.13
	C2	80	3.9	12.0	0.94
1999.9	Core	439	0	0	0.41
	C1	78	2.07	7.8	1.00
	C2	84	3.83	11.1	1.18

---

[3]If ϑ is the angle enclosed by the line of sight and the direction of motion and if β is the intrinsic velocity, one finds $\beta_{\mathrm{app}} = \frac{\beta\,\sin\vartheta}{1 - \beta\,\cos\vartheta}$. The minimal intrinsic velocity $\beta_{\mathrm{min}} = \sqrt{(\beta_{\mathrm{app}}^2)/(1 + \beta_{\mathrm{app}}^2)}$ implies an angle ϑ_{min} fulfilling: $\cot(\vartheta_{\mathrm{min}}) = \beta_{\mathrm{app}}$.
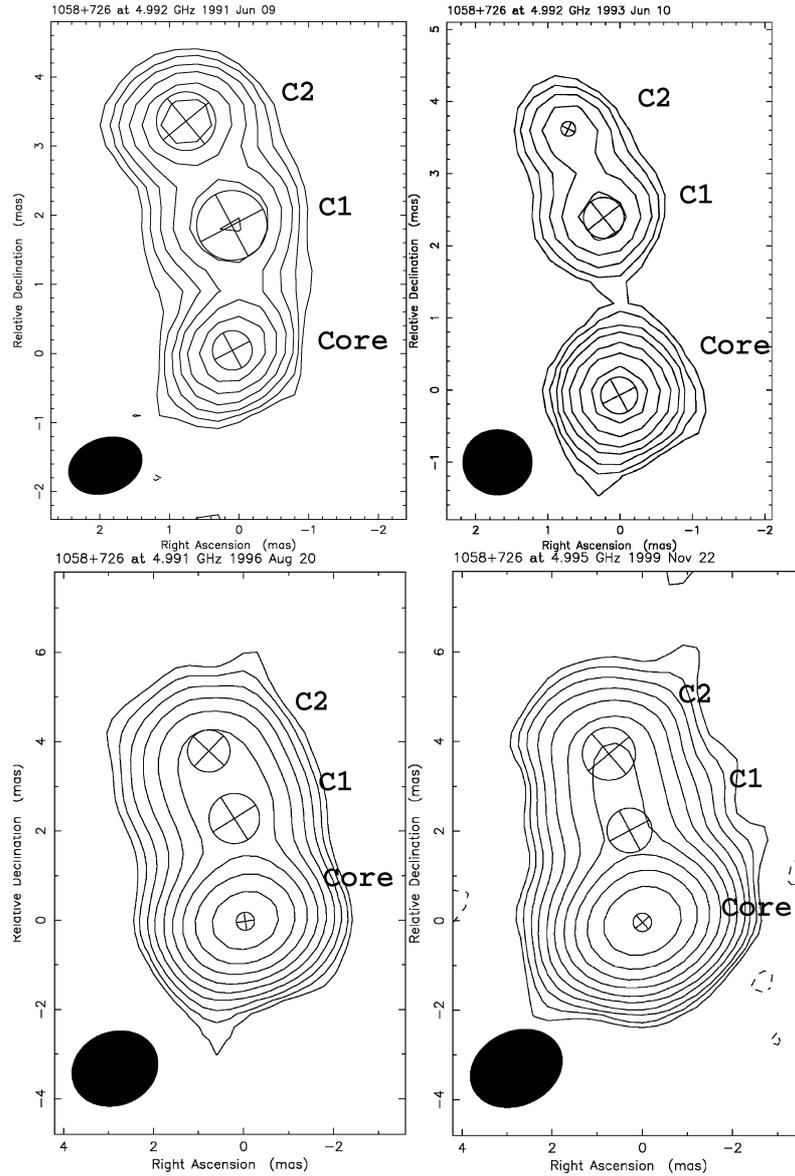
Figure 6.4: 5 GHz maps of the central 5 mas. The details of the individual epochs are given in the sequence: peak brightness; contour levels in %; beam size. First epoch: 0.097 mJy/beam; levels are -8, 8, 12, 18, 27, 40.5, 60.8 %; beam: 1.08×0.79 mas at PA -70°. Second epoch: 0.209 mJy/beam; levels are 6, 9, 13.5, 20.3, 30.4, 45.6, 68.3 %; beam: 0.96×0.90 mas at PA -90°. Third epoch: 0.314 mJy/beam; levels are 1.6, 2.56, 4.1, 6.55, 10.5, 16.8, 26.8, 42.9, 68.7, %; beam: 1.95×1.64 mas at PA -67°. Fourth epoch: 0.417 mJy/beam; levels are -0.9, 0.9, 1.44, 2.3, 3.69, 5.9, 9.44, 15.1, 24.2, 38.7, 61.8 %; beam: 2.11×1.64 mas at PA -65°. Crosses indicate the positions of circular Gaussian model fit components. The detailed model parameters are presented in Table 6.7.

The higher-resolution maps of the 5 GHz snapshots are presented in Fig. 6.4. They explicitly show that the *Core* region of the 1.66 GHz map is not totally compact on the 1 mas scale of the 5 GHz observations. Extended Gaussian components could be fitted to the data beside the dominant[4] central source. This was already suggested by the C-component, fitted to the 1.66 GHz data (Table 6.4), and it confirms the power of the model fits in analyzing the data.

---

[4]e.g. at the last epoch the extended components show flux densities of 20% of the central flux density
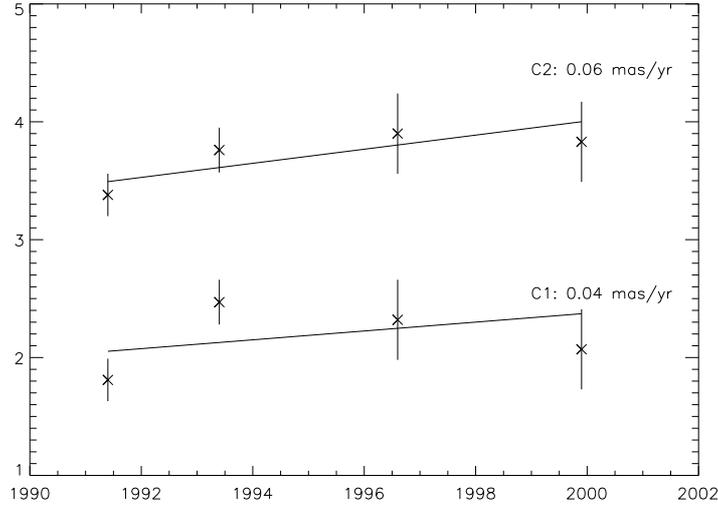
Figure 6.5: Evolving core-distance (in mas) of the best-fit Gaussians, taken from Table 6.7 over the years. A least-squares fit of a linear time-dependence is shown with respect to the error-bars. The standard deviation of the resulting apparent separation velocities is $\sigma \approx 0.04 \text{mas yr}^{-1}$.

The fitted Gaussian components are shown in Table 6.7. A linear fit of the core-distance with respect to the observing epochs (Fig. 6.5) demonstrates the apparently superluminal motion of both components and shows mean separation velocities of

$$\beta_{app}^{C1} \approx (2.5 \pm 2.5) \quad \text{and} \quad \beta_{app}^{C2} \approx (3.7 \pm 2.5)\,. \tag{6.2}$$

The given standard deviations of the fitted velocities are relatively large due to the few available data points. Because a significant intrinsic acceleration of the jet material is very unlikely from the 4 mas regime of the inner *C*-components toward the 20 mas regime far away from the central engine, I adopt the $\beta_{\min}^{A} \approx 0.999$ from Eq. 6.1 as the intrinsic separation velocity also for the inner jet components. From the observed apparent separation velocities of *C1* and *C2* one uses the equations of special relativity[3] to calculate *two* possible jet orientation angles $\vartheta_{s,l}$ to the line-of-sight for each component (with $\beta_{\min}^{A} = 0.999_{-0.0005}^{+0.0003}$)

$$\beta_{app}^{C1} \approx (2.5 \pm 2.5): \quad \vartheta_{s}^{C1} \in [0°, 0.45°], \quad \vartheta_{l}^{C1} \in [22°, 180°]$$
$$\text{and} \quad \beta_{app}^{C2} \approx (3.7 \pm 2.5): \quad \vartheta_{s}^{C2} \in [0.06°, 0.56°], \quad \vartheta_{l}^{C2} \in [18°, 80°]\,. \tag{6.3}$$

The uncertainty of $\beta_{app}^{C1,2}$ dominates the errors of Eq. 6.3. For both components the calculated orientations differ significantly from $\vartheta_{\min}^{A} \approx (2.54_{-0.38}^{+0.55})°$ of Eq. 6.1.

A closer look at the model fits in Table 6.7 reveals some trends over the observing epochs. The separation motion seems to decrease at later epochs in correlation with a decrease in the respective component brightnesses and an increasing position angle of *C1* from 0.2° to 7.8° over the four epochs. With the given, relatively poor time-resolution of four observations within eight years it is not possible to fit these trends reliably. Nevertheless in combination with the different calculated angles in Eq. 6.1&6.3, they can be interpreted as indications of a spatially curved jet structure. Different line-of-sight orientations account for different brightnesses, position angles, and apparent separation velocities.

Table 6.8: The radio values characterize the compact core at 5 GHz as discussed in Sect. 6.3.4. The turn-over properties are mean values of the model fits in Table 6.7. The cut-off frequency ν_2 of the synchrotron spectrum is extrapolated from the optical-radio spectrum. The right column gives the calculated values. [a] From Fiore et al. (2001, 5 keV) and (Brinkmann et al. 1997,1 keV).

radio	X-ray	results
$S_{\mathrm{m}}@\nu_{\mathrm{m}};\ \nu_2$	$\alpha_{\mathrm{X}}^{(1\mathrm{keV};5\mathrm{keV})\ a)}$	Doppler factor
$300\pm15\mathrm{mJy}@5\,\mathrm{GHz};\ 2\,\mathrm{THz}$	-0.5 ± 0.2	$\delta = 0.5^{+1.8}_{-0.3}$
$\theta_{\mathrm{m}}^{\mathrm{circ}}$	$S_{\mathrm{obs}}^{\mathrm{X}}(1\mathrm{keV})\ ^{a)}$	magnetic field B_0
(0.9 ± 0.45) mas	$0.1\mu\mathrm{Jy}$	$(0.15^{+0.2}_{-0.12})\mathrm{G}$

The core flux density has strongly increased over the four epochs, which suggests that over the later epochs either a new jet component has emerged from the compact core region or the unresolved jet has changed its orientation with respect to the line of sight. During the fitting process I found indications that indeed a third component in sub-mas distance to the core is hidden; but probably due to its proximity to the core, this new component could not be fitted separately without doubts.

On the other hand, the increased brightness of the core at the later epochs may affect uncertainties in the model fitting process of the close *C* components. The values of one fifth of the beam size (cf. caption of Table 6.7 and discussion in Sect. 6.3.2), which are used for the linear fit in Fig. 6.5, may still slightly underestimate the real errors due to increased over-blending of the *C* components by the close core radiation. Because this effect is not quantifiable with my data, I kept using these errors.

The idea of a jet curvature over the observed core-distances does not rule out a ballistic situation at the origin of the jet, as was described recently by Stirling et al. (2003). As origin of the radio jet in BL Lacertae they found a 'precessing nozzle' which ejects the single components along straight trajectories. But outside 2 mas (corresponding to 0.4 mas at the redshift of J1101+7225) these trajectories became curved as well.

Summarizing the motion of all detected jet components including *A* and *B*, the situation resembles the different measured apparent component speeds of the radio jet of the S5 quasar 0836+710 which extends over more than 150 mas at $z \sim 2.17$ (Hummel et al. 1992) and where no systematic correlation between the component speed and its distance to the core seems to be present (Otterbein et al. 1998,and references therein).

6.3.4 Indirect estimation of relativistic bulk motion in the core

The VLBI-data of J1101+7225 allow, in combination with published data at other wavelengths, a straightforward analysis of the observed VLBI core flux density by applying a *relativistic beaming* model. The crucial idea of such models is that due to *relativistic* bulk motion of the sources, the radiation is amplified or attenuated significantly in the rest-frame of the observer, depending on the direction of motion with respect to the line of sight. Of course the bulk motion cannot be observed directly due to the lack of spatial resolution. But I share the common assumption that the X-ray emission of the core consists mainly of synchrotron photons scattered to shorter wavelengths via the inverse Compton effect. Marscher (1983) quantitatively derived the connection between radio and X-ray flux densities, their spectral indices, and the Doppler factor[5] δ for a homogeneous source of spherical shape. This implies that δ can be estimated from the other *measured* values.

---

[5]With the terms of footnote 3 it is $\delta = (\gamma (1 - \beta \cos \vartheta))^{-1}$ with $\gamma = 1/\sqrt{1 - \beta^2}$

The ingoing values of the calculations are given in Table 6.8. The notation of the radio properties follows Marscher (1983). Typically the unresolved core consists of several components each of which dominates the unresolved spectrum at a different frequency (e.g. Marscher 1988). Therefore I can assume that the measured properties at 5 GHz describe the *turn-over point* (index *m*) of one underlying source component and that the formulae can be applied for that component. The X-ray measurements were taken independently in the 1990s. Therefore a mean of the different 5 GHz measurements is the most appropriate way to combine both datasets.

The mean measured Gaussian source size is transformed into θ^{circ} assuming an underlying circular source shape (see Marscher 1983,and Table 6.8). The angular source size should be understood as an order of magnitude estimate[6]. Further I can use only the measured peak flux density S_{m} in contrast to the extrapolated one as foreseen by Marscher (1983). This results in a slight underestimation of δ. The calculations lead to $\delta = (0.5^{+1.8}_{-0.3})$ and a magnetic field strength of $B_0=(0.15^{+0.2}_{-0.12})$ G of the unresolved synchrotron-self absorbed source (cf. Table 6.8).

However further radio components, peaking at higher frequencies, and other processes than inverse Compton scattering may contribute to the observed X-ray flux densities. This results in a probable underestimation of δ and B_0. In fact a flat to inverted spectral index as indicator for several components is suggested by the VCS1 map at 8.4 GHz (B02). Although the lack of a detailed model fit inhibits reproducible calculations, visual inspection of the map reveals a dominating core, probably unresolved. Under the latter assumption the given peak brightness resembles the flux density of the component in mid 1995, which is slightly larger than the respective values of the 5 GHz experiment at that time (cf. Fig. 6.1).

With the angular source size and the Doppler factor, the intrinsic brightness temperature can be calculated as

$$T_{intr} = T_{app}/\delta = (2.8^{+0.5}_{-0.2} \cdot 10^{11}\,\mathrm{K})\,. \tag{6.4}$$

These values fit well in the range of brightness temperature in which the simultaneously observed synchrotron emission and the inverse Compton-scattering are both effective enough to fulfill the *inverse Compton* scenario adopted here ($2 \cdot 10^{11}$ K $\leq T_{\mathrm{IC}} \leq 10^{12}$ K; Kraus (e.g. 1986); Bloom & Marscher (e.g. 1991)). Without applying a Doppler factor the *apparent* brightness temperature at 5 GHz rises from 0.5-$3.1\cdot10^{11}$ K over the four epochs. Both this strong rise and the fact that the earlier estimates are below the lower inverse Compton limit can be interpreted as indicators of relativistic beaming.

Furthermore I calculate the equipartition Doppler factor δ_{equ} following Readhead (1994) and Guijosa & Daly (1996), which implies that the radiating particles have the same energy as the penetrating magnetic field. The result (assuming as above $h = 0.71$)

$$\delta_{equ} = (0.5^{+2.6}_{-0.3}) \tag{6.5}$$

is very similar to the inverse-Compton Doppler factor (Table 6.8). This supports Readhead's conclusion that many powerful, non-thermal extragalactic radio sources are close to energy equipartition and their finding that the brightness temperatures of the respective sources range far below the maximum brightness temperature of 10^{12} K (see above).

As in the previous section, I now assume that the intrinsic velocities along the jet are equal to the highest minimal intrinsic velocity, as given by the apparent separation speeds. Then the angle

---

[6]If much more (spectral and multi-epoch) data are available as e.g. in the case of the quasar 3C 345, inhomogeneities in the particle number density can also be estimated. Lobanov & Zensus (1999) used more detailed analyses to explain the observed flux density variations with time of 3C 345 quantitatively.

between the direction of motion and the line of sight can be estimated from the Doppler factor

$$\delta_{core} = (0.5^{+1.8}_{-0.3}); \beta^A_{min} \approx (0.999^{+0.0003}_{-0.0005}) \rightarrow \vartheta_{core} \approx (24^{+19}_{-14})^\circ . \qquad (6.6)$$

Thus ϑ_{core} includes only the large angle solutions of Eq. 6.3 and supports the idea of a straight inner jet nozzle as described in Stirling et al. (2003).

6.4 Discussion of the results

Multi-epoch multi-frequency GHz VLBI data of the radio-loud quasar J1101+7225 were analyzed to estimate the proper motion of extended optically thin, non-thermal radio jet components. I reanalyzed the 1.66 GHz data presented elsewhere and investigated the inner jet components, observable with VLBI at 5 GHz for the first time. I calculated the apparent motions of the two extended components, observable at low GHz-frequencies from VLBI-measurements. I found an apparent superluminal separation speed of $\beta_{app}(Core - A) = (22.5 \pm 4)$ for the A-component over the past decade at an exceptionally large de-projected distance to the core ($22\,\text{mas} \sim 4\,\text{kpc}$). Typically in other quasars such high separation velocities are only found much closer to the core component. The even more distant B-component was found to be stationary within the errors at a core-distance of $\sim 53\,\text{mas}$.

Furthermore a Doppler factor $\delta = (0.5^{+1.8}_{-0.3})$ was estimated for the compact optically thick (at the observing frequencies) synchrotron radiation of the core of J1101+7225. The strength of the magnetic field, which is necessary for the synchrotron process, was estimated to be $B_0 = (0.15^{+0.2}_{-0.12})$ G. The estimated size of the optically thick nuclear component is close to the resolution limit of an interferometric observation at cm-wavelengths, which suggests that – in combination with the estimated Doppler factor and intrinsic jet velocities – additional VLBI-components could appear outside the core in the future.

More observations of these nuclear components might reveal if a deceleration of the A-component appears while A is approaching the B-component. This would be similar to the well known case of 4C 39.25 (Alberdi et al. 1993a). Deceleration at these distances from the core can confirm an interaction of the jet component with the circumnuclear matter of the host galaxy as described by Taylor et al. (1989) for Seyfert nuclei. Such an interaction is strongly supported by comparing the VLBI maps presented here with the jet geometry as observed with the VLA (Xu et al. 1995). In their 1.4 GHz map two corresponding radio jets appear, extending along $\sim 5''$ from the core. While the southwestern jet extends in the opposite direction of the VLBI jet, the northeastern VLA-jet does *not* coincide with the position angle of the VLBI structure. Instead it appears to be bent towards a northwesterly direction, perhaps induced by ram pressure of the surrounding material.

Apparent superluminal velocities are explained by motion towards the observer at relativistic velocity. The additionally presented 5 GHz maps and Gaussian model fits of the central 5 mas show further jet components with significantly smaller apparent velocities. Thus the separation velocities of the different VLBI radio jet components of J1101+7225 show no simple correlation with their distance to the core. But this does *not* rule out a constant intrinsic velocity, because already small variations of the angle between jet and the line of sight can introduce variations of the apparent speeds of the observed order of magnitude. In the case of such a constant intrinsic velocity along the whole jet, the very high velocity, derived from the A-component, has to be chosen. Such high intrinsic velocities explain both the large extension of the radio jet over several arcsec as estimated with the VLA and the high luminosity of the core.

I believe that the findings may indicate a helical bending of the jet, where the fast components are moving in a section that is curved towards the observer. This is supported by the estimated differing jet orientations with respect to the line of sight. Zensus et al. (1995) could explain the acceleration of a jet component of 3C 345 by a curved jet of constant intrinsic bulk velocity. It has been shown that helical jet patterns result from Kelvin-Helmholtz and current-driven jet instabilities in relativistic flows (Birkinshaw 1991; Istomin & Pariev 1996).

Beside this interpretation of the observed motion as an intrinsic bulk motion of the radiating plasma, shock waves may travel along the jet (Alberdi et al. 1993b). Different component velocities may also be observed if the slower components are *trailing* in the wake of faster ones. This hydrodynamical explanation could be adopted successfully to the complex component motion in the radio jet of the radio galaxy 3C 120 (Gómez et al. 2001). Hardee et al. (2001) found mechanisms to produce differentially moving and stationary features in a jet by analyzing the relativistic hydrodynamic equations.

J1101+7225 turned out to be a standard quasar for studying different aspects of radio jet kinematics out to kpc-scales. The nuclear region of J1101+7225 provides the rare possibility of observing the total range of jet kinematics including apparent superluminal separation velocities even far out of the central parsec-region. The results presented here can give observational constraints far from the jet origin for numerical jet models.

Bibliography

Alberdi, A., Krichbaum, T. P., Marcaide, J. M., et al. 1993a, A&A, 271, 93

Alberdi, A., Marcaide, J. M., Marscher, A. P., et al. 1993b, ApJ, 402, 160

Alef, W. & Graham, D. A. 2002, in Proceedings of the 6th EVN Symposium, ed. E. Ros, R. W. Porcas, A. P. Lobanov, & J. A. Zensus, 31

Alloin, D., Barvainis, R., Gordon, M. A., & Antonucci, R. R. J. 1992, A&A, 265, 429

Alvarez, R., Lançon, A., Plez, B., & Wood, P. R. 2000, A&A, 353, 322

Antonucci, R. R. J. & Miller, J. S. 1985, ApJ, 297, 621

Arsenault, R., Alonso, J., Bonnet, H., et al. 2003, in Adaptive Optical System Technologies II. Edited by Wizinowich, Peter L.; Bonaccini, Domenico. Proceedings of the SPIE, Volume 4839 (2003), 174

Bahcall, J. N., Kirhakos, S., Saxe, D. H., & Schneider, D. P. 1997, ApJ, 479, 642

Beasley, A. J., Gordon, D., Peck, A. B., et al. 2002, ApJS, 141, 13

Becklin, E. E., Matthews, K., Neugebauer, G., & Willner, S. P. 1978, ApJ, 219, 121

Belitsky, V., Lapkin, I., Monje, R., et al. 2006, in Millimeter and Submillimeter Detectors and Instrumentation for Astronomy III. Edited by Zmuidzinas, Jonas; Holland, Wayne S.; Withington, Stafford; Duncan, William D.. Proceedings of the SPIE, Volume 6275 (2006), 14

Bernstein, R. A., Freedman, W. L., & Madore, B. F. 2002, ApJ, 571, 107

Birkinshaw, M. 1991, The stability of jets (Beams and Jets in Astrophysics), 278

Blandford, R. D. 1995, Nature, 377, 477

Blandford, R. D. & Konigl, A. 1979, ApJ, 232, 34

Bloom, S. D. & Marscher, A. P. 1991, ApJ, 366, 16

Blum, R. D., Depoy, D. L., & Sellgren, K. 1995, ApJ, 441, 603

Blum, R. D., Sellgren, K., & Depoy, D. L. 1996a, ApJ, 470, 864

Blum, R. D., Sellgren, K., & Depoy, D. L. 1996b, AJ, 112, 1988

Born, M. & Wolf, E., eds. 1999, Principles of optics : electromagnetic theory of propagation, interference and diffraction of light

Brinkmann, W., Yuan, W., & Siebert, J. 1997, A&A, 319, 413

Britzen, S. 2002, Reviews in Modern Astronomy, 15, 199

Burke, B. F. & Graham-Smith, F. 2002, Infrared Astronomy

Carroll, B. W. & Ostlie, D. A. 1996, An introduction to modern astrophysics (Reading, Mass. : Addison-Wesley Pub., c1996)

Chaisson, E. & McMillan, S. 2005, Astronomy Today (Astronomy Today, 5th Edition, by E. Chaisson and S. McMillan. Prentice Hall, 2005. ISBN 0-13-144596-0)

Chiar, J. E. & Tielens, A. G. G. M. 2006, ApJ, 637, 774

Cohen, M., Walker, R. G., Carter, B., et al. 1999, AJ, 117, 1864

Condon, J. J. 1992, ARA&A, 30, 575

Cox, A. N. 2000, Allen's astrophysical quantities (Allen's astrophysical quantities, 4th ed. Publisher: New York: AIP Press; Springer, 2000. Editedy by Arthur N. Cox. ISBN: 0387987460)

Cox, P., Beelen, A., Bertoldi, F., et al. 2005, in The Dusty and Molecular Universe: A Prelude to Herschel and ALMA, 115–120

D'Addario, L. & Holdaway, M. 2000, ALMA Memo # 521, *Joint Distribution of Atmospheric Transparency and Phase Fluctuations at Chajnantor*, accessible at http://www.alma.nrao.edu/memos/html-memos/abstracts/abs521.html.

Domiciano de Souza, A., Kervella, P., Jankov, S., et al. 2003, A&A, 407, L47

Donaldson, R., Bonaccini, D., Brynnel, J., et al. 2000, in Proc. SPIE Vol. 4007, Adaptive Optical Systems Technology, Peter L. Wizinowich; Ed., ed. P. L. Wizinowich, 82–93

Draine, B. T. & Lee, H. M. 1984, ApJ, 285, 89

Draine, B. T. & Lee, H. M. 1987, ApJ, 318, 485

Dutrey, A. 2000, Proceedings from the IRAM Millimeter Interferometry Summer School, accessible at http://www.iram.fr/IRAMFR/IS.

Eckart, A., Baganoff, F. K., Morris, M., et al. 2004a, A&A, 427, 1

Eckart, A. & Genzel, R. 1996, Nature, 383, 415

Eckart, A., Moultaka, J., Viehmann, T., Straubmeier, C., & Mouawad, N. 2004b, ApJ, 602, 760

Eckart, A., Schödel, R., Meyer, L., et al. 2006, A&A, 455, 1

Eckart, A., Schödel, R., & Straubmeier, C. 2005, The black hole at the center of the Milky Way (London:Imperial College Press ; Hackensack, NJ : Distributed by World Scientific Pub. Co., c2005)

Eisenhauer, F., Genzel, R., Alexander, T., et al. 2005, ApJ, 628, 246

Evans, A. S., Frayer, D. T., Surace, J. A., & Sanders, D. B. 2001, AJ, 121, 3285

Fiore, F., Giommi, P., Vignali, C., et al. 2001, MNRAS, 327, 771

Fomalont, E. B. 1989, in ASP Conf. Ser. 6: Synthesis Imaging in Radio Astronomy, ed. R. A. Perley, F. R. Schwab, & A. H. Bridle, 213

Gai, M., Corcione, L., Lattanzi, M. G., et al. 2003, Memorie della Societa Astronomica Italiana, 74, 472

Gao, Y. & Solomon, P. M. 2004, ApJ, 606, 271

García-Burillo, S., Combes, F., Hunt, L. K., et al. 2003, A&A, 407, 485

Genzel, R., Pichon, C., Eckart, A., Gerhard, O. E., & Ott, T. 2000, MNRAS, 317, 348

Genzel, R., Schödel, R., Ott, T., et al. 2003a, Nature, 425, 934

Genzel, R., Schödel, R., Ott, T., et al. 2003b, ApJ, 594, 812

Gerhard, O. 2001, ApJ, 546, L39

Gezari, D. Y., Shu, P., Lamb, G., et al. 1985, ApJ, 299, 1007

Ghez, A. M., Duchêne, G., Matthews, K., et al. 2003, ApJ, 586, L127

Ghez, A. M., Morris, M., Becklin, E. E., Tanner, A., & Kremenek, T. 2000, Nature, 407, 349

Goldschmidt, P., Kukula, M. J., Miller, L., & Dunlop, J. S. 1999, ApJ, 511, 612

Gómez, J.-L. & Marscher, A. P. 2000, ApJ, 530, 245

Gómez, J.-L., Marscher, A. P., Alberdi, A., Jorstad, S. G., & Agudo, I. 2001, ApJ, 561, L161

Gower, J. F. R., Scott, P. F., & Wills, D. 1967, MmRAS, 71, 49

Graves, G. J. M., Challis, P. M., Chevalier, R. A., et al. 2005, ApJ, 629, 944

Gregory, P. C., Scott, W. K., Douglas, K., & Condon, J. J. 1996, ApJS, 103, 427

Guijosa, A. & Daly, R. A. 1996, ApJ, 461, 600

Güsten, R., Nyman, L. Å., Schilke, P., et al. 2006, A&A, 454, L13

Haas, M., Klaas, U., Müller, S. A. H., et al. 2003, A&A, 402, 87

Hales, S. E. G., Waldram, E. M., Rees, N., & Warner, P. J. 1995, MNRAS, 274, 447

Hanner, M. 1988, in Infrared Observations of Comets Halley and Wilson and Properties of the Grains, ed. M. S. Hanner, 22

Hardee, P. E., Hughes, P. A., Rosen, A., & Gomez, E. A. 2001, ApJ, 555, 744

Heckman, T. M., Smith, E. P., Baum, S. A., et al. 1986, ApJ, 311, 526

Helfer, T. T. & Blitz, L. 1995, ApJ, 450, 90

Hummel, C. A., Muxlow, T. W. B., Krichbaum, T. P., et al. 1992, A&A, 266, 93

Istomin, Y. N. & Pariev, V. I. 1996, MNRAS, 281, 1

Ivezic, Z. & Elitzur, M. 1995, ApJ, 445, 415

Ivezic, Z. & Elitzur, M. 1996a, MNRAS, 279, 1019

Ivezic, Z. & Elitzur, M. 1996b, MNRAS, 279, 1011

Ivezic, Z., Nenkova, M., & Elitzur, M. 1999, User Manual for DUSTY, University of Kentucky Internal Report, accessible at `http://www.pa.uky.edu/~moshe/dusty`.

Jackson, N. & Browne, I. W. A. 1991, MNRAS, 250, 414

Jaffe, W., Meisenheimer, K., Röttgering, H. J. A., et al. 2004, Nature, 429, 47

Jaffe, W. J. 2004, in New Frontiers in Stellar Interferometry, Proceedings of SPIE Volume 5491. Edited by Wesley A. Traub. Bellingham, WA: The International Society for Optical Engineering, 2004, ed. W. A. Traub, 715

Jiang, L., Fan, X., Hines, D. C., et al. 2006, AJ, 132, 2127

Kohno, K. 2005, in AIP Conf. Proc. 783: The Evolution of Starbursts, 203

Kohno, K., Ishizuki, S., Matsushita, S., Vila-Vilaró, B., & Kawabe, R. 2003, PASJ, 55, L1

Konigl, A. 1981, ApJ, 243, 700

Kormendy, J. & Gebhardt, K. 2001, in AIP Conf. Proc. 586: 20th Texas Symposium on relativistic astrophysics, ed. J. C. Wheeler & H. Martel, 363

Kormendy, J. & Richstone, D. 1995, ARA&A, 33, 581

Krabbe, A., Genzel, R., Eckart, A., et al. 1995, ApJ, 447, L95

Kraus, J. D. 1986, Radio astronomy (Powell, Ohio: Cygnus-Quasar Books, 1986)

Kuehr, H., Pauliny-Toth, I. I. K., Witzel, A., & Schmidt, J. 1981, AJ, 86, 854

Kurucz, R. 1994, Solar abundance model atmospheres for 0,1,2,4,8 km/s. Kurucz CD-ROM No. 19. Cambridge, Mass.: Smithsonian Astrophysical Observatory, 1994, 19

Kurucz, R. L. 1992, in IAU Symp. 149: The Stellar Populations of Galaxies, ed. B. Barbuy & A. Renzini, 225

Langer, N. & Maeder, A. 1995, A&A, 295, 685

Lawson, P. R., ed. 2000, Principles of Long Baseline Stellar Interferometry

Leinert, C., Graser, U., Richichi, A., et al. 2003, The Messenger, 112, 13

Leinert, C., van Boekel, R., Waters, L. B. F. M., et al. 2004, A&A, 423, 537

Lobanov, A. P. & Zensus, J. A. 1999, ApJ, 521, 509

Lu, J. R., Ghez, A. M., Hornstein, S. D., Morris, M., & Becklin, E. E. 2005, ApJ, 625, L51

Lutz, D. 1999, in ESA SP-427: The Universe as Seen by ISO, ed. P. Cox & M. Kessler, 623

Magorrian, J., Tremaine, S., Richstone, D., et al. 1998, AJ, 115, 2285

Marscher, A. P. 1983, ApJ, 264, 296

Marscher, A. P. 1988, ApJ, 334, 552

Mathis, J. S., Rumpl, W., & Nordsieck, K. H. 1977, ApJ, 217, 425

McConnachie, A. W., Irwin, M. J., Ferguson, A. M. N., et al. 2005, MNRAS, 356, 979

Melia, F. & Falcke, H. 2001, ARA&A, 39, 309

Men'shchikov, A. B., Balega, Y., Blöcker, T., Osterbart, R., & Weigelt, G. 2001, A&A, 368, 497

Moneti, A., Stolovy, S., Blommaert, J. A. D. L., Figer, D. F., & Najarro, F. 2001, A&A, 366, 106

Monnier, J. D. 2000, in Principles of Long Baseline Stellar Interferometry, ed. P. R. Lawson, 203

Morris, M. 1993, ApJ, 408, 496

Moultaka, J., Eckart, A., Viehmann, T., et al. 2004, A&A, 425, 529

Müller, H. S. P., Thorwirth, S., Roth, D. A., & Winnewisser, G. 2001, A&A, 370, L49

Muxlow, T. W. B., Pedlar, A., Holloway, A. J., Gallimore, J. F., & Antonucci, R. R. J. 1996, MNRAS, 278, 854

Najarro, F., Krabbe, A., Genzel, R., et al. 1997, A&A, 325, 700

Netzer, N. & Elitzur, M. 1993, ApJ, 410, 701

Ossenkopf, V., Henning, T., & Mathis, J. S. 1992, A&A, 261, 567

Ott, T., Eckart, A., & Genzel, R. 1999, ApJ, 523, 248

Otterbein, K., Krichbaum, T. P., Kraus, A., et al. 1998, A&A, 334, 489

Papadopoulos, P. P. & Seaquist, E. R. 1999, ApJ, 516, 114

Patnaik, A. R., Browne, I. W. A., Wilkinson, P. N., & Wrobel, J. M. 1992, MNRAS, 254, 655

Paumard, T., Genzel, R., Martins, F., et al. 2006, ApJ, 643, 1011

Pearson, T. J. 1995, in ASP Conf. Ser. 82: Very Long Baseline Interferometry and the VLBA, ed. J. A. Zensus, P. J. Diamond, & P. J. Napier, 268–+

Pearson, T. J., Shepherd, M. C., Taylor, G. B., & Myers, S. T. 1994, Bulletin of the American Astronomical Society, 26, 1318

Pearson, T. J. & Zensus, J. A. 1987, in Superluminal Radio Sources, ed. J. A. Zensus & T. J. Pearson, 1

Peterson, B. M. 1997, An Introduction to Active Galactic Nuclei (Publisher: Cambridge, New York Cambridge University Press, 1997 ISBN 0521473489)

Peterson, D. M., Hummel, C. A., Pauls, T. A., et al. 2006, Nature, 440, 896

Petrov, R. G., Malbet, F., Weigelt, G., et al. 2003, in Interferometry for Optical Astronomy II. Edited by Wesley A. Traub . Proceedings of the SPIE, Volume 4838, (2003), ed. W. A. Traub, 924

Pineau des Forêts, G., Flower, D. R., Aguillon, F., Sidis, V., & Sizun, M. 2001, MNRAS, 323, L7

Planesas, P., Gomez-Gonzalez, J., & Martin-Pintado, J. 1989, A&A, 216, 1

Plez, B., Brett, J. M., & Nordlund, A. 1992, A&A, 256, 551

Pott, J.-U. 2003, Diploma Thesis:
    Nuclei of Active Galaxies - The Cases of NGC 3718 and J1101+7225, available at
    `http://www.ph1.uni-koeln.de/archives/DiplDiss/pott2003.pdf`

Pott, J.-U., Eckart, A., Glindemann, A., et al. 2005a, The Messenger, 119, 43

Pott, J.-U., Eckart, A., Krips, M., et al. 2005b, A&A, 438, 785

Pott, J.-U., Eckart, A., Krips, M., Tacconi-Garman, L. E., & Lindt, E. 2006, A&A, 456, 505

Quirrenbach, A. 2000, in Principles of Long Baseline Stellar Interferometry, ed. P. R. Lawson, 71

Readhead, A. C. S. 1994, ApJ, 426, 51

Rees, N. 1990, MNRAS, 244, 233

Richards, G. T., Strauss, M. A., Fan, X., et al. 2006, AJ, 131, 2766

Rieke, G. H., Rieke, M. J., & Paul, A. E. 1989, ApJ, 336, 752

Rieke, G. H., Telesco, C. M., & Harper, D. A. 1978, ApJ, 220, 556

Roche, P. F. & Aitken, D. K. 1984, MNRAS, 208, 481

Roche, P. F. & Aitken, D. K. 1985, MNRAS, 215, 425

Rohlfs, K. & Wilson, T. L. 1996, Tools of Radio Astronomy (Tools of Radio Astronomy, XVI,
    423 pp. 127 figs., 20 tabs.. Springer-Verlag Berlin Heidelberg New York. Also Astronomy and
    Astrophysics Library)

Rubilar, G. F. & Eckart, A. 2001, A&A, 374, 95

Rybicki, G. B. & Lightman, A. P. 1986, Radiative Processes in Astrophysics (Radiative Pro-
    cesses in Astrophysics, by George B. Rybicki, Alan P. Lightman, pp. 400. ISBN 0-471-82759-
    2. Wiley-VCH , June 1986.)

Sanders, D. B. 2003, Journal of Korean Astronomical Society, 36, 149

Sanders, D. B., Mazzarella, J. M., Kim, D.-C., Surace, J. A., & Soifer, B. T. 2003, AJ, 126, 1607

Sanders, D. B. & Mirabel, I. F. 1996, ARA&A, 34, 749

Sanders, D. B., Phinney, E. S., Neugebauer, G., Soifer, B. T., & Matthews, K. 1990, ApJ, 357,
    291

Sanders, D. B., Soifer, B. T., Elias, J. H., et al. 1988, ApJ, 325, 74

Schödel, R. e. a. 2006a, *The detectability of Sgr A* at 8.6 μm*, in prep.

Schödel, R. e. a. 2006b, *The structure of the nuclear stellar cluster of the Milky
    Way*, submitted to A&A

Schinnerer, E., Eckart, A., Tacconi, L. J., Genzel, R., & Downes, D. 2000, ApJ, 533, 850

Schmidt, M. 1963, Nature, 197, 1040

Schmidt, M. & Green, R. F. 1983, ApJ, 269, 352

Schödel, R., Eckart, A., Iserlohe, C., Genzel, R., & Ott, T. 2005, ApJ, 625, L111

Schödel, R., Ott, T., Genzel, R., et al. 2002, Nature, 419, 694

Schröder, K.-P., Wachter, A., & Winters, J. M. 2003, A&A, 398, 229

Scoville, N. Z., Frayer, D. T., Schinnerer, E., & Christopher, M. 2003a, ApJ, 585, L105

Scoville, N. Z., Stolovy, S. R., Rieke, M., Christopher, M., & Yusef-Zadeh, F. 2003b, ApJ, 594, 294

Smith, C. H., Aitken, D. K., & Roche, P. F. 1990, MNRAS, 246, 1

Solomon, P. M., Downes, D., & Radford, S. J. E. 1992, ApJ, 387, L55

Solomon, P. M. & vanden Bout, P. A. 2005, ARA&A, 43, 677

Sternberg, A., Genzel, R., & Tacconi, L. 1994, ApJ, 436, L131

Stirling, A. M., Cawthorne, T. V., Stevens, J. A., et al. 2003, MNRAS, 341, 405

Surace, J. A., Sanders, D. B., & Evans, A. S. 2001, AJ, 122, 2791

Tacconi, L. J., Genzel, R., Blietz, M., et al. 1994, ApJ, 426, L77

Tanner, A., Figer, D. F., Najarro, F., et al. 2006, ApJ, 641, 891

Tanner, A., Ghez, A. M., Morris, M. R., & Christou, J. C. 2005, ApJ, 624, 742

Tanner, A. M., Ghez, A. M., Morris, M., & Becklin, E. E. 2003, Astronomische Nachrichten Supplement, 324, 597

Taylor, D., Dyson, J. E., Axon, D. J., & Pedlar, A. 1989, MNRAS, 240, 487

Taylor, G. B., Vermeulen, R. C., Readhead, A. C. S., et al. 1996, ApJS, 107, 37

Teräsranta, H., Urpo, S., Wiren, S., & Valtonen, M. 2001, A&A, 368, 431

Thakkar, D. D., Xu, W., Readhead, A. C. S., et al. 1995, ApJS, 98, 33

Thompson, A. R., Moran, J. M., & Swenson, Jr., G. W. 2001, Interferometry and Synthesis in Radio Astronomy (2nd ed. New York : Wiley, c2001, ISBN : 0471254924)

Tubbs, R. N. 2004, in New Frontiers in Stellar Interferometry, Proceedings of SPIE Volume 5491. Edited by Wesley A. Traub. Bellingham, WA: The International Society for Optical Engineering, 2004, ed. W. A. Traub, 1240

Tubbs, R. N., Meisner, J. A., Bakker, E. J., & Albrecht, S. 2004, in New Frontiers in Stellar Interferometry, Proceedings of SPIE Volume 5491. Edited by Wesley A. Traub. Bellingham, WA: The International Society for Optical Engineering, 2004, ed. W. A. Traub, 588

Usero, A., García-Burillo, S., Fuente, A., Martín-Pintado, J., & Rodríguez-Fernández, N. J. 2004, A&A, 419, 897

van Boekel, R. 2004, Ph.D. Thesis

van Boekel, R., Min, M., Leinert, C., et al. 2004, Nature, 432, 479

van Boekel, R., Min, M., Waters, L. B. F. M., et al. 2005, A&A, 437, 189

van der Hucht, K. A. 2001, VizieR Online Data Catalog, 3215, 0

Véron-Cetty, M.-P. & Véron, P. 2001, A&A, 374, 92

Viehmann, T., Eckart, A., Schödel, R., et al. 2005, A&A, 433, 117

Viehmann, T., Eckart, A., Schödel, R., Pott, J.-U., & Moultaka, J. 2006, ApJ, 642, 861

White, R. L. & Becker, R. H. 1992, ApJS, 79, 331

Wilson, A. S. 2003, New Astronomy Review, 47, 417

Witzel, A., Heeschen, D. S., Schalinski, C., & Krichbaum, T. 1986, Mitteilungen der Astronomischen Gesellschaft Hamburg, 65, 239

Woosley, S. E., Heger, A., & Weaver, T. A. 2002, Reviews of Modern Physics, 74, 1015

Xu, W., Readhead, A. C. S., Pearson, T. J., Polatidis, A. G., & Wilkinson, P. N. 1995, ApJS, 99, 297

Zensus, J. A., Cohen, M. H., & Unwin, S. C. 1995, ApJ, 443, 35

Zijlstra, A. A., Matsuura, M., Wood, P. R., et al. 2006, MNRAS, 370, 1961

List of Figures

List of Tables

Glossary

1 $M_\odot$	Solar Mass: 1.989×10^{33} g
1 $L_\odot$	Solar Luminosity: 3.826×10^{33} ergs s^{-1}
1 $R_\odot$	Solar Radius: 6.960×10^{10} cm
1 AU	Astronomical Unit: 1.496×10^{13} cm
1 pc	parsec: 3.0857×10^{18} cm
1 ly	light year: 9.46×10^{17} cm
AGB	Asymptotic Giant Branch
AGN	Active Galactic Nucleus
AMBER	VLTI NIR three-beam combiner
APEX	Sub-mm telescope of ESO at Llano Chajnantor
FINITO	External Fringe-trackr, to be used in addition of MIDI and AMBER
ESO	European Southern Observatory
HB	Horizontal Branch
HR	Hertzsprung-Russel diagram
H, K, L, M, N, Q	Atmospheric windows at 1.65, 2.2, 3.45, 4.7, 10, 20 μm
KI	Keck Interferometer
MACAO	VLTI-AO system
MS	Main Sequence
MIDI	VLTI MIR two-beam
MIR	Mid Infrared
NACO	VLT NIR AO imager / spectrometer
NIR	Near Infrared
OLBI	Optical Long Baseline Interferometer
OPD	Optical Path Difference
PSF	Point Spread Function
PRIMA	VLTI Dual star and astrometry facility
QSO, quasar	Quasi-Stellar Object, high luminosity AGN
RGB	Red Giant Branch
rms	Root-Mean-Square
RT	Radiative Transfer
SED	Spectral Energy Distribution
SF	Star Formation
SFR	Star Formation Rate
SFE	Star Formation Efficiency
SMBH	Supermassive Black Hole
SNR	Signal-to-Noise-Ratio
STRAP	VLTI tip-tilt correction system
VISIR	VLT MIR imager and spectrometer
VLT	Very Large Telescope
VLTI	Very Large Telescope Interferometer

Acknowledgements

First of all I would like to thank my family for all the support I was offered to benefit from.

"Declaration of Independence"– Selbständigkeitserklärung

Ich versichere, dass ich die von mir vorgelegte Dissertation selbständig angefertigt, die benutzten Quellen und Hilfsmittel vollständig angegeben und die Stellen der Arbeit – einschliesslich Tabellen, Karten und Abbildungen –, die anderen Werken im Wortlaut oder dem Sinn nach entnommen sind, in jedem Einzelfall als Entlehnung kenntlich gemacht habe; dass diese Dissertation noch keiner anderen Fakultät oder Universität zur Prüfung vorgelegen hat; dass sie – abgesehen von unten angegebenen Teilpublikationen – noch nicht veröffentlicht worden ist sowie, dass ich eine solche Veröffentlichung vor Abschluss des Promotionsverfahrens nicht vornehmen werde. Die Bestimmungen des Promotionsverfahren sind mir bekannt. Die von mir vorgelegte Dissertation ist von Prof. Dr. A. Eckart und Dr. habil. A. Glindemann betreut worden.

Köln, den   (Jörg-Uwe Pott)

Teilpublikationen:

Pott, J.-U.; Eckart, A.; Glindemann, A. et al. 2005, The Messenger, Vol.119, p.43,
  VLTI Observations of IRS 3
Pott, J.-U.; Eckart, A.; Krips, M. et al. 2005, Astronomy & Astrophysics, Vol.438, p.785,
  Relativistic jet motion in the core of the radio-loud quasar J1101+7225
Pott, J.-U.; Eckart, A.; Krips, M. et al. 2006, Astronomy & Astrophysics, Vol.456, p.505,
  Search for dense molecular gas in two QSO host galaxies

Curriculum Vitae

Name:	Jörg-Uwe Pott
Derzeitiger Arbeitgeber:	I. Physikalisches Institut, Universität zu Köln
	Zülpicher Str. 77, 50937 Köln, Deutschland
11.10.1975:	geboren in Düsseldorf, Deutschland als dritter Sohn von Roswitha und Wolfgang Pott
1982-86:	*St. Marien Grundschule Korschenbroich-Pesch*
1986-95:	*Gymnasium Korschenbroich*
Frühjahr 1995:	Erlangung des *Abitur*
Oct. 1995- Dec. 2001:	Studium der *Diplom-Physik* an der *Universität zu Köln*
in 1997:	*Vordiplom* in theoretischer und experimenteller Physik, Mathematik und Chemie in Köln
1998-'99:	Erhalt eines Sokrates/Erasmus-Stipendiums der Europäischen Union für einen einjährigen Studienaufenthalt an der *Universitá degli Studi Roma Tre*, Italien; Lehrveranstaltungen zu den Themen Allgemeine und AGN Astrophysik bei Prof. G.C. Perola und Dr. G. Matt
2001:	Ablegen der Abschlussprüfungen in theoretischer und experimenteller Physik, Mathematik und Astrophysik in Köln
Feb. 2002-Feb. 2003:	Anfertigung der Diplomaarbeit am I. Physikalischen Institut der Universität zu Köln, betreut von Prof. A. Eckart; Titel: *Nuclei of Active Galaxies, The Cases of NGC 3718 and J1101+7225.*[a]
17.2.2003:	Erlangung des Diplomgrades der Universität zu Köln
Mär. 2003 - Aug. 2003:	*wissenschaftlicher Mitarbeiter* an der Universität zu Köln
Sep. 2003-Nov. 2006:	Anfertigung der Doktorarbeit in Kollaboration zwischen der Universität zu Köln und der Europäischen Südsternwarte (ESO) in Garching bei München, betreut von Prof. A. Eckart und Dr. A. Glindemann; Erhalt eines ESO studentship Stipendiums, um 2.5 Jahre in der ESO Zentrale forschen zu können
Seit Feb. 2002	aktive Teilnahme an zahlreichen workshops, Konferenzen und Beobachtungsläufen

[a] http://www.ph1.uni-koeln.de/archives/DiplDiss/pott2003.pdf